Spectroscopic Properties of Luminescent Molecular Systems Coupled to a Tunable Sub-Wavelength Microcavity at Room and Low Temperatures

Dissertation

der Mathematisch-Naturwissenschaftlichen Fakultät

der Eberhard Karls Universität Tübingen

zur Erlangung des Grades eines

Doktors der Naturwissenschaften

(Dr. rer. nat.)

vorgelegt von

Saeed Nosrati

aus Mashhad/Iran

Tübingen

2025

Gedruckt mit Genehmigung der Mathematisch-Naturwissenschaftlichen Fakultät der Eberhard Karls Universität Tübingen.

Tag der mündlichen Qualifikation:	09.07.2025
Dekan:	Prof. Dr. Thilo Stehle
1. Berichterstatter/-in:	Prof. Dr. Alfred J. Meixner
2. Berichterstatter/-in:	Prof. Dr. Monika Fleischer

CONTENTS

Abbreviations

APD	Avalanche photodiode
AFM	Atomic force microscopy
CCD	Charge-coupled device
CW	Continuous wave
FWHM	Full width half maximum
NA	Numerical aperture
FRET	Förster resonance energy transfer
IC	Internal conversion
IRF	Instrument response function
ISC	Inter system crossing
LDOS	Local density of optical states
PW	Phonon wing
TCSPC	Time-correlated single photon counting
ZPL	Zero-phonon-line
AuNP	Gold nanoparticle
BS	Beam splitter
QD	Quantum dot
QS	Quantum yield
SMSM	Single molecule spectroscopy and microscopy
LHe	Liquid helium
MO	Microscope objective
PVA	Poly (vinyl alcohol)
TDM	Transition dipole moment
QED	Quantum electrodynamics
EBE	Electron beam evaporation
AIE	Aggregation-induced emission

Abstract

Optical microcavities are fascinating optical micro-devices that allow to control and modify light-matter interaction and open up exciting possibilities for advanced applications in photonics, quantum technologies, and materials science. This dissertation investigates the control of light-matter interactions in optical microcavities at room and low temperatures, with an emphasis on how the photonic mode density affects the light emission of single-photon emitters and non-radiative energy transfer processes between donor and acceptor. The research includes the study of single nitrogen-vacancy (NV) centers in a diamond at cryogenic temperatures, the control of multi-color Förster resonance energy transfer (FRET), and the exploration of strong coupling regimes in coupled Fabry-Pérot (F-P) microcavities. Control of light-matter interactions in optical microcavities at low temperatures presents several challenges like maintaining stable cryogenic temperatures for single-molecule spectroscopy, detecting single molecules within microcavities when the emission intensity is weak or molecules exhibit poor photostability, and suppressing unwanted background signals interfere with emission from single molecules within the cavity. In addition, fabricating high-quality $\lambda/2$ Fabry-Pérot microcavities with precise dimensions is essential for achieving the desired optical properties and coupling strengths.

A key aspect of this work is the use of single-molecule imaging and spectroscopy at cryogenic temperatures, which is the powerful technique to study the behavior of individual molecules with high accuracy where reduction of temperature leads to minimizing the thermal vibrations of molecules and resulting in sharper spectral lines. This technique enables high-resolution spectral measurements of individual molecules. Comparable in size to single molecules, NV centers act as highly stable single-photon emitters. NV centers are point defects in the diamond lattice, consisting of a nitrogen atom adjacent to a vacant lattice site. When a single NV center is placed in a microcavity, the spectral mode density influences the spectral and radiative properties of the NV center, leading to selective emission at resonance, narrow spectral linewidth, and enhanced photon emission through the Purcell effect. The unique optical

and quantum properties of NV centers, as well as their photostability, make them suitable samples to study single-photon imaging and spectroscopy.

Förster resonance energy transfer is a non-radiative process where energy can be transferred from a donor molecule to a close acceptor molecule through dipole-dipole coupling. A triple FRET process between three different dyes embedded in a single polystyrene nanosphere with excitation maxima at 505 nm, 575 nm, and 655 nm is studied here, where the single nanospheres were placed inside a Fabry−Pérot microcavity at low temperatures. To understand the impact of cavities on triple FRET, the lifetime and spectral properties of the individual nanospheres were measured as a function of the spectral optical mode density at low mode order. This allows us to control the interactions between the dyes effectively and to select enhancement of desired FRET processes while suppressing undesired interactions. The results show that the energy transfer rate between the three different dyes can be controlled by microcavity.

Combining optical strong mode coupling with polaritonic coupling in hybrid systems enhances light-matter interactions, leading to the formation of new hybrid modes and supermodes. Such a combination provides greater flexibility in manipulating both optical and electronic properties of the hybrid system. In this work a hybrid system is presented that combines optically strong mode coupling with polaritonic coupling within a $\lambda/2$ Fabry-Pérot microcavity. By integrating a thin TDBC J-aggregate film into an optical $\lambda/2$ microcavity coupled to a second microcavity, the study demonstrates the simultaneous occurrence of two strong coupling types: between purely optical modes of adjacent microcavities and between the TDBC J-aggregate molecules and the optical modes. This hybrid system's coupling strength and damping are highly sensitive to the position and concentration of the molecules in the microcavity, and the system can be modeled very effectively with coupled damped oscillators. The results highlight that the components of the coupled system cannot be treated independently; altering one parameter impacts the entire system.

Zusammenfassung

Optische Mikrokavitäten sind faszinierende optische Mikrovorrichtungen, die es ermöglichen, die Wechselwirkung zwischen Licht und Materie zu kontrollieren und zu verändern und eröffnen spannende Möglichkeiten für fortschrittliche Anwendungen in der Photonik, Quantentechnologien und Materialwissenschaft. In dieser Dissertation wird die Kontrolle von Licht-Materie-Wechselwirkungen in optischen Mikrokavitäten bei Raum- und Tieftemperaturen untersucht, wobei der Schwerpunkt darauf liegt, wie die photonische Modendichte, die Lichtemission von Einzelphotonen-Emitter und nichtstrahlende Energieübertragungsprozesse zwischen Donor und Akzeptor beeinflussen. Die Forschung umfasst die Untersuchung einzelner Stickstoff-Fehlstellen (NV-Zentren) in Diamanten bei kryogenen Temperaturen, die Kontrolle des mehrfarbigen Förster-Resonanz-Energieübertrags (FRET) und die Erforschung des starken Kopplungsregims in gekoppelten Fabry-Pérot (F-P) Mikrokavitäten. Die Kontrolle von Licht-Materie-Wechselwirkungen in optischen Mikroresonatoren bei niedrigen Temperaturen stellt mehrere Herausforderungen dar, wie etwa die Aufrechterhaltung stabiler kryogener Temperaturen für die Einzelmolekülspektroskopie, die Detektion einzelner Moleküle innerhalb von Mikrokavitäten, wenn deren Emissionsintensität schwach ist oder die Moleküle eine schlechte Fotostabilität aufweisen, oder di Unterdrückung unerwünschte Hintergrundsignale welche die Emission einzelner Moleküle innerhalb der Kavität überlagern. Darüber hinaus ist die Herstellung von qualitativ hochwertigen $\lambda/2$ Fabry-Pérot-Mikrokavitäten mit präzisen Abmessungen entscheidend, um die gewünschten optischen Eigenschaften und Kopplungsstärken zu erreichen.

Ein entscheidender Aspekt dieser Arbeit ist die Verwendung von Einzelmolekül-Bildgebung und -Spektroskopie bei kryogenen Temperaturen, sehr leistungsstarker Technik zur Untersuchung des Verhaltens einzelner Moleküle mit hoher Genauigkeit, bei der die Temperaturreduktion die thermischen Vibrationen der Moleküle minimiert und zu schärferen Spektrallinien führt. Diese Technik ermöglicht hochauflösende Spektralmessungen einzelner Moleküle. NV-Zentren, die in ihrer Größe mit Einzelmolekülen vergleichbar sind, fungieren als äußerst stabile

Einzelphotonen-Emitter. NV-Zentren sind Punktdefekte im Diamantgitter, bestehend aus einem Stickstoffatom, das an einem leeren Gitterplatz benachbart ist. Wenn ein einzelnes NV-Zentrum in eine Mikrokavität platziert wird, beeinfluss die spektrale Modendichte die spektralen und radiativen Eigenschaften des NV-Zentrums, was zu selektiver Emission bei Resonanz, engen Spektralbreiten und verstärkter Photonemission durch den Purcell-Effekt führt. Die einzigartigen optischen und quantenmechanischen Eigenschaften von NV-Zentren sowie ihre Fotostabilität machen sie zu geeigneten Proben für die Untersuchung der Einzelphotonen-Bildgebung und -Spektroskopie.

Förster-Resonanz-Energieübertragung ist ein nicht-radiativer Prozess, bei dem Energie von einem Donormolekül auf ein nahegelegenes Akzeptormolekül durch Dipol-Dipol-Kopplung übertragen wird. In dieser Arbeit wird ein dreifacher FRET-Prozess zwischen drei verschiedenen Farbstoffen mit Anregungsmaxima bei 505 nm, 575 nm und 655 nm untersucht, welche in einer einzelnen Polystyrol-Nanokugel eingebaut sind. Die einzelnen Nanosphären wurden bei niedrigen Temperaturen in eine Fabry−Pérot-Mikrokavität eingesetzt. Um die Auswirkungen der Kavitäten auf die dreifache FRET zu verstehen, wurden die Lebensdauern und spektralen Eigenschaften der einzelnen Nanosphären als Funktion der spektralen optischen Modendichte, bei niedrige Modenordnung gemessen. Dies ermöglicht es, die Wechselwirkungen zwischen den Farbstoffen gezielt zu steuern und die Verstärkung gewünschter FRET-Prozesse auszuwählen, während unerwünschte Wechselwirkungen unterdrückt werden. Die Ergebnisse zeigen, dass die Energieübertragungsrate zwischen den drei Farbstoffen durch die Mikrokavität gesteuert werden kann.

Die Kombination von starker optischer Modenkopplung und polaritonischer Kopplung in hybriden Systemen verstärkt die Licht-Materie-Wechselwirkungen und führt zur Bildung neuer hybrider Moden und Supermoden. Eine solche Kombination bietet größere Flexibilität bei der Manipulation sowohl optischer als auch elektronischer Eigenschaften des hybriden Systems. In dieser Arbeit wird ein hybrides System vorgestellt, das starke optisch Modenkopplung mit polaritonischer Kopplung in einer $\lambda/2$ Fabry-Pérot-Mikrokavität kombiniert.

Durch die Integration eines dünnen TDBC J-Aggregatfilms in eine optische $\lambda/2$ Mikrokavität, die mit einer zweiten Mikrokavität gekoppelt ist, zeigt die Studie das gleichzeitige Auftreten von zwei starken Kopplungstypen: zwischen rein optischen Moden benachbarter Mikrokavitäten und zwischen den TDBC J-Aggregat-Molekülen und den optischen Moden. Die Kopplungsstärke und Dämpfung dieses hybriden Systems sind äußerst empfindlich gegenüber der Position und Konzentration der Moleküle in der Mikrokavität. Das System lässt sich sehr gut effektiven mit gekoppelten gedämpften Oszillatoren modellieren. Die Ergebnisse heben hervor, dass die Komponenten des gekoppelten Systems nicht unabhängig behandelt werden können; die Veränderung eines Parameters hat Auswirkungen auf das gesamte System.

Motivation

In the modern world, understanding of light–matter interactions and energy transfer processes is crucial to address the critical challenges in technology and science. For example, optimizing energy transfer efficiency, enhancing biosensing sensitivity, and improving light-harvesting systems for renewable energy solutions require innovative approaches to enhance molecular-level precision and control.

This work studies energy transfer and coupling mechanisms at molecular and nanoscale levels in controlled environments, such as tunable microcavities and cryogenic conditions. The goal is to investigate the energy transfer dynamics within donor-acceptor pairs via dipole-dipole coupling in a tunable $\lambda/2$ microcavity which enables manipulation of the photonic density of states. By embedding FRET systems within cavities, this approach allows for precise control over light-matter interactions and the energy transfer rate of the coupled systems. In addition, doing single-molecule experiments at cryogenic temperatures ensure high-quality data, free from the effects of inhomogeneous spectral broadening, vibronic band overlapping, or conformational changes. Moreover, this study investigates the transition from weak to strong coupling, where the coupling strength surpasses damping rates, leading to hybridized modes like polaritons. These findings provide a deeper knowledge of how molecular systems behave under strong optical coupling conditions.

The aim of this study is to control the energy transfer process and to achieve selective emission by tuning microcavity resonance at the molecular level, by addressing fundamental questions about how molecules interact in optical environments. This knowledge is critical for practical applications in areas such as renewable energy, where light-harvesting efficiency can be improved; biosensing, where molecular interactions can be detected with greater precision; and quantum technologies, where coherence and hybridized states can be utilized for advanced devices.

Introduction

The invention of the microscope in the late 16th century has revolutionized the field of scientific research.[1] Among the various microscopic techniques created, optical microscopy has emerged as a crucial tool for using electromagnetic radiation in the ultraviolet, visible, and near-infrared spectral range.[2]

Fluorescence microscopy is a highly effective technique for studying molecular biology. It allows researchers to achieve exceptional spatial and temporal resolution, which is essential for detecting weak fluorescence signals.[3, 4] Over time, continuous advancements in optical microscopy instruments and electronic equipment, particularly in light sources, diode lasers, and detectors have led to significant advancements in sensitivity and molecular contrast. As an example, confocal microscopy could overcome the limitations of traditional fluorescence microscopy, and offers higher image quality, resolution, and contrast by suppressing out-of-focus light using a pinhole aperture.[5] This can be used to detect individual molecules and to measure fluorescence lifetime using time-correlated single photon counting (TCSPC) technique,[3, 6-8] which involves measuring the time delay between excitation and emission of individual photons. TCSPC provides more information about the interactions between molecules by calculating their lifetime and fluorescence decay rates. In addition, advanced techniques like fluorescence lifetime imaging microscopy (FLIM),[9-13] fluorescence correlation spectroscopy (FCS),[14-20] with labelling the molecules by fluorescent dyes can be used to study complex molecular interactions and dynamics.

One particularly interesting application of confocal microscopy is in the study of FRET[21] where an excited fluorescent molecule, known as a donor, transfers its energy to another fluorescent molecule, known as the acceptor, without emitting a photon through non-radiative dipole-dipole coupling.[22, 23] In addition, the efficiency of energy transfer in a FRET pair can be influenced by microcavity which is composed of two reflective mirrors.[22, 24] When a donor and acceptor are placed in a microcavity, the interaction between the light and the molecules can modify properties such as emission intensity, energy transfer efficiency, and radiative decay rates of the FRET pairs.[25-28] Tuning the resonant frequency

of the cavity by changing the cavity length, influences on fluorescence lifetimes of donor and acceptor.[23, 24, 29-43] A shorter fluorescence lifetime of the donor fluorophore in the cavity and a corresponding increase in the fluorescence lifetime and intensity of the acceptor fluorophore is a sign of increasing FRET efficiency while a reduction in FRET efficiency depends on change in the orientation factor, the quenching effect, the refractive index of the cavity[44] and the modification of the spectral overlap between the donor and acceptor.[3, 31, 45, 46] FRET is an essential tool in biology and biochemistry research. It is widely used for studying molecular imaging[47] and conformational changes in biomolecules. In drug discovery,[48] FRET-based assays are used to screen potential drugs that affect protein-protein interactions. Integrating FRET with optical microcavities provides a platform to offer promising applications for biosensing[49]. These microcavities are in various types, each with distinct optical properties and applications, enhancing the capabilities of FRET-based sensing systems. One common type is the Fabry-Pérot cavity, which consists of two parallel mirrors that are separated by multiple of half a wavelength of light.[28, 50, 51] The performance of a Fabry-Pérot cavity can be optimized by adjusting the reflectivity of the mirrors and reducing losses due to absorption and scattering. The tunable Fabry-Pérot cavity allows tunning the resonant frequency of the cavity to a specific wavelength of light. The cavity length can be adjusted by varying the distance between the mirrors using a tuning mechanism, such as a piezoelectric actuator.[52] The tunable cavities are able to select a narrow range of frequencies from a continuous spectrum of light while they are typically sensitive to changes in temperature and vibration, which can cause shifts in the cavity length.

Other types of microcavity are Micropillar cavities[53] (typically cylindrical structures that are made up of a central pillar surrounded by a Bragg mirror), photonic crystal cavities[54-60] (structures that are designed to have a periodic variation in their refractive index), and Whispering gallery mode cavities[61, 62] (spherical or cylindrical structures that trap light through total internal reflection). The performance of an optical microcavity is typically characterized by its quality factor (Q-factor) which is a measure of how well the cavity can store energy and is related to the width of the resonant peak in the cavity's spectral

response. The Q-factor of different types of resonant cavities can range from approximately 10 to 10^8, depending on their design, materials, and operating conditions.[53, 63-65] However, it is important to note that the actual Q-factor of a resonant cavity can be influenced by many factors, including temperature, pressure, material properties, and the presence of impurities or defects.

In high-Q microcavities, strong interactions can occur between molecules and cavity resonances[44, 66] leading to spectral changes such as mode splitting, mode coupling, and mode hybridization.[67-71] For example, mode splitting can be used to create two resonant peaks with different frequencies, while mode hybridization can be used to create new hybrid modes with unique properties which can be observed as a vacuum Rabi splitting in the emission spectrum.[72-79] There has been lot of research effort on strong coupling of light-matter in F-P microcavity.[52, 70, 80-84] The light-matter interaction[85] inside a Fabry-Pérot cavity is influenced by the resonant nature of the cavity, which enhances the coupling between light and the material by modifying the photonic density of states. In non-resonant conditions, the coupling is generally weaker but can still be affected by the cavity to alter the local density of states.

These improvements in light-matter interaction, especially the enhancement of spontaneous emission rates via the Purcell effect, are particularly valuable in advancing microscopy techniques. The development of sensitive photon detectors and imaging techniques has enabled investigations at the single-molecule level where the movement of molecules and the interactions between molecules can be tracked within cells. Single molecule microscopy also allows for the observation of dynamic processes in real-time, which is not possible with ensemble samples where the detected signal is an average of all the molecules in the sample.[86-88]

To achieve accurate and reliable results in single molecule experiments, it is important to consider not only the high-resolution imaging technique but also the stability of the molecule and the environment in which the molecule is placed. One extraordinarily photostable sample is NV centers in fluorescing nanodiamonds. An NV center is a point defect in the diamond lattice where a nitrogen atom is adjacent to a vacant lattice site. These centers serve as stable single-photon emitters, offering remarkable photostability and resistance to

photobleaching and blinking.[89-91] Decreasing the temperature of the system can significantly enhance the accuracy and reliability of experimental results. Reduced thermal energy enhances photostability by minimizing photobleaching fluorophores or emitters. Furthermore, the suppression of thermal motion and spectral diffusion at lower temperatures contributes to sharper spectral features and increased measurement precision.[92-94] At low temperatures, the zero-phonon line (ZPL) becomes well-defined and narrower. The ZPL corresponds to the transition of an electron between two energy states without the involvement of phonons. The phonon sidebands are weak and well-separated from the ZPL allowing for accurate measurements of the phonon density of states.[95-97]

The experiments and results in this thesis are based on optical microscopy and spectroscopy with a particular focus on the confocal microscopy technique. This approach was used to study the impact of light-matter interaction on a triple-FRET system[98-105] within a tunable F-P microcavity at room and cryogenic temperatures. A tunable microcavity that can be controlled in three axes (x, y, z) has been designed and developed to operate in a cryostat. In addition, a coupled microcavity system[70] comprising of a fixed and tunable cavity is used to achieve strong mode coupling between two cavities, as well as polaritonic coupling between the cavity modes and the excitons of the TDBC molecules. It allows for the investigation of the position and quantity of molecules within the cavity on the coupling and damping parameters of coupled optical systems.

Chapter 1 of this thesis provides an in-depth description of theoretical background of the interaction between light and matter starting with an introduction into the principles of fluorescence microscopy, lifetime, FRET, and TCSPC. The chapter discusses photobleaching and photoblinking of a single molecule, as well as antibunching.

Chapter 2 introduces the concept of an optical microcavity and its characterization, including the properties of a Fabry–Pérot microcavity. The chapter further discusses the coupling of cavity and quantum emitters, including weak and strong coupling.

Chapter 3 provides a comprehensive overview of the experimental techniques used in this research, including detailed information on the optical setup, home-built confocal scanning microscope, cryogenic setup, as well as sample preparation procedures for the molecules.

Then **Chapter 4** describes the confocal scanning microscope setup used to perform experiments of single molecule imaging and spectroscopy in a multiple of half a wavelength tunable microcavity at low temperatures ≤ 5 Kelvin.

Chapter 5 then discusses the ability to control triple FRET energy transfer between three fluorescent dyes embedded within a single polystyrene nanosphere using the Purcell effect in an optical Fabry-Pérot microcavity. The microcavity modulates the radiative rates and fluorescence intensities of the dyes, leading to significant enhancement in the fluorescence intensity of the second acceptor.

Chapter 6 focuses on using an optical microcavity to study light-matter interactions, specifically the coupling of a quantum emitter to the optical field. A coupled harmonic oscillator model is defined to determine the coupling and damping constants of the system. The study demonstrates strong coupling of the TDBC J-aggregate film with the coupled microcavities, with the Rabi splitting of the molecule/cavity hybrid system.

Chapter 7 highlights the potential of merging semiconductor nanocrystals with molecular aggregates to produce novel optical properties such as dual fluorescence with oscillating intensity fluctuations. The feedback loop mechanism in the hybrid thin film of CdSe nanocrystals and aryleneethynylene aggregates presents a promising avenue for developing nanothermometry applications.

1.1 Introduction of Fluorescence

Fluorescence microscopy is a powerful and highly sensitive optical technique that is extensively used in different fields such as biology, medicine, and materials science. This technique uses fluorescent probes or dyes that emit light when excited by a specific wavelength of light. Despite the emergence of advanced imaging technologies, this method remains a critical tool to show the mysteries of life at the molecular level and offers valuable insights into the dynamics and interactions of individual molecules.[4]

One of the main drawbacks of fluorescence microscopy is photobleaching, a process where fluorescent molecules or probes lose their ability to emit light after repeated exposure to illumination which leads to limitation of the duration of imaging experiments. This method requires fluorescent probes with specific excitation and emission wavelengths, which can limit the variety of probes available for certain experiments. While conventional fluorescence microscopy is useful for imaging thin samples, as it has challenges to produce high-quality images in thicker tissues due to light scattering and out-of-focus fluorescence,[3] Confocal fluorescence microscopy offers an advantage by using optical sectioning, which allows for high-resolution, three-dimensional imaging of thicker transparent samples. This technique involves scanning the sample with a focused laser beam, either by moving the sample under a stationary laser focus (sample scanning) or by scanning the laser focus across the sample (laser scanning). Confocal microscopy provides multiple advantages including improved resolution, increased contrast, and reduced background noise. It is also suitable for imaging live cells and tissues, making it a valuable tool in biological and medical research.[5]

1.2 Jablonski Diagram

This chapter outlines the principles of fluorescence emission from excited quantum emitters (QE), which form the basis of most experiments in this work. To gain a comprehensive understanding of the light absorption and emission

processes in quantum emitters, such as fluorescent dye molecules, a Jablonski diagram is provided in Figure 1. The diagram illustrates the various photophysical processes when a molecule absorbs a photon, it can undergo a transition from the initial ground state S_0 to a higher vibronic level of excited states, such as S_1 or S_2, if the energy of the incident photon is equivalent to the energy gap between the initial occupied state and the final unoccupied state. The energy difference E_0 between the first electronic excited state and the initial ground state is also explained as:

$$E_0 = h\nu_0 \qquad (1)$$

whereby h is Planck constant and ν_0 is the light frequency. Once the absorption process is complete, the energy of the excited molecule can undergo various pathways, as illustrated in the Jablonski diagram in Figure 1. These include fluorescence, intersystem crossing, vibrational relaxation, internal conversion, and phosphorescence.

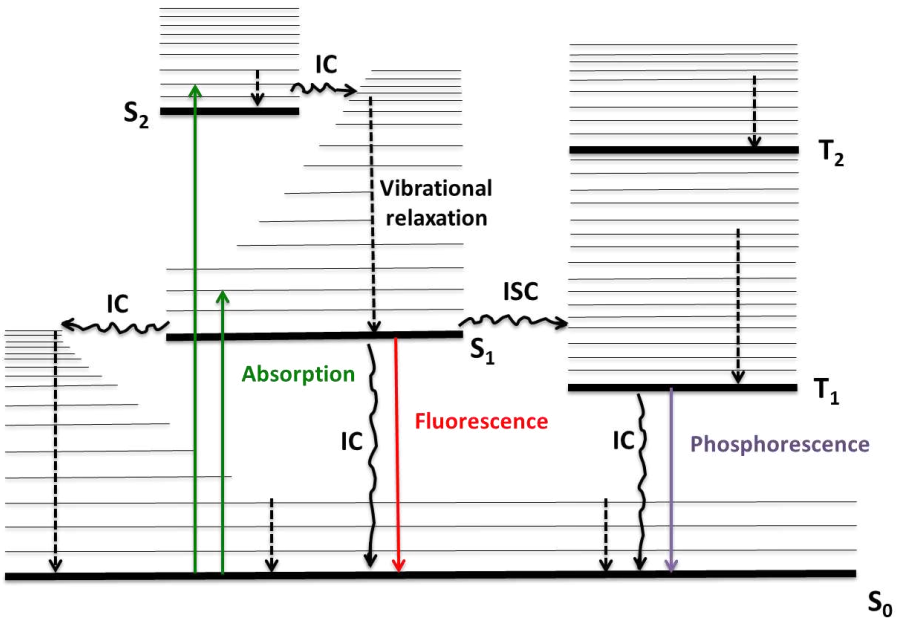

Figure 1: Jablonski diagram representing the electronic states of a fluorescent molecule and possible transitions between them (Inspired by[4]). Absorption (green arrow): A transition from the ground state to the excited electronic states by absorption of a photon. Fluorescence (red arrow): A radiative transition on the order of nanoseconds by emission of photons. Phosphorescence (purple

arrow): Light emission by de-excitation from triplet states to singlet ground state. Internal conversion (IC) and intersystem crossing (ISC) as black waved arrows are non-radiative transitions between the electronic states of the same and different spin multiplicity, respectively. Vibrational relaxation (dashed black arrows) is a rapid non-radiative transition to lower vibrational levels within the same electronic state.

The electronically excited states of molecules can include multiple vibronic energy levels as shown in Figure 1. As a result, when a molecule is excited, it can return to a lower energy level by undergoing vibrational relaxation to the 0 vibrational level of S_1. Additionally, a non-radiative transition from a higher electronic state S_2 to a lower electronic state S_1 can occur through internal conversion.[106] Fluorescence is a radiative transition that involves the emission of a photon from the first electronically excited levels to the electronic ground state, which occurs in a timescale of nanoseconds for an organic dye molecule. Typically, there is a red shift in the fluorescence spectrum relative to the absorption spectrum, which is referred to as a Stokes shift. This shift is caused by vibrational relaxation and energy loss that occurs in the excited state after excitation and before emission of the photon. Another possible de-excitation process is non-radiative, known as intersystem crossing (ISC), which occurs between S_1 and an isoenergetic vibrational level of T_1. In this process, the excited molecule can move to the triplet state T_1 and relax to the lowest vibrational level before radiatively de-exciting to the ground state as phosphorescence emission. However, the forbidden transition from T_1 to S_0 leads to a low radiative rate constant for the phosphorescence process and a long triplet lifetime, which can range from microseconds to seconds, depending on the molecule.[3] An alternative relaxation path to the emission of a photon is always internal conversion which is non radiative.

1.3 Franck-Condon Principle

The Franck–Condon principle precisely describes the intensities of vibronic transitions both in absorption and emission. According to the Born-

Oppenheimer approximation, the movement of electrons is faster than the nuclear movement due to low electron mass. Consequently, during an electronic transition, the nuclei retain their initial dynamic state, meaning the nuclear wavefunction does not change during the electronic transition.[3, 107] The vertical electronic transition shown in Figure 2 is in accordance with the Franck-Condon principle.

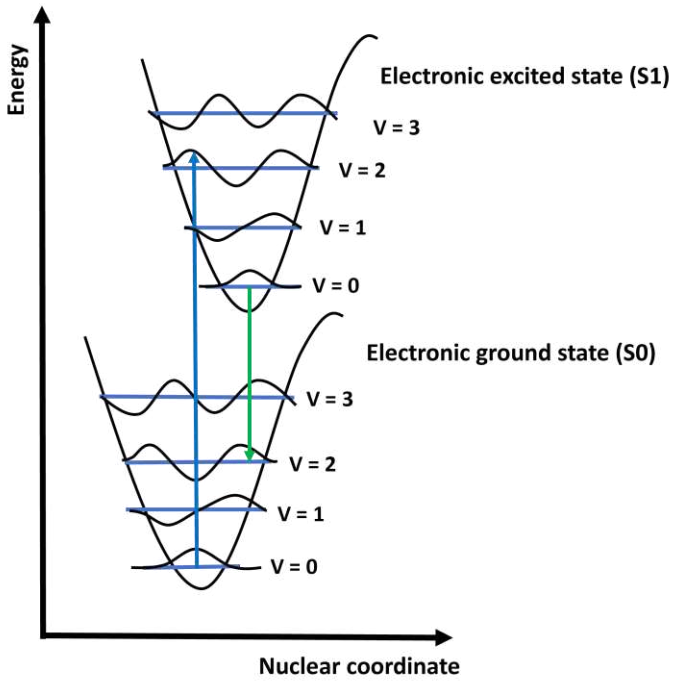

Figure 2. (a) Franck-Condon principle illustrated for a bi-atomic molecule: The potential energy is plotted in term of the nuclear with vertical transitions (Inspired by[4]). Absorption transition (blue arrow) and fluorescence transition (green arrow) are shown for ground (S_0) and excited (S_1) states together with the nuclear wave functions for the energy levels v = 0, 1, 2, 3.

High-intensity vibronic transitions can occur from the lowest vibrational level of the ground state to the upper vibrational level of the lower electronic level when the overlap of the respective nuclear wave functions is large. Transitions to other vibronic levels can also occur with lower intensity. The absorption of light occurs when the energy of the incident photon matches the energy difference

between two electronic states of a molecule.[107] To determine the strength of coupling between the electronic transition and the electromagnetic field, it is necessary to calculate the transition dipole moment (TDM) of the molecule. The TDM of a molecule is expressed as follows:

$$\mu_{if} = \langle \psi_f \mid \hat{\mu} \mid \psi_i \rangle \qquad (2)$$

Where $\psi_i \; and \; \psi_f$ are the electronic wavefunctions of the initial and final states, respectively and $\hat{\mu}$ is the transition dipole moment operator. Since the transition intensity is proportional to the square of the magnitude of the transition dipole moment $|\mu_{if}|^2$, absorption intensity is proportional to $|S(v_f, v_i)|^2$, which is called Franck–Condon factor and quantifies the probability of a vibronic transition between the initial and final vibrational level in the electronically excited state. The absorption intensity for vibrational and electronic transitions is directly related to the degree of overlap between the nuclear wavefunctions of the upper and lower electronic states. As this overlap becomes greater, the absorption intensity increases.[107]

1.4 Fluorescence Lifetime and Quantum Yields

The fluorescence lifetime refers to the duration a molecule remains in its excited state before returning to its ground state and emitting a photon.[4] The decay constant of excited state S_1 is given by:

$$\tau = \frac{1}{\kappa_r^s + \kappa_{nr}^s} \qquad (3)$$

Where τ is the lifetime and κ_r^s, κ_{nr}^s are rate constants for radiative and non-radiative deactivation from S_1 to S_0, respectively. When a fluorescent molecule absorbs a photon and is excited, it can either return to its ground state by emitting a photon through fluorescence, or through non-radiative processes. In case of de-excitation of a molecule only *via* radiative decay and neglecting the non-radiative decay rate, the fluorescence lifetime can be expressed as:

$$\tau = \frac{1}{\kappa_r^s} \tag{4}$$

The fluorescence lifetime of a molecule is sensitive to the surrounding environment. Environmental variations such as temperature, solvent polarity, and energy transfer to acceptors can change the rates of radiative and non-radiative decay, leading to fluorescence lifetime shortening or extension.

The fluorescence quantum yield[4] is a fundamental parameter used to describe the efficiency of a fluorescent molecule in converting absorbed light into emitted fluorescence. It is described as the proportion of photons emitted via fluorescence to the number of photons absorbed by the molecule. A high fluorescence quantum yield indicates a high efficiency of fluorescence emission, while a low fluorescence quantum yield indicates a high rate of non-radiative decay. The intensity of fluorescence relies on the quantum yield; therefore, the fluorescence quantum yield is a fraction of the emitted photons with respect to the photons absorbed:

$$\phi = \frac{\text{number of photons emitted}}{\text{number of photons absorbed}} \tag{5}$$

In form of κ_r^s, κ_{nr}^s can be written as:

$$\phi = \frac{\kappa_r^s}{\kappa_r^s + \kappa_{nr}^s} \tag{6}$$

In principle, the fluorescence quantum yield is affected by a variety of factors, including the molecular structure of the fluorophore, the solvent environment, temperature, and the presence of quenching agents. For example, the fluorescence quantum yield of a molecule can be increased by modifying its structure to reduce non-radiative decay pathways, or by changing the solvent environment to reduce collisional quenching.[3]

1.5 Förster Resonance Energy Transfer

Förster resonance energy transfer[108] is a widely used technique for studying molecular interactions and conformational changes. This process was first described by Theodor Förster in 1948,[108] who derived a theoretical model to explain the distance dependence of the energy transfer efficiency. It involves the transfer of energy from an excited donor fluorophore to an acceptor fluorophore in proximity, without the emission of a photon. FRET is based on the dipole-dipole interaction between the donor and acceptor fluorophores, which occurs when the emission spectrum of the donor overlaps with the absorption spectrum of the acceptor. The efficiency of FRET depends on the distance and orientation between the donor and acceptor molecules, which should be within a range of 1-10 nm, as well as their spectral overlap between their emission and absorption spectra.[43, 109-111] FRET can be detected by monitoring changes in the fluorescence emission of the donor and acceptor fluorophores, such as changes in fluorescence intensity, lifetime, or polarization. When energy is transferred from donor to acceptor the fluorescence intensity of donor decreases while the intensity of acceptor increases.

FRET efficiency is characterized by the proportion of energy successfully transferred from the donor molecule to the acceptor molecule relative to the total energy initially absorbed by the donor. The transfer rate constant K_T represents the rate at which energy is transferred from the donor to the acceptor and is described in detail as an expression of energy transfer:

$$K_T = \left(\frac{Q_D \kappa^2}{\tau_D r^6}\right)\left(\frac{9000\ (ln10)}{128\pi^5 N n^4}\right).J(\lambda) \qquad (7)$$

Where Q_D and τ_D are the fluorescence quantum yield and lifetime of the donor without acceptor, respectively. n is the refractive index of the matrix. r describes the distance between donor and acceptor chromophore which is defined as the center distance of the respective transition dipole vectors. N is the Avogadro number and κ^2 denotes the spatial orientation of the respective transition dipole moments. The orientation factor κ^2 in equation 8 has to be

taken into account according to:

$$\kappa^2 = (\cos\Theta_T - 3\cos\Theta_D \cos\Theta_A)^2 \quad (8)$$

Where Θ_T denotes the angle between blue and brown plane in Figure 3a and is the angle between the transition dipole moment of donor emission and acceptor absorption, while Θ_D and Θ_A depict the angle of the transition dipole moment of donor and acceptor, respectively. $J(\lambda)$ is the integral of the spectral overlap between the absorption spectrum of the acceptor and the emission spectrum of donor, given by:

$$J(\lambda) = \int_0^\infty F_D(\lambda)\ \varepsilon_A(\lambda)\ \lambda^4 d\lambda \quad (9)$$

Whereas ε_A denotes the absorption coefficient of the acceptor and $F_D(\lambda)$ the donor emission spectrum normalized to the area. To determine the coinciding eigenfrequencies of donor and acceptor oscillations, this spectral overlap is necessary. The oscillation generated by the donor can be coupled to the acceptor and leads to oscillation of the acceptor with its distinct eigenfrequency when the emission spectrum of the donor overlaps with the absorption spectrum of the acceptor. In this region, the photons emitted by the donor possess enough energy to be absorbed by the acceptor. FRET mechanism is presented in Figure 3b.

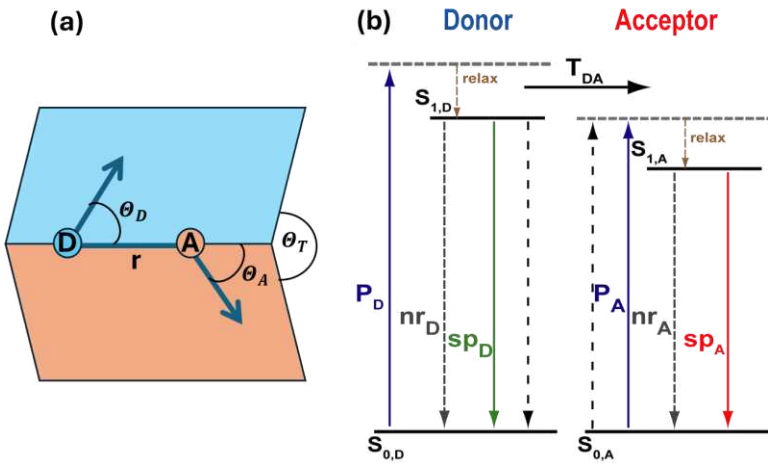

Figure 3. (a) Illustration of the orientation factor κ. (b) Scheme of FRET mechanism and energy diagram of donor and acceptor (Inspired by[4]).

In Figure 3b, the donor is excited from the ground state $S_{0,D}$ to a higher vibronic level of the first excited state with a pumping rate P_D and relaxes very fast to the lowest vibronic level of the first excited state $S_{1,D}$. The donor may relax to its ground state either with a non-radiative nr_D or the spontaneous emission sp_D rate. Energy transfer occurs from the donor by the rate T_{DA} to excite the acceptor to a higher vibronic level of its excited state. Acceptor can relax from its electronically excited state ($S_{1,A}$) to its ground state ($S_{0,A}$) by non-radiative (nr_A) or radiative (sp_A) decay pathways. This release of the transferred energy by the acceptor *via* nr_A and sp_A prevents the possibility of energy transferring back to the donor. In FRET, the dominant mechanism is typically the long-range dipole-dipole interaction. The energy transfer efficiency is inversely related to the sixth power of the distance between the acceptor and donor. The efficiency, η_T, of resonance energy transfer is defined as:

$$\eta_T = \frac{R_0^6}{R_0^6 + r^6} \tag{10}$$

Where R_0 is Förster radius and r is the center-to-center distance of each donor-acceptor pair. The Förster radius is the distance where the energy transfer efficiency is 50%, and it depends on the quantum yield of the donor, the refractive index of the medium, the spectral overlap between donor emission and acceptor absorption, and an orientation factor.[108, 112] Equation 10 demonstrates that the transfer efficiency is dependent on the distance when the donor and acceptor distance is near R_0. Once the value of R_0 is known the rate of energy transfer from donor to acceptor is given by:

$$k_T = \frac{1}{\tau_D}\left(\frac{R_0}{r}\right)^6 \tag{11}$$

Where τ_D is the fluorescence lifetime of the donor in the absence of acceptor. Transfer efficiency can be measured directly from the relative fluorescence intensity of the donor with (I_{DA}) and without acceptor (I_D):

$$\eta_T = 1 - \frac{I_{DA}}{I_D} \quad (12)$$

Or can be calculated by the lifetime:

$$\eta_T = 1 - \frac{\tau_{DA}}{\tau_D} \quad (13)$$

In fluorescence microscopy, FRET can be used to visualize molecular interactions in live cells and tissues, and to investigate molecular interactions, such as protein-nucleic acid interactions, protein-protein interactions, and protein-lipid interactions, where the proximity of the donor and acceptor fluorophores can be influenced by the interaction. FRET is more effective as a tool for detecting proximity between molecules rather than for measuring exact distances.[4]

1.6 Single-Molecule Spectroscopy and Microscopy

A single molecule is not isolated as an individual element of nature, and it can be covered by neighboring molecules which have an impact on its individual spectral properties. However, single-molecule spectroscopy can be also useful to provide information for the local chemical environment. Single-molecule spectroscopy provides new opportunities to study a wide range of analytical, chemical, biological, and physical properties and behavior of a single molecule. In addition, it gives detailed information about the rate of molecular conformational changes, short-lived or transient states, and rare molecular events. Single-molecule microscopy uses advanced imaging techniques to study individual molecules in real time. This is a highly sensitive technique which makes it susceptible to noise and other sources of interference. This technique can be time consuming as it requires the acquisition of large amounts of data to detect, measure and analyze even small changes in the behavior of individual molecules. The unique feature of single-molecule spectroscopy and microscopy (SMSM) is that it deviates from the standard ensemble averaging approach, and it reveals complex fluctuation phenomena that are hidden in standard ensemble methods. The SMSM technique focuses on the study of

dynamical fluctuations such as photon counting, spectral diffusion, antibunching, triplet blinks and quantum jumps, and study of distribution of line shapes of single molecules at low temperatures.[113]

The main challenge of single-molecule measurements is the detection of molecule's fluorescence signal from the background noise due to the weak signals. Single molecules can be embedded into a non-fluorescent matrix to isolate and observe individual fluorophores. Non-fluorescent entities within this matrix can unexpectedly contribute to the generated background signals through mechanisms such as light scattering, refractive index modulations, and subtle chemical interactions that alter the local optical properties and negatively affect the detection and analysis of the target molecules. Additionally, the origin of background photons might be from fluorescence or Raman and Rayleigh scattering impurities and the imperfections in the matrix material. When this background signal becomes excessively prominent, the signal-to-noise ratio falls below the detection threshold and distinguishing the emission of individual molecules can be impossible.[3]

To accurately distinguish the emission of a molecule from background signals, it is important to consider the maximum number of detected photons over a certain time. This estimation can be helpful to set appropriate detection thresholds and optimize the imaging conditions for improved sensitivity. By scanning a sample with a focused laser beam, fluorescent molecules undergo repeated cycles of photon absorption and emission. The emitted photons signal the presence of the molecule and help differentiate it from background noise. To understand this process quantitatively, it is necessary to estimate the maximum number of photons that can be emitted by a molecule. The photon emission rate of a molecule is limited by its excited-state lifetime. The maximum number of emitted photons can be approximated by dividing the transit time of the molecule through the beam by its excited-state lifetime, assuming near-unity quantum yield.

For example, if a molecule has a transit time of 1 ms through the laser focus and an excited-state lifetime of 1 ns, it could theoretically emit up to 10^6 photons. However, the maximum number of emitted photons can be limited by photobleaching effects to around 10^5. To maximize the detection of emitted

photons and minimize background noise, it is important to use optical systems designed with high numerical aperture.[4] Therefore, to mitigate the background issue, the most straightforward approach is to minimize the background signal by reducing the detection volume and using highly cleaned substrates (see section 3.6). Thus, a critical prerequisite for ensuring accurate and reliable measurements in single-molecule spectroscopy is to minimize the influence of undesirable neighboring molecules by restricting the sample volume. Due to the inherent large sample volumes of cuvette-based methods, this technique is unsuitable for single-molecule spectroscopy. In such a setting, a single dye molecule is surrounded by a substantial number of solvent molecules. While the solvent molecules themselves generally do not produce significant background signals, impurities within the solvent can introduce unwanted background noise, potentially affecting the fluorescence of the molecules of interest. To achieve a minimal detection volume, the molecules can be located in a thin polymer film, which greatly restricts the sample volume along the axial direction and using confocal microscopy to block out-of-focus light and confine the detection volume to the optical diffraction limit. For instance, when considering a surrounding matrix with an average thickness of 50 nm and assuming a molecular size of approximately 1 nm^3, the focal volume contains approximately 1 to 5 million molecules. To have a reasonable signal-to-noise ratio and successfully detect a single individual molecule among a million, the molecules of matrix should not absorb or emit at the excitation wavelength of samples molecules. In addition, the results of the fluorescence quantum yield and the absorbance cross-section values at the excitation wavelength of the single molecule must be high enough to be detected by detector. This requirement can be achieved by using ultrapure transparent polymers such as polyvinylalcohol (PVA) or polymethylmethacrylate (PMMA).[106]

1.7 Time-Correlated Single-Photon Counting (TCSPC)

The principle of time-correlated single-photon counting[6] is to record the arrival time of photons emitted by a fluorescent molecule in response to a short pulse of excitation light. TCSPC counts the single emitted photons in time intervals

correlated to the excitation laser pulse. This method is based on a short pulse laser with a high repetition rate and precise time acquisition of single emitted photons with a sensitive single-photon detector. The detection system of TCSPC consists of a single-photon detector and a time-to-digital converter (TDC) circuit. The TDC circuit records the arrival time of each photon. The detected photons create a waveform which is a distribution of the photon probability over time in the detector. This waveform is like a decay curve and by fitting the decay curve to a theoretical model, the fluorescence lifetime of the molecule can be determined with high precision.[8] The principle of TCSPC shown in Figure 4.

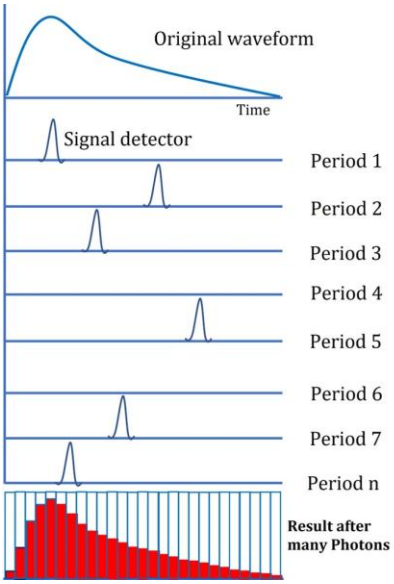

Figure 4. Principle of the TCSPC technique. Each period shows the detection of single photons corresponding to the original waveform. The bottom histogram aggregates the detected photons over many periods, illustrating the photon counting statistics and reconstructing the original waveform (Inspired by[3]).

The detector signal in TCSPC comprises of a series of distributed pulses which are related to the detection of individual photons. Numerous periods are in the signal with no photons, while other periods contain only one photon pulse. When a photon is detected, the corresponding time of the detector pulse is recorded. Therefore, detection of two or more photons in a single interval is

unlikely. By detecting numerous photons in different periods, the histogram of detection times is accumulated in the memory, resulting in the formation of the waveform of the optical pulse. Time resolution in TCSPC systems is determined by the transit time spread (TTS) of the single-photon pulses, which is much narrower—by a factor of 10—compared to the single-photon response of the detector. Therefore, the instrument response function (IRF) has a much narrower pulse width than the single-photon response. Fast time recording and no loss of photons are two important features of TCSPC, which lead to high photon efficiency in fluorescence lifetime measurements. TCSPC modules have several advantages such as high sensitivity to detect photons emitted by a single molecule and have a wide dynamic range to measure fluorescence lifetimes from picoseconds to microseconds.

1.8 Photobleaching and Photoblinking of a Single Molecule

In fluorescence microscopy, a high-intensity light source excites fluorophores within the sample, leading to the emission of fluorescent. However, prolonged light exposure and absorption by the molecule can result in a photochemical reaction, causing structural changes and subsequent loss of fluorescence. This process is known as photobleaching. The photobleaching effect of a single molecule refers to the loss of fluorescence intensity over time as a result of a photochemical reaction. The loss of fluorescence can lead to difficulties in tracking individual molecules over time or in obtaining accurate measurements of molecular interactions. Photobleaching is a major concern in fluorescence techniques, as it can cause irreversible damage to the fluorophore. This phenomenon occurs due to the interaction of the excited fluorophore with molecular oxygen or impurities in the solution, resulting in a reduction of the fluorescence intensity of the fluorophore over time. Some fluorophores are more susceptible to photobleaching and can only undergo a few excitation and emission cycles before degrading, while others are more robust and can tolerate thousands or even millions of cycles.

Photobleaching can be mitigated by optimizing experimental conditions, such as reducing the intensity and exposure duration of the excitation light to minimize photo-induced damage, using fluorophores with higher photostability, or performing experiments in an inert atmosphere, such as nitrogen or argon. Additionally, some single molecule techniques, such as single-molecule Förster resonance energy transfer, take advantage of the photobleaching effect to determine the presence or absence of specific molecules in a sample.

Photoblinking is a phenomenon where a fluorescent molecule switches between "bright" (on) and "dark" (off) states during continuous excitation. In the bright state, the molecule emits light as electrons in the fluorophore occupy the singlet excited state S_1 and undergo normal fluorescence cycles of absorption and emission. In contrast, in the dark state, the molecule does not emit light as electrons enter long-lived non-fluorescent states. This can occur due to various processes such as transitions to triplet states, conformational changes, or non-radiative decay pathways. An important mechanism for fluorophore blinking is intersystem crossing from a singlet excited state to a triplet state. For an ensemble with a total number of fluorophores S_T the fluorescence intensity is proportional to the population of the S_1 state which can be described by following kinetic equation:[3]

$$S_1 = \frac{\sigma I_e S_T}{\tau^{-1} + \sigma I_e (1 + \frac{k_{isc}}{k_{ph}})} = \frac{\tau \sigma I_e S_T}{1 + \frac{I_e}{I_s}}. \qquad (14)$$

The rate of excitation is directly proportional to both the cross-section for absorption σ and the excitation intensity I_e. The intensity of the S_1 population shows a hyperbolic dependence on I_e.[3] The dependence of S_1 on the rate constants is the steady-state solution of these equations.

1.9 Antibunching

The antibunching experiment is designed to investigate the statistical properties of photon emission from individual emitting species, such as single molecules or quantum dots. This is typically achieved by isolating a single emitter and

controlling the rate at which it emits photons. The radiative lifetime of a transition (τ_R) is the duration it takes for a photon to be emitted after the initial photon emission, resulting in a time interval between successive photon emissions. The second-order correlation function $g^2(\tau)$ offers an approach to classify light, as antibunched light when the photons emit with regular time intervals. This is investigated via Hanbury Brown-Twiss experiments in 1950s. The observation of antibunched light is convincing proof of the quantum nature of light. The normalized second correlation function is defined as

$$g^2(\tau) = \frac{\langle I(t)I(t+\tau)\rangle}{\langle I(t)\rangle^2}, \tag{15}$$

where $I(t)$ is the intensity at a time t and the intensity at the time $(t+\tau)$ is $I(t+\tau)$ and the time interval τ can be positive or negative. The brackets stand for time averaging over a timespan that is much larger than τ.

If $\tau = 0$, therefore

$$g^2(0) = \frac{\langle I(t)^2\rangle}{\langle I(t)\rangle^2}. \tag{16}$$

For an intensity signal that consists of single photons, three different cases have to be considered:

For the photons arrive at the detector in bunches $g^2(0) > 1$, for coherent light $g^2(0) = 1$ consistent with classical results. It is important to note that a single molecule emits only one photon at a time. If the molecule is re-excited immediately after the first photon has been detected, the fluorescence lifetime must pass before the second photon will be detected, hence for antibunched light

$$g^2(0) < 1, \tag{17}$$

and

$$g^2(0) < g^2(\tau). \qquad (18)$$

Figure 5 shows the Hanbury Brown–Twiss (HBT) experiment, where a photon stream is directed onto a 50% beam splitter and detected by two single-photon counting detectors. The numerical analysis evaluates the temporal correlation between the recorded arrival times. It is crucial to mention that using two detectors is a common practice to compensate for the detectors' dead times following the photon-counting procedure. The correlation between photon arrival times allows for the calculation of the probability of detecting a photon by two detectors within a specific time period ($t + \tau$). When τ = 0, the probability for a single emitter drops to zero, making it impossible to detect photons simultaneously in both detectors. By correlating the photon arrival times in both detectors, a zero correlation at a specific time t can be observed, which represents the zero probability of detecting two photons in that time. A zero correlation is typically anticipated for a single molecule, which is shown with a dip in the correlation curve. The presence of dark counts created by the noise of electronic devices and detectors, produces random photon-counting events. Consequently, the $g^2(\tau)$ curve may not reach zero at $\tau = 0$. Theoretical results of antibunching are shown in Figure 5b and 5c, respectively for continuous wave laser and pulsed laser excitation. To prove the detection of a single molecule a value of $g^2(\tau)$ ≤0.5 is commonly accepted as evidence which is shown as a dip in Figure 5b for a single molecule represented by the blue line. By increasing the number of molecules to 5, second-order correlation function $g^2(\tau)$ increases up to 0.8 (green line). Pulsed excitation results in a series of correlation peaks in which the height of the peak at the center depends on the number of molecules in the focal area.[66]

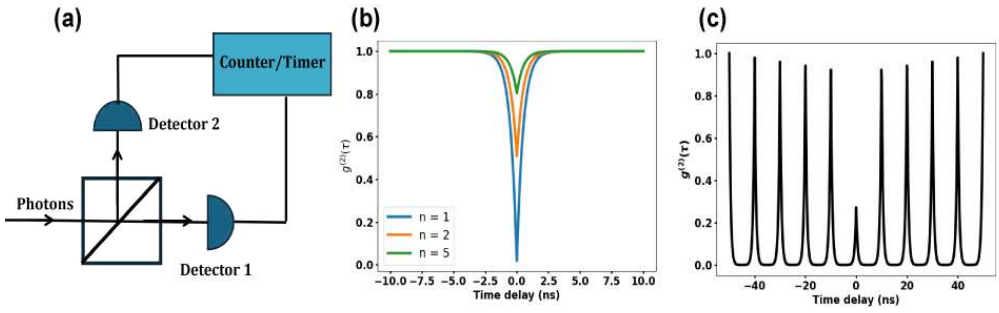

Figure 5. (a) Schematic of the Hanbury Brown–Twiss (HBT) experimental setup (Inspired by[66]). The signal of a single photon source is split into two beams of equal intensity using a beamsplitter, and the resulting beams are directed to two single-photon detectors (Detectors 1 and 2). The signals from these detectors are then processed by a counter/timer to measure the time delay between detected photons. (b) Theoretical results of Hanbury Brown–Twiss (HBT) experiment. Second-order correlation function $g^2(\tau)$ versus time delay for continuous wave (CW) laser excitation. The curves correspond to different numbers of emitters (n = 1, 2, 5), showing a dip at zero-time delay indicative of photon antibunching. A single emitter (n = 1) exhibits the most pronounced antibunching effect. (c) Second-order correlation function $g^2(\tau)$ versus time delay for pulsed laser excitation. The periodic peaks correspond to the repetition rate of the pulsed laser, with the zero-delay peak significantly reduced, demonstrating the antibunching characteristic of the single photon source.

Results and Discussion

2. Light–Matter Interactions via Optical Cavity at Room and Low Temperatures

2.1 Light–Matter Interactions

Resonant light-matter interactions occur when a single molecule is illuminated by a light beam with a frequency that matches one of its natural frequencies. To simplify the analysis of these interactions, the two-level molecule approximation is often used. This approach focuses on the resonant interaction by considering only the two energy levels involved in the optical transition, while neglecting other off-resonant energy levels due to their weak coupling with the light.

At resonance, the light's frequency matches the molecule's natural transition frequency, leading to strong dipole oscillations and maximizing the probability of photon absorption and subsequent emission. In contrast, when the light's frequency significantly deviates from the molecule's natural transition frequency, the induced dipole oscillations are weaker, reducing the interaction strength and thereby decreasing the efficiency of energy transfer. Understanding resonant light-matter interactions is crucial to comprehend phenomena such as Rabi oscillations and absorption transitions which are described more in detail later in this chapter.[66]

An interesting system for studying light-matter interactions is optical cavities. An optical microcavity consists of two highly reflective mirrors, either dielectric or metallic, positioned parallel to each other at a small distance, creating a high density of electromagnetic modes in this confined space. This configuration significantly enhances light-matter interactions, making it an effective platform for amplifying these typically weak interactions that occur in free space. When matter is placed inside the cavity, the light beam bounces back and forth, resulting in a coupling between the light field and the matter. This discipline is known as cavity quantum electrodynamics (cQED), and it has significant implications in many areas of research, including quantum optics, and spectroscopy.[114]

2.2 Characterization of Microcavity

An optical cavity consists of optical components designed to create a closed pathway for light, enabling it to resonate within the cavity. This resonant behavior allows the cavity to selectively enhance the intensity of certain wavelengths of light while suppressing others. The design typically involves two mirrors that reflect light back and forth, creating constructive interference for specific wavelengths that match the cavity's resonant frequencies. The simplest type of cavity is a planar cavity, consisting of two plane mirrors *M1* and *M2* separated with cavity distance L_{cav} and reflectivity *R1* and *R2*. In a planar cavity, the two mirrors are aligned parallel in front of each other, which allows the incident light beam to travel between the mirrors inside a medium with refractive index n and create multiple-beam interference. When the light with a particular wavelength λ is incident from one of the end mirrors, the planar cavity acts as a Fabry-Pérot interferometer. Figure 6 shows an example of a planar cavity.

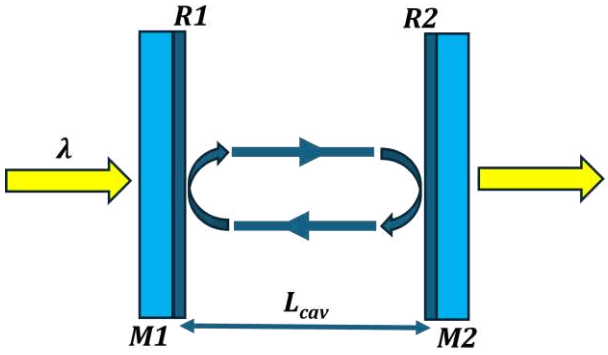

Figure 6. The planar cavity acts as a Fabry–Pérot interferometer when light of wavelength λ is incident in M1 mirror (Inspired by[66]).

A microcavity uses two parallel dielectric interfaces, such as mirrors, to manipulate light effectively. In a typical configuration, a light beam is directed at these interfaces at a small angle. This setup can be created using two parallel glass substrates coated with silver, commonly referred to as a Fabry-Pérot microcavity. In this setup, light bounces back and forth between the two mirrors, with the cavity length L_{cav} determining the distance over which the light undergoes multiple reflections. The optical path length difference between the

two reflecting surfaces is expressed by:

$$\Delta S = 2L_{cav}\sqrt{n^2 - sin^2\alpha} \tag{19}$$

where n is the refractive index and L_{cav} is the distance between two surfaces and α is the angle of incidence beam. The difference in path length between two reflected beams can result in a phase difference. The phase difference is calculated by:

$$\varphi = \frac{2\pi\Delta S}{\lambda} + \Delta\varphi \tag{20}$$

where the additional phase shift $\Delta\varphi$ may occur due to reflections.

By neglecting the scattering loss and absorption, the intensity of reflection I_R and transmission I_T is equal to $I_R + I_T = I_0$

$$I_R = I_0 \frac{F sin^2(\frac{\varphi}{2})}{1 + F\ sin^2(\frac{\varphi}{2})} \tag{21}$$

$$I_T = I_0 \frac{1}{1 + F\ sin^2(\frac{\varphi}{2})} \tag{22}$$

and coefficient of finesse F is given by:

$$F = \frac{4\sqrt{R_1R_2}}{(1 - \sqrt{R_1R_2})^2} \tag{23}$$

A calculated transmission spectrum of a Fabry-Pérot cavity is represented in Figure 7. The free spectral range $\delta\nu$ is defined as the spectral distance between two adjacent intensity maxima,

$$\delta\nu = \frac{c}{\Delta S} = \frac{c}{2L_{cav}\sqrt{n^2 - sin^2\alpha}}. \tag{24}$$

If the incidence angle is equal to zero the free spectral range is:

$$\delta\nu = \frac{c}{2nL_{cav}} \tag{25}$$

The finesse can also be expressed by a ratio of the free spectral range $\delta\nu$ and the full width at half maximum $\Delta\nu$ of a cavity transmission peak.[115]

$$\mathcal{F} = \frac{\delta\nu}{\Delta\nu} = \frac{\pi}{2}\sqrt{F} \tag{26}$$

The finesse of a cavity formed by ideal plane-parallel mirrors is primarily influenced by the reflectivity *R* of its surfaces. However, there might be slight deviations from an ideal plane and inclinations between the surfaces, leading to a decrease in the total finesse and causing an amplitude reduction and broadening of the transmission maxima. Therefore, to achieve a high finesse in microcavity, it is essential to optimize key parameters such as high mirror reflectivity, precise parallel alignment of the reflecting surfaces, and maintaining optimal optical surface quality of an empty microcavity.

The resonance condition occurs when the round-trip phase is equal to $2\pi m$ or the cavity length L_{cav} is proportional to *m* as an integer number of intracavity half wavelengths:

$$L_{cav} = m\lambda/2n \tag{27}$$

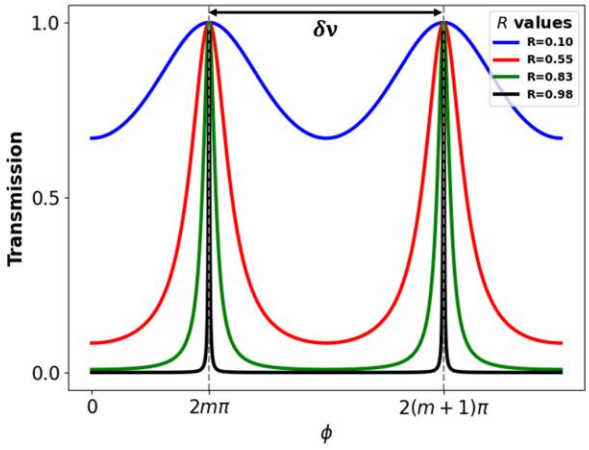

Figure 7. Transmittance of a Fabry–Pérot interferometer with different mirror reflectivities as a function of phase difference (ϕ) (Inspired by[66]).

This figure shows the transmission spectrum as a function of the phase ϕ for

different reflectivity values R of a Fabry-Pérot cavity. The sharpness of the transmission peaks increases with higher reflectivity, as demonstrated by narrower linewidths for larger R values (*e.g.*, $R = 0.98$). The distance between adjacent peaks corresponds to the free spectral range $\delta\nu$, which is independent of R.

The light modes that are compatible with the resonance condition can be selected by the cavity and called resonant modes. The resonant mode shows higher intensity by a factor of $4/(1-R)$ and non-resonant modes suppressed the intensity by a factor of $(1-R)$ compared to the intensity of incoming beam. From equation 28, the spectral width $\Delta\omega$ of the resonant modes is calculable as:

$$\Delta\omega = \frac{\pi c}{n\mathcal{F}L_{cav}} \tag{28}$$

Another parameter that influences the width of resonant mode is the photon loss rate in the cavity, which is related to the reflectivity of the cavity mirrors and other sources of optical loss. Photon decay rate κ is defined as:

$$\kappa = \frac{1}{\tau_{cav}} \tag{29}$$

This statement is related to the quality factor of an optical cavity. The Q-factor is a measure of the ability of the cavity to store light energy. A high-Q cavity can store light energy for longer periods of time, which leads to narrow and sharp resonant modes. The quality factor of the cavity given by the resonance frequency over its linewidth is defined by:

$$Q = \frac{\omega}{\Delta\omega} \tag{30}$$

The mode frequencies can be tuned by changing the cavity length e.g. by moving one of the mirrors with a piezoelectric. The emission properties of molecules in the cavity are significantly influenced by the properties of the resonant modes.[66]

2.3 Coupling of Cavity and Quantum Emitters

When a molecule is placed inside an optical cavity, it can interact with the cavity modes by absorbing photons and emitting them through radiative processes. This interaction leads to two possible coupling regimes: weak coupling and strong coupling. To achieve resonance, the cavity can be tuned until one of its resonant modes matches the transition frequency of the molecule. The interaction for a two-level molecule with a single cavity mode is described by the Jaynes-Cummings Hamiltonian:[116, 117]

$$H = \hbar\omega_c a^\dagger a + \frac{\hbar\omega_a}{2}\sigma_z + \hbar g_0(a^\dagger\sigma_- + a\sigma_+) \quad (31)$$

where ω_c is the frequency of the cavity mode, $a^\dagger$and a are the creation and annihilation operators for photons in the cavity mode, respectively, ω_a is the transition frequency of the molecule, the $\sigma_z = \begin{pmatrix} 1 & 0 \\ 0 & -1 \end{pmatrix}$ is Pauli z-operator representing the energy difference between the excited and ground states, while σ_x and σ_y are associated with operations that involve superposition states and are orthogonal to σ_z. σ_- and σ_+ are the lowering and raising operators that describe the transitions between the excited and ground states.

The electric dipole interaction sets the magnitude of the interaction energy, denoted as ΔE, between the molecule and the vacuum field within the cavity.

$$\Delta E = |\mu_{12}\varepsilon_{vac}| \quad (32)$$

where the value of μ_{12} represents the electric dipole matrix element of the transition and ε_{vac} the magnitude of the vacuum field. Molecule-cavity coupling strength g_0 depends on the orientation of the electric dipole moment of the molecule, the angular frequency the cavity mode ω, and the mode volume of the cavity V_0:

$$g_0 = \left(\frac{\mu_{12}^2\omega}{2\epsilon_0\hbar V_0}\right)^{1/2} \quad (33)$$

The strength of the interaction between the molecule and cavity can be determined by the photon decay rate of the cavity, the molecule-photon coupling, and non-resonant decay rate of the molecule.

2.4 Weak and Strong Coupling

The weak and strong coupling regimes can be distinguished by comparing the respective coupling rates between the molecule and the optical cavity mode to the rate of dissipative losses of the cavity. In the weak coupling regime, coupling strength $g_0 \ll (\kappa, \gamma)$ is smaller than the photon decay rate of the cavity κ and the non-resonant decay rate γ. Consequently, the losses of the system or dissipation of energy in the cavity are the dominant mechanism. In the weak coupling regime, the loss of photons from the molecule-cavity system occurs more rapidly than the emission and reabsorption of photons, leading to irreversible light emission from the molecule within the cavity. When a quantum emitter is placed inside a microcavity, it interacts with cavity modes. This interaction can enhance the emission of photons into specific cavity modes through Purcell effect,[108] which is the modification of the spontaneous emission rate of the emitter due to the presence of the cavity.[118] In strong coupling regime $g_0 \gg (\kappa, \gamma)$, the coupling strength is much larger than the losses in the cavity and there is a significantly faster photon-exchange between the molecule and the cavity mode than irreversible processes.[119-121] In the strong coupling regime, the emission of a photon by the molecule becomes a reversible process, as the photon can be reabsorbed by the molecule prior to its loss from the cavity.

Perturbation theory can be used to analyze the interaction between the molecule and the cavity. This typically involves calculating the emission rate of the molecules in free space using Fermi's golden rule and then determining the modified rate when the molecule is resonantly coupled to a single mode of the cavity.

The primary influence of the cavity is due to the modification of the photon density of states, either through enhancement or suppression of the radiative

emission rate compared to free space. Fermi's golden rule expresses the transition rate for spontaneous emission in free space and can be written as

$$W_{free} = \frac{\mu_{12}^2\, \omega^3}{3\pi\epsilon_0 \hbar c^3}, \tag{34}$$

where μ_{12} is the molecular transition dipole moment, ω is the angular frequency of the transition, ϵ_0 is the permittivity of free space, $\hbar$ is the reduced Planck's constant, and c is the speed of light. The transition rate in a cavity is

$$W_{cav} = \frac{2Q\mu_{12}^2}{\epsilon_0 \hbar V_0}\, \xi^2 \frac{\Delta\omega_c^2}{4(\omega_0 - \omega_c)^2 + \Delta\omega_c^2}, \tag{35}$$

where the angular frequency of the cavity mode is ω_c and linewidth is $\Delta\omega_c$, the frequency of the molecular transition is ω_0, ξ is the normalized dipole orientation factor, representing the alignment between the molecular dipole moment and the cavity field, Q is the quality factor of the cavity and, V_0 is the effective mode volume of the cavity. At exact resonance and with the dipoles orientated precisely along the field direction, the Purcell factor[122] F_p is defined by:

$$F_p = \frac{3Q(\lambda/n)^3}{4\pi^2 V_0}. \tag{36}$$

The Purcell factor is a useful parameter for describing the influence of the cavity on the optical transition of a molecule. If the Purcell factor is larger than one, it indicates that the spontaneous emission rate is enhanced by the cavity, while a value of F_p < 1 leads to suppression of the spontaneous emission.[123] To Achieve a large Purcell factor one requires the use of high-Q cavities with small modal volumes, as well as a close match of the orientation of the field of the cavity mode with the molecular transition dipole moment.

In the strong coupling regime, it is essential for the molecule-cavity coupling rate g_0 to exceed both the cavity decay rate and the non-resonant decay rate of the molecule. This creates reversible interaction between photons in the cavity mode and the molecule. It means that the emission of photons into resonant mode, bouncing back and forth between mirrors and reabsorption by

the molecule is faster than the photon loss rate in the cavity. This interaction is characterized by the exchange of energy between the molecule and the cavity mode, leading to the oscillation of the system between two states which are known as Rabi oscillations. A strongly coupled system, where the molecular transition frequency matches the cavity resonance, can be modeled as a pair of damped classical harmonic oscillators. The equation of motion of two oscillators can be,[124-126]

$$\ddot{x_1}(t) + \gamma_1 \dot{x_1}(t) + \omega_1^2 x_1(t) + g_0 x_2(t) = 0 \qquad (37)$$

$$\ddot{x_2}(t) + \gamma_2 \dot{x_2}(t) + \omega_2^2 x_2(t) + g_0 x_1(t) = 0 \qquad (38)$$

where γ and g_0 are the damping and coupling constant of the coupled system, x_1 and x_2 are the displacement, $\dot{x_1}$ and $\dot{x_1}$ are the velocity, $\ddot{x_1}$ and $\ddot{x_2}$ are the acceleration, ω_1 and ω_2 are the natural frequencies of the first and second oscillators, respectively. Two harmonic coupled oscillators with natural frequencies of uncoupled oscillators and coupled strength Ω are shown in Figure 8a.

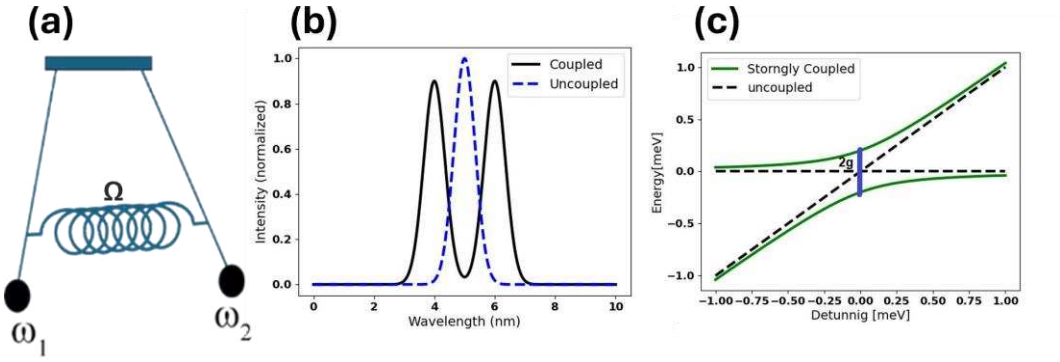

Figure 8. (a) System of two strongly coupled mechanical pendulums (Inspired by[126]). Two harmonic coupled oscillators with coupling strength Ω where ω_1 and ω_2 denote the natural frequencies of the uncoupled oscillators. (b) Transmission intensity of a Fabry-Pérot cavity with molecules between two mirrors as a function of detuning the cavity resonance frequency without (blue

dashed line) and with (black line) emitters in the cavity. The magnitude of splitting increases proportionally with the square root of the number of emitters in the cavity. (c) Energy dispersion as a function of detuning Δ between the emitter and cavity resonances. The energy of the excited state of the molecule without coupling ($g_0 = 0$) is represented by the horizontal dashed lines, while the energy of a photon resonant with the cavity in the absence of coupling is shown as the diagonal dashed line. The energy levels coupled system $g_0 > 0$ are depicted by the green lines. The energy splitting at zero detuning is approximately $2g_0$.

The interaction of the two coupled oscillators leads to splitting of the modes which can also be observed in the molecule-cavity system when the frequency of the tuned resonator approaches the constant frequency of the molecule, forming two new hybrid states, known as polaritons.[127, 128] These polaritons exhibit a splitting in their energy levels, known as Rabi splitting. Figure 8b shows the spectral response of the system under weak and strong coupling conditions. In the weak coupling regime, a single peak in the transmission spectrum corresponds to the individual resonance frequency of emitters in the cavity. In the strong coupling regime, the interaction between the emitters and the cavity at resonance frequency results in the splitting of the spectral peak into two distinct peaks, referred to Rabi splitting. The Rabi splitting is proportional to the strength of the coupling between the emitter and the cavity mode, and the energy levels are given by:[66, 126]

$$E_{\pm} = \hbar \left(\frac{\Delta}{2} \pm \sqrt{\left(\frac{\Delta}{2}\right)^2 + {g_0}^2} \right). \tag{39}$$

Where Δ is the detuning between the cavity resonance frequency and the emitter's transition frequency.

Energy dispersion as a function of detuning between the emitter and cavity resonance is shown in Figure 8c. In the weak coupling regime (black dashed lines), the energy levels of the emitter and the cavity remain independent, crossing each other linearly as the detuning changes. In the strong coupling regime (green solid lines), the coupling strength g_0 between the emitter and the

cavity is larger than the decay rates of the emitter and cavity. This results in an anti-crossing behavior. The magnitude of energy difference on the resonance for $\Delta = 0$ is equal to:

$$\Delta E_{vac} = 2\hbar g_0, \tag{40}$$

Observing vacuum Rabi splitting from a single molecule is highly challenging. The number of molecules in the cavity can influence whether the system operates in a weak or strong coupling regime. In general, single molecule systems are in the weak coupling regime, especially when there is a significant loss rate to non-resonance modes. However, when N molecules are resonantly coupled to a cavity mode, the vacuum Rabi splitting scales proportionally to the square root of N:

$$\Delta E_{vac}(N) = \sqrt{N} \cdot \Delta E_{vac}, \tag{41}$$

The strong coupling regime refers to the situation where the interaction between a molecule and a cavity mode is comparable or stronger than the rates at which energy is lost from the system. In terms of classical oscillators, this can be explained as the damping coefficients are smaller than the coupling strength where the oscillators exchange energy back and forth without significant loss. In practice, damping mechanisms, like spontaneous emission, limit the observation of Rabi oscillations. During damping processes, the excited state of a molecule spontaneously decays to lower energy levels, causing the loss of coherence and leading to permanent interruption of Rabi oscillations. Furthermore, for effective interaction between the molecule and the cavity mode, the absorption and emission wavelengths must match. A mismatch in these wavelengths prevents efficient energy exchange, making it difficult to observe Rabi oscillations.

2.5 Temperature-Dependent Molecular Spectroscopy

Spectroscopy at room temperature is a highly demanding technique to use for many researchers compared to cryogenic spectroscopy due to the high cost

and complexity of cryogenic systems. Room temperature setups are simpler, avoiding the need for expensive equipment like cryostats or liquid helium. They are also easier to maintain and enable researchers to perform experiments efficiently without delays from cooling and warming cycles in cryogenic systems. However, to observe the frozen molecular folding, this investigation must be done at cryogenic temperatures. At higher temperatures, molecules experience faster vibrational and rotational dynamics, which can lead to additional broadening of spectral lines. However, when molecules are embedded in the solid host, rotational motion is largely restricted due to spatial constraints imposed by the host matrix. These effects make it difficult to resolve closely spaced spectral lines and obscure fine spectral details. In contrast, at very low temperatures, molecular vibrations of the dye molecule and vibrations of the matrix molecules surrounding the dye molecule are significantly reduced, leading to sharper spectral lines that better reflect the intrinsic excited-state properties. In addition, at very low temperatures, some molecules undergo spontaneous phase transitions which means that the structure of their local environments changes significantly associated with a reduction of thermal energy leading to shifts of their energy levels, impacting factors like emission spectra, fluorescence intensity, and lifetime. This result in frequency shift of the transition for excitation and emission spectra.[88, 129]

Interaction of molecules and phonons determines the shape of the vibronic bands. A zero-phonon line with a broad phonon wing (PW) form the emission profile of each vibronic band.[106] The ZPL and PW for the emission of a single fluorophore is shown in Figure 9a.

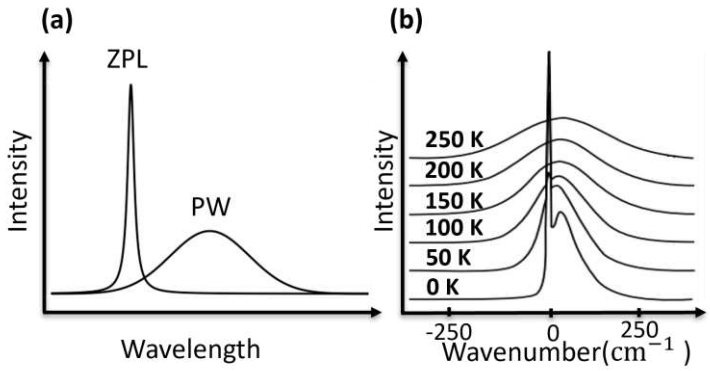

Figure 9. (a) A single emitter's line shape which includes a ZPL and a PW. (b) The temperature dependence of the electron-vibrational band (Adapted from[96])

The ZPL shown in Figure 9a is a narrow spectral peak that corresponds to the emission of a photon without any accompanying phonons, while the PW is a broad spectral feature that corresponds to the emission of a photon with one or more accompanying phonons.

Figure 9b shows the relationship between temperature and a uniform spectral band. It is important to observe that the zero-phonon line quickly vanishes as the temperature rises, and beyond 100 K the entire band can be effectively represented by a single Gaussian profile. In molecular transitions, the ZPL corresponds to electronic transitions without changes in phonon number, while PWs result from transitions involving the creation or annihilation of phonons. The strength of electron-phonon coupling determines the relative intensities of the ZPL and PWs. Strong electron-phonon coupling enhances the PWs relative to the ZPL, while weak coupling results in a more prominent ZPL. It is important to note that the presence of the ZPL doesn't indicate weak electron-phonon coupling; rather, the relative intensities of the ZPL and PWs reflect the coupling strength.[95] The intensities of the ZPL and the PW are related by the Debye-Waller factor (DWF) which is a function of both temperature and crystal structure. The Debye-Waller factor is expressed as:

$$DWF = \frac{I_{ZPL}}{I_{PW} + I_{ZPL}} \tag{42}$$

Where I_{ZPL} is the intensity of the zero-phonon line and I_{pw} is the intensity of the phonon wing. The range of Debye-Waller factor is from 0 to 1. At higher temperatures, the movement of the molecules in the crystal lattice increases, which leads to a reduction in the intensity of the ZPL relative to the phonon wing and in the Debye-Waller factor.[130, 131] This factor describes the effect of thermal vibrations on the intensity of a spectral line. For a dye molecule embedded in a solid host at low temperature the spectral line profile can be described as:

$$S = I_{ZPL}DWF + I_{pw}(1 - DWF) \quad (43)$$

A sample with a crystal structure is a perfect system to observe ZPL in the emission spectrum. When chromophores are embedded in a well-ordered crystal lattice with minimal integration defects and weak coupling between the chromophores and the host matrix at low temperatures, the fluorescence spectrum represents a high intense and sharp ZPL with narrow linewidth and suppressed phonon wings. Weak coupling leads to suppression of phonon wings and reduction of the probability of collective vibrations of host matrix and chromophore.

3. Materials and Methods

Two optical setups are used, one for room temperature and another for low temperature measurements. Although the low-temperature setup enabled the experiment to be performed at room temperature, it required the sample to be placed inside the cryostat and required the use of the air objective lens with limited numerical aperture. Conversely, the room temperature setup permitted the use of an oil immersion objective lens with a higher numerical aperture and allowed for the sample to be in an ambient environment.

The chapter also outlines the methods used to prepare the appropriate samples for measurements, to design a tunable microcavity in a cryostat, and to fabricate, measure, and evaluate the multiple coupled cavities. This information is crucial for readers to understand the experiments conducted and the validity of the research findings.

3.1 Confocal Scanning Microscope (Room Temperature Setup)

Confocal microscopy offers significant advantages compared to the conventional wide-field microscopy, by providing higher axial (z-axis) resolution, improved contrast, and the ability to image thicker transparent samples. By applying spatial filtering with a pinhole to eliminate out-of-focus

light, it produces in-focus images through optical sectioning, resulting in enhanced axial resolution and improved image quality. This method is based on the integration of a pinhole aperture in the detection path and a laser. In a confocal laser microscope, a laser beam is focused by an objective lens to a diffraction limited focal volume on the specimen. The emitted light from the focal volume is then re-collected by the objective lens, and the pinhole aperture placed in the detection path allows only the photons emitted from the focal volume reach the detector while blocking out-of-focus light coming from the other planes of specimen. To capture high-resolution images of molecules, the focus of the laser beam may be held at a fixed position and the sample is scanned point-by-point. This allowing to generate images that show the distribution of detected photon intensities at different locations in the sample. For single molecule spectroscopy the dye molecules are fixed in a transparent, non-fluorescent medium, and the concentration of the dye molecules has to be very low, such that on average only one dye molecule is present in the focal volume.

The emitted photons that pass through the pinhole are detected by a photo detection device such as an avalanche photodiode (APD) or a spectrophotometer with a CCD-camera. The APD converts the detected photons into electrical pulses that are counted by a computer while the spectrophotometer records spectral information of fluorescence. The APD can also be used to acquire time-resolved fluorescence decay curves and spatial intensity mapping images. Each pixel in the resulting image is a representation of the detected photons emerging from the focal volume of the sample. The whole image is captured pixel-by-pixel and line-by-line as the sample is scanned in the x-y direction from the different planes in the z-axis.

A typical home-built confocal scanning microscope which is used for room temperature measurements in this thesis is represented in Figure 10.

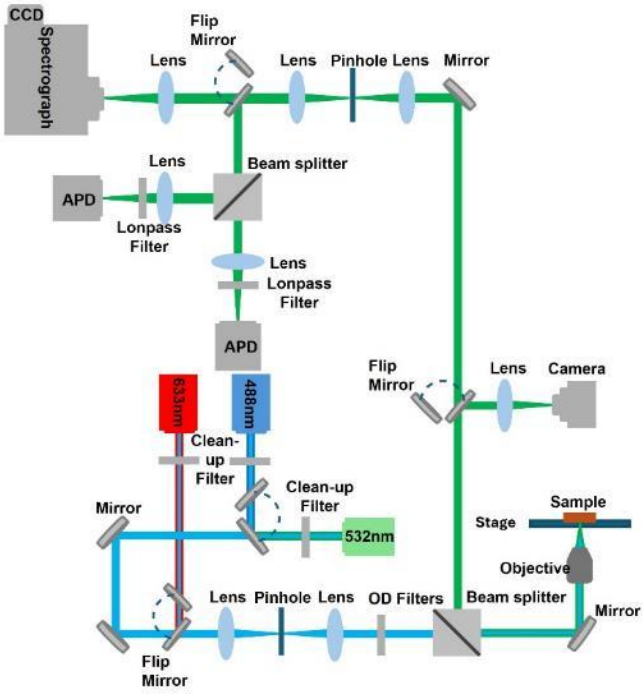

Figure 10. Schematic of the room temperature setup: The microscope is equipped with a scanning stage for sample scanning measurements, air and oil objectives and three laser sources coupled into the excitation path. The detection path contains a pinhole aperture, beam splitter, two APDs and a spectrometer with a CCD-camera.

The setup consists of three laser sources, each with different wavelengths coupled into the excitation path. The first laser has a wavelength of 488 nm (Pulsed, PicoQuant D-C-485), the second one has a wavelength of 530 nm (pulsed/CW, PicoQuant LDH-P-FA-530L) and the third one is a CW HeNe laser with 630 nm. The configuration of telescope lenses is used to increase the size of the excitation beam to match the back aperture of the objectives. Two oil (63x, NA = 1.46, Carl Zeiss) and air objectives (40x, NA = 0.6, Edmund Optics) are used for the experiments. The scanning piezo stage (P-527.3CL, Physik Instruments) is used to scan the specimen in both the x and y directions. The fluorescence light is recollected by the objective and then directed to a 50:50 cubic beam splitter (Thorlabs) and a 50 µm pinhole aperture (Thorlabs). From there, the light is split equally and sent to either the spectrometer (SP-2500i, Princeton Instruments) or APDs (SPCM-AQR-14, PerkinElmer). This APD has a detection range from 400 nm to 1060 nm, with a photon detection efficiency

of 65% at 650 nm. These APDs offer a maximum dark count rate of 100 counts per second (c/s) and feature a dead time of 32 ns, making them well-suited for high-sensitivity photon detection. To detect and measure the arrival time of single photons for single molecule measurements, a Time-Correlated single photon counting module (HydraHarp 400, PicoQuant) is connected to the APD. TCSPC module works by measuring the time delay between the excitation pulse and the emitted photon pulse which is then used to calculate the fluorescence decay curve of the sample. The TCSPC module achieves time resolutions down to a few tens of picoseconds by measuring the arrival time of the emitted photons with respect to a reference signal. The recorded photon arrival times are binned into a histogram, which represents the distribution of photon counts as a function of time delay. The histogram is then fitted to a mathematical model, typically a mono-exponential or multi-exponential decay function, using a nonlinear least-squares fitting algorithm.

To assess histograms of photon arrival times for fluorescence lifetime measurement, various crucial factors must be taken into account such as the repetition rate, the laser pulses, the pulse duration, the time resolution of the TCSPC module, and IRF. When the histogram displays mono-exponential decay behavior, it is very likely that it corresponds to a single fluorescent molecule and can be represented by the convolution of the IRF with a mono-exponential function. However, for single molecules within an inhomogeneous environment or more complex systems, the decay behavior may require modification like multi-exponential decays.[3]

Two short-pass filters with the cutoff wavelength shorter than emission wavelength of molecules are necessary to use before APDs in antibunching measurements to reduce the amount of background signal. The recorded data are evaluated with SymPhoTime 64 software (PicoQuant).

3.2 Cryostat

The Interior of an open-loop bath cryostat (SVT-200-5, Janis, USA) used in this work are shown in Figure 11. The central part of the cryostat is the sample tube,

where the sample is placed for cooling and experimental measurements. The tube provides thermal isolation and is designed for minimal heat conduction. This tube is surrounded by a helium reservoir, shown in light blue. Liquid helium (LHe) is stored here to cool the sample to extremely low temperatures. The dark blue region represents the liquid nitrogen (LN_2) compartments, which provide additional cooling. Liquid nitrogen is used to pre-cool the system before helium is used, reducing the consumption of more helium. These three compartments are separated from each other by high vacuum to minimize thermal conductivity and maintain low temperatures. All components are mounted within a cylindrical steel container that protects the system from atmospheric pressure. At the bottom, optical access to the sample is provided through optical windows, allowing for spectroscopy or imaging experiments. There is a ventilation port near the helium reservoir to safely release excess gas pressure. This is a critical feature to prevent over-pressurization during operation.

The range of temperature in this bath cryostat is adjustable from 2.17 Kelvin to the room temperature. There are also two important reservoirs inside the cryostat for LHe and LN_2 to decrease the temperature to 2.17 K. Two sensors are used to control the temperature, one for helium reservoir and another one (DT-670-SD, Diode sensor, Lake Shore Cryotronics) is placed very close to the sample area to measure the temperature of the sample. The temperature was monitored and controlled by an electrical temperature controller (Model 336, LakeShore).

One of the key features of Janis cryostat is the ability to thermally isolate the liquid helium (LHe) and liquid nitrogen (LN_2) reservoirs using super insulation by making a vacuum space between two reservoirs. The vacuum space is pumped out to 3.3×10^{-6} mbar with an oil pump (Leroy Somer, France) followed by turbo pump (PFEIFFER Vacuum). This super insulation reduces the rate of heat transfer from the environment to the cryogenic liquids and greatly reduces the amount of liquid helium required to maintain low temperatures, resulting in significant cost savings. Additionally, the isolation of the reservoirs allows for longer hold times, which can be especially useful for experiments that require extended cooling periods.

The sample is placed on top of piezo stages which is movable in x, y, and z direction at the bottom of the sample tube of the cryostat and the LHe can be transferred to this sample area via a small capillary tube from helium reservoir.

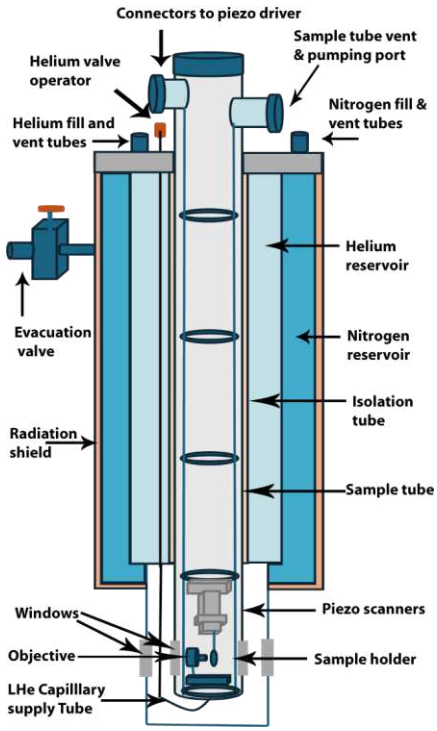

Figure 11. Drawing of interior of Janis open-loop bath cryostat. The cryostat is initially pre-cooled using liquid nitrogen (LN_2), followed by further cooling with liquid helium (LHe) to reach temperatures as low as 4.2 K using a Helium valve to fill LHe from Helium reservoir to the sample compartment. To reach superfluid helium at 2.17 K (λ-point) and temperatures below, the sample compartment has to be evacuated by a powerful pump.

To achieve 2.17 K, it is necessary to start the pre-cool process by transferring the LN_2 into the LN_2 reservoir of cryostat and when the temperature is approximately 100 K then filling the LHe reservoir with LN_2 to reach to 50 K. It is necessary to evacuate the transfer line one day before starting the cooling process to avoid the consumption of LHe during the transferring process from LHe tank to the LHe reservoir of cryostat. The transfer line has to be inserted

inside the LHe tank completely where the bottom of transfer line tube is completely inside the LHe tank during the whole measurement.

By transferring the LHe through the LHe reservoir, LHe can pass through the capillary *via* a Helium valve operator and reach the sample compartment. The temperature of the sample compartment is then cooled to a minimum of 4.2 K once the liquid helium covers it. However, to reach the superfluid and stable state of liquid helium without any bubbles, the entire chamber, including the sample area, must be evacuated to remove any evaporated helium within the chamber.

It is crucial to find a balance between applying pressure to the LHe tank to control the transfer rate of LHe into the reservoir and regulating the filling valve related to the capillary part during the cooling process. If the rate of transferring LHe inside the cryostat is less than the rate of LHe flowing into the sample area, the LHe will vaporize quickly, causing the temperature to rise above the desired 2.17 K. Therefore, careful management of the LHe transfer rate is essential for achieving accurate low-temperature measurements.

Although a manual with instructions for using the cryostat was available in the laboratory, it is crucial to gain a comprehensive understanding of the cooling process and acquire sufficient experience to effectively control the pressure inside the cryostat and helium tank. Additionally, working with evacuation valves and knowing when to insert or remove the helium transfer line inside the cryostat and tank is of utmost importance for accurate low temperature measurements.

3.3 Low Temperature Setup

A home-built confocal microscope head inside the bath cryostat is used to perform spectroscopic measurements with samples at low temperature. The detailed scheme of the low temperature setup is illustrated in Figure 12.

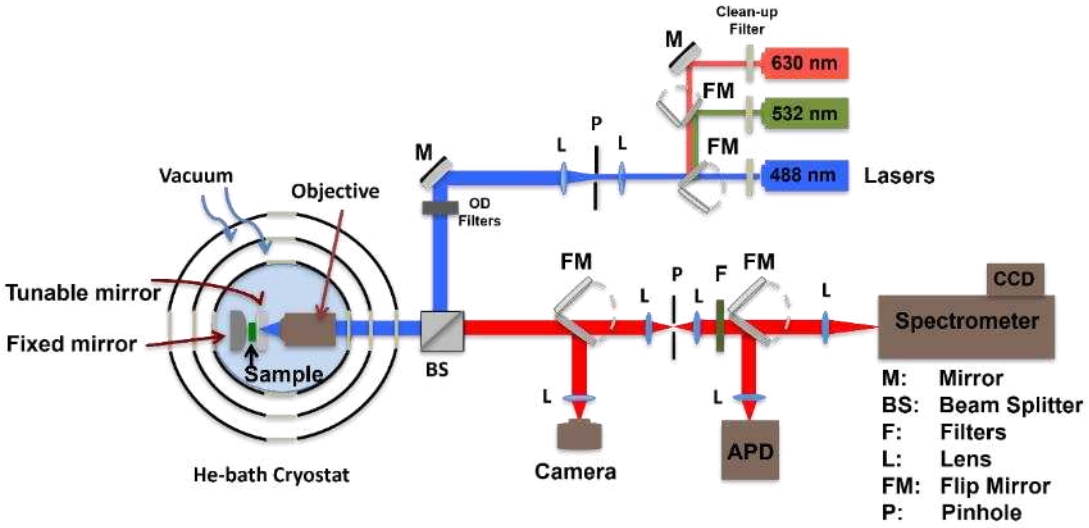

Figure 12. Schematics of the home-built confocal microscope for low-temperature fluorescence lifetime and spectroscopy measurements. Laser light sources (488 nm, 532 nm, and 630 nm) are combined using beam splitter and focused onto the sample situated inside a Fabry Pérot cavity consisting of a fixed mirror and a tunable mirror within the cryostat. The sample is mounted at the center of the cavity, maintained at cryogenic temperatures. The emitted or transmitted light from the sample is collected and directed through optical elements including lenses and beam splitters. The detection system comprises an APD for time-resolved measurements and a spectrometer coupled with a CCD for spectral analysis. This configuration enables precise low-temperature optical measurements of the sample properties.

This setup uses diode laser light sources across three distinct wavelength ranges. The first is a fiber-coupled CW diode laser at 630 nm (iBEAM-630-3v2, TOPTICA Photonics) which is focused and collimated by an output coupler (60SMS-1-4- A11-02, Schäfter+Kirchhoff GmbH), The second is a CW and pulsed laser at 520 nm (LDH-D-C-520, PicoQuant), and a pulsed/CW laser $\lambda = 532$ nm from room temperature setup. The third is a CW laser diode at 488 nm (OBIS LS ,Coherent Inc.), and a pulsed laser operating at 485 nm (LDH-D-C-485, PicoQuant). To suppress the spectral side bands of the lasers, three clean up band pass filters are placed in front of the lasers. Furthermore, a beam expander is used to match the laser beam diameter to the back aperture of the objective lens installed in the cryostat. The beam is transmitted via a beam splitter 30:70 (BSS10R, Torlabs) to the cryostat windows. This

beam splitter can enhance signal collection efficiency by directing a higher proportion of the fluorescence emission to the detector, which facilitates the detection of low fluorescence intensities. Additionally, it can help to reduce background noise from the excitation source by minimizing the amount of excitation light entering the detection path. The high numerical aperture objective (60X, N.A. = 0.85, Edmund optics) is used to focus the laser beam on the sample.

The low temperature setup is capable of functioning in two configurations. The first configuration enables the alteration of the sample at varying temperatures, especially at very low temperatures, via a removeable magnetic sample holder.[132] The second configuration involves a fixed sample holder within a tunable microcavity, which does not change at different temperatures (see section 3.5). In both configurations the objective and the sample are placed inside the bath cryostat, the objective moves only in z direction along the optical axis, and the sample is movable in x, y, and z direction. The coarse approach (ANPx320 and ANPz101eXT, attocube Systems) and scanners (ANSxy100lr and ANSz100lr, attocube Systems) offer the opportunity to scan the sample inside the cryostat, providing the benefit of minimal alignment difficulties due to the stationary objective. This feature reduces the risk of misalignment and drift, in contrast to the laser scanning method, which is susceptible to even the slightest misalignment of the objective lens, leading to significant image distortion and loss of resolution.

The beam of fluorescence photons is collected by the objective, passed through the beam splitter and focused on to an appropriate pinhole (50 µm diameter) in front of the detector to eliminate the out of focus photons. The ideal pinhole size is determined by several factors, including the numerical aperture of the objective, the wavelength of light being used, and the thickness of the sample. If the pinhole is too small, less light will reach the detector, resulting in a decrease in image intensity and signal-to-noise ratio. Conversely, if the pinhole is too large, more out-of-focus light will be detected, leading to a decrease in image contrast and resolution.

The fluorescence photons are filtered via short, band, or long pass filters (AHF analysentechnik) and are directed to an APD (SPCM-AQR-14, Photon Counting Module, PerkinElmer Optoelectronics) or a grating spectrograph (Shamrock 500i, L.O.T. Oriel GmbH) with a CCD camera (SR-500i-B2-SIL, CCD12126, Andor Technology). To provide the appropriate spectral resolutions for different experimental requirements, the spectrograph is equipped with two reflection gratings: one with 200 lines/mm and another with 400 lines/mm.

3.4 Tunable Coupled Cavities

Multiple cavity fabrication techniques are used to produce a coupled system of cavities consisting of a fixed and tunable cavity.[133] To do this, an Electron Beam Evaporation (EBE) system is used in this study.

EBE is a thin-film deposition process that involves the use of an electron beam to vaporize a solid material in a vacuum chamber and then deposit it onto a substrate. To prepare a coupled microcavity the following protocol was used: an ultra-clean coverslip as substrates is placed inside the vacuum chamber. The vacuum chamber is evacuated to a high vacuum pressure of 1.0×10^{-6} mbar to prevent any unwanted contamination during the deposition process. A solid silver or gold source material is placed in a crucible inside the vacuum chamber. An electron beam gun is used to generate an electron beam that is focused onto the surface of the source material, causing the material to be vaporized. The vaporized silver (Ag) or gold (Au) atoms then condense onto the surface of the coverslip, forming a thin film. The thickness of the film can be controlled by adjusting the deposition rate, which is controlled by the electron beam current and the rate at which the source material is vaporized. A built-in quartz crystal sensor was used to monitor the film thickness. Figure 13a shows a schematic of two coupled microcavities consisting of a fixed (lower) and tunable (upper) cavities. The mirror coatings were produced according to the above protocol. The first mirror layer was fabricated by a deposition of a 50 nm silver, a 10 nm gold layer and a 148 nm glass (SiO_2) layer onto an ultra-clean glass coverslip. The thickness of the SiO_2 layer used as a spacer layer is specifically chosen to adjust the resonance frequency of the fixed resonator

and to coincide with the maximum absorption peak of sample's molecules. A central shared mirror between fixed and tunable cavity was produced by deposition of a 24 nm silver layer on top of glass spacer layer. Then, the shared mirror was coated with a 10 nm gold and a SiO_2 spacer layer. The thickness of the second spacer layer can be different depending on the position of the thin molecular film within the tunable cavity. The tunable cavity was formed using a lens coated with an eighty-nanometer thick silver film. Additionally, a 10 nm gold, and a 10 nm glass layer was also used to enhance the mirror's reflectivity, and to prevent oxidation of the silver layer.

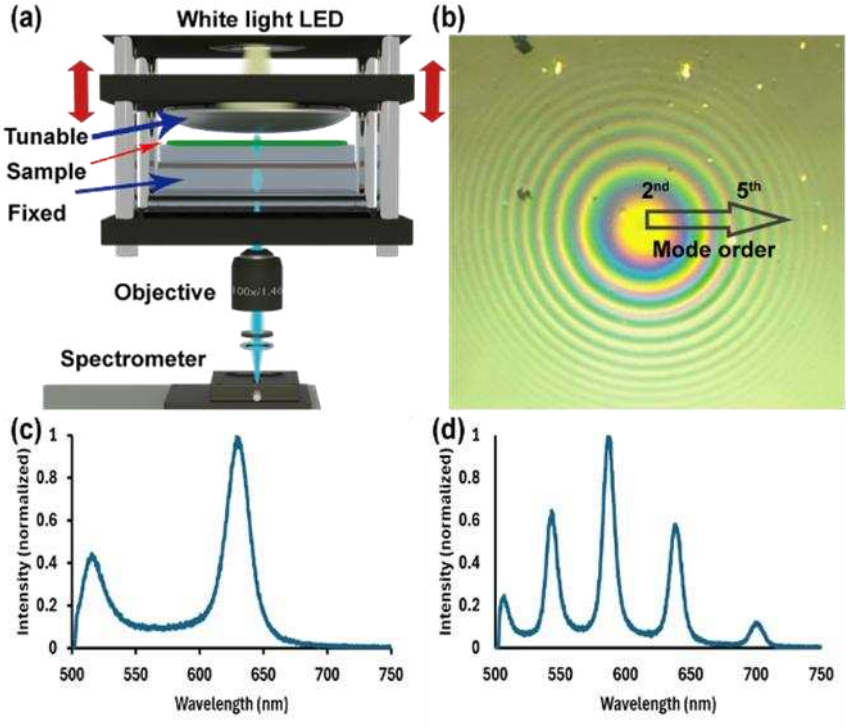

Figure 13. Schematic showing two microcavities adjacent to each other for room temperatures measurements. a) The coupled microcavities consist of three mirror layers, the lower, the center shared mirror and upper lens mirror. The lower and the center shared mirror form the fixed cavity while a tunable upper cavity contains the molecules (represented in green) where placed above the center mirror. The air spacing between the center mirror and the upper mirror allows tunning the resonance of the upper cavity. A white light source illuminates the coupled cavities from the top. The transmitted signal is collected with an objective and directed on a CCD-camera or alternatively on a

spectrometer. b) Newton's ring fringe pattern recorded by the CCD camera from a single cavity composed of a fixed mirror and a tunable silver coated lens. The vivid coloration of the rings is indicative of the varying wavelengths of light undergoing interference. (c) and (d) Transmission spectra of white light through a single microcavity with different cavity lengths. A shorter cavity length (c) supports a lower-order mode, typically resulting in only one resonant peak as it restricts the cavity to a single dominant mode. A longer cavity length (d) supports higher-order modes, permitting several wavelengths to resonate and transmit through the cavity.

In the tunable cavity, the slightly curved mirror leads to a center-to-edge variation of the path length in the cavity. This variation causes interference between light beams reflecting from the two surfaces, producing a visually striking fringe pattern known as Newton rings, as depicted for a single tunable cavity in Figure 13b. By adjusting the optical path length d within a cavity containing a medium with refractive index n, it is possible to achieve successive transmission orders m for a specific wavelength. This relationship is described by the equation $m=2dn$. The cavity mode order proceeds from low to high as one moves from the center of the pattern to the outer rings. At the center, where the cavity length is shortest, the fundamental mode is observed. The transmission spectra of white light through a single microcavity from low to high mode order are shown in Figure 13c and 13d. When the distance from the center increases, higher-order transverse modes appear due to the increment in the effective cavity length. These modes correspond to the multiple of half wavelengths fitting into the cavity, providing valuable insights into the cavity's resonant frequencies. The cavity length is adjusted using a piezo actuator (8302 Picomotor Actuator, Newport), and the silver-coated lens is illuminated with a white light source from the top of the cavity’s holder. The white light transmission is collected by an oil objective lens (NA = 1,4) and detected with a spectrometer.

3.5 Single Tunable Microcavity in a Cryostat

The tunable microcavity structure is made up of two mirrors: one fixed and one adjustable. These mirrors are separated by distance equivalent to a few wavelengths in the visible light spectrum.

A home-built cavity was designed and implemented, consisting of a planar mirror and a convex lens in this study. This design avoids the difficulties of adjusting a Fabry-Pérot cavity with plane mirrors, which tend to produce parallel fringes rather than the desired Newton ring pattern for optimal alignment. In addition, the adjustment process is simplified, as varying the cavity length allows different cavity modes to be easily created and tuned.[134]

The adjustable mirror of the microcavity is fabricated by coating a clean glass cover slide with a 50 nm layer of silver, followed by a 10 nm layer of gold, and then an 80-120 nm dielectric SiO_2 layer (depends on the size of different emitters used in this thesis), which provides a surface for positioning the sample. The fixed lens is coated with an 80 nm layer of silver, followed by a 10 nm gold layer, and topped with a 20 nm SiO_2 layer for protection. The microcavity design and the microscope head consists of objective, microcavity, and piezo steppers are illustrated in Figure 14.

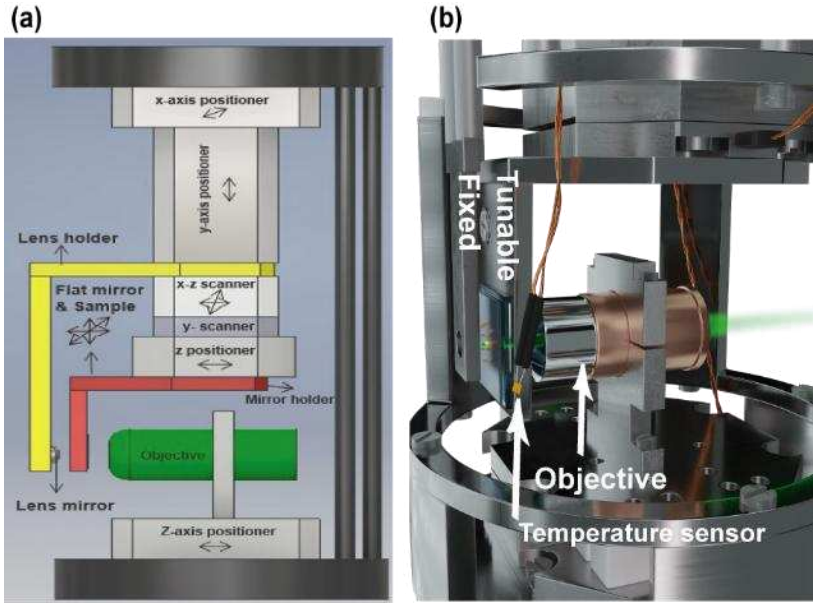

Figure 14. (a) A schematic of the low temperature microscope head. The flat mirror including the sample is moveable in x, y, and z directions. (b) Scheme of the tunable microcavity with a temperature sensor very close to the sample to control the temperature of the sample. Courtesy of Frank Wackenhut.

A home-built low temperature microscope head consists of stepper positioners, scanners, an objective lens, a flat mirror including the sample, and silver coated lens is shown in Figure 14. The flat mirror is movable in x, y, and z directions to scan the target area on samples. The silver coated lens moves only in x and y directions via coarse positioner. The sample can be scanned in x and y-axis within a maximum scanning range of 30 x 30 µm, depending on the temperature. The objective lens can be moved in z-axis along the optical path in front of the flat mirror to focus the excitation light on the sample. To make a cavity with multiple of half a wavelength length, the flat mirror is moved toward the silver coated lens where the cavity length is controlled with piezo coarse positioner and scanner. The centers of the objective and mirror lens have to be concentric on the optical axis. A white light source was placed outside of the cryostat and was focused with a lens on the back side of the lens mirror which was inside the cryostat. Transmission spectra were collected with the air objective lens and detected with the spectrometer. To avoid any damage to the system, it is imperative that any movements involving the flat mirror surface and lens occur gradually. A collision between the two components may result in the creation of microcavity scratches and the destruction of the low-order resonance cavity.

3.6 Sample Preparation

Small quadratic fused silica coverslips with a side length of 12 mm and a thickness of 0.2 mm and the lowest fluorescent background spectrum as compared to the normal coverslips were used for preparing the samples for cryogenic measurements (from Quartzglas Komponenten und Service QCS GmbH, Germany). Larger glass coverslips (22 × 22 mm) used for fabrication of coupled cavities were purchased from Menzel-Gläser (Germany).

Before preparing the sample by spin-coating a polymer layer with embedded dye molecules on top of the coverslip, it is essential to thoroughly clean the coverslip. To clean the coverslips a 50:50 (v/v) mixture of hydrochloric acid (HCl) and methanol (MeOH) was prepared by adding equal volumes of concentrated HCl in MeOH. The coverslips were immersed for 1 hour in this solution, then rinsed with double-distilled water to remove any detergent residues from the coverslips and dried under a Nitrogen flow.

To investigate the effect of strong coupling between coupled cavities, a 30 nm thick film of TDBC from FEW Chemicals was used. This was accomplished by dissolving TDBC in a 1 wt % solution of a poly (vinyl alcohol) (PVA) in water leading to the creation of J-aggregates. To create the TDBC J-aggregate solution the TDBC was sonicated for 20 minutes at a concentration of 10^{-2} mol/L. The film thickness was measured about 30 nm using an atomic force microscope (AFM) after spin-coating a 5 µL droplet of the TDBC J-aggregate/PVA solution on top of the SiO_2 layer for 30 seconds at an angular velocity of 1700 rpm.

Triple FRET experiment: To prepare samples for spectroscopy of single TetraSpeck nanospheres with a nominal diameter of 100 nm, a TetraSpeck ultraclean polystyrene nanosphere solution with a density of 1.8×10^{11} particles/mL diluted in triply distilled water was used. The nanospheres contained four fluorescent dyes with absorption maximum at 350 nm, 505 nm, 575 nm, and 655 nm. The nanospheres (Invitrogen TetraSpeck nanospheres T7229 from Thermo Fisher Scientific, Germany) were used without any further purification. To prepare the samples, a 5 µL droplet of the TetraSpeck solution was placed on top of a clean coverslip for measurements in free space or on top of the flat mirror of a disassembled microcavity. The droplet was then dried for 20 minutes; this leads to an average distance of several micrometers between dyes. The chemical structures and concentration of the dyes are proprietary information of Invitrogen.

For single NV centers measurement, nanodiamonds with 1-2 NV per particle are used. These nanodiamonds were purchased from Adámas Nanotechnologies in the USA (ND-NV-10nm-MD-10ml). They were suspended

in deionized water at a concentration of 1 mg/mL and were used without further purification. Each particle of the fluorescent diamond contains a minimal quantity of NV centers. To ensure that only one fluorescent molecule resided within the diffraction limited detection volume, the concentration of the nanodiamonds had to be reduced. This was achieved by sonication NVs in a 1 wt % solution of PVA in triple distilled water for 10 minutes and depositing a droplet of 5 µL of the 10^{-3} mol/L solution by spin-coating onto an ultra-clean fused silica coverslip.

4. Single Emitter in a Microcavity at Low Temperature

4.1 Optical Properties of NV Centers

The nitrogen-vacancy center in diamond is one of the most extensively studied point defects in solid-state systems, particularly due to its remarkable optical and spin properties. NV centers are defects formed in the diamond lattice where a nitrogen atom (N) substitutes a carbon atom adjacent to a vacancy (V-missing carbon atom). The NV center introduces localized electronic states within the diamond's band gap, which allows optical excitation and subsequent emission of fluorescence. The NV center exists in two primary charge states: neutral (NV^0) and negatively charged (NV^-), with the latter being the most studied due to its favorable optical and spin properties. In its negatively charged state NV^-, the NVs consist of a spin-triplet ground state, $^3A_2$ with spin sublevels of $m_s = 0$, $m_s = -1$, and $m_s = +1$. The fluorescence intensity of the NV^- center depends on its spin state, the $m_s = 0$ state is brighter than the $m_s = \pm 1$ states, due to different pathways in the intersystem crossing between the excited and ground states.[135]

A structural representation of the nitrogen-vacancy center in nanodiamond[136] is shown in Figure 15a where the blue spheres represent carbon atoms and orange sphere represents the nitrogen atom, and the gray sphere represents the vacancy, respectively.

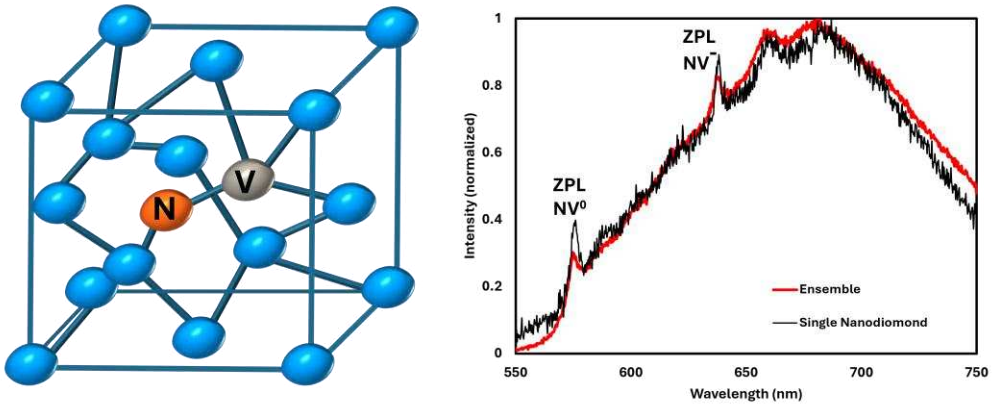

Figure 15. (a) The atomic structure of the nitrogen-vacancy (NV) center in a diamond (Inspired by[136]). The NV center consists of a substitute nitrogen atom (N) adjacent to a vacancy (V) within the diamond lattice. (b) Emission spectra of NV centers in a nanodiamond at 275 K excited with a 488 nm laser, comparing an ensemble of nanodiamonds (red curve) to a single nanodiamond (black curve). Sharp peaks are ZPL of NV centers at 575 nm and 637 nm respectively.

Experimental emission spectra of an ensemble of nanodiamonds (red curve) and a single nanodiamond (black curve) containing NV centers at 275 K, obtained from unpublished data are depicted in Figure 15b. When the NV centers are excited by a laser 488 nm, their fluorescence is in the range of 570–800 nm, particularly the ZPL of NV^0 and NV^- occur at 575 nm and 638 nm, respectively. The NV center has been extensively studied both at the ensemble level, where many NV centers are present, and at the single-molecule level, where the behavior of individual NV centers can be probed with high precision. At the ensemble level, where multiple NV centers are present in the same sample, the fluorescence spectrum becomes broader due to the collective emission from many NV centers. This broadening is caused by the averaging of many NV centers, each with slightly different environments (such as strain, local electric fields, or nanodiamond size), leading to inhomogeneous broadening of the optical transitions. This averaging effect results in a loss of sharp spectral features that are observable at the single NV level. However, ensemble NV centers are still useful, where the collective emission enhances the signal-to-noise ratio, making it easier to detect weak signals. In contrast,

the spectrum from a single nanodiamond with NV centers exhibits sharper peaks and allows for the observation of the intrinsic properties of an individual NV center, such as ZPL emissions and more defined vibronic sidebands. These features are important for applications requiring single-photon emitters.

For single-molecule studies, it is preferable to use nanodiamonds that contain only one or two NV centers to ensure that the optical and spin properties observed originate from a single emitter. Characterization of individual particles (from Adamas Nanotechnologies) revealed that, on average, for 20 nm nanodiamond particles specifically, most contain one- or two-NV centers. The brightness of these particles depends on the number of NV centers per particle. The fluorescence intensity decreases noticeably in particles with fewer NV centers.

In single-molecule spectroscopy, NV centers provide an excellent platform for probing nanoscale environments. These particles are highly resistant to photobleaching, ensuring consistent performance over time in experimental settings. These properties make the particles particularly suitable for high-precision applications such as quantum optics,[137, 138] imaging of individual cells and single-molecule tracking, and nanoscale sensing applications[89, 139] where brightness plays a crucial role in the accuracy of detection.

To further investigate the optical properties of NV centers and to focus on the spatial localization of individual ones, an imaging and spectral analysis of NV centers are represented in Figure 16. Single-molecule level refers to the detection and manipulation of individual NV centers, which behave as single quantum emitters. This can be confirmed by measuring the second-order correlation function $g^2(\tau)$. A dip below 0.5 in the correlation curve is indicative of antibunching, which is a clear sign that only one photon is emitted at a time from a single NV center.

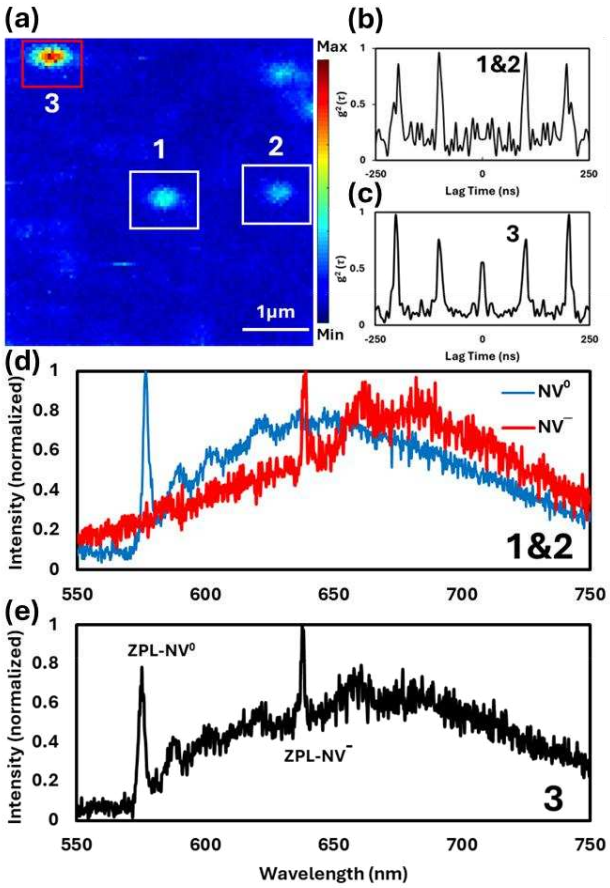

Figure 16. (a) Confocal fluorescence image of nanodiamonds on an ultra-clean coverslip, showing isolated spots corresponding to single NV centers (white box-labeled 1 and 2) and a brighter spot likely representing multiple NV centers (red box-labeled 3). The color maps indicate relative fluorescence intensity, brighter regions indicating higher emission intensity. (b, c) Second-order photon correlation function $g^2(\tau)$ for the emitters in regions (1, 2) and (3). (b) The dip at $\tau = 0$ for emitters in regions (1 and 2) indicates strong antibunching, confirming single-photon emission from a single NV center. (c) The absence of significant antibunching for region (3) proofs the presence of double or multiple NV centers in a nanodiamond. (d) Normalized emission spectra two nanodiamonds at 160 K in the region (1 and 2) including only a single NV^0 (blue line) and a single NV^- (red line). Detailed comparison of the ZPLs for NV^0 and NV^-, highlighting the spectral differences between them. (e) Emission spectra of a nanodiamond in region 3 with two NV centers at 160 K.

Figure 16 provides a comprehensive analysis of single NV centers in nanodiamonds, with spatial imaging, photon correlation (antibunching) measurements, and spectroscopic comparison of the two charge states, NV^0 and NV^-. A thin film containing nanodiamonds in a 1% wt solution of PVA in triple distilled water was deposited (a droplet of 5 µL of the 10^{-3} mol/L solution) by spin-coating onto an ultra-clean fused silica coverslip and is excited by a pulsed laser at 488 nm.

Figure 16a shows a confocal PL-intensity map of the nanodiamond sample at 160 K, where individual fluorescent spots in white box labeled 1 and 2 correspond to single NV emitters while a red region marked 3 corresponds to a brighter spot, potentially indicating a nanodiamond containing double or multiple NV centers. Figure 16b and 16c displays the second-order photon correlation function, $g^2(\tau)$, which is used to determine single photon emitting. In Figure 16b, the $g^2(\tau)$ curve for the emission from region 1 and 2 shows suppression below 0.5 and a pronounced dip at $\tau = 0$. This confirms the antibunching behavior and indicates that the emitter is a single NV center. In contrast, Figure 16c shows the correlation measurement from a nanodiamond in region 3, where the absence of a pronounced dip reflects the presence of multiple NV centers, leading to bunching behavior indicative of a multi-emitter system.

The spectra in Figure 16d shows the normalized emission spectra of two individual single NV centers, NV^0 (blue curve) and NV^- (red curve), measured from the nanodiamonds in region 1 and 2. The NV^0 center exhibits a broad phonon side band with a sharp ZPL at 575 nm, while the NV^- center has a ZPL at approximately 637 nm, followed by phonon sidebands. This clear distinction between the two charge states is important for understanding the optical transitions and electronic states associated with the NV center. The broader spectra typically observed in nanodiamonds with multiple NV centers shown in Figure 16e, when the nanodiamond in region 3 contains two NV centers.

4.2 Single NV Centers in Free Space at Low Temperatures

To investigate the effect of temperature on the spectral behavior of NV centers, the emission spectra of the nanodiamonds are measured in different temperatures from 5 K to 250 K that is shown in Figure 17.

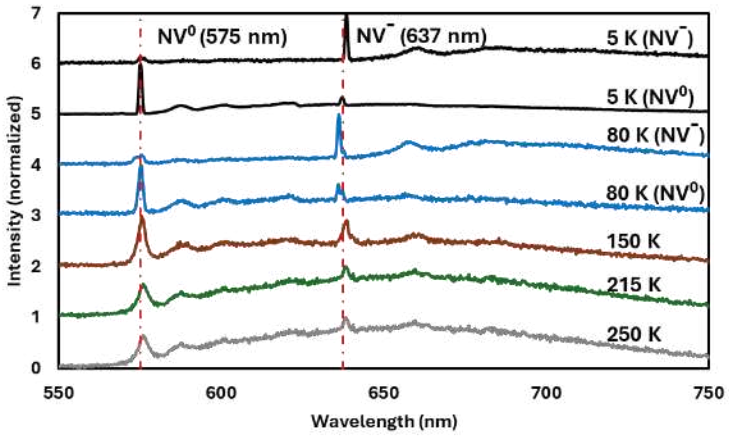

Figure 17. Emission spectra of NV centers at different temperatures from 5 K to 250 K. Broadening change of ZPL for NV^0 and NV^- at 575 and 637 nm, respectively by varying temperatures from 5 K to 250 K. The dashed red lines indicate the positions of ZPLs.

Emission spectra of NV centers in nanodiamonds measured at different temperatures, ranging from 5 K (low temperature) to 250 K (high temperature), as indicated by the color-coded lines in Figure 17. The ZPLs of NV centers are shown with dashed red lines. The temperature dependence of the NV center spectra can be explained by considering the interactions between the electronic states of the NV centers and the phonons (quantized vibrations of the lattice) in the diamond crystal.[135] At lower temperatures (e.g., 5 K), the ZPLs of both NV^0 and NV^- are very sharp and well-defined. This is because reduced thermal vibrations minimize electron-phonon interactions which allow the NV center to emit most of its photons directly through the ZPL. At higher temperatures, the phonon population in the diamond lattice grows due to increased thermal energy. These phonons interact more strongly with the electronic states of the

NV centers, causing spectral broadening, intensity reduction of ZPL and increasing phonon sidebands. The slight shift in the ZPL position with increasing temperature is a result of the changing lattice constant and strain effects as the diamond crystal expands with heat. The thermal expansion alters the local environment of the NV centers, which in turn slightly shifts the energy levels associated with the NV^0 and NV^- charge states.

4.3 Single NV Centers in a Tunable Microcavity at Low Temperatures

To investigate the effects of light-matter interaction, spectral tuning, and the optimization of photon emission efficiency of single particles, NV centers are placed within a tunable microcavity integrated into a home-built microscope. This setup allows for investigations at both room and cryogenic temperatures, as discussed in section 3.5.

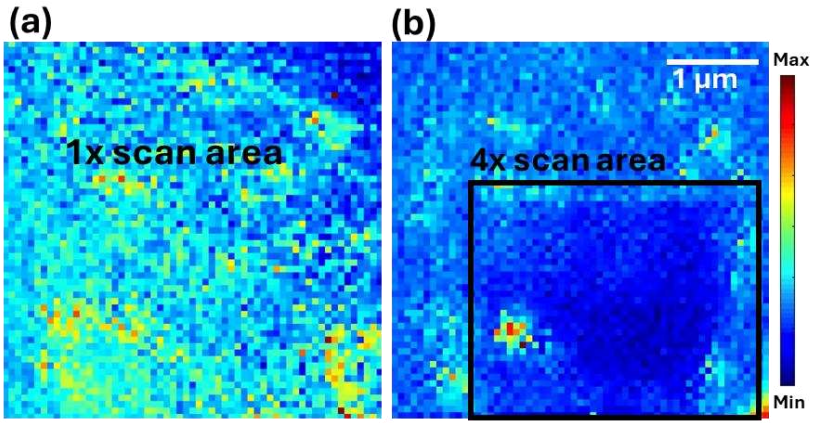

Figure 18. (a, b) Fluorescence images of single nanodiamonds embedded in 1 wt % PVA on top of the SiO_2 spacer layer of tunable mirror in a multiple of half a wavelength microcavity.

Figure 18 shows two fluorescence imaging scans of a sample containing single nanodiamonds, positioned inside a tunable microcavity. A film containing the nanodiamonds spin-coated onto tunable mirror of the microcavity. The microcavity is placed into a cryostat and the experiment was conducted at a

temperature of 160 K. In Figure 18a, a single scan of the area is shown. Despite the presence of nanodiamonds, the high background and scattered light obscure the single emitters. In Figure 18b, after performing four sequential scans in the same area, a single bright spot corresponding to a nanodiamond emitter can be seen within the black box. Nanodiamonds show relatively weak fluorescence in the microcavity environment due to the high background signal and low signal-to-noise ratio, therefore detecting single emitters becomes challenging. Imperfections in the mirror surfaces of the cavity can cause scattering of the incident light, while impurities or contamination on the silver-coated surfaces can lead to unwanted fluorescence. As a result, a background signal within the cavity, potentially interferes with the emitted signal. To minimize background effects and improve the SNR for detecting single emitters in a microcavity, several techniques can be used, including repeated scans (as shown in Figure 18) to bleach unwanted fluorescence, better filtering methods, or use of a higher Q-factor cavity.

Next, the fluorescence emission spectra of NV centers within a tunable microcavity are investigated to study the Purcell effect induced by the cavity. This approach examines how the cavity modifies the radiative decay rate of the NV centers, influencing their fluorescence properties. Two-dimensional plots in Figure 19a and 19b depict sequential experimental white light transmission spectra of the microcavity, and the emission spectra of NV centers as influenced by the cavity modes, respectively.

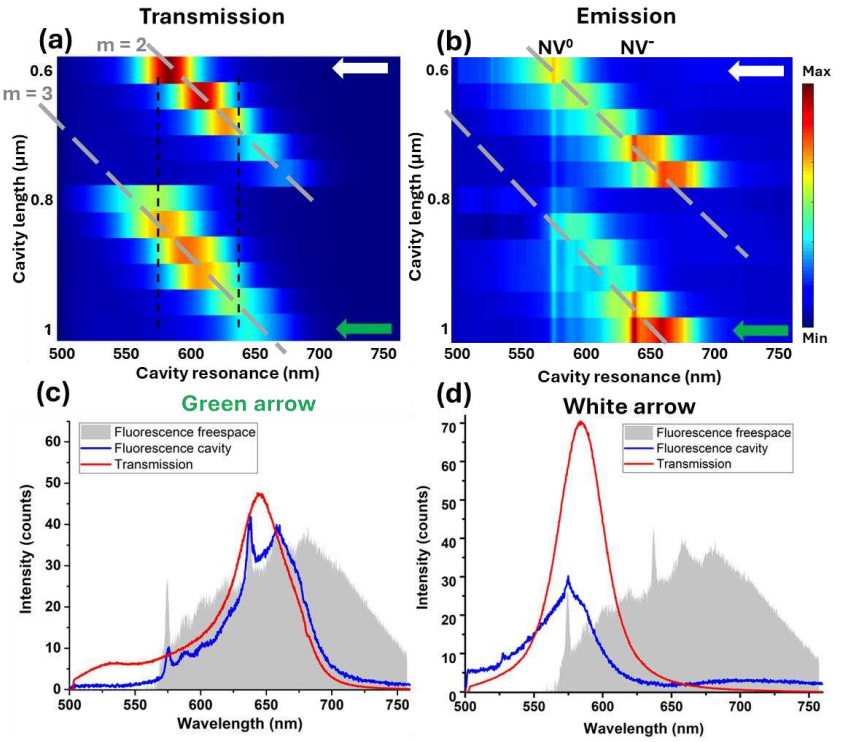

Figure 19. (a) Experimental white light transmission spectra of the microcavity at 160 K were obtained consecutively while the distance between mirrors in the cavity is decreased from third to second cavity mode. The emission of ZPL on NV^0 and NV^- in free space are indicated by dashed black lines. The cavity mode is marked with orders m = 2 and 3 (gray solid lines). (b) Corresponding experimental emission spectra for a single nanodiamond within the microcavity. The gray solid lines indicate the same cavity modes for emission and transmission. The strongest Purcell effect for a cavity setting is marked by white and green arrow in (a) and (b). Two individual spectra, transmission (red curve) and emission (blue curve) at the positions marked with arrows are shown in (c) and (d). These illustrate how different cavity settings affect the fluorescence intensity of the ZPL of the NV centers. The gray background is the fluorescence spectrum of a nanodiamond in free space.

Figure 19a and 19b illustrate transition from the third to the second cavity mode as a function of the decreasing separation between the cavity mirrors. The black dashed lines indicate the free space emission peaks of the ZPL of NVs. The decrease in intensity of the transmission spectra at longer wavelengths, as seen in Figure 19a, is due to the spectral emission profile of the LED used to

acquire the data. The sharpness of the resonance frequencies reflects the quality factor of the cavity modes.

Figures 19c and 19d show the individual spectra marked by the green and white arrows. The red curve corresponds to the white light transmission through the cavity, while the blue curve shows the emission of the NV centers in the nanodiamond. The gray background shows the spectrum of a nanodiamond in free space. As cavity separation between two mirrors decreases from the 3rd mode in Figure 19c to the 2nd mode in Figure 19d, the intensity of the NVs' emission can be altered due to the Purcell effect. In both cases, the excitation conditions remain constant, while the intensity ratios of the NV emissions are highly dependent on the specific cavity mode settings.

In Figure 19c, the NV^- emission is in resonance with the 3rd cavity mode, while the NV^0 emission is significantly reduced. In Figure 19d, where the mirror spacing is reduced, the NV^0 emission is in resonance with the 2nd cavity mode, leading to a significant enhancement due to the Purcell effect while the NV^- emission is off resonance and is completely suppressed compared to its behavior in Figure 19c. The Purcell effect enhances spontaneous emission at the ZPL of the NV centers, indicating efficient coupling of the NV centers emission with the cavity mode. By tuning the cavity to align with the NV ZPL, efficient photon extraction can be achieved, which can be essential for the development of quantum systems.[140]

4.4 Lifetime of Single NV Centers in Free Space and Cavity

The recorded lifetimes of 53 nanodiamonds including one or two NVs in free space at a temperature of 160 K are shown in Figure 20a. Each dot corresponds to a lifetime measurement taken from a single nanodiamond. The neutral charge state NV^0 center has an average fluorescence lifetime of 14.9 ns (blue boxplot) and the negatively charged state NV^- has an average lifetime of 17.5 ns. The distribution reveals variations in lifetimes across different nanodiamonds, likely due to differences in their local environments and crystal quality. The lifetime differences also indicate that both charge states have

distinct emission properties and responses to environmental factors such as temperature and local electric fields.

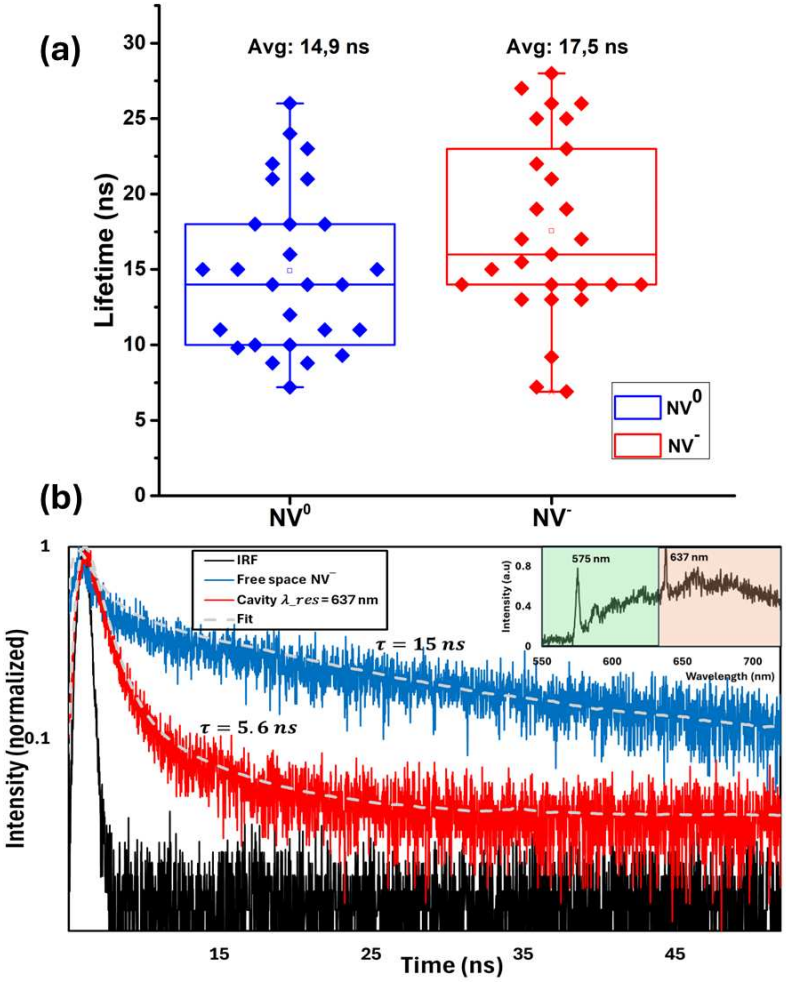

Figure 20. (a) An average-weighted lifetime diagram of NV^0 (blue), NV^- (red) in free space. (b) Fluorescence lifetime decay curves of the NV^- at 160 K in free space (blue curve) and in the cavity (red curve) when it is on resonance with the NV^-. The inset is the transmission spectra of the band-pass 580 nm (green) and long pass 630 nm (orange) filters to measure the lifetime of NV^0 and NV^- individually. Fits (gray dashed lines) are calculated by convolution of a mono-exponential decay curve and the instrument response function (black line).

Fluorescent nanodiamonds were positioned between the two mirrors of the tunable microcavity to explore how the optical microcavity affects the radiative properties of the NVs. The optical path length of the microcavity was precisely modified to adjust the position of the tunable mirror relative to the fixed mirror. Fluorescence lifetime decay curves of a single NV center, comparing the results in free space and within a microcavity at 160 K are shown in Figure 20b. The fluorescence lifetime of the single NV^- center was acquired by TCSPC to achieve high precision in measuring photon arrival time. The inset displays the transmission spectra of the band-pass 580 nm (green) and long pass 630 nm (orange) filters used in the experiment, emphasizing their transmission windows near ZPL of NVs to measure the corresponding lifetime of NV center individually. The measured lifetimes (the corresponding fit functions - gray dashed lines) are based on convolution of the instrument response function (IRF, black line) with the exponential decay functions. The lifetime of a single NV^- in free space ($\tau = 15 \pm 0.09\ ns$) shown with blue line is consistent with the average lifetime values observed in Figure 20a. In contrast, the red curve shows the lifetime of the NV^- center when placed inside a microcavity tuned to $\lambda \approx 637$ nm, which is close to the ZPL of NV^-. When the ZPL of NV^- center is in resonance with cavity mode, the measured lifetime is significantly shorter ($\tau = 5.6 \pm 0.07\ \mathrm{ns}$). This reduction in lifetime indicates the Purcell effect, where the presence of the resonant cavity accelerates the spontaneous emission rate of the NV^- center. This is nearly in accordance with the theoretical maximum lifetime reduction of about 3, as indicated by the Purcell factor under these specific conditions.[122]

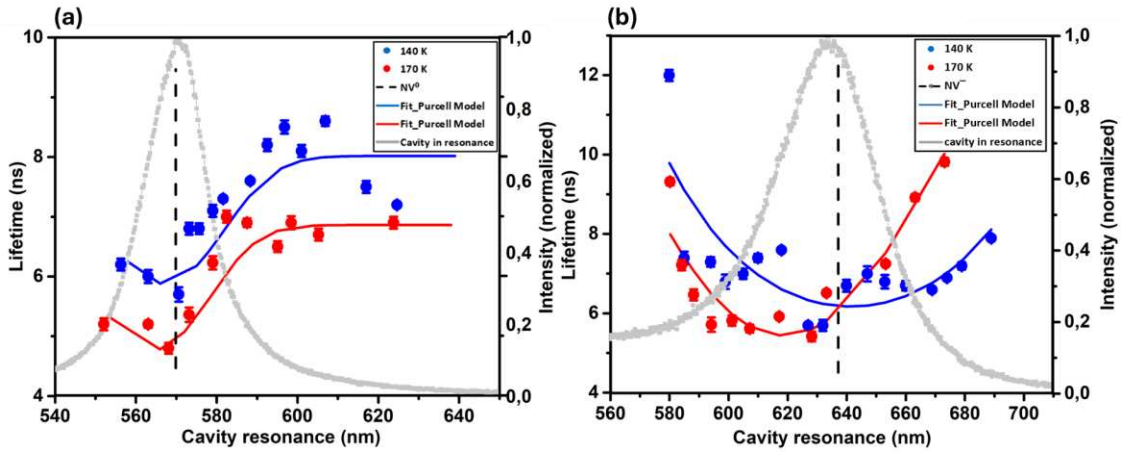

Figure 21. (a, b) Experimental cavity-modified fluorescence lifetimes of ensemble sample for NV^0 and NV^- at 140 K (blue dots) and 170 K (red dots) as a function of cavity resonances overlaid with normalized intensity of cavity in resonance (gray curve) with ZPL of NVs on the second y-axis. The blue and red solid curves correspond to the theoretical model fits based on the Purcell factor, used to determine how the cavity resonances affect the variation in fluorescence lifetimes of NVs. The error-bars result from fitting the fluorescence lifetime decay curve. The grey curve in the background indicates the cavity resonance, which aligns with the ZPL of NVs.

In Figure 21a and 21b the effect of Purcell factor and temperatures on the lifetime of ensemble NV^0 and NV^- are demonstrated as function of cavity resonance at 140 K (blue dots) and 170 K (red dots), respectively. The cavity mode (gray curve) is in resonance with the ZPL of NVs (black dashed line). The microcavity resonance was tuned between 500 nm and 700 nm, and the lifetime decay measurements were taken at different spectral positions. By increasing the mirror spacing, the cavity resonance was shifted towards longer wavelengths. A theoretical model used to fit the data points based on the Purcell factor (are displayed as blue and red solid curve) is in good agreement with the experimental data. The fluorescence lifetime of NV^0 and NV^- decreases as a dip due to the Purcell effect when the microcavity is on resonance with the ZPL of NVs.

In Figure 21a and 21b the effect of temperature on the fluorescence lifetime of NV centers can be studied by comparing the behavior at two different temperatures, 140 K (blue curve) and 170 K (red curve). At a temperature of 140 K, as represented by the blue curve, both NV^0 and NV^- lifetimes increase slightly compared to their values at 170 K. This could be due to reduced phonon interactions at lower temperatures, leading to less non-radiative decay and thus longer lifetimes.[141] However, this change is not substantial, indicating that a 30 K rise in temperature does not dramatically alter the overall fluorescence lifetime of NV centers, especially within the observed wavelength range. This suggests that while the 30 K increase results in a moderate decrease in fluorescence lifetime, it is not drastic enough to alter the fundamental characteristics of both NV^0 and NV^-. Even at 170 K, the system retains its essential properties, demonstrating only a slight loss in efficiency.

5. Controlling Three-Color Förster Resonance Energy Transfer in an Optical Fabry−Pérot Microcavity at Low Mode Order

This chapter is based on:
Nosrati, Saeed, et al. "Controlling three-color Förster resonance energy transfer in an optical Fabry–Pérot microcavity at low mode order." The Journal of Physical Chemistry C 127.25 (2023): 12152-12159.

This study focuses on the interactions between three spectrally distinct fluorescent dyes—a donor and two acceptors—embedded within a single polystyrene (TetraSpeck) nanosphere. The presence of triple FRET energy transfer is confirmed through selective acceptor photobleaching, demonstrating that the fluorescence lifetimes of the dyes can be controlled using the Purcell effect when the nanospheres are embedded in an optical Fabry−Pérot microcavity. This effect modulates the radiative rates and relative fluorescence intensities, leading to a significant enhancement in the fluorescence intensity of the second acceptor when the microcavity mode is tuned to suppress the intermediate dye emission and transfer more energy from the donor to the second acceptor. Single nanospheres with a nominal diameter of 100 nm containing fluorescent dyes with excitation maxima at 505 nm, 575 nm, and 655 nm were embedded at low concentration between the adjacent mirrors of a low mode order of a Fabry−Pérot microcavity. By varying the mirror separation, the cavity resonance can be precisely tuned over the spectral region of the excitation or emission spectra to modulate the absorption rate and the spontaneous emission rates of the embedded dyes.
The microcavity's influence on the radiative rated of the dyes is evident, with the strongest fluorescence intensity enhancement observed for the second acceptor, signifying efficient energy transfer from the donor to the second acceptor. The study successfully demonstrates the ability to control a three-color FRET system within a Fabry−Pérot microcavity.

Results and Discussion

The triple FRET process was validated through photobleaching experiments,

where donor fluorescence lifetime increased progressively from 5.7 ns to 6.8 ns, and to 7.2 ns after sequentially photobleaching acceptor2 and acceptor1, demonstrating energy transfer interactions among the dyes. This confirms energy transfer pathways between the donor and two acceptors in single TetraSpeck nanospheres, as well as the intermediate role of acceptor1 in transferring energy to acceptor2.

To study how the optical microcavity affects the radiative properties of the dye molecules, single nanospheres were embedded within a Fabry−Pérot microcavity, allowing precise control over the optical path length of the cavity and to modulate the spontaneous emission rates of dyes. Resonance tuning of the microcavity altered the radiative decay rates of the donor and acceptor molecules. This resulted in significantly reduced lifetimes for both donor and acceptor1, from approximately 7.0 ns and 8.1 ns in free space to around 2.7 ns and 2.8 ns within the cavity, respectively. These observations align closely with theoretical predictions derived from the Purcell factor, which estimates a maximum lifetime reduction factor of about 3.
Further investigation at cryogenic temperatures (130 K) allowed a detailed evaluation of how fluorescence lifetimes depend on changes in cavity resonance. The fluorescence lifetimes of the dyes within a single nanosphere decrease due to the Purcell effect when the cavity resonance approaches their fluorescence peak. Theoretical modeling, including the Purcell factor, successfully matched the experimental data, confirming that spectral control can influence the radiative properties of dyes within the cavity.

The interplay between cavity resonance and the FRET process was further analyzed by varying the microcavity mode to selectively enhance or suppress specific dye emissions. Three distinct cavity settings are presented with the signatures of the FRET process between donor and acceptors. When the cavity resonance suppressed the donor's emission, energy was transferred to acceptor1. Tuning the cavity to suppress the intermediate acceptor1 while resonating with acceptor2 resulted in energy transfer to acceptor2, which clearly demonstrates controlled FRET modulation through microcavity resonance. The experimental results were supported by a theoretical model

using six coupled rate equations, which included the Purcell effect on the radiative rates and triple energy transfer between the donor and acceptors. This study focused on the impact of microcavity on the fluorescence emission of the dyes, without considering potential effects on the energy transfer rate constant resulting from the tuning of the microcavity or excitation rates.

Overall, this study advances the understanding of multi-FRET systems within the tunable microcavity. This novel approach enables precise manipulation of energy transfer pathways, offering significant potential for advanced applications in complex molecular sensing, light-harvesting systems, and nanoscale photonics devices. The findings contribute to a deeper understanding of how photonic environments can influence the FRET processes, paving the way for future research and technological advancements in energy transfer mechanisms.

6. Combining Optical Strong Mode Coupling with Polaritonic Coupling in a $\lambda/2$ Fabry–Pérot Microresonator

This chapter is based on:
Nosrati, Saeed, et al. "Combining Optical Strong Mode Coupling with Polaritonic Coupling in a $\lambda/2$ Fabry–Pérot Microresonator." The Journal of Physical Chemistry C 125.23 (2021): 13024-13032.

An optical microcavity is an interesting tool to study light-matter interaction, e.g. the coupling of a quantum emitter to the optical field in a microcavity. The coupling rate is a measure of the interaction strength between the quantum emitter and cavity mode and can be used to differentiate between weak or strong coupling. This chapter focuses on a hybrid system consisting of a thin TDBC J-aggregate film inside an optical microresonator coupled to another microresonator. This setup combines a strong coupling of purely optical modes with strong light-matter interaction.

The experimental setup includes two adjacent $\lambda/2$ Fabry-Pérot microresonators and a thin film of TDBC J-aggregate placed on top of a SiO_2 spacer layer, which is deposited on the shared central mirror of one of the microresonators. The design of the coupled system allows tuning the resonance of one microcavity across the other, which enables to study the dispersion of the strongly coupled system without tilting of the sample. The coupling rate between the spatially separated microcavities can be adjusted by the thickness of a shared central silver mirror.

Results and Discussion

A hybrid system was investigated that combines two types of strong coupling: coupling between optical modes in adjacent microresonators and coupling between optical modes and TDBC J-aggregates.
The experiments demonstrated that coupling between purely optical modes in the two microresonators results in the formation of supermodes, characterized by a Rabi splitting of approximately 23 nm and an anticrossing dispersion at

600 nm. This splitting, visible in the transmission spectra, confirmed the strong coupling regime, as the coupling constant exceeded the damping rates of the individual microresonators.

Introducing the TDBC J-aggregate film added a second layer of interaction, where light–matter coupling further split the hybrid system modes into distinct polaritonic states. The position of the TDBC film within the tunable resonator was varied systematically by adjusting the thickness of a dielectric spacer layer on shared central mirror between two microresonators from 70 nm to 185 nm. The coupling constants of the hybrid system demonstrated a unique interplay. For instance, as the resonator–resonator coupling constant decreased due to the presence of the TDBC film in the tunable microresonator, the resonator–molecule coupling constant exhibited an opposite trend, reaching its maximum when the film was centrally positioned. Conversely, moving the film closer to the central shared mirror reduced this interaction and increased strongly damping constant of the tunable microresonator due to the TDBC molecular absorption. Interestingly, the combined coupling strength of the system remained relatively constant over a range of spacer thicknesses, reflecting the complementary nature of the two coupling mechanisms. These observations underscore the critical role of spatial positioning in achieving optimal coupling in a system.
The coupling and damping constants of the system can be determined using a coupled harmonic oscillator model. This theoretical modeling approach effectively reproduced the experimental results. The model revealed that the hybrid system must be treated as a whole, where changes in one component invariably affect the entire system. As an example, detuning the resonance of the fixed microresonator directly influenced the coupling of the molecules within the tunable resonator, even without altering its physical configuration.

To verify that the Rabi splitting energy depends on the number of coherently coupled molecules, an experiment using the photobleaching of TDBC molecules in the coupled system was performed. By reducing the number of coupled TDBC molecules, a gradual decrease from 14 nm to 5 nm in Rabi splitting before and after photobleaching was observed. This finding is

particularly relevant for applications requiring controlled coupling, as it highlights the importance of precisely managing molecular concentration.

Overall, this work demonstrates that combining optical mode coupling with light–matter interaction in a hybrid system offers unprecedented control over coupling dynamics. By carefully tuning geometric and molecular parameters, it is possible to optimize these interactions for various advanced applications, including long-range energy transfer and chemical reaction control. These findings open the way for more sophisticated designs in optical and polaritonic devices, emphasizing the need for integrated approaches in system engineering.

7. Periodic Fluorescence Variations of CdSe Quantum Dots Coupled to Aryleneethynylenes with Aggregation Induced Emission

This chapter is based on:
Kumar, Krishan, et al. "Periodic Fluorescence Variations of CdSe Quantum Dots Coupled to Aryleneethynylenes with Aggregation-Induced Emission." ACS nano 15.1 (2021): 480-488.

This chapter explores the interaction between CdSe nanocrystals (NCs) and aryleneethynylene derivatives exhibiting aggregation-induced emission. The primary focus is on understanding the emergent optical properties arising from this combination, especially the dual fluorescence and its oscillating intensity fluctuations in a hybrid thin film. Aggregation-induced emission (AIE) is a phenomenon where certain luminophores exhibit enhanced and red-shifted fluorescence upon forming aggregates. This happens because of the restriction of intramolecular motion in the solid-state blocks non-radiative pathways that would otherwise suppress fluorescence in solution. The aryleneethynylene derivative AE 1 demonstrates pronounced AIE characteristics.

The fluorescence intensity fluctuations are attributed to a feedback loop involving excitation energy transfer (EET) and photothermal heating. EET from the NCs to AE 1 aggregates induces photothermal heating, causing an order-disorder transition in the aggregates, which affects their fluorescence intensity. This transition reduces the fluorescence intensity of the aggregates and subsequently decreases the EET rate, resulting in increased fluorescence from the NCs. As the system cools, the aggregates gradually return to their initial structure, restoring their fluorescence and restarting the cycle.

Results and Discussion

The assembly of NCs with AE 1 into a hybrid thin film makes a system to explore AIE and its interactions with semiconductor nanocrystals. The hybrid thin film demonstrated dual fluorescence, with both fluorophores contributing to emerge

optical properties. Notably, periodic fluorescence intensity variations were observed under continuous laser excitation that highlights a dynamic feedback mechanism driven by energy transfer and structural changes.
The aryleneethynylene derivative displayed distinct absorption and fluorescence behaviors depending on its environment. In solution, AE 1 showed a broad absorption peak at 350 nm and weak fluorescence at 480 nm. While in the solid state, its fluorescence shifted significantly to 650 nm. At low temperatures, these emissions shifted further to 750 nm due to enhanced structural planarization, confirming the influence of temperature on AIE properties.

Continuous excitation at 488 nm in a nitrogen atmosphere led to fluorescence intensity fluctuations in AE 1. These variations were attributed to the photothermal effects, which altered the structural order of the aggregates and led to reduced restriction of intramolecular motion and faster nonradiative recombination. The transitions between ordered and disordered states modulated the degree of AIE and reduced fluorescence quantum yield during the disordered state.

At room temperature, when AE 1 aggregates coupled to the surface of iodide-capped CdSe nanocrystals (CdSe/I^- NCs), the hybrid system (CdSe/I^-/AE 1) exhibited dual fluorescence bands, with the NCs emitting at 636 nm and the AE 1 aggregates at 734 nm. These bands displayed anticorrelated fluctuations over time where an increase in the fluorescence intensity of the NCs coincided with a decrease in the fluorescence intensity of AE 1. Initially, EET from the NCs to the AE 1 aggregates occurred efficiently, which is due to the spectral overlap between NC emission and AE 1 absorption. The energy transfer induced photothermal heating, causing the AE 1 aggregates to undergo a transition to a disordered state. This structural disruption reduced their fluorescence intensity and weakened the EET efficiency, allowing the NC fluorescence to recover. Over time, as photothermal heating diminished, the AE 1 aggregates reassembled into their ordered state, restoring efficient EET and restarting the cycle. At 160 K, the fluorescence fluctuations became periodic, with the cycle duration inversely correlated with excitation power.

higher laser power increases the heat transfer and leads to reduce period of oscillations, highlighting the role of photothermal effects in regulating the feedback loop. These findings provide insights into the design and application of hybrid materials with emergent optical properties. The system's periodic fluorescence dynamics have potential applications in nanothermometry, and other temperature-sensitive technologies. Moreover, this work demonstrates the capabilities of combining AE 1 with inorganic nanocrystals to create hybrid systems.

Acknowledgment

- First and foremost, I would like to express my deepest gratitude to Prof. Dr. Meixner for introducing me to the world of science and letting me join his research group and supporting me with any scientific issue. He consistently encouraged my growth as a scientist and provided invaluable creative ideas throughout my research.

- I am very grateful to Prof. Dr. Marc Brecht, for sharing his knowledge, enthusiasm and expertise with me. Every discussion with him was an honor, and he taught me to consider different perspectives.

- My sincere thanks go to Dr. Frank Wackenhut for teaching me about optics and providing quick solutions for setup issues. His creative input, help with paper corrections, and explanations about physical chemistry were invaluable. Working under his guidance was a great honor.

- I would like to thank Dai, Kai, Tim, Achim, Quan, Jakob, Christoph, Lexi, and Mr. Karsten Stampke for their support and for making my time a wonderful experience, both professionally and personally. Their help and the collaborative environment they provided enriched my research and professional development.

- To my dear wife, Niloofar, I owe my deepest gratitude for her unwavering love, patience, and support throughout this challenging journey. Her constant encouragement and belief in me have been a profound source of strength and motivation.

- I am profoundly grateful to my parents, Hossein and Fahimeh, and my sister, Roya, for standing by me every step of the way, despite the distance between us. Their unwavering support, encouragement, and sacrifices have made this achievement possible.

- Finally, I would like to acknowledge all my friends who, although not mentioned by name, have provided unconditional support.

References

(1) Kriss, T. C.; Kriss, V. M. History of the operating microscope: from magnifying glass to microneurosurgery. *Neurosurgery* **1998**, *42* (4), 899-907.
(2) Murphy, D. B.; Davidson, M. W. *Fundamentals of light microscopy and electronic imaging*; John Wiley & Sons, 2012.
(3) Lakowicz, J. R. *Principles of fluorescence spectroscopy*; Springer, 2006.
(4) Valeur, B.; Berberan-Santos, M. N. *Molecular fluorescence: principles and applications*; John Wiley & Sons, 2013.
(5) Sheppard, C. J. R. *Confocal microscopy: Principles, practice and options*; Academic Press, London, UK, 1999.
(6) O'Connor, D. V.; Phillips, D. *Time-correlated single photon counting*; Academic Press, 1984.
(7) Castleman, A.; Toennies, J.; Zinth, W. *Advanced Time-Correlated Single Photon Counting Techniques*; 2005. DOI: 10.1007/3-540-28882-1.
(8) Becker, W. *Advanced time-correlated single photon counting applications*; Springer, 2015.
(9) Niehörster, T.; Löschberger, A.; Gregor, I.; Krämer, B.; Rahn, H.-J.; Patting, M.; Koberling, F.; Enderlein, J.; Sauer, M. Multi-target spectrally resolved fluorescence lifetime imaging microscopy. *Nature methods* **2016**, *13* (3), 257-262.
(10) Bastiaens, P. I. H.; Squire, A. Fluorescence lifetime imaging microscopy: spatial resolution of biochemical processes in the cell. *Trends in cell biology* **1999**, *9* (2), 48-52.
(11) Gadella Jr, T. W. J.; Jovin, T. M.; Clegg, R. M. Fluorescence lifetime imaging microscopy (FLIM): spatial resolution of microstructures on the nanosecond time scale. *Biophysical chemistry* **1993**, *48* (2), 221-239.
(12) van Munster, E. B.; Gadella, T. W. J. Fluorescence lifetime imaging microscopy (FLIM). *Microscopy Techniques: -/-* **2005**, 143-175.
(13) Suhling, K.; Hirvonen, L. M.; Levitt, J. A.; Chung, P.-H.; Tregidgo, C.; Le Marois, A.; Rusakov, D. A.; Zheng, K.; Ameer-Beg, S.; Poland, S. Fluorescence lifetime imaging (FLIM): Basic concepts and some recent developments. *Medical photonics* **2015**, *27*, 3-40.
(14) Magde, D.; Elson, E.; Webb, W. W. Thermodynamic fluctuations in a reacting system—measurement by fluorescence correlation spectroscopy. *Physical review letters* **1972**, *29* (11), 705.
(15) Krichevsky, O.; Bonnet, G. Fluorescence correlation spectroscopy: the technique and its applications. *Reports on Progress in Physics* **2002**, *65* (2), 251.
(16) Rigler, R.; Elson, E. S. *Fluorescence correlation spectroscopy: theory and applications*; Springer Science & Business Media, **2012**.
(17) Kapusta, P.; Wahl, M.; Benda, A.; Hof, M.; Enderlein, J. Fluorescence lifetime correlation spectroscopy. *Journal of fluorescence* **2007**, *17*, 43-48.
(18) Böhmer, M.; Wahl, M.; Rahn, H.-J.; Erdmann, R.; Enderlein, J. Time-resolved fluorescence correlation spectroscopy. *Chemical Physics Letters* **2002**, *353* (5-6), 439-445.
(19) Ghosh, A.; Isbaner, S.; Veiga-Gutiérrez, M.; Gregor, I.; Enderlein, J. r.; Karedla, N. Quantifying microsecond transition times using fluorescence lifetime

correlation spectroscopy. *The journal of physical chemistry letters* **2017**, *8* (24), 6022-6028.
(20) Ghosh, A.; Karedla, N.; Thiele, J. C.; Gregor, I.; Enderlein, J. Fluorescence lifetime correlation spectroscopy: Basics and applications. *Methods* **2018**, *140*, 32-39.
(21) Roy, R.; Hohng, S.; Ha, T. A practical guide to single-molecule FRET. *Nature methods* **2008**, *5* (6), 507-516.
(22) Kobayashi, T.; Zheng, Q.; Sekiguchi, T. Resonant dipole-dipole interaction in a cavity. *Physical Review A* **1995**, *52* (4), 2835.
(23) Hopmeier, M.; Guss, W.; Deussen, M.; Göbel, E.; Mahrt, R. Enhanced dipole-dipole interaction in a polymer microcavity. *Physical review letters* **1999**, *82* (20), 4118.
(24) Agarwal, G. S.; Gupta, S. D. Microcavity-induced modification of the dipole-dipole interaction. *Physical Review A* **1998**, *57* (1), 667.
(25) Bär, S.; Chizhik, A.; Gutbrod, R.; Schleifenbaum, F.; Chizhik, A.; Meixner, A. J. Microcavities: tailoring the optical properties of single quantum emitters. *Analytical and bioanalytical chemistry* **2010**, *396*, 3-14.
(26) Dovzhenko, D.; Lednev, M.; Mochalov, K.; Vaskan, I.; Rakovich, Y.; Karaulov, A.; Nabiev, I. Polariton-assisted manipulation of energy relaxation pathways: donor–acceptor role reversal in a tuneable microcavity. *Chemical Science* **2021**, *12* (38), 12794-12805.
(27) Schleifenbaum, F.; Kern, A. M.; Konrad, A.; Meixner, A. J. Dynamic control of Förster energy transfer in a photonic environment. *Physical Chemistry Chemical Physics* **2014**, *16* (25), 12812-12817.
(28) Konrad, A.; Metzger, M.; Kern, A. M.; Brecht, M.; Meixner, A. J. Controlling the dynamics of Förster resonance energy transfer inside a tunable sub-wavelength Fabry–Pérot-resonator. *Nanoscale* **2015**, *7* (22), 10204-10209.
(29) Finlayson, C. E.; Ginger, D. S.; Greenham, N. C. Enhanced Förster energy transfer in organic/inorganic bilayer optical microcavities. *Chemical physics letters* **2001**, *338* (2-3), 83-87.
(30) Fujiwara, H.; Sasaki, K.; Masuhara, H. Enhancement of Förster energy transfer within a microspherical cavity. *ChemPhysChem* **2005**, *6* (11), 2410-2416.
(31) Zhang, J.; Fu, Y.; Lakowicz, J. R. Enhanced Förster resonance energy transfer (FRET) on a single metal particle. *The journal of physical chemistry C* **2007**, *111* (1), 50-56.
(32) Komarala, V. K.; Bradley, A. L.; Rakovich, Y. P.; Byrne, S. J.; Gun'ko, Y. K.; Rogach, A. L. Surface plasmon enhanced Förster resonance energy transfer between the CdTe quantum dots. *Applied Physics Letters* **2008**, *93* (12), 123102.
(33) L.-Viger, M.; Brouard, D.; Boudreau, D. Plasmon-enhanced resonance energy transfer from a conjugated polymer to fluorescent multilayer core− shell nanoparticles: a photophysical study. *The Journal of Physical Chemistry C* **2011**, *115* (7), 2974-2981.
(34) Ghenuche, P.; de Torres, J.; Moparthi, S. B.; Grigoriev, V.; Wenger, J. r. m. Nanophotonic enhancement of the Förster resonance energy-transfer rate with single nanoapertures. *Nano letters* **2014**, *14* (8), 4707-4714.
(35) Lu, D.; Cho, S. K.; Ahn, S.; Brun, L.; Summers, C. J.; Park, W. Plasmon enhancement mechanism for the upconversion processes in NaYF4: Yb3+, Er3+ nanoparticles: Maxwell versus Forster. *ACS nano* **2014**, *8* (8), 7780-7792.

(36) Rustomji, K.; Dubois, M.; Kuhlmey, B.; de Sterke, C. M.; Enoch, S.; Abdeddaim, R.; Wenger, J. Direct Imaging of the Energy-Transfer Enhancement between Two Dipoles in a Photonic Cavity. *Physical Review X* **2019**, *9* (1), 011041. DOI: 10.1103/PhysRevX.9.011041.
(37) Jana, S.; Xu, X.; Klymchenko, A.; Reisch, A.; Pons, T. Microcavity-Enhanced Fluorescence Energy Transfer from Quantum Dot Excited Whispering Gallery Modes to Acceptor Dye Nanoparticles. *ACS nano* **2020**.
(38) Jana, S.; Xu, X.; Klymchenko, A.; Reisch, A.; Pons, T. Microcavity-enhanced fluorescence energy transfer from quantum dot excited whispering gallery modes to acceptor dye nanoparticles. *ACS nano* **2020**, *15* (1), 1445-1453.
(39) Wang, J.-F.; Zhou, H.-L.; Xiong, X.; Li, Q.; Cheng, Z.-D.; Liu, Z.-H.; Yan, F.-F.; Lin, S.-R.; Xu, J.-S.; Wang, G.-Z. Cavity-enhanced energy transfer between nano-emitters and monolayer graphene. *Carbon* **2020**, *161*, 794-799.
(40) Yunke, Z.; Zhiyi, Y.; Xuerui, G.; Muhammad, D. B.; Cuong, H. D.; Yu-Cheng, C. Dynamic photonic barcodes for molecular detection based on cavity-enhanced energy transfer. *Advanced Photonics* **2020**, *2* (6), 1-9. DOI: 10.1117/1.AP.2.6.066002.
(41) Schleifenbaum, F.; Elgass, K.; Steiner, M.; Enderlein, J.; Peter, S.; Meixner, A. Optical microresonator modifies the efficiency of the fluorescence resonance energy transfer in the autofluorescent protein DsRed. In *Single Molecule Spectroscopy and Imaging II*, 2009; International Society for Optics and Photonics: Vol. 7185, p 718504.
(42) Schleifenbaum, F.; Elgass, K.; Steiner, M.; Enderlein, J.; Peter, S.; Meixner, A. J. Optical microresonator modifies the efficiency of the fluorescence resonance energy transfer in the autofluorescent protein DsRed. In *Proc.SPIE*, 2009; Vol. 7185. DOI: 10.1117/12.809325.
(43) Olejko, L.; Bald, I. FRET efficiency and antenna effect in multi-color DNA origami-based light harvesting systems. *RSC Advances* **2017**, *7* (39), 23924-23934, 10.1039/C7RA02114C. DOI: 10.1039/C7RA02114C.
(44) Hodgson, N.; Weber, H. *Optical resonators: fundamentals, advanced concepts and applications*; Springer Science & Business Media, 2013.
(45) Kühn, S.; Håkanson, U.; Rogobete, L.; Sandoghdar, V. Enhancement of single-molecule fluorescence using a gold nanoparticle as an optical nanoantenna. *Physical review letters* **2006**, *97* (1), 017402.
(46) Clapp, A. R.; Medintz, I. L.; Mattoussi, H. Förster resonance energy transfer investigations using quantum ‐ dot fluorophores. *ChemPhysChem* **2006**, *7* (1), 47-57.
(47) Jares-Erijman, E. A.; Jovin, T. M. Imaging molecular interactions in living cells by FRET microscopy. *Current opinion in chemical biology* **2006**, *10* (5), 409-416.
(48) Murade, C. U.; Chaudhuri, S.; Nabti, I.; Fahs, H.; Refai, F. S. M.; Xie, X.; Pearson, Y. E.; Gunsalus, K. C.; Shubeita, G. T. FRET-based probe for high-throughput DNA intercalator drug discovery and in vivo imaging. *ACS sensors* **2021**, *6* (6), 2233-2240.
(49) Medintz, I. L.; Clapp, A. R.; Mattoussi, H.; Goldman, E. R.; Fisher, B.; Mauro, J. M. Self-assembled nanoscale biosensors based on quantum dot FRET donors. *Nature materials* **2003**, *2* (9), 630-638.
(50) Konrad, A.; Metzger, M.; Kern, A. M.; Brecht, M.; Meixner, A. J. Revealing the radiative and non-radiative relaxation rates of the fluorescent dye Atto488 in a

λ/2 Fabry–Pérot-resonator by spectral and time resolved measurements. *Nanoscale* **2016**, *8* (30), 14541-14547.
(51) Hunger, D.; Steinmetz, T.; Colombe, Y.; Deutsch, C.; Hänsch, T. W.; Reichel, J. A fiber Fabry–Perot cavity with high finesse. *New Journal of Physics* **2010**, *12* (6), 065038.
(52) Konrad, A.; Kern, A. M.; Brecht, M.; Meixner, A. J. Strong and Coherent Coupling of a Plasmonic Nanoparticle to a Subwavelength Fabry–Pérot Resonator. *Nano Letters* **2015**, *15* (7), 4423-4428. DOI: 10.1021/acs.nanolett.5b00766.
(53) Schneider, C.; Gold, P.; Reitzenstein, S.; Hoefling, S.; Kamp, M. Quantum dot micropillar cavities with quality factors exceeding 250,000. *Applied Physics B* **2016**, *122*, 1-6.
(54) Zhang, Y.-n.; Zhao, Y.; Lv, R.-q. A review for optical sensors based on photonic crystal cavities. *Sensors and Actuators A: Physical* **2015**, *233*, 374-389.
(55) Canet-Ferrer, J.; Martínez, L. J.; Prieto, I.; Alén, B.; Muñoz-Matutano, G.; Fuster, D.; González, Y.; Dotor, M. L.; González, L.; Postigo, P. A. Purcell effect in photonic crystal microcavities embedding InAs/InP quantum wires. *Optics express* **2012**, *20* (7), 7901-7914.
(56) Noda, S.; Fujita, M.; Asano, T. Spontaneous-emission control by photonic crystals and nanocavities. *Nature photonics* **2007**, *1* (8), 449-458.
(57) Atlasov, K. A.; Karlsson, K. F.; Rudra, A.; Dwir, B.; Kapon, E. Wavelength and loss splitting in directly coupled photonic-crystal defect microcavities. *Optics express* **2008**, *16* (20), 16255-16264.
(58) Atlasov, K. A.; Rudra, A.; Dwir, B.; Kapon, E. Large mode splitting and lasing in optimally coupled photonic-crystal microcavities. *Optics express* **2011**, *19* (3), 2619-2625.
(59) Chalcraft, A.; Lam, S.; Jones, B.; Szymanski, D.; Oulton, R.; Thijssen, A.; Skolnick, M.; Whittaker, D.; Krauss, T.; Fox, A. Mode structure of coupled L3 photonic crystal cavities. *Optics express* **2011**, *19* (6), 5670-5675.
(60) Yoshie, T.; Scherer, A.; Hendrickson, J.; Khitrova, G.; Gibbs, H.; Rupper, G.; Ell, C.; Shchekin, O.; Deppe, D. Vacuum Rabi splitting with a single quantum dot in a photonic crystal nanocavity. *Nature* **2004**, *432* (7014), 200-203.
(61) Sun, L.; Chen, Z.; Ren, Q.; Yu, K.; Bai, L.; Zhou, W.; Xiong, H.; Zhu, Z. Q.; Shen, X. Direct observation of whispering gallery mode polaritons and their dispersion in a ZnO tapered microcavity. *Physical review letters* **2008**, *100* (15), 156403.
(62) Yang, S.; Wang, Y.; Sun, H. Advances and prospects for whispering gallery mode microcavities. *Advanced Optical Materials* **2015**, *3* (9), 1136-1162.
(63) Armani, A. M.; Kulkarni, R. P.; Fraser, S. E.; Flagan, R. C.; Vahala, K. J. Label-free, single-molecule detection with optical microcavities. *science* **2007**, *317* (5839), 783-787.
(64) Zhang, X.; Choi, H. S.; Armani, A. M. Ultimate quality factor of silica microtoroid resonant cavities. *Applied physics letters* **2010**, *96* (15).
(65) Yoshie, T.; Tang, L.; Su, S.-Y. Optical Microcavity: Sensing down to Single Molecules and Atoms. In *Sensors*, 2011; Vol. 11, pp 1972-1991.
(66) Fox, A. M. *Quantum optics: an introduction*; Oxford University Press, USA, 2006.
(67) Zhong, X.; Chervy, T.; Wang, S.; George, J.; Thomas, A.; Hutchison, J. A.; Devaux, E.; Genet, C.; Ebbesen, T. W. Non-Radiative Energy Transfer Mediated by Hybrid Light-Matter States. *Angewandte Chemie International Edition* **2016**, *55* (21),

6202-6206,https://doi.org/10.1002/anie.201600428.DOI:
https://doi.org/10.1002/anie.201600428 (acccessed 2021/03/17).
(68) Kim, K.-S.; Kim, J.-H.; Kim, H.; Laquai, F.; Arifin, E.; Lee, J.-K.; Yoo, S. I.; Sohn, B.-H. Switching off FRET in the hybrid assemblies of diblock copolymer micelles, quantum dots, and dyes by plasmonic nanoparticles. *ACS nano* **2012**, *6* (6), 5051-5059.
(69) Coles, D. M.; Somaschi, N.; Michetti, P.; Clark, C.; Lagoudakis, P. G.; Savvidis, P. G.; Lidzey, D. G. Polariton-mediated energy transfer between organic dyes in a strongly coupled optical microcavity. *Nature Materials* **2014**, *13* (7), 712-719. DOI: 10.1038/nmat3950.
(70) Nosrati, S.; Rammler, T.; Meixner, A. J.; Wackenhut, F. Combining Optical Strong Mode Coupling with Polaritonic Coupling in a λ/2 Fabry–Pérot Microresonator. *The Journal of Physical Chemistry C* **2021**, *125* (23), 13024-13032. DOI: 10.1021/acs.jpcc.1c03004.
(71) Li, Q.; Wang, T.; Su, Y.; Yan, M.; Qiu, M. Coupled mode theory analysis of mode-splitting in coupled cavity system. *Optics express* **2010**, *18* (8), 8367-8382.
(72) Yoshie, T.; Scherer, A.; Hendrickson, J.; Khitrova, G.; Gibbs, H. M.; Rupper, G.; Ell, C.; Shchekin, O. B.; Deppe, D. G. Vacuum Rabi splitting with a single quantum dot in a photonic crystal nanocavity. *Nature* **2004**, *432* (7014), 200-203.
(73) Dovzhenko, D.; Mochalov, K.; Vaskan, I.; Kryukova, I.; Rakovich, Y.; Nabiev, I. Polariton-assisted splitting of broadband emission spectra of strongly coupled organic dye excitons in tunable optical microcavity. *Optics Express* **2019**, *27* (4), 4077-4089. DOI: 10.1364/OE.27.004077.
(74) Xu, C.; Zhou, B.; Wang, X.; Tian, C.; Zhang, Y.; Dong, H.; Wang, G.; Zhou, W. Dynamics of excited-state condensate for optically confined exciton-polaritons. *Optics Express* **2019**, *27* (18), 24938-24944. DOI: 10.1364/OE.27.024938.
(75) Norris, T. B.; Rhee, J. K.; Sung, C. Y.; Arakawa, Y.; Nishioka, M.; Weisbuch, C. Time-resolved vacuum Rabi oscillations in a semiconductor quantum microcavity. *Physical Review B* **1994**, *50* (19), 14663-14666. DOI: 10.1103/PhysRevB.50.14663.
(76) Weisbuch, C.; Nishioka, M.; Ishikawa, A.; Arakawa, Y. Observation of the coupled exciton-photon mode splitting in a semiconductor quantum microcavity. *Physical Review Letters* **1992**, *69* (23), 3314-3317. DOI: 10.1103/PhysRevLett.69.3314.
(77) Peter, E.; Senellart, P.; Martrou, D.; Lemaître, A.; Hours, J.; Gérard, J. M.; Bloch, J. Exciton-Photon Strong-Coupling Regime for a Single Quantum Dot Embedded in a Microcavity. *Physical Review Letters* **2005**, *95* (6), 067401. DOI: 10.1103/PhysRevLett.95.067401.
(78) Pelton, M.; Storm, S. D.; Leng, H. Strong coupling of emitters to single plasmonic nanoparticles: exciton-induced transparency and Rabi splitting. *Nanoscale* **2019**, *11* (31), 14540-14552, 10.1039/C9NR05044B. DOI: 10.1039/C9NR05044B.
(79) George, J.; Wang, S.; Chervy, T.; Canaguier-Durand, A.; Schaeffer, G.; Lehn, J.-M.; Hutchison, J. A.; Genet, C.; Ebbesen, T. W. Ultra-strong coupling of molecular materials: spectroscopy and dynamics. *Faraday Discussions* **2015**, *178* (0), 281-294, 10.1039/C4FD00197D. DOI: 10.1039/C4FD00197D.
(80) Vasista, A. B.; Barnes, W. L. Molecular Monolayer Strong Coupling in Dielectric Soft Microcavities. *Nano Letters* **2020**, *20* (3), 1766-1773. DOI: 10.1021/acs.nanolett.9b04996.

(81) Konrad, A.; Trost, A.-L.; Skandary, S.; Hussels, M.; Meixner, A. J.; Karapetyan, N. V.; Brecht, M. Manipulating the excitation transfer in Photosystem I using a Fabry–Perot metal resonator with optical subwavelength dimensions. *Physical Chemistry Chemical Physics* **2014**, *16* (13), 6175-6181, 10.1039/C3CP55195D. DOI: 10.1039/C3CP55195D.
(82) Kern, A. M.; Zhang, D.; Brecht, M.; Chizhik, A. I.; Failla, A. V.; Wackenhut, F.; Meixner, A. J. Enhanced single-molecule spectroscopy in highly confined optical fields: from λ/2-Fabry–Pérot resonators to plasmonic nano-antennas. *Chemical Society Reviews* **2014**, *43* (4), 1263-1286, 10.1039/C3CS60357A. DOI: 10.1039/C3CS60357A.
(83) Chizhik, A.; Schleifenbaum, F.; Gutbrod, R.; Chizhik, A.; Khoptyar, D.; Meixner, A. J.; Enderlein, J. Tuning the fluorescence emission spectra of a single molecule with a variable optical subwavelength metal microcavity. *Physical review letters* **2009**, *102* (7), 073002.
(84) Wang, D.; Kelkar, H.; Martin-Cano, D.; Utikal, T.; Götzinger, S.; Sandoghdar, V. Coherent coupling of a single molecule to a scanning Fabry-Perot microcavity. *Physical Review X* **2017**, *7* (2), 021014.
(85) Dovzhenko, D. S.; Ryabchuk, S. V.; Rakovich, Y. P.; Nabiev, I. R. Light–matter interaction in the strong coupling regime: configurations, conditions, and applications. *Nanoscale* **2018**, *10* (8), 3589-3605, 10.1039/C7NR06917K. DOI: 10.1039/C7NR06917K.
(86) Chizhik, A. I.; Chizhik, A. M.; Khoptyar, D.; Bär, S.; Meixner, A. J.; Enderlein, J. r. Probing the radiative transition of single molecules with a tunable microresonator. *Nano letters* **2011**, *11* (4), 1700-1703.
(87) Piatkowski, L.; Schanbacher, C.; Wackenhut, F.; Jamrozik, A.; Meixner, A. J.; Waluk, J. Nature of large temporal fluctuations of hydrogen transfer rates in single molecules. *The Journal of Physical Chemistry Letters* **2018**, *9* (6), 1211-1215.
(88) Ashraf, I.; Konrad, A.; Lokstein, H.; Skandary, S.; Metzger, M.; Djouda, J. M.; Maurer, T.; Adam, P. M.; Meixner, A. J.; Brecht, M. Temperature dependence of metal-enhanced fluorescence of photosystem I from Thermosynechococcus elongatus. *Nanoscale* **2017**, *9* (12), 4196-4204.
(89) Hsiao, W. W.-W.; Hui, Y. Y.; Tsai, P.-C.; Chang, H.-C. Fluorescent nanodiamond: a versatile tool for long-term cell tracking, super-resolution imaging, and nanoscale temperature sensing. *Accounts of chemical research* **2016**, *49* (3), 400-407.
(90) Laube, C.; Oeckinghaus, T.; Lehnert, J.; Griebel, J.; Knolle, W.; Denisenko, A.; Kahnt, A.; Meijer, J.; Wrachtrup, J.; Abel, B. Controlling the fluorescence properties of nitrogen vacancy centers in nanodiamonds. *Nanoscale* **2019**, *11* (4), 1770-1783.
(91) Johnson, S.; Dolan, P.; Grange, T.; Trichet, A.; Hornecker, G.; Chen, Y.-C.; Weng, L.; Hughes, G.; Watt, A.; Auffèves, A. Tunable cavity coupling of the zero phonon line of a nitrogen-vacancy defect in diamond. *New Journal of Physics* **2015**, *17* (12), 122003.
(92) Berlin, Y.; Burin, A.; Friedrich, J.; Köhler, J. Low temperature spectroscopy of proteins. Part II: Experiments with single protein complexes. *Physics of life reviews* **2007**, *4* (1), 64-89.
(93) Schleifenbaum, F.; Blum, C.; Subramaniam, V.; Meixner, A. J. Single-molecule spectral dynamics at room temperature. *Molecular Physics* **2009**, *107* (18), 1923-1942.

(94) Lu, H. P.; Xie, X. S. Single-molecule spectral fluctuations at room temperature. *Nature* **1997**, *385* (6612), 143-146.
(95) Peterman, E. J. G.; Pullerits, T.; van Grondelle, R.; van Amerongen, H. Electron–phonon coupling and vibronic fine structure of light-harvesting complex II of green plants: temperature dependent absorption and high-resolution fluorescence spectroscopy. *The Journal of Physical Chemistry B* **1997**, *101* (22), 4448-4457.
(96) Pullerits, T.; Monshouwer, R.; van Mourik, F.; van Grondelle, R. Temperature dependence of electron-vibronic spectra of photosynthetic systems. Computer simulations and comparison with experiment. *Chemical physics* **1995**, *194* (2-3), 395-407.
(97) Rätsep, M.; Pajusalu, M.; Freiberg, A. Wavelength-dependent electron–phonon coupling in impurity glasses. *Chemical Physics Letters* **2009**, *479* (1-3), 140-143.
(98) Nosrati, S.; Wackenhut, F.; Kertzscher, C.; Brecht, M.; Meixner, A. J. Controlling three-color forster resonance energy transfer in an optical Fabry–Pérot microcavity at low mode order. *The Journal of Physical Chemistry C* **2023**, *127* (25), 12152-12159.
(99) Haustein, E.; Jahnz, M.; Schwille, P. Triple FRET: A tool for studying long‐range molecular interactions. *ChemPhysChem* **2003**, *4* (7), 745-748.
(100) Aneja, A.; Mathur, N.; Bhatnagar, P.; Mathur, P. Triple-FRET technique for energy transfer between conjugated polymer and TAMRA dye with possible applications in medical diagnostics. *Journal of biological physics* **2008**, *34* (5), 487-493.
(101) Milles, S.; Koehler, C.; Gambin, Y.; Deniz, A. A.; Lemke, E. A. Intramolecular three-colour single pair FRET of intrinsically disordered proteins with increased dynamic range. *Molecular Biosystems* **2012**, *8* (10), 2531-2534.
(102) Hohng, S.; Joo, C.; Ha, T. Single-molecule three-color FRET. *Biophysical journal* **2004**, *87* (2), 1328-1337.
(103) Lee, S.; Lee, J.; Hohng, S. Single-molecule three-color FRET with both negligible spectral overlap and long observation time. *PloS one* **2010**, *5* (8), e12270.
(104) Yoo, J.; Louis, J. M.; Gopich, I. V.; Chung, H. S. Three-color single-molecule FRET and fluorescence lifetime analysis of fast protein folding. *The Journal of Physical Chemistry B* **2018**, *122* (49), 11702-11720.
(105) Barth, A.; Voith von Voithenberg, L.; Lamb, D. C. Quantitative Single-Molecule Three-Color Förster Resonance Energy Transfer by Photon Distribution Analysis. *The Journal of Physical Chemistry B* **2019**, *123* (32), 6901-6916.
(106) Gauglitz, G.; Moore, D. S. *Handbook of spectroscopy*; Wiley-Vch Weinheim, Germany, 2014.
(107) Atkins, P. W.; De Paula, J.; Keeler, J. *Atkins' physical chemistry*; Oxford university press, 2023.
(108) Förster, T. Zwischenmolekulare energiewanderung und fluoreszenz. *Annalen der physik* **1948**, *437* (1-2), 55-75.
(109) Baldo, M.; ThompSOn, M. E.; Forrest, S. High-efficiency fluorescent organic light-emitting devices using a phosphorescent sensitizer. *Nature* **2000**, *403* (6771), 750-753.

(110) Blum, C.; Zijlstra, N.; Lagendijk, A.; Wubs, M.; Mosk, A. P.; Subramaniam, V.; Vos, W. L. Nanophotonic control of the Förster resonance energy transfer efficiency. *Physical review letters* **2012**, *109* (20), 203601.
(111) Rabouw, F. T.; Den Hartog, S. A.; Senden, T.; Meijerink, A. Photonic effects on the Förster resonance energy transfer efficiency. *Nature communications* **2014**, *5* (1), 1-6.
(112) Főrster, T. 10th Spiers Memorial Lecture. Transfer mechanisms of electronic excitation. *Discussions of the Faraday Society* **1959**, *27*, 7-17.
(113) Barkai, E.; Jung, Y.; Silbey, R. Theory of single-molecule spectroscopy: beyond the ensemble average. *Annu. Rev. Phys. Chem.* **2004**, *55*, 457-507.
(114) Steiner, M.; Schleifenbaum, F.; Stupperich, C.; Virgilio Failla, A.; Hartschuh, A.; Meixner, A. J. Microcavity‐Controlled Single‐Molecule Fluorescence. *ChemPhysChem* **2005**, *6* (10), 2190-2196.
(115) Demtröder, W. *Laser spectroscopy*; Springer, 1973.
(116) Predojević, A.; Mitchell, M. W. *Engineering the Atom-Photon Interaction*; Springer, 2015.
(117) Shore, B. W.; Knight, P. L. The Jaynes-Cummings Model. *Journal of Modern Optics* **1993**, *40* (7), 1195-1238. DOI: 10.1080/09500349314551321.
(118) De Dood, M.; Knoester, J.; Tip, A.; Polman, A. Förster transfer and the local optical density of states in erbium-doped silica. *Physical Review B* **2005**, *71* (11), 115102.
(119) Samutpraphoot, P.; Đorđević, T.; Ocola, P. L.; Bernien, H.; Senko, C.; Vuletić, V.; Lukin, M. D. Strong Coupling of Two Individually Controlled Atoms via a Nanophotonic Cavity. *Physical Review Letters* **2020**, *124* (6), 063602. DOI: 10.1103/PhysRevLett.124.063602.
(120) Skolnick, M.; Fisher, T.; Whittaker, D. Strong coupling phenomena in quantum microcavity structures. *Semiconductor Science and Technology* **1998**, *13* (7), 645.
(121) Hobson, P. A.; Barnes, W. L.; Lidzey, D.; Gehring, G.; Whittaker, D.; Skolnick, M.; Walker, S. Strong exciton–photon coupling in a low-Q all-metal mirror microcavity. *Applied Physics Letters* **2002**, *81* (19), 3519-3521.
(122) Purcell, E. M.; Torrey, H. C.; Pound, R. V. Resonance absorption by nuclear magnetic moments in a solid. *Physical review* **1946**, *69* (1-2), 37.
(123) Cang, H.; Liu, Y.; Wang, Y.; Yin, X.; Zhang, X. Giant Suppression of Photobleaching for Single Molecule Detection via the Purcell Effect. *Nano Letters* **2013**, *13* (12), 5949-5953. DOI: 10.1021/nl403047m.
(124) Gentile, M. J.; Núñez-Sánchez, S.; Barnes, W. L. Optical Field-Enhancement and Subwavelength Field-Confinement Using Excitonic Nanostructures. *Nano Letters* **2014**, *14* (5), 2339-2344. DOI: 10.1021/nl404712t.
(125) He, Z.; Xu, C.; He, W.; He, J.; Zhou, Y.; Li, F. Principle and applications of multimode strong coupling based on surface plasmons. *Nanomaterials* **2022**, *12* (8), 1242.
(126) Gagliardi, G.; Loock, H.-P. *Cavity-enhanced spectroscopy and sensing*; Springer, 2014.
(127) Vasa, P.; Lienau, C. Strong Light–Matter Interaction in Quantum Emitter/Metal Hybrid Nanostructures. *ACS Photonics* **2018**, *5* (1), 2-23. DOI: 10.1021/acsphotonics.7b00650.
(128) Kang, E. S. H.; Chen, S.; Sardar, S.; Tordera, D.; Armakavicius, N.; Darakchieva, V.; Shegai, T.; Jonsson, M. P. Strong Plasmon–Exciton Coupling with Directional

Absorption Features in Optically Thin Hybrid Nanohole Metasurfaces. *ACS Photonics* **2018**, *5* (10), 4046-4055. DOI: 10.1021/acsphotonics.8b00679.
(129) Skandary, S. Spectroscopic properties of photosystems revealed by single-molecule spectroscopy at low temperature. **2014**.
(130) Davies, G.; Hamer, M. F. Optical studies of the 1.945 eV vibronic band in diamond. *Proceedings of the Royal Society of London. A. Mathematical and Physical Sciences* **1976**, *348* (1653), 285-298.
(131) Fleming, J. W.; Weber, M. J.; Day, G. W.; Feldman, A.; Chai, B. H. T.; Kuzyk, M. G.; Holland, W. R.; Rapp, C. F.; Minden, M.; Moore, D. T. *Handbook of optical materials*; CRC press, 2018.
(132) Metzger, M.; Konrad, A.; Skandary, S.; Ashraf, I.; Meixner, A. J.; Brecht, M. Resolution enhancement for low-temperature scanning microscopy by cryo-immersion. *Optics express* **2016**, *24* (12), 13023-13032.
(133) Junginger, A.; Wackenhut, F.; Stuhl, A.; Blendinger, F.; Brecht, M.; Meixner, A. J. Tunable strong coupling of two adjacent optical λ/2 Fabry-Pérot microresonators. *Optics express* **2020**, *28* (1), 485-493.
(134) Meschede, D. *Optics, light and lasers: the practical approach to modern aspects of photonics and laser physics*; John Wiley & Sons, 2017.
(135) Manson, N. B.; Hedges, M.; Barson, M. S. J.; Ahlefeldt, R.; Doherty, M. W.; Abe, H.; Ohshima, T.; Sellars, M. J. NV−−N+ pair centre in 1b diamond. *New Journal of Physics* **2018**, *20* (11), 113037.
(136) Ishii, S.; Saiki, S.; Onoda, S.; Masuyama, Y.; Abe, H.; Ohshima, T. Ensemble Negatively-Charged Nitrogen-Vacancy Centers in Type-Ib Diamond Created by High Fluence Electron Beam Irradiation. In *Quantum Beam Science*, 2022; Vol. 6.
(137) Santori, C.; Barclay, P. E.; Fu, K. C.; Beausoleil, R. G.; Spillane, S.; Fisch, M. Nanophotonics for quantum optics using nitrogen-vacancy centers in diamond. *Nanotechnology* **2010**, *21* (27), 274008.
(138) Chu, Y.; Lukin, M. D. Quantum optics with nitrogen-vacancy centers in diamond. *Quantum Optics and Nanophotonics* **2015**, 229-270.
(139) Schirhagl, R.; Chang, K.; Loretz, M.; Degen, C. L. Nitrogen-vacancy centers in diamond: nanoscale sensors for physics and biology. *Annual review of physical chemistry* **2014**, *65* (1), 83-105.
(140) Gould, M.; Schmidgall, E. R.; Dadgostar, S.; Hatami, F.; Fu, K.-M. C. Efficient extraction of zero-phonon-line photons from single nitrogen-vacancy centers in an integrated gap-on-diamond platform. *Physical Review Applied* **2016**, *6* (1), 011001.
(141) Happacher, J.; Bocquel, J.; Dinani, H. T.; Tschudin, M. A.; Reiser, P.; Broadway, D. A.; Maze, J. R.; Maletinsky, P. Temperature-Dependent Photophysics of Single NV Centers in Diamond. *Physical Review Letters* **2023**, *131* (8), 086904. DOI: 10.1103/PhysRevLett.131.086904.

Appendix

List of Publications and Personal Contributions

This dissertation, submitted as part of the 'application for acceptance to the doctoral graduation process,' includes three published papers (publications 1–3). These papers, which were published prior to the submission of this work, are provided as appendices to this dissertation.

List of Publications:

1) Nosrati, Saeed, et al. "Controlling three-color forster resonance energy transfer in an optical Fabry–Pérot microcavity at low mode order." *The Journal of Physical Chemistry C* 127.25 (2023): 12152-12159.
2) Nosrati, Saeed, et al. "Combining Optical Strong Mode Coupling with Polaritonic Coupling in a λ/2 Fabry–Pérot Microresonator." The Journal of Physical Chemistry C 125.23 (2021): 13024-13032.
3) Kumar, Krishan, et al. "Periodic fluorescence variations of CdSe quantum dots coupled to aryleneethynylenes with aggregation-induced emission." *ACS nano* 15.1 (2021): 480-488.

	Accepted for publication yes/no	Number of all author	Position of the candidate in the list of authors	Scientific ideas of candidate (%)	Data generation by candidate (%)	Analysis and Interpretation by candidate (%)	Paper writing by candidate (%)
1	Yes	5	1	70	90	70	80
2	Yes	4	1	70	90	80	80
3	Yes	13	4	10	20	10	10

THE JOURNAL OF PHYSICAL CHEMISTRY C
A JOURNAL OF THE AMERICAN CHEMICAL SOCIETY

pubs.acs.org/JPCC

Article

Controlling Three-Color Förster Resonance Energy Transfer in an Optical Fabry–Pérot Microcavity at Low Mode Order

Saeed Nosrati, Frank Wackenhut,* Christoph Kertzscher, Marc Brecht, and Alfred J. Meixner*

Cite This: *J. Phys. Chem. C* 2023, 127, 12152–12159

Read Online

ACCESS | Metrics & More | Article Recommendations | Supporting Information

ABSTRACT: We study three-color Förster resonance energy transfer (triple FRET) between three spectrally distinct fluorescent dyes, a donor and two acceptors, which are embedded in a single polystyrene nanosphere. The presence of triple FRET energy transfer is confirmed by selective acceptor photobleaching. We show that the fluorescence lifetimes of the three dyes are selectively controlled using the Purcell effect by modulating the radiative rates and relative fluorescence intensities when the nanospheres are embedded in an optical Fabry–Pérot microcavity. The strongest fluorescence intensity enhancement for the second acceptor can be observed as a signature of the FRET process by tuning the microcavity mode to suppress the intermediate dye emission and transfer more energy from donor to the second acceptor. Additionally, we show that the triple FRET process can be modeled by coupled rate equations, which allow to estimate the energy transfer rates between donor and acceptors. This fundamental study has the potential to extend the classical FRET approach for investigating complex systems, e.g., optical energy switching, photovoltaic devices, light-harvesting systems, or in general interactions between more than two constituents.

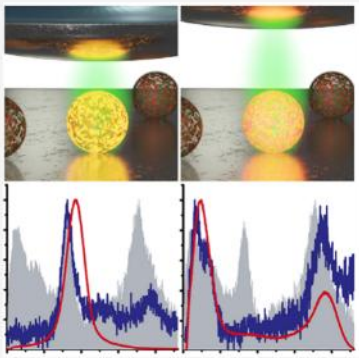

INTRODUCTION

Förster resonance energy transfer (FRET) plays an eminent role in light harvesting, the initial step in photosynthesis,[1−3] and plays a key role in photovoltaic devices,[4−6] organic lighting sources,[7−9] and molecular biosensing. Furthermore, it is a prominent method to measure molecular distances or to detect molecular interactions in the angstrom range (10−100 Å).[10−12] In FRET, an excited fluorophore (donor) transfers its energy nonradiatively to a neighboring fluorophore (acceptor) via induced dipole−dipole interaction.[13−16] The rate of energy transfer is strongly dependent on the spatial distance between donor and acceptor (r^{-6}), the overlap between the emission spectrum of the donor and the absorption spectrum of the acceptor, and the relative orientation of the transition dipoles.[17,18] FRET manifests itself in a decrease of the donor lifetime, quenching of donor fluorescence, and an increase of the acceptor fluorescence intensity.[4,16,19,20] Hence, FRET is often detected by acceptor photobleaching, in which the donor fluorescence lifetime is recorded before and after acceptor photobleaching.[21,22]

In the past decade, multicolor FRET approaches have become increasingly attractive to study complex molecular systems. Compared to the conventional FRET, triple FRET[23] occurs between an excited donor and two spectrally different acceptors. In addition, there can also be an energy transfer from the donor to the lowest-energy acceptor via the intermediate acceptor. Several recent studies have successfully demonstrated the development of single-molecule triple FRET techniques.[23−37] However, the extension of FRET to triple FRET is not as straightforward as it appears, and there are many challenges that limit the quantitative analysis of triple FRET data, e.g., severe photobleaching, small absorption/emission spectral overlap, and large distances between multicolor fluorescent dyes.

Optical microcavities allow to modify the optical mode density compared to free space. A simple example of such a system is a Fabry–Pérot resonator, which allows to modify the radiative properties of an emitter placed inside: In the so-called weak coupling regime, the Purcell effect[38−40] can occur, which describes a modification of the spontaneous emission rate which is enhanced if the emission frequency of the emitter is resonant with a cavity mode (and suppressed if not). This is quantified by the Purcell factor F_P, which is the ratio of the spontaneous emission rate of the emitter inside the cavity and in free space.

In the past, people attempted to manipulate the energy transfer by placing FRET pairs in a photonic cavity,[41−55] photonic bandgap material,[56] plasmonic nanoantennas,[57−59] and photonic crystals.[60] The results show that the energy transfer can be enhanced,[41,42,61−68] suppressed,[69,70] or stay the same.[71−74] Spontaneous emission modification at resonant modes of a cavity can be described by the aforementioned

Received: April 18, 2023
Revised: May 30, 2023
Published: June 14, 2023

https://doi.org/10.1021/acs.jpcc.3c02566
J. Phys. Chem. C 2023, 127, 12152−12159

Purcell effect, which was shown to have an impact on the energy transfer between closely spaced dipole emitters.[49]

Here, we present a novel approach for the study of the mechanism of a multiple FRET system that relies on controlling the energy transfer between the acceptors and the donors by spatially confined electromagnetic fields within a photonic environment in a tunable Fabry–Pérot microcavity. Our triple FRET system consists of three spectrally distinct fluorescent dyes, which are embedded in 100 nm diameter polymer nanospheres (which are commercially available under the trademark TetraSpeck microspheres). The optical measurements were performed on single nanospheres dispersed in a microcavity with an average intersphere distance >1 μm at cryogenic temperatures to increase the photostability of the fluorescent dyes.

EXPERIMENTAL SECTION

Preparation of Single TetraSpeck Nanosphere Samples. Four fluorescent dyes with excitation maxima at 350, 505, 575, and 655 nm are embedded in a TetraSpeck ultraclean polystyrene nanosphere with a nominal diameter of 100 nm and a density of 1.8×10^{11} particles/mL. Three of these dyes are excited by a laser at 488 nm with green (515 nm), orange (580 nm), and red (680 nm) fluorescence maxima and are termed donor, acceptor1, and acceptor2, respectively. The nanospheres were purchased from Thermo Fisher Scientific, Germany (Invitrogen TetraSpeck nanospheres T7229) and used without further purification. A 5 μL droplet of the TetraSpeck solution was placed on top of the flat mirror of the disassembled microcavity (or on top of a clean coverslip for measurements in free space) and dried for 20 min. This resulted in an average separation of several micrometers between individual nanospheres. The chemical structures and the concentration of the dyes used in TetraSpeck nanospheres are proprietary information of Invitrogen. Therefore, we have estimated the number of molecules in a single TetraSpeck sphere and obtained about 5600 fluorophores (details in the Supporting Information).

Microcavity Preparation. The microcavity consists of a fixed and a tunable silver mirror spatially separated by few wavelengths in the visible spectral region. The tunable flat mirror is created by evaporating a 50 nm thick silver layer on a clean glass cover slide, followed by a 10 nm gold and a dielectric SiO_2 layer of 100 nm to position the nanospheres. In this way, we avoid fluorescence quenching by the silver mirror[75,76] and make sure that the fluorophores are located in the first spatial intensity maximum of the cavity modes and experience a high field strength. The fixed mirror is a lens with a curvature radius of 18.6 mm, coated with an 80 nm silver layer, a 10 nm thick gold layer, and 20 nm SiO_2 as a protection layer.

Experimental Setup. A schematic drawing of the experimental setup consisting of a home-built confocal microscope and an optical cryostat (SVT-200, Janis) is shown in Figure S1. A graphic sketch of the microscope head and a tunable Fabry–Pérot microcavity installed in the sample compartment are illustrated in Figure 1a,b. The objective lens and the mirror separation of the microcavity can be controlled precisely by four piezoelectric actuators (ANPx311/RES stepper positioner, Attocube). In this geometry, the flat mirror can be approached towards the fixed mirror to reach the $\lambda/2$ region in the visible spectral range. A lens and a white light LED mounted outside of the

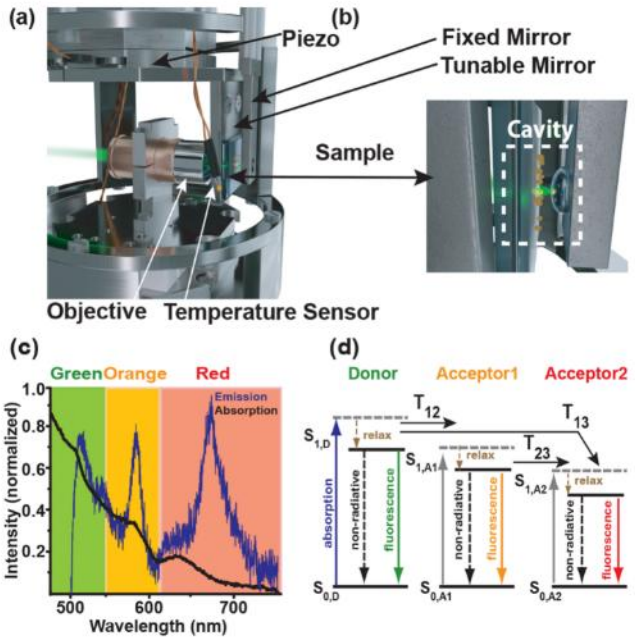

Figure 1. (a) Graphic sketch of the microscope head suitable for cryogenic temperatures with the objective lens and the translator stages. (b) Sketch of the tunable Fabry–Pérot microcavity with nanospheres to investigate the influence of cavity on the radiative properties of the dyes of a single TetraSpeck nanosphere. (c) Experimental emission and absorption spectrum of a single TetraSpeck nanosphere in free space, containing a green, orange, and red dye. (d) Schematic energy-level scheme of a triple FRET system containing donor, acceptor1, and acceptor2.

cryostat are used to acquire transmission spectra (see details in the Supporting Information). The transmitted light is collected via an air objective lens (NA = 0.85), and the detected signal is guided to a spectrometer with a thermoelectrically cooled CCD camera (Shamrock, Andor Technology, UK). These transmission spectra are used to determine the spectral position of the cavity resonances. A sensitive temperature sensor (DT-670-SD, Diode sensor, Lake Shore Cryotronics) is located next to the sample position (indicated in Figure 1a). To measure fluorescence spectra and lifetimes of the dyes embedded in fluorescent nanospheres, three pulsed lasers are used at λ = 488, 532, and 630 nm, with pulse lengths <100 ps at a repetition rate of 40 MHz. The excitation lasers are focused by the objective lens on the microcavity, and the same objective is used for fluorescence signal collection. The signal is detected with a sensitive avalanche photodiode (APD) followed by a time-correlated single photon counting system (SPCM-AQR-14, Photon Counting Module, PerkinElmer Optoelectronics).

RESULTS AND DISCUSSION

Experimental absorption and emission spectra of a single nanosphere in free space (no cavity) are shown in Figure 1c. It has to be noted that the direct excitation of acceptor1 and acceptor2 by the 488 nm laser is weak. The green, orange, and red areas in Figure 1c represent the transmission range of the filters (<550 nm short pass, 548–612 nm band-pass, and >630 nm long pass) installed in front of the APD to separately detect the emission of the three dyes and to measure the corresponding lifetimes individually.

https://doi.org/10.1021/acs.jpcc.3c02566
J. Phys. Chem. C 2023, 127, 12152–12159

Figure 1d shows an energy-level diagram of the triple FRET process in a TetraSpeck nanosphere consisting of the donor, acceptor1, and acceptor2. The donor molecules are excited by a pulsed laser at 488 nm from the electronic ground state ($S_{0,D}$) to an intermediate vibronic level of the first electronically excited state and relax quickly to the vibronic ground state of the first excited state ($S_{1,D}$), from where the donor molecules can relax to $S_{0,D}$ either by emitting fluorescence photons or via a nonradiative decay channel. FRET opens up an additional deexcitation channel for the donor, by which the excitation energy can be transferred to the acceptor1 (T_{12}) or the acceptor2 (T_{13}). Additionally, in a triple FRET process, acceptor1 can also play the role of a donor to transfer energy to acceptor2 (T_{23}). T_{12}, T_{13}, and T_{23} are illustrated as black solid arrows in Figure 1d. The excited acceptors can relax back to their electronic ground state either by nonradiative decay or by emitting fluorescence photons. The energy transfer depends on the spectral overlap of the donor emission spectrum and the absorption spectrum of acceptor1 and acceptor2, respectively. For TetraSpeck nanospheres, the spectral overlap[77] of donor−acceptor1 is much higher than donor−acceptor2, and direct excitation by the 488 nm laser is rather weak for acceptor1 and acceptor2.

One possibility to detect the FRET process is based on photobleaching the acceptor because the donor lifetime increases in the absence of the acceptor.[22] To confirm the triple FRET process, the fluorescence lifetime of the bare donor and the donor with acceptors was acquired by time-correlated single-photon counting (TCSPC) at room temperature and is shown in Figure 2a,b.

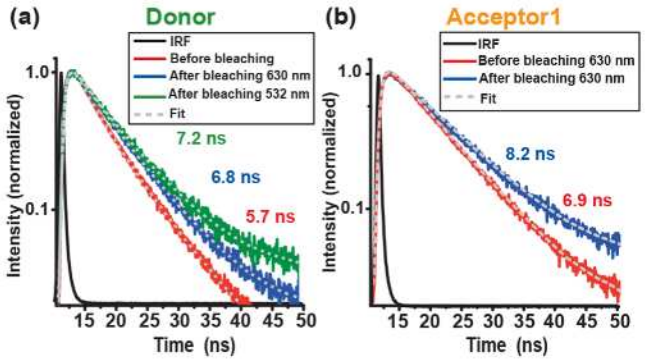

Figure 2. (a) Fluorescence lifetime decay curves of the donor before (red curve) and after photobleaching the acceptor2 (blue curve) and subsequently acceptor1 (green curve) for a single nanosphere at room temperature. (b) Fluorescence lifetime decay curves of acceptor1 before and after photobleaching of acceptor2 for a single nanosphere. Fits (gray dashed lines) are obtained by convolution of the instrument response function (black line) and a double-exponential decay curve. The shown lifetime values are the average lifetime values of the respective fit.

Fluorescence decay curves are shown in Figure 2a,b for two different scenarios, and the corresponding fit functions (gray dashed lines) are based on convolution of exponential decay functions with the instrument response function (IRF, black line). The donor fluorescence decay (red curve in Figure 2a) is acquired before photobleaching of the acceptors at room temperature and yields a fluorescence lifetime of 5.7 ± 0.15 ns for this particular fluorescence nanosphere. The blue line shows a fluorescence decay curve of the donor in the same nanosphere after photobleaching of acceptor2 with a 630 nm laser, and the fluorescence lifetime of the donor increases to 6.8 ± 0.12 ns. A further increase to 7.2 ± 0.14 ns of the donor fluorescence lifetime is observed after additional photobleaching of acceptor1 by irradiation with the 532 nm laser. It has to be noted that determining the donor fluorescence lifetime in the presence of only acceptor2 was not successful due to coincident photobleaching of acceptor1 and acceptor2 by the 532 nm excitation. In addition, the fluorescence decay curves of the acceptor1 (blue solid line) are shown in Figure 2b, where the fluorescence lifetime increases from 6.9 ± 0.15 to 8.2 ± 0.18 ns after photobleaching of acceptor2 by a 630 nm laser. We note that the lifetimes of the donor measured in different nanospheres can vary slightly as shown in Figure S2. These results show that triple FRET occurs between the three dyes inside single TetraSpeck nanospheres.

To investigate the influence of the optical microcavity on the radiative properties of the dyes, fluorescent nanospheres were embedded between the two mirrors of the tunable microcavity, as schematically presented in Figure 1b. Single nanospheres were deposited with an average separation of several micrometers on top of a 100 nm thick SiO_2 spacer layer on the tunable mirror.[75] The optical path length of the microcavity can be tuned by precisely approaching the tunable mirror toward the fixed mirror by piezoelectric actuators.

Exemplary fluorescence decay curves of the donor and acceptor1 of a single nanosphere at room temperature in free space (blue curve) and inside a resonant microcavity (red curve) are shown in Figures 3a and 3b. The cavity mode can be

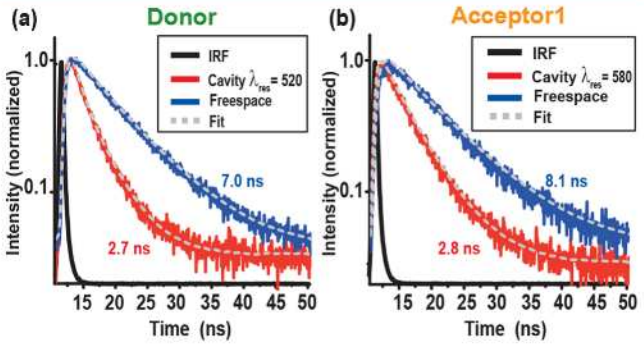

Figure 3. Fluorescence lifetime decay curves of the donor (a) and the acceptor1 (b) at room temperature in free space (blue curve) and in the microcavity (red curve) when it is on resonance with the donor or acceptor1, respectively.

tuned to be on resonance with maximum emission of the donor (a) and acceptor1 (b). Because of the Purcell effect, the fluorescence lifetimes of both dyes are remarkably reduced from $\tau_{\text{free space–donor}}$ = 7.0 ns and $\tau_{\text{free space–acceptor1}}$ = 8.1 ns to $\tau_{\text{cavity–donor}}$ = 2.7 ns and $\tau_{\text{cavity–acceptor1}}$ = 2.8 ns when the microcavity is on-resonance. This is close to the theoretical maximum lifetime reduction given by the Purcell factor of about 3 for such conditions.[38,39]

Furthermore, we investigated the effect of tuning the cavity resonance on the fluorescence lifetimes of the donor, acceptor1, and acceptor2 for a particular single nanosphere. To avoid photobleaching of the single nanosphere, the measurement was performed at 130 K. The temperature was controlled by a sensor mounted close to the microcavity. Figure 4 shows how the fluorescence lifetimes of the donor, acceptor1, and acceptor2 of a single nanosphere are influenced

https://doi.org/10.1021/acs.jpcc.3c02566
J. Phys. Chem. C 2023, 127, 12152−12159

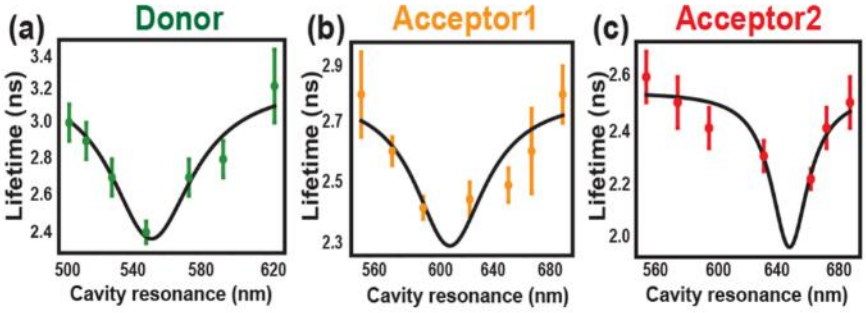

Figure 4. (a−c) Experimental cavity-modified fluorescence lifetimes of the donor, acceptor1, and acceptor2 for a single nanosphere as a function of cavity resonances. The black lines represent fits of a theoretical model based on the Purcell factor to calculate the fluorescence lifetime variation of the donor and two acceptors as a function of cavity resonances. The error bars originate from the fit of the fluorescence lifetime decay curve.

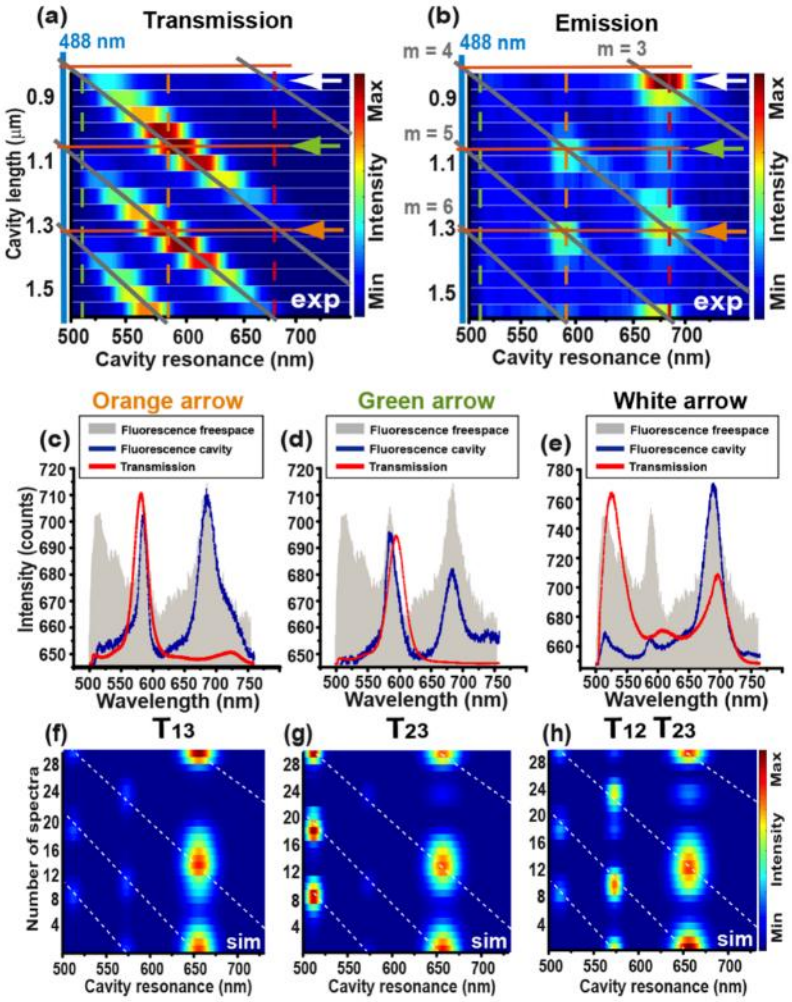

Figure 5. (a) Experimental white light transmission spectra of the microcavity at 130 K recorded successively as a function of decreasing the cavity mirror separation between sixth and third cavity mode. Respective experimental emission spectra of a single TetraSpeck nanosphere in the microcavity as a function of decreasing mirror separation are shown in (b). The emission maxima of the donor and the two acceptors in free space are marked by dashed green, orange, and red lines, respectively. The energy transfer for different cavity settings is marked by white, green, and orange arrows in (a) and (b). The excitation laser at 488 nm (blue solid line) and cavity mode orders m = 3, 4, 5, and 6 (gray solid lines) as well as intersection of marked cavity settings in resonance with excitation laser (red solid line) are shown in (a) and (b). The gray solid lines show the same modes for transmission (a) and emission (b). Three individual transmission (red curve) and emission (blue curve) spectra at the positions marked with arrows are depicted in (c) to (e), showing how the intensity ratio between donor and acceptor2 changes for the three different cavity settings. Simulated emission spectra of a single TetraSpeck nanosphere for excitation of the donor and the two acceptors, where energy is transferred from donor to acceptor2 (T_{13}) in (f), from acceptor1 to acceptor2 (T_{23}) in (g), and from donor to acceptor1 as well as from acceptor1 to acceptor2 (T_{12}, T_{23}) in (h). Calculated white light transmission maxima are indicated by white dashed lines in (f) to (h).

https://doi.org/10.1021/acs.jpcc.3c02566
J. Phys. Chem. C 2023, 127, 12152−12159

by the Purcell effect when the microcavity resonance is tuned from 500 to 700 nm. The measured lifetime decays are acquired for seven spectral positions as the cavity resonance is shifted to the red by increasing the mirror spacing. A theoretical model (details in the Supporting Information) based on the Purcell factor is fitted to the experimental data, and the results are shown as black lines in Figure 4. The fluorescence lifetime of each dye decreases due to the Purcell effect, when the cavity resonance is spectrally close to its fluorescence maximum. The acquired data for different nanospheres in different cavity resonances are shown in Figures S3−S5.

Next, we investigate the fluorescence emission spectra of the triple FRET system to study the interplay of energy transfer and the cavity-induced Purcell effect. Figure 5 represents two-dimensional plots of successive experimental white light transmission spectra of the microcavity and emission spectra of one and the same single TetraSpeck nanosphere as a function of decreasing cavity mirror separation from sixth to third cavity mode. The intensity reduction of the transmission spectra toward longer wavelengths in Figure 5a is caused by the spectral emission profile of LED used to acquire spectra (see the Supporting Information). The free space emission maxima of the individual dyes are indicated by the green, orange, and red dashed lines. The cavity settings in which the laser excitation at 488 nm (blue vertical line on the left of the spectral maps) intersect with cavity resonances (gray lines) are shown by horizontal red lines in Figures 5a,b. The signatures of the FRET process appear in the emission spectra marked by the orange, red, and white arrows in Figure 5b. Figures 5c−e show the individual spectra marked by the arrows.

For the spectrum marked by the orange arrow, the 6th mode is resonant with the excitation laser at 488 nm, the acceptor1 emission is resonant with the 5th cavity mode, acceptor2 is resonant with the 4th mode, and the donor emission is suppressed. When the mirror spacing is reduced in the spectrum marked by the red arrow, the excitation laser is again resonant with the cavity in the 5th mode; for this cavity setting acceptor1 emission is resonant with the 4th mode, and acceptor2 emission lies about halfway between the 4th and the 3rd mode and is reduced by about 50% with respect to the previous spectrum. This shows that although the donor fluorescence is suppressed, energy can be transferred to acceptor1. Finally, for the emission spectrum marked by the white arrow, the 4th order mode is close to resonance with the excitation laser, acceptor2 emission is resonant with the 3rd order mode and is largely enhanced while acceptor1 is spectrally located halfway between the 4th and the 3rd mode and largely suppressed, and donor emission is near resonance with the 4th order and weak. Hence, the white marked spectrum clearly shows that energy is transferred to acceptor2 although acceptor1 is suppressed. In all three cases the excitation of the donor should be the same, and the intensity ratios between the donor, acceptor1, and acceptor2 emission depend critically on the respective cavity mode setting. Obviously, the interplay between the Purcell effect and FRET can lead to complex cavity-dependent behavior of the fluorophores.

To complement these measurements, we have performed theoretical simulations of the fluorescence spectra to fit the experimental data. The model is based on six coupled rate equations for the donor, acceptor1, and acceptor2 populations (eqs 1−6), which allows us to calculate the ground and excited state populations of the donor and the two acceptors as a function of cavity resonance. The six coupled differential rate equations include all the processes indicated in Figure 1d and can be written as follows:

$$\frac{dS_{0,D}}{dt} = -P_1 S_{0,D} + nr_1 S_{1,D} + sp_1 S_{1,D} + T_{12} S_{1,D} + T_{13} S_{1,D} \quad (1)$$

$$\frac{dS_{1,D}}{dt} = P_1 S_{0,D} - nr_1 S_{1,D} - sp_1 S_{1,D} - T_{12} S_{1,D} - T_{13} S_{1,D} \quad (2)$$

$$\frac{dS_{0,A1}}{dt} = -P_2 S_{0,A1} + nr_2 S_{1,A1} + sp_2 S_{1,A1} - T_{12} S_{1,D} + T_{23} S_{1,A1} \quad (3)$$

$$\frac{dS_{1,A1}}{dt} = P_2 S_{0,A1} - nr_2 S_{1,A1} - sp_2 S_{1,A1} + T_{12} S_{1,D} - T_{23} S_{1,A1} \quad (4)$$

$$\frac{dS_{0,A2}}{dt} = -P_3 S_{0,A2} + nr_3 S_{1,A2} + sp_3 S_{1,A2} - T_{23} S_{1,A1} - T_{13} S_{1,D} \quad (5)$$

$$\frac{dS_{1,A2}}{dt} = P_3 S_{0,A2} - nr_3 S_{1,A2} - sp_3 S_{1,A2} + T_{23} S_{1,A1} + T_{13} S_{1,D} \quad (6)$$

Here, eqs 1 and 2 describe the temporal evolution of the donor populations in the ground and excited state; $S_{0,D}$ and $S_{1,D}$ are the respective probabilities. Equations 3−6 are related to acceptor1 and acceptor2. The excitation of each fluorophore occurs via the pumping rates P_{1-3}. Nonradiative rates and spontaneous emission rates are described by nr_{1-3} and sp_{1-3}, respectively. The energy transfer pathways in the equations can occur from donor to acceptor1 (T_{12}), to acceptor2 (T_{13}), and from acceptor1 to acceptor2 (T_{23}) with the respective rate constants in parentheses. The nonradiative rate constant is kept constant. Hence, to fit this model to the experimental data, only parameters describing the pumping rate and energy transfer rate are varied. To calculate the equations, the energy transfer rate is considered 1 in free space, and all others are relative to it. The influence of the microcavity is included by the parameters sp_{1-3} as a reduction or an increase of the spontaneous emission rate due to the Purcell effect. Solving these equations numerically gives the ground and excited state populations of the involved dyes, which are subsequently used to calculate fluorescence emission spectra of the nanospheres.

Results for these calculations are shown in Figures 5f−h. The white dashed lines represent the resonance wavelengths of the microcavity, which are fitted to the experimental data in Figure 5a. Energy transfer and excitation rates are varied in this model to reproduce the experimental data in Figure 5b. All parameters used in the calculations as well as additional simulations without energy transfer are presented in the Supporting Information. In Figure 5f−h the donor experiences the highest relative excitation rate ($P_1 = 1$). Furthermore, to account for the small spectral overlap between the excitation laser and the absorption spectrum of acceptor1 and acceptor2, the excitation rate of acceptor1 and acceptor2 is set to 10% of the donor excitation rate. Figure 5f shows the case when there is only energy transfer between the donor and acceptor2, and

https://doi.org/10.1021/acs.jpcc.3c02566
J. Phys. Chem. C 2023, 127, 12152−12159

the spectral feature marked by the green arrow (emission of acceptor2) in Figure 5b is missing. However, as soon as energy transfer from acceptor1 to acceptor2 (Figure 5g) is included, this emission can be weakly observed. This feature is further enhanced in Figure 5h, where the energy transfer occurs from donor to acceptor1 and from acceptor1 to acceptor2. This theoretical result gives the best agreement with the experimental data in Figure 5b, also reproducing the intensity ratios for the different dyes. In these simulations, we only consider the influence of microcavity on the fluorescence emission of the donor, aceptor1, and acceptor2 and did not include a possible influence on the excitation rates (p_{1-3}) or the energy transfer rate constants due to the microcavity tuning. Nevertheless, we achieve good agreement between the experiment and the simulation. This allows us to directly compare the fluorescence emission ratios of acceptor1 and acceptor2 for the three conditions: (1) when both are in resonance with a cavity mode, (2) only acceptor1 is in resonance with a cavity mode while acceptor2 is suppressed, and (3) finally acceptor1 is suppressed and only acceptor2 is in resonance. To keep the transfer rate constants constant, seems intuitively reasonable in terms of Förster's model for energy transfer because the coupling between donor and acceptor occurs in the optical near field and scales as the inverse of the sixth power of the donor−acceptor distance, whereas the optical mode density is determined by the boundary conditions dictated by the resonator, for which the mirror spacing is on the order of a micrometer. Therefore, it seems to be justified to expect no significant influence from a change of the microcavity length on the optical near fields of the excited fluorophores and hence on the energy transfer rate constant.

In Figure 5b we only observe the intense aceptor1 or acceptor2 emission at those cavity lengths where the excitation laser wavelength (488 nm) is in resonance with the cavity, while for this condition the donor emission is always off-resonance due to the Stocks shift. Hence, the radiative relaxation of the donor molecules is suppressed, and FRET occurs efficiently to the acceptor molecules. In other words, although the excitation rates of the donor (P_1) and the acceptors ($P_{2,3}$) depend on the optical mode density and influence on the absolute fluorescence intensities of the donor, acceptor1, and acceptor2, the excitation rates are equal for the spectra marked by the orange, green, and white arrows.

CONCLUSIONS

In summary, we have presented a study and detailed analysis of the triple FRET process using three different fluorescent dyes embedded into a single nanosphere in a tunable microcavity at cryogenic temperature of 130 K. We have demonstrated the detection of the triple FRET process between the dyes in a single TetraSpeck nanosphere using acceptor photobleaching. We have shown that the Purcell effect from a tunable microcavity leads to strong reduction of the lifetime of fluorophores compared to free space, especially when the microcavity mode is close to resonance with emission of dyes. Furthermore, we have demonstrated that the energy transfer rate can be controlled by the position of the microcavity resonance; for example, we observed that energy is efficiently transferred from donor to the acceptor molecules when the donor emission is suppressed by the resonator. Both acceptors can then emit if they are in resonance cavity (orange spectrum in Figure 5b), or their emission can selectively be suppressed by the cavity. For the situation when acceptor1 is off-resonance, energy transfer from donor or acceptor 1 to acceptor2 occurs, and acceptor emission is enhanced (white spectrum in Figure 5b). In addition, we have shown that the triple FRET system can be modeled by six coupled rate equations, considering two energy transfer channels from donor to acceptor1 and from acceptor1 to acceptor2 as well as the influence of the Purcell effect on the radiative rates. As a consequence, the single TetraSpeck nanospheres can serve as an excellent model system to study the influence of the optical mode density on the multi-FRET process. Multi-FRET techniques could have broad applications in detecting DNA sequences[32] and development of DNA biosensors[78] or for studying the dynamics of complex biomolecular systems with more than two interaction partners[25,33,79] and harvesting systems[2,3] and for revealing new insight into the flexibility of molecules' structures.[30,33]

ASSOCIATED CONTENT

Supporting Information

The Supporting Information is available free of charge at https://pubs.acs.org/doi/10.1021/acs.jpcc.3c02566.

Description of the optical setup for low-temperature fluorescence lifetime and spectroscopy measurements; experimental lifetime of green, orange, and red dye as a function of cavity resonance and corresponding theoretical calculation of the Purcell effect; details of the theoretical triple FRET model and parameters used to model three different dyes embedded in a single nanosphere in the tunable cavity; estimation the number of molecules in a single TetraSpeck sphere; spectral emission profile of the LED (PDF)

AUTHOR INFORMATION

Corresponding Authors

Alfred J. Meixner − *Institute of Physical and Theoretical Chemistry, Eberhard Karls University Tübingen, 72076 Tübingen, Germany;* orcid.org/0000-0002-0187-2906; Email: alfred.meixner@uni-tuebingen.de

Frank Wackenhut − *Institute of Physical and Theoretical Chemistry, Eberhard Karls University Tübingen, 72076 Tübingen, Germany; Process Analysis and Technology PA & T, Reutlingen University, 72762 Reutlingen, Germany;* orcid.org/0000-0001-6554-6600; Email: frank.wackenhut@reutlingen-university.de

Authors

Saeed Nosrati − *Institute of Physical and Theoretical Chemistry, Eberhard Karls University Tübingen, 72076 Tübingen, Germany*

Christoph Kertzscher − *Institute of Physical and Theoretical Chemistry, Eberhard Karls University Tübingen, 72076 Tübingen, Germany*

Marc Brecht − *Institute of Physical and Theoretical Chemistry, Eberhard Karls University Tübingen, 72076 Tübingen, Germany; Process Analysis and Technology PA & T, Reutlingen University, 72762 Reutlingen, Germany*

Complete contact information is available at: https://pubs.acs.org/10.1021/acs.jpcc.3c02566

Notes

The authors declare no competing financial interest.

■ ACKNOWLEDGMENTS

The authors gratefully acknowledge funding by the German Research Foundation (DFG, ME 1600/13-3).

■ REFERENCES

(1) Olejko, L.; Bald, I. FRET Efficiency and Antenna Effect in Multi-Color DNA Origami-Based Light Harvesting Systems. *RSC Adv.* **2017**, *7* (39), 23924−23934.
(2) Melnychuk, N.; Egloff, S.; Runser, A.; Reisch, A.; Klymchenko, A. S. Light-Harvesting Nanoparticle Probes for FRET-Based Detection of Oligonucleotides with Single-Molecule Sensitivity. *Angew. Chem.* **2020**, *132* (17), 6878−6885.
(3) Altıntas, Y.; Kiremitler, N. B.; Genç, S.; Onses, M. S.; Mutlugün, E. FRET Enabled Light Harvesting within Quantum Dot Loaded Nanofibers. *J. Phys. D: Appl. Phys.* **2018**, *51* (6), 065111.
(4) Cortes, C. L.; Jacob, Z. Fundamental Figures of Merit for Engineering Förster Resonance Energy Transfer. *Opt. Express* **2018**, *26* (15), 19371−19387.
(5) Hardin, B. E.; Snaith, H. J.; McGehee, M. D. The Renaissance of Dye-Sensitized Solar Cells. *Nat. Photonics* **2012**, *6* (3), 162−169.
(6) Wallrabe, H.; Periasamy, A. Imaging Protein Molecules Using FRET and FLIM Microscopy. *Curr. Opin. Biotechnol.* **2005**, *16* (1), 19−27.
(7) Baldo, M.; Thompson, M. E.; Forrest, S. High-Efficiency Fluorescent Organic Light-Emitting Devices Using a Phosphorescent Sensitizer. *Nature* **2000**, *403* (6771), 750−753.
(8) Mei, J.; Leung, N. L.; Kwok, R. T.; Lam, J. W.; Tang, B. Z. Aggregation-Induced Emission: Together We Shine, United We Soar! *Chem. Rev.* **2015**, *115* (21), 11718−11940.
(9) D'Andrade, B. W.; Forrest, S. R. White Organic Light-Emitting Devices for Solid-State Lighting. *Adv. Mater.* **2004**, *16* (18), 1585−1595.
(10) Lerner, E.; Cordes, T.; Ingargiola, A.; Alhadid, Y.; Chung, S.; Michalet, X.; Weiss, S. Toward Dynamic Structural Biology: Two Decades of Single-Molecule Förster Resonance Energy Transfer. *Science* **2018**, *359* (6373), No. eaan1133.
(11) Medintz, I. L.; Clapp, A. R.; Mattoussi, H.; Goldman, E. R.; Fisher, B.; Mauro, J. M. Self-Assembled Nanoscale Biosensors Based on Quantum Dot FRET Donors. *Nat. Mater.* **2003**, *2* (9), 630−638.
(12) Roy, R.; Hohng, S.; Ha, T. A Practical Guide to Single-Molecule FRET. *Nat. Methods* **2008**, *5* (6), 507−516.
(13) Förster, T. Zwischenmolekulare Energiewanderung und Fluoreszenz. *Ann. Phys.* **1948**, *437* (1−2), 55−75.
(14) Förster, T. 10th Spiers Memorial Lecture. Transfer Mechanisms of Electronic Excitation. *Discuss. Faraday Soc.* **1959**, *27*, 7−17.
(15) Clegg, R. M. Fluorescence Resonance Energy Transfer. *Curr. Opin. Biotechnol.* **1995**, *6* (1), 103−110.
(16) Herman, B.; Gordon, G.; Mahajan, N.; Centonze, V. Measurement of Fluorescence Resonance Energy Transfer in the Optical Microscope. In *Methods in Cellular Imaging*; Springer: 2001; pp 257−272.
(17) Barnes, W. L.; Andrew, P. Quantum Optics: Energy Transfer under Control. *Nature* **1999**, *400* (6744), 505−506.
(18) Sapsford, K. E.; Berti, L.; Medintz, I. L. Materials for Fluorescence Resonance Energy Transfer Analysis: Beyond Traditional Donor−Acceptor Combinations. *Angew. Chem., Int. Ed.* **2006**, *45* (28), 4562−4589.
(19) Kenworthy, A. K. Imaging Protein-protein Interactions Using Fluorescence Resonance Energy Transfer Microscopy. *Methods* **2001**, *24* (3), 289−296.
(20) Sekar, R. B.; Periasamy, A. Fluorescence Resonance Energy Transfer (FRET) Microscopy Imaging of Live Cell Protein Localizations. *J. Cell Biol.* **2003**, *160* (5), 629−633.
(21) Bastiaens, P.; Jovin, T. M. Microspectroscopic Imaging Tracks the Intracellular Processing of a Signal Transduction Protein: Fluorescent-Labeled Protein Kinase C Beta I. *Proc. Natl. Acad. Sci. U. S. A.* **1996**, *93* (16), 8407−8412.
(22) Van Munster, E.; Kremers, G.; Adjobo-Hermans, M.; Gadella Jr, T. Fluorescence Resonance Energy Transfer (FRET) Measurement by Gradual Acceptor Photobleaching. *J. Microsc.* **2005**, *218* (3), 253−262.
(23) Yoo, J.; Kim, J.-Y.; Louis, J. M.; Gopich, I. V.; Chung, H. S. Fast Three-Color Single-Molecule FRET Using Statistical Inference. *Nat. Commun.* **2020**, *11* (1), 3336.
(24) Barth, A.; Voith von Voithenberg, L.; Lamb, D. C. Quantitative Single-Molecule Three-Color Förster Resonance Energy Transfer by Photon Distribution Analysis. *J. Phys. Chem. B* **2019**, *123* (32), 6901−6916.
(25) Haustein, E.; Jahnz, M.; Schwille, P. Triple FRET: A Tool for Studying Long-Range Molecular Interactions. *ChemPhysChem* **2003**, *4* (7), 745−748.
(26) Milles, S.; Koehler, C.; Gambin, Y.; Deniz, A. A.; Lemke, E. A. Intramolecular Three-Colour Single Pair FRET of Intrinsically Disordered Proteins with Increased Dynamic Range. *Mol. Biosyst.* **2012**, *8* (10), 2531−2534.
(27) Hohng, S.; Joo, C.; Ha, T. Single-Molecule Three-Color FRET. *Biophys. J.* **2004**, *87* (2), 1328−1337.
(28) Lee, S.; Lee, J.; Hohng, S. Single-Molecule Three-Color FRET with Both Negligible Spectral Overlap and Long Observation Time. *PloS one* **2010**, *5* (8), No. e12270.
(29) Chung, H. S.; Meng, F.; Kim, J.-Y.; McHale, K.; Gopich, I. V.; Louis, J. M. Oligomerization of the Tetramerization Domain of p53 Probed by Two-and Three-Color Single-Molecule FRET. *Proc. Natl. Acad. Sci. U. S. A.* **2017**, *114* (33), E6812−E6821.
(30) Yoo, J.; Louis, J. M.; Gopich, I. V.; Chung, H. S. Three-Color Single-Molecule FRET and Fluorescence Lifetime Analysis of Fast Protein Folding. *J. Phys. Chem. B* **2018**, *122* (49), 11702−11720.
(31) Lee, J.; Lee, S.; Ragunathan, K.; Joo, C.; Ha, T.; Hohng, S. Single-Molecule Four-Color FRET. *Angew. Chem., Int. Ed.* **2010**, *49* (51), 9922−9925.
(32) Aneja, A.; Mathur, N.; Bhatnagar, P.; Mathur, P. Triple-FRET Technique for Energy Transfer between Conjugated Polymer and TAMRA Dye with Possible Applications in Medical Diagnostics. *J. Biol. Phys.* **2008**, *34* (5), 487−493.
(33) Liu, J.; Lu, Y. FRET Study of a Trifluorophore-Labeled DNAzyme. *J. Am. Chem. Soc.* **2002**, *124* (51), 15208−15216.
(34) Watrob, H. M.; Pan, C.-P.; Barkley, M. D. Two-Step FRET as a Structural Tool. *J. Am. Chem. Soc.* **2003**, *125* (24), 7336−7343.
(35) Lerner, E.; Barth, A.; Hendrix, J.; Ambrose, B.; Birkedal, V.; Blanchard, S. C.; Börner, R.; Chung, H. S.; Cordes, T.; Craggs, T. D.; et al. FRET-Based Dynamic Structural Biology: Challenges, Perspectives and an Appeal for Open-Science Practices. *Elife* **2021**, *10*, No. e60416.
(36) Voith von Voithenberg, L.; Barth, A.; Trauschke, V.; Demarco, B.; Tyagi, S.; Koehler, C.; Lemke, E. A.; Lamb, D. C. Comparative Analysis of the Coordinated Motion of Hsp70s from Different Organelles Observed by Single-Molecule Three-Color FRET. *Proc. Natl. Acad. Sci. U. S. A.* **2021**, *118* (33), No. e2025578118.
(37) Glöckner, N.; zur Oven-Krockhaus, S.; Rohr, L.; Wackenhut, F.; Burmeister, M.; Wanke, F.; Holzwart, E.; Meixner, A. J.; Wolf, S.; Harter, K. Three-Fluorophore FRET Enables the Analysis of Ternary Protein Association in Living Plant Cells. *Plants* **2022**, *11* (19), 2630.
(38) Purcell, E. M.; Torrey, H. C.; Pound, R. V. Resonance Absorption by Nuclear Magnetic Moments in a Solid. *Phys. Rev.* **1946**, *69* (1−2), 37.
(39) Fox, A. M.; Fox, M. *Quantum Optics: An Introduction*; Oxford University Press: 2006.
(40) Bär, S.; Chizhik, A.; Gutbrod, R.; Schleifenbaum, F.; Chizhik, A.; Meixner, A. J. Microcavities: Tailoring the Optical Properties of Single Quantum Emitters. *Anal. Bioanal. Chem.* **2010**, *396* (1), 3−14.
(41) Andrew, P.; Barnes, W. L. Förster Energy Transfer in an Optical Microcavity. *Science* **2000**, *290* (5492), 785−788.
(42) Hopmeier, M.; Guss, W.; Deussen, M.; Göbel, E.; Mahrt, R. Enhanced Dipole-Dipole Interaction in a Polymer Microcavity. *Phys. Rev. Lett.* **1999**, *82* (20), 4118.

(43) Agarwal, G. S.; Gupta, S. D. Microcavity-Induced Modification of the Dipole-Dipole Interaction. *Phys. Rev. A* **1998**, *57* (1), 667.
(44) Kobayashi, T.; Zheng, Q.; Sekiguchi, T. Resonant Dipole-Dipole Interaction in a Cavity. *Phys. Rev. A* **1995**, *52* (4), 2835.
(45) Jana, S.; Xu, X.; Klymchenko, A.; Reisch, A.; Pons, T. Microcavity-Enhanced Fluorescence Energy Transfer from Quantum Dot Excited Whispering Gallery Modes to Acceptor Dye Nanoparticles. *ACS Nano* **2021**, *15* (1), 1445−1453.
(46) Konrad, A.; Metzger, M.; Kern, A. M.; Brecht, M.; Meixner, A. J. Controlling the Dynamics of Förster Resonance Energy Transfer Inside a Tunable Sub-Wavelength Fabry−Pérot-Resonator. *Nanoscale* **2015**, *7* (22), 10204−10209.
(47) Konrad, A.; Metzger, M.; Kern, A. M.; Brecht, M.; Meixner, A. J. Revealing the Radiative and Non-radiative Relaxation Rates of the Fluorescent Dye Atto488 in a $\lambda/2$ Fabry−Pérot-Resonator by Spectral and Time Resolved Measurements. *Nanoscale* **2016**, *8* (30), 14541−14547.
(48) Schleifenbaum, F.; Elgass, K.; Steiner, M.; Enderlein, J.; Peter, S.; Meixner, A. Optical Microresonator Modifies the Efficiency of the Fluorescence Resonance Energy Transfer in the Autofluorescent Protein DsRed. In *Single Molecule Spectroscopy and Imaging II*; International Society for Optics and Photonics: 2009; Vol. *7185*, p 718504.
(49) Wang, J.-F.; Zhou, H.-L.; Xiong, X.; Li, Q.; Cheng, Z.-D.; Liu, Z.-H.; Yan, F.-F.; Lin, S.-R.; Xu, J.-S.; Wang, G.-Z.; et al. Cavity-Enhanced Energy Transfer between Nano-Emitters and Monolayer Graphene. *Carbon* **2020**, *161*, 794−799.
(50) Zhou, Y.; Yuan, Z.; Gong, X.; Birowosuto, M. D.; Dang, C.; Chen, Y.-C. Dynamic Photonic Barcodes for Molecular Detection based on Cavity-Enhanced Energy Transfer. *Adv. photonics* **2020**, *2* (6), 1−9.
(51) Coles, D. M.; Somaschi, N.; Michetti, P.; Clark, C.; Lagoudakis, P. G.; Savvidis, P. G.; Lidzey, D. G. Polariton-Mediated Energy Transfer between Organic Dyes in a Strongly Coupled Optical Microcavity. *Nat. Mater.* **2014**, *13* (7), 712−719.
(52) Zhong, X.; Chervy, T.; Wang, S.; George, J.; Thomas, A.; Hutchison, J. A.; Devaux, E.; Genet, C.; Ebbesen, T. W. Non-Radiative Energy Transfer Mediated by Hybrid Light-Matter States. *Angew. Chem., Int. Ed.* **2016**, *55* (21), 6202−6206.
(53) Zhong, X.; Chervy, T.; Zhang, L.; Thomas, A.; George, J.; Genet, C.; Hutchison, J. A.; Ebbesen, T. W. Energy Transfer between Spatially Separated Entangled Molecules. *Angew. Chem., Int. Ed.* **2017**, *56* (31), 9034−9038.
(54) Georgiou, K.; Michetti, P.; Gai, L.; Cavazzini, M.; Shen, Z.; Lidzey, D. G. Control over Energy Transfer between Fluorescent BODIPY Dyes in a Strongly Coupled Microcavity. *ACS Photonics* **2018**, *5* (1), 258−266.
(55) Rustomji, K.; Dubois, M.; Kuhlmey, B.; de Sterke, C. M.; Enoch, S.; Abdeddaim, R.; Wenger, J. Direct Imaging of the Energy-Transfer Enhancement between Two Dipoles in a Photonic Cavity. *Phys. Rev. X.* **2019**, *9* (1), 011041.
(56) John, S.; Quang, T. Photon-Hopping Conduction and Collectively Induced Transparency in a Photonic Band Gap. *Phys. Rev. A* **1995**, *52* (5), 4083−4088.
(57) de Torres, J.; Mivelle, M.; Moparthi, S. B.; Rigneault, H.; Van Hulst, N. F.; García-Parajó, M. F.; Margeat, E.; Wenger, J. Plasmonic Nanoantennas Enable Forbidden Förster Dipole−Dipole Energy Transfer and Enhance the FRET Efficiency. *Nano Lett.* **2016**, *16* (10), 6222−6230.
(58) Sanz-Paz, M.; Wenger, J.; van Hulst, N. F.; Mivelle, M.; Garcia-Parajo, M. F. Nanoscale Control of Single Molecule Förster Resonance Energy Transfer by a Scanning Photonic Nanoantenna. *Nanophotonics* **2020**, *9* (12), 4021−4031.
(59) De Roque, P.; van Hulst, N.; Sapienza, R. Nanophotonic Boost of Intermolecular Energy Transfer. *New J. Phys.* **2015**, *17* (11), 113052.
(60) Galisteo-López, J. F.; Ibisate, M.; Muñoz, A.; López, C. 3D Photonic Crystals from Highly Monodisperse FRET-based Red Luminescent PMMA Spheres. *J. Mater. Chem. C* **2015**, *3* (16), 3999−4006.
(61) Finlayson, C. E.; Ginger, D. S.; Greenham, N. C. Enhanced Förster Energy Transfer in Organic/Inorganic Bilayer Optical Microcavities. *Chem. Phys. Lett.* **2001**, *338* (2−3), 83−87.
(62) Fujiwara, H.; Sasaki, K.; Masuhara, H. Enhancement of Förster Energy Transfer within a Microspherical Cavity. *ChemPhysChem* **2005**, *6* (11), 2410−2416.
(63) Lakowicz, J. R.; Shen, Y.; D'Auria, S.; Malicka, J.; Fang, J.; Gryczynski, Z.; Gryczynski, I. Radiative Decay Engineering: 2. Effects of Silver Island Films on Fluorescence Intensity, Lifetimes, and Resonance Energy Transfer. *Anal. Biochem.* **2002**, *301* (2), 261−277.
(64) Komarala, V. K.; Bradley, A. L.; Rakovich, Y. P.; Byrne, S. J.; Gun'ko, Y. K.; Rogach, A. L. Surface Plasmon Enhanced Förster Resonance Energy Transfer between the CdTe Quantum Dots. *Appl. Phys. Lett.* **2008**, *93* (12), 123102.
(65) Zhang, J.; Fu, Y.; Lakowicz, J. R. Enhanced Förster Resonance Energy Transfer (FRET) on a Single Metal Particle. *J. Phys. Chem. C* **2007**, *111* (1), 50−56.
(66) L.-Viger, M.; Brouard, D.; Boudreau, D. Plasmon-Enhanced Resonance Energy Transfer from a Conjugated Polymer to Fluorescent Multilayer Core- Shell Nanoparticles: a Photophysical Study. *J. Phys. Chem. C* **2011**, *115* (7), 2974−2981.
(67) Ghenuche, P.; de Torres, J.; Moparthi, S. B.; Grigoriev, V.; Wenger, J. r. m. Nanophotonic Enhancement of the Förster Resonance Energy-Transfer Rate with Single Nanoapertures. *Nano Lett.* **2014**, *14* (8), 4707−4714.
(68) Lu, D.; Cho, S. K.; Ahn, S.; Brun, L.; Summers, C. J.; Park, W. Plasmon Enhancement Mechanism for the Upconversion Processes in NaYF4: Yb3+, Er3+ Nanoparticles: Maxwell versus Forster. *ACS Nano* **2014**, *8* (8), 7780−7792.
(69) Kim, K.-S.; Kim, J.-H.; Kim, H.; Laquai, F.; Arifin, E.; Lee, J.-K.; Yoo, S. I.; Sohn, B.-H. Switching off FRET in the Hybrid Assemblies of Diblock Copolymer Micelles, Quantum Dots, and Dyes by Plasmonic Nanoparticles. *ACS Nano* **2012**, *6* (6), 5051−5059.
(70) Tumkur, T. U.; Kitur, J. K.; Bonner, C. E.; Poddubny, A. N.; Narimanov, E. E.; Noginov, M. A. Control of Förster Energy Transfer in the Vicinity of Metallic Surfaces and Hyperbolic Metamaterials. *Faraday Discuss.* **2015**, *178*, 395−412.
(71) De Dood, M.; Knoester, J.; Tip, A.; Polman, A. Förster Transfer and the Local Optical Density of States in Erbium-Doped Silica. *Phys. Rev. B* **2005**, *71* (11), 115102.
(72) Blum, C.; Zijlstra, N.; Lagendijk, A.; Wubs, M.; Mosk, A. P.; Subramaniam, V.; Vos, W. L. Nanophotonic Control of the Förster Resonance Energy Transfer Efficiency. *Phys. Rev. Lett.* **2012**, *109* (20), 203601.
(73) Rabouw, F. T.; Den Hartog, S. A.; Senden, T.; Meijerink, A. Photonic Effects on the Förster Resonance Energy Transfer Efficiency. *Nat. Commun.* **2014**, *5* (1), 1−6.
(74) Schleifenbaum, F.; Kern, A. M.; Konrad, A.; Meixner, A. J. Dynamic Control of Förster Energy Transfer in a Photonic Environment. *Phys. Chem. Chem. Phys.* **2014**, *16* (25), 12812−12817.
(75) Nosrati, S.; Rammler, T.; Meixner, A. J.; Wackenhut, F. Combining Optical Strong Mode Coupling with Polaritonic Coupling in a $\lambda/2$ Fabry−Pérot Microresonator. *J. Phys. Chem. C* **2021**, *125* (23), 13024−13032.
(76) Takele, W. M.; Wackenhut, F.; Liu, Q.; Piatkowski, L.; Waluk, J.; Meixner, A. J. Tailoring Tautomerization of Single Phthalocyanine Molecules through Modification of Chromophore Photophysics by the Purcell Effect of an Optical Microcavity. *J. Phys. Chem. C* **2021**, *125* (27), 14932−14939.
(77) Nan, W.; Jinping, H.; Jun, M.; Hiromichi, T.; Takayoshi, K. Sub-Diffraction-Limit Imaging Using mode Multiplexing. *Proc. SPIE* **2015**, *9636*, 96360A.
(78) Woehler, A. Simultaneous Quantitative Live Cell Imaging of Multiple FRET-based Biosensors. *PLoS One* **2013**, *8* (4), No. e61096.
(79) Sun, Y.; Wallrabe, H.; Booker, C. F.; Day, R. N.; Periasamy, A. Three-Color Spectral FRET Microscopy Localizes Three Interacting Proteins in Living Cells. *Biophys. J.* **2010**, *99* (4), 1274−1283.

https://doi.org/10.1021/acs.jpcc.3c02566
J. Phys. Chem. C 2023, 127, 12152−12159

Supporting information:

Controlling Three-Color Förster Resonance Energy Transfer in an Optical Fabry Pérot Microcavity at Low Mode Order

Saeed Nosrati,[1] Frank Wackenhut,[1,2,*] Christoph Kertzscher,[1] Marc Brecht,[1,2] and Alfred J. Meixner[1,*]

[1]*Institute of Physical and Theoretical Chemistry, Eberhard Karls University Tübingen, 72076 Tübingen, Germany*
[2]*Process Analysis and Technology PA & T, Reutlingen University, 72762 Reutlingen, Germany*

Corresponding Authors
E-mail: alfred.meixner@uni-tuebingen.de
E-mail: frank.wackenhut@reutlingen-university.de

Experimental setup

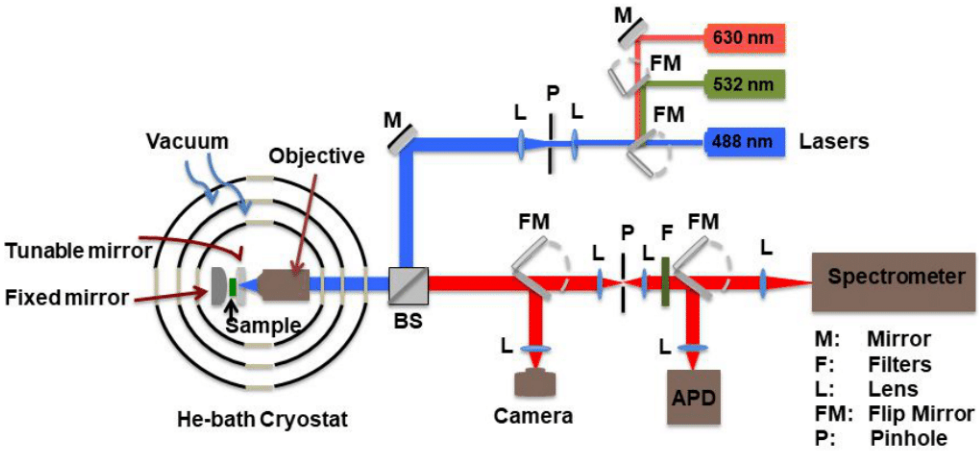

Figure S1. Sketch of the optical setup for low-temperature fluorescence lifetime and spectroscopy measurements.

Figure S1 shows a home-built confocal microscope in a bath cryostat (SVT-200, Janis). A temperature sensor (DT-670-SD, Diode sensor, Lake Shore Cryotronics) close to the sample is used to control the temperature at 130 K. Three diode lasers at 488 nm, 532 nm, and 630 nm

are aligned into the cryostat using a 30:70 plate beam splitter (BSS10R, Torlabs) and can be focused on the sample through an objective (Newport, 60X NA = 0.85). The emitted light is passed through a 50 µm pinhole, and a 488 nm long pass filter (AHF Analysentechnik), and it can be detected by a spectrometer (Shamrock 500, Andor Technology) and an APD with a subsequent time correlated single photon counting system (SPCM-AQR-14, Photon Counting Module, PerkinElmer Optoelectronics). To separately measure the fluorescence lifetime of the three dyes, three different filters (550 short pass, 580/65 band pass, and 630 long pass) are installed in front of the APD. White light can be generated by a LED outside of the cryostat to acquire transmission spectra. A self-developed LabVIEW software is used to control the motorized flip mirrors on the optical setup and the piezoelectric actuators inside the cryostat.

Lifetime measurements

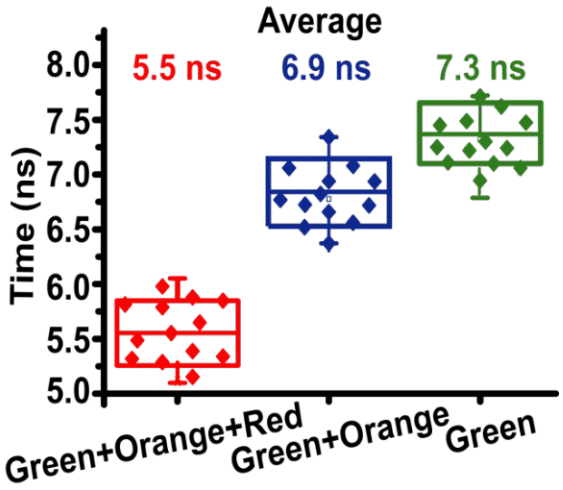

Figure S2. An average-weighted lifetime diagram of the donor (green), donor with acceptor1 (blue) and donor with acceptor1 and acceptor2 (red) in free space.

The recorded lifetimes of the green dye without acceptors (green dots) and with acceptors (blue and red dots) are summarized in Figure S2. Every dot represents a lifetime measurement from an individual nanosphere. For the green dye (in the absence of the orange and red dyes), an average value of $\tau = 7.3 \pm 0.3$ ns is recorded, while the average lifetime before photobleaching of the red and orange dye was 6.9 ± 0.35 ns and 5.5 ± 0.33 ns, respectively.

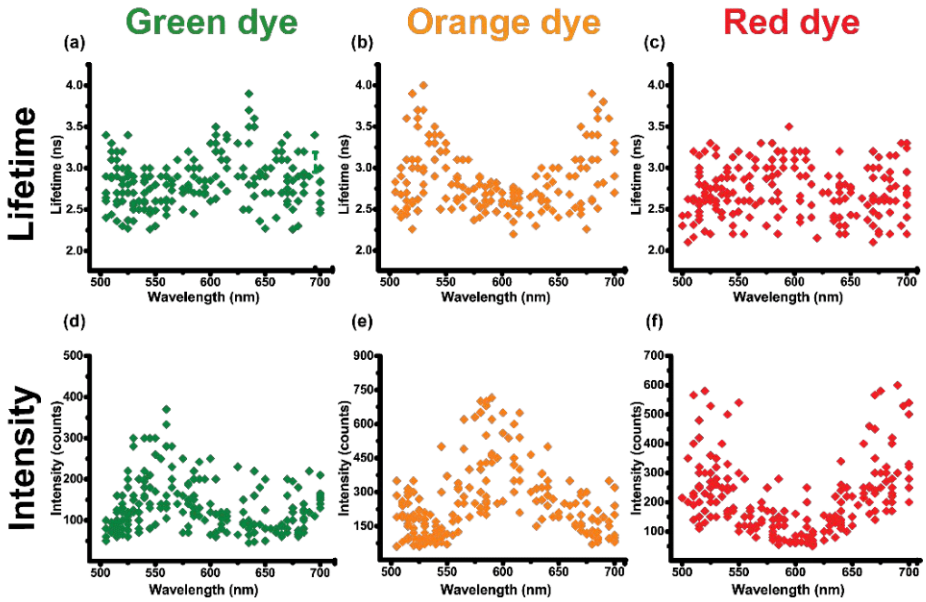

Figure S3. (a)-(f) Experimental lifetimes and the respective amplitudes of the fluorescence decay curve of the donor, acceptor1, and acceptor2 for the different single nanospheres as a function of cavity resonance at low temperature accomplished by tuning the mirror spacing with piezo actuators.

Measured lifetimes and amplitudes of the decay curves of the donor, acceptor1, and acceptor2 of 41 nanospheres are shown in Figure S3 for multiple independent cavity tunings at 130 Kelvin. For every nanoparticle the microcavity mode was tuned step by step in the visible spectral range and the lifetime of individual dyes was measured with 550 nm short pass, 580 nm bandpass and 630 nm long pass filters in front of the APD. Measurements are binned in 15 nm increments to improve the statistics. The average values together with the error bars are shown in Figure S4.

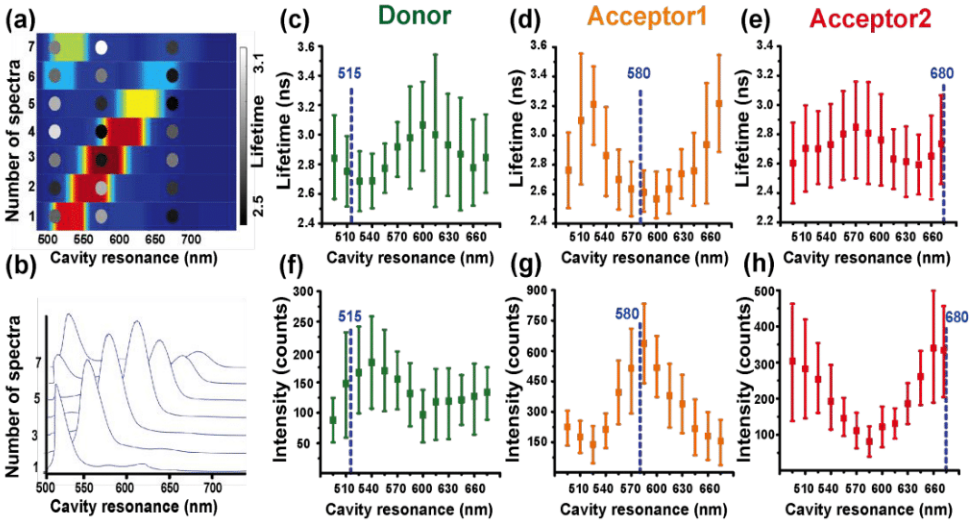

Figure S4. (a) Two-dimensional false color map showing the shift of white light transmission maximum as a function of increasing the mirror spacing from 2nd to 3rd cavity mode. The emission spectrum of the white light LED is shown in Figure S9. The gray-scaled dots at 515 nm, 580 nm and 680 nm represent the lifetime of the donor,

acceptor1 and acceptor2, respectively. (b) Waterfall plot of (a) for better visibility of the cavity resonance. (c) to (e) Ensemble average of the measured cavity-modified lifetimes of the donor, acceptor1 and acceptor2 as a function of cavity resonance. (f) to (h) The amplitudes of the respective fluorescence decay curves of the three dyes as a function of the cavity resonance. The measured data are binned in 15-nm increments and are the average of 220 data points. The error bars originate from the fit of the fluorescence lifetime decay curves and possibly from the variation of the particles in the local environment of the dyes in each sphere which can vary from one sphere to the others. The free space emission maxima of the individual dyes are shown as blue dashed lines in (c) to (h).

Figure S4(a) represents a 2D plot of white light microcavity transmission spectra, where the microcavity resonance is tuned across the visible spectral range by increasing the mirror separation (vertical axis). Low transmission intensity is represented by blue color and high transmission is presented in red. The emission spectrum of the white light LED is shown in Figure S9. A waterfall plot of these white light transmission spectra is presented in Figure S4(b) for better visibility. In these spectra we clearly see the appearance of the next higher mode as the mirror spacing increases and the initial mode shifts to the red. The gray-scaled dots in Figure S4(a) illustrate the corresponding fluorescence lifetimes of the three dyes. Dark gray dots represent a short lifetime, whereas light gray represents long lifetimes. Figures S4(c) to (e) show the influence of the cavity resonance on the fluorescence lifetime of the three dyes measured independently for 41 particles. The error bar shows that the lifetime of individual dyes in different nanospheres varies considerably from one sphere to the other possibly due to a variation of particles in the local environment of the dyes from particle to particle and / or from the uncertainties in determining the cavity resonance for a specific mirror separation. The fluorescence lifetimes of the donor, accpetor1, and acceptor2 for three different single nanospheres are shown in Figure S5 as a function of cavity resonances.

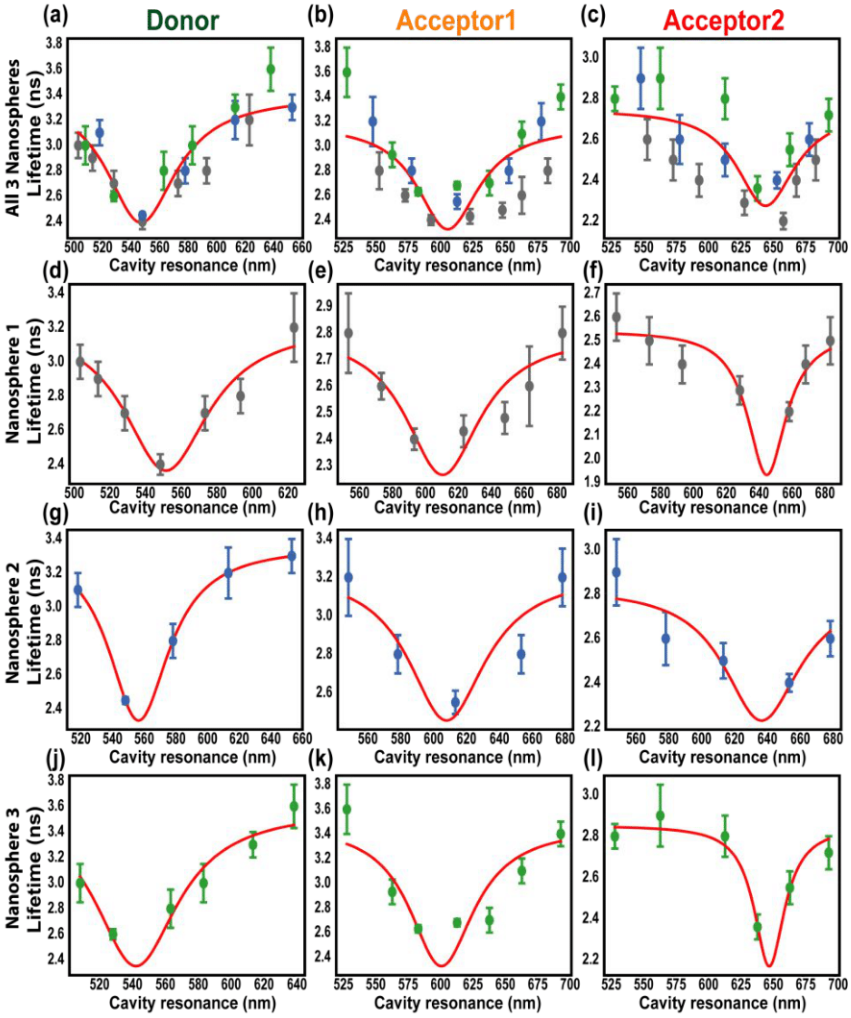

Figure S5. (a)-(l) Fluorescence lifetimes of donor, acceptor1 and acceptor2 for three different nanospheres represented as grey, blue and green dots as a function of the cavity resonance wavelength. The error bars are from the fits of the time dependent fluorescence intensity decay curves. The red lines represent fits of Lorentzian shaped functions to the data points with the spectral widths, dip position and amplitudes as fit parameters.

The fluorescence lifetimes of three different single nanospheres as a function of cavity resonance are shown in Figure S5. A theoretical model for the Purcell factor[1,2] shown by red lines is fitted to the experimental data to study the effect of cavity resonance on the lifetimes of donor, accpetor1, and acceptor2. Spectral dependence of the resonator and molecules are modeled by a Lorentzian line shape function with a full width at half maximum $\Delta\omega$ centered at the maximum emission frequency ω_0 of the molecules. Spectral dependence of the Purcell factor F_P as a function of the cavity resonance ω_c can be expressed as

$$F_P = \frac{W^{cav}}{W^{free}} = \frac{\tau_R^{free}}{\tau_R^{cav}} = 6\pi\left(\frac{c}{\omega_c}\right)^3 \frac{Q}{V_0}\xi^2 \frac{\Delta\omega_c^2}{4(\omega_0-\omega_c)^2+\Delta\omega_c^2},$$

where F_P is the Purcell factor, W^{cav} (W^{free}) is the radiative transition rate of the emitter inside the cavity (in free space), τ_R^{cav} (τ_R^{free}) is the radiative lifetime of the dye inside the cavity

(in free space), c is the vacuum speed of light, Q is the quality factor of the cavity, V_0 is the mode volume of the cavity, ξ^2 is the dipole orientation factor of the molecule, $\Delta\omega$ is the sum of the FWHMs of the cavity mode and the emission profile of the molecules.
The following equation is used to fit the data for the lifetime (where we assumed that the lifetime converges to τ_0 far away from the cavity resonance).

$$\tau_R^{cav} = \frac{\tau_0}{(F_P + 1)}$$

The experimental lifetimes from different nanospheres and the curve fit function from the Python module SciPy (scipy.optimize.curve_fit) are used to fit the data. Fit parameters are defined as the lifetime of the nanosphere far away from cavity resonance, the amplitude of the Purcell effect (which consists of Q, V_0 and ξ^2), FWHM, and the maximum emission frequency of the dyes.

Triple FRET model

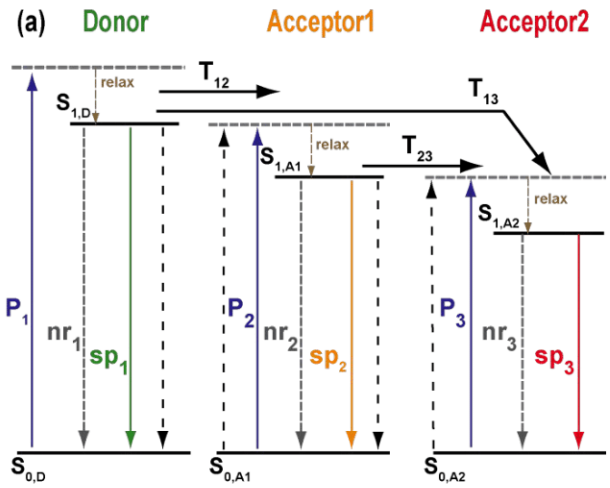

Figure S6. Simplified energy-level scheme of a triple FRET system consisting of one donor and two acceptors.

Figure S6 shows a simplified energy-level scheme of the triple FRET system illustrating the different excitation/deexcitation/transfer routes. The donor is excited from the ground state $S_{0,D}$ to a higher vibronic level of the first excited state with a pumping rate P_1 and relaxes very fast to the lowest vibronic level of the first excited state $S_{1,D}$. The donor may relax to its ground state either with a non-radiative nr_1 or the spontaneous emission sp_1 rate. Energy transfer occurs from the donor by the rates T_{12} and T_{13} to excite the acceptor1 or acceptor2 to a higher vibronic level of their excited state. Acceptor1 and acceptor2 can relax from their electronically excited state ($S_{1,A1}$, $S_{1,A2}$) by non-radiative (nr_2, nr_3) or radiative decay channel (sp_2, sp_3) to its ground state ($S_{0,A1}$, $S_{0,A2}$). In addition, acceptor1 can be a donor to excite acceptor2. Finally, acceptor2 can relax to the ground state by the spontaneous emission sp_3 or by the non-radiative rate nr_3.
The equations to model the energy exchange between donor and acceptors in a triple FRET system shown in the main text were solved numerically using the ODE solvers included in

Matlab. All simulated spectra presented in the main text are the results from differential rate equations and the corresponding parameters used for the calculations in the main text are given in Table S1. All rate constants are relative to the free space radiative rate, whose radiative rate constant is set to 1.

Simulated parameter	Figure S7(a)	Figure S7(b)	Figure S7(c)	Figure 5(f)	Figure 5(g)	Figure 5(h)
Pump rate Donor (P_1)	1	1	1	1	1	1
Pump rate Acceptor1 (P_2)	0	0.1	0.1	0.1	0.1	0.1
Pump rate Acceptor2 (P_3)	0	0	0.1	0.1	0.1	0.1
Transfer rate (T_{12}) Donor-Acceptor1	0	0	0	0	0	1
Transfer rate (T_{13}) Donor-Acceptor2	0	0	0	1	0	0
Transfer rate (T_{23}) Acceptor1-Acceptor2	0	0	0	0	1	0.25
Non-radiative emission rate (nr)	0.1	0.1	0.1	0.1	0.1	0.1
Spontaneous emission rate (sp)	1	1	1	1	1	1

Table S1. Simulation parameters used for the six coupled differential rate equations given in the main manuscript to model the emission spectra of a single TetraSpeck nanosphere located in the tunable cavity.

Theoretical emission spectra of a TetraSpeck nanosphere are shown in Figure S7 for exclusive excitation of the donor only (P_1) in (a), for excitation of donor and acceptor1 (P_1, P_2) in (b), and for excitation of the donor and both acceptors (P_1, P_2, P_3) in (c) with neglecting energy transfer. Calculated white light transmission maxima are indicated by white dashed lines in (a) to (c).

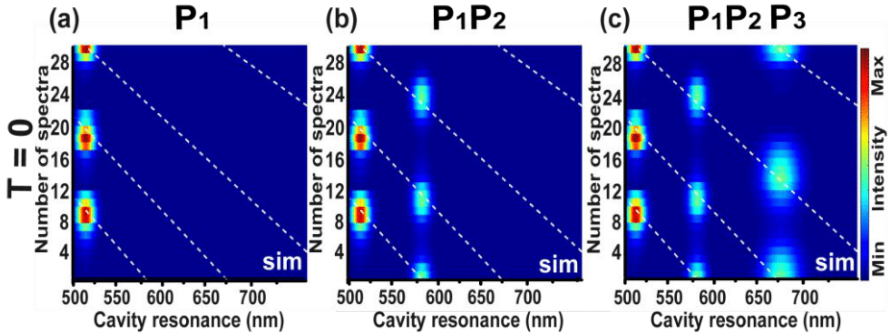

Figure S7. Emission spectra modeled based on six-coupled rate equations in the main manuscript for the situation where there is no energy transfer (T = 0) between dyes.

Estimation of the number of molecules in a single TetraSpeck sphere

We estimate the number of molecules in a single TetraSpeck sphere using the Beer-Lambert´s law, by assuming that the donor molecules have a similar absorption cross-section as dye molecules with a similar absorption spectrum:

$$I = I_0 \exp\ (-\sigma \cdot L \cdot\ N/V\ )$$

where I is the transmitted intensity, I_0 is incident intensity, σ is the absorption cross-section, N is the number of absorbers (molecules), L is the absorption path length, and V is the particle volume. The figure below shows the transmission spectrum of the excitation laser line at 531 nm measured for a single sphere (blue line) and from the same sample with no sphere in the focal volume (red line). The transmitted beam is decreased in presence of a single sphere due to the light absorption, while the transmitted intensity (red peak) is higher for the sample without a sphere.

To calculate the number of donor molecules in the TetraSpeck sphere we use the known absorption cross-section of Rhodamine 6G ($\sigma = 4 \cdot 10^{-16}\ cm^2$)[3,4] which has a nearly similar absorption spectrum.

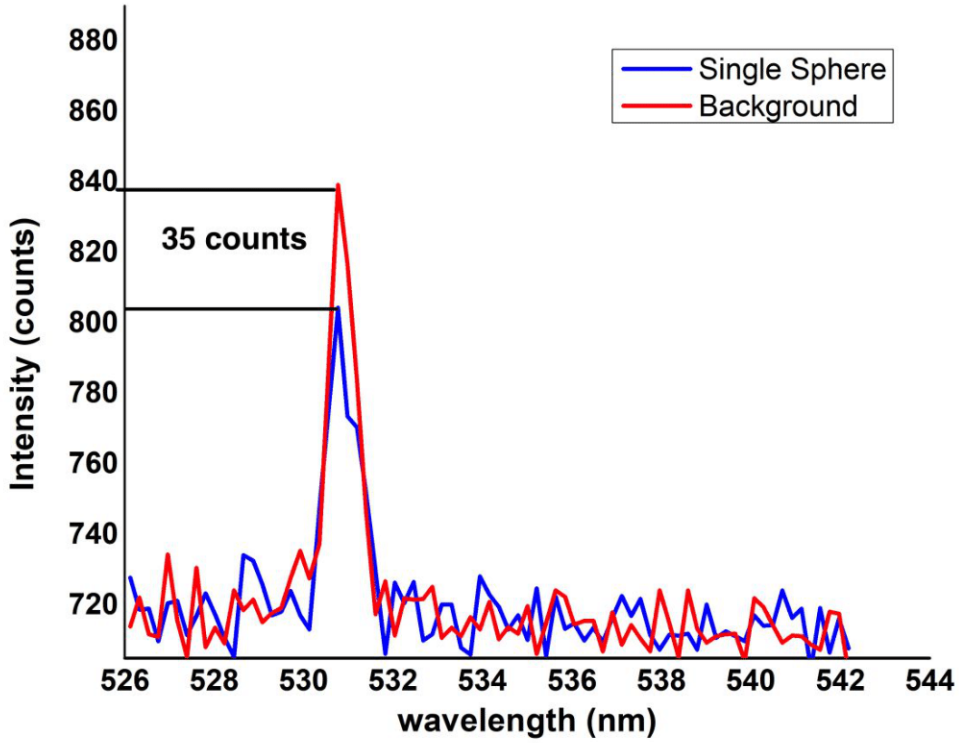

Figure S8. Transmission spectrum of excitation laser line at 531 nm with (blue) and without (red) a single nanosphere.

$$N = \frac{V}{\sigma \cdot L} Ln\left(\frac{I_0}{I}\right) = \frac{\frac{4}{3}\pi(50nm)^3}{4 \cdot 10^{-16}\ cm^2 \cdot 100\ nm} \cdot\ Ln\left(\frac{840}{805}\right) = 5571$$

With the above numbers we calculated the number of donor fluorophores in a single TetraSpeck sphere to be about 5600 molecules probed by the linear polarized excitation with a mean distance of 4.5 nm between them. Of course, for an isotropic sample, the total number of molecules is three times higher.

Spectral emission profile of the LED

Spectral emission profile of LED in free space is measured and shown in Figure S9.

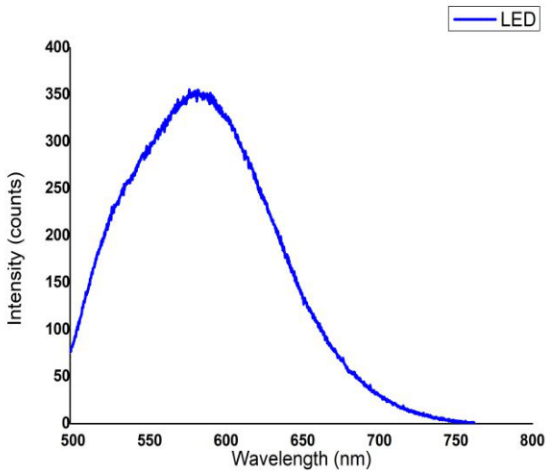

Figure S9. Spectral emission profile of LED used to acquire transmission spectra

[1] Purcell, E. M.; Torrey, H. C.; Pound, R. V. Resonance absorption by nuclear magnetic moments in a solid. Physical review 1946, 69 (1-2), 37.

[2] Fox, A. M.; Fox, M. Quantum optics: an introduction; Oxford university press, 2006.

[3] Dolan, Giora, and Chmouel R. Goldschmidt. "A new method for absolute absorption cross-section measurements: rhodamine-6G excited singlet-singlet absorption spectrum." Chemical Physics Letters 39.2 (1976): 320-322.

[4] Wiedmann, J., and Alfons Penzkofer. "Excited-state absorption cross-sections in rhodamine dyes determined after molecular reorientation." Il Nuovo Cimento B (1971-1996) 63.1 (1981): 459-469.

THE JOURNAL OF PHYSICAL CHEMISTRY C
A JOURNAL OF THE AMERICAN CHEMICAL SOCIETY

pubs.acs.org/JPCC

Article

Combining Optical Strong Mode Coupling with Polaritonic Coupling in a λ/2 Fabry–Pérot Microresonator

Saeed Nosrati, Tim Rammler, Alfred J. Meixner,* and Frank Wackenhut*

Cite This: *J. Phys. Chem. C* 2021, 125, 13024–13032

Read Online

ACCESS | Metrics & More | Article Recommendations | Supporting Information

ABSTRACT: Strong coupling has attracted much research interest motivated by the possibility to tune the energy levels of molecules enabling to control and modify chemical reactions. Strong coupling leads to the formation of new hybrid modes and is caused by coherent energy exchange between the individual constituents. Such a coherent energy exchange occurs when the coupling rate exceeds the damping rate of the individual components and has been observed for highly diverse systems. Here, we present a strongly coupled hybrid system consisting of a thin TDBC J-aggregate film inside an optical subwavelength microresonator coupled to a second microresonator. This hybrid structure combines strong coupling of purely optical modes with strong light–matter interaction. The coupling strength and damping sensitively depend on the position and concentration of the coupled molecules in the microresonator structure. Such a coupled system can be modeled by coupled damped oscillators, which allows to determine the coupling and damping constants. We show that the individual components making up the coupled hybrid system cannot be treated individually, but the coupled system needs to be considered as a whole. As a consequence, altering one parameter does influence the whole coupled system, and the individual components need to be carefully adapted to each other to achieve efficient coupling. These results can have important consequences for the field of optoelectronics or polaritonic chemistry.

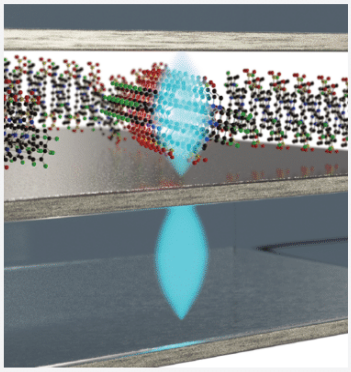

■ INTRODUCTION

The ability of optical microresonators to confine light to subwavelength dimensions and to control light–matter interaction has drawn considerable research attention during the past decades. The interaction between an emitter and a confined optical field can be classified into weak and strong coupling,[1,2] which is defined by the ratio of the damping and coupling rates of the emitter and the microresonator. The coupled system is in the weak coupling regime when the individual damping rates are larger than the coupling rate. In this case, the emission properties of the emitter are exclusively altered by the Purcell effect,[3−8] which has been reported in plasmonic antennas,[9] microcavities,[10−12] or photonic crystals[13,14] and can be used to control Förster resonant energy transfer and photobleaching in optical environments.[15−20] In contrast, strong coupling occurs when the coupling rate exceeds the individual damping rates, and the individual modes are hybridized into new polaritonic modes[21] or supermodes.[22] The hybridized modes are spectrally separated by the Rabi splitting, and strong coupling manifests itself by anticrossing of the coupled modes in the dispersion of the coupled hybrid system.[23,24] This is a very attractive aspect of strong coupling because it enables to tune the energy levels of the hybrid system and to modify and control chemical reactivity.[25−27] In general, strong coupling can be achieved in a variety of diverse systems, which can be subdivided into coupling of purely optical modes and coupling of an optical mode with matter. Strong coupling of purely optical modes, leading to the formation of supermodes, has been observed in phase-locked semiconductor laser arrays,[28] coupled optical or photonic fibers,[29,30] or photonic crystal cavities,[31−33] just to mention a few. On the other hand, strong light–matter coupling has been studied extensively and was realized for microresonators,[1,34−40] photonic crystals,[41−43] micropillars,[44,45] microdisks,[46] microtubes,[47] and plasmonic systems.[48−54] Especially λ/2 Fabry–Pérot microresonators are attractive to achieve strong coupling due to their ease of fabrication, flexible geometry, and accessibility; hence, many examples have been reported in the literature, for example, microresonators containing photonic molecules,[55−58] polymers,[59,60] inorganic quantum wells,[61−64] quantum dots,[45,65] or organic semiconductors.[66−68] More recently, studies of organic materials have been focused on J-aggregates of cyanine dye molecules due to the fact that they possess narrow and sharp peaks in their absorption and photoluminescence spectra, making them ideal to achieve strong light–matter coupling.[69−74]

Received: April 3, 2021
Revised: May 22, 2021
Published: June 4, 2021

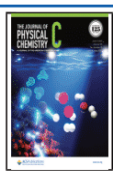

https://doi.org/10.1021/acs.jpcc.1c03004
J. Phys. Chem. C 2021, 125, 13024–13032

In this paper, we focus on strong coupling between a thin TDBC J-aggregate film and a pair of optically coupled $\lambda/2$ Fabry–Pérot microresonators. We demonstrate that two types of strong coupling occur simultaneously in the coupled system. The first type is strong coupling of two purely optical modes of the adjacent microresonators, in which the coupling strength can be tuned by varying the thickness of the central shared mirror and is described in detail in our previous work.[2] The second type is strong coupling between matter, that is, the TDBC J-aggregate molecules and the optical modes of the coupled microresonators. We demonstrate that the coupling strength and damping of the hybrid system can be tuned by the optical microresonator modes, the lateral position of the TDBC film, and the TDBC concentration in the film. Additionally, we show that the hybrid system can be modeled by a coupled harmonic oscillator approach, which allows to determine all important parameters, that is, the coupling and damping constants. These results prove that such a coupled system is well suited to investigate the basic concepts of strong coupling between optical modes and electronically excited molecules because it enables to have full control over all parameters. Finally, we point out the importance to precisely control the systems' geometry, which needs to be taken carefully into account in the fields of polaritonic chemistry or long-range coupling of two emitters.

EXPERIMENTAL SECTION

Preparation of TDBC–PVA Film. A thin film of 5,6-dichloro-2-[[5,6-dichloro-1-ethyl-3-(4-sulfobutyl)-benzimidazol-2-ylidene]propenyl]-1-ethyl-3-(4-sulfobutyl)-benzimidazolium hydroxide, inner salt, sodium salt (TDBC; purchased from FEW Chemicals, Germany, and used without further purification), in a poly(vinyl alcohol) (PVA) matrix was deposited by spin-coating on the SiO_2 spacer layer covering the central mirror. TDBC molecules are dissolved in a solution of PVA (1 wt %) in water, where they are forming J-aggregates.[75] The TDBC J-aggregate solution was prepared at a concentration of 10^{-2} mol/L, if no other concentration is explicitly mentioned. The solution was sonicated for 20 min, and a 5 μL droplet of the TDBC J-aggregate/PVA solution was spin-coated on top of the SiO_2 layer for 30 s at 1700 rpm angular velocity. This procedure has been precisely repeated for all microresonators. The average thickness of obtained film is 30 nm as measured with an atomic force microscope (AFM).

Coupled Microresonator Preparation. The layers forming the microresonator structure are deposited by electron beam evaporation. The lower microresonator with a fixed optical path length consists of two silver mirrors, where a 50 nm thick silver layer is evaporated on a clean glass cover slide, followed by a 10 nm gold and a dielectric SiO_2 layer of 148 nm. The thickness of this SiO_2 layer is chosen to tune the resonance of the fixed resonator and to spectrally overlap it with the maximum absorption peak of TDBC J-aggregate molecules at 590 nm (Figure 1a). Afterward, the central shared mirror is created by evaporating a 24 nm silver layer on top of this SiO_2 layer. In addition, the central mirror is coated with a 10 nm gold layer and a SiO_2 spacer layer with variable thicknesses ranging from 50 to 185 nm. This dielectric SiO_2 spacer layer allows to control the spatial position of a thin TDBC–PVA film inside the upper microresonator. The topmost mirror is a lens coated with an 80 nm silver layer, a 10 nm thick gold layer, and a 10 nm SiO_2 layer and forms, together with the central mirror, the tunable microresonator.

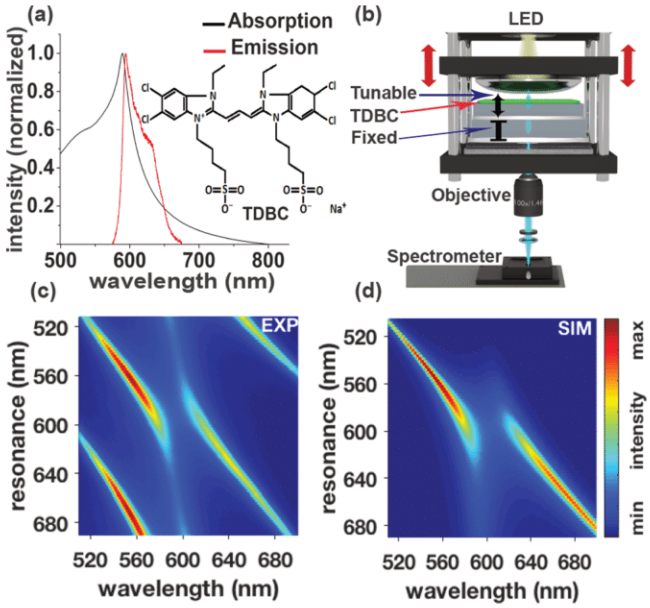

Figure 1. (a) Absorption and emission spectra of a TDBC J-aggregate film including the chemical structure of TDBC. (b) Graphic sketch of two adjacent Fabry–Pérot microresonators, where the upper resonator is tunable and the lower one is fixed. The two resonators are separated by a shared central silver mirror. A white light LED is used to record the transmission spectrum of the coupled microresonators. (c) Experimental transmission spectra of the strongly coupled microresonators with an anticrossing dispersion of the two resonator modes. The horizontal axis is the wavelength of the transmitted light as recorded by the spectrometer, and the vertical axis indicates the resonance of the tunable resonator. (d) Corresponding simulation using coupled harmonic oscillators, where the resonance frequencies are fitted to the experimental data. In (c) two additional resonator modes are visible, which have not been considered in the simulations. The color map illustrates the intensity of the transmission spectra.

Experimental Setup. A home-built holder and a piezo actuator (8302 Picomotor Actuator, Newport) are used to assemble the coupled microresonators.[2] The two coupled microresonators consist of three silver mirrors, where the central silver mirror is shared between the two microresonators. In this geometry, the topmost mirror (a silver-coated lens) can be moved toward the shared mirror to reach the $\lambda/2$ region of the visible spectral range. A white light LED is mounted on top of the microresonator holder to acquire transmission spectra. The transmitted light is collected via an oil immersion objective lens (NA = 1.4) from below, and the detected signal is guided to a spectrometer with a thermoelectrically cooled CCD camera (PIXIS 100, Princeton Instruments, USA).

RESULTS AND DISCUSSION

The molecular structure of TDBC is shown in Figure 1a, together with the experimental absorption and emission spectra of TDBC J-aggregate film that have a small Stokes shift between the absorption and emission maximum. A schematic drawing of the experimental setup consisting of two adjacent Fabry–Pérot microresonators and a home-built confocal microscope is shown in Figure 1b. It consists of two adjacent microresonators with an additional thin TDBC film on top of a SiO_2 spacer layer deposited on the central mirror. The optical path length of the upper resonator can be

https://doi.org/10.1021/acs.jpcc.1c03004
J. Phys. Chem. C 2021, 125, 13024–13032

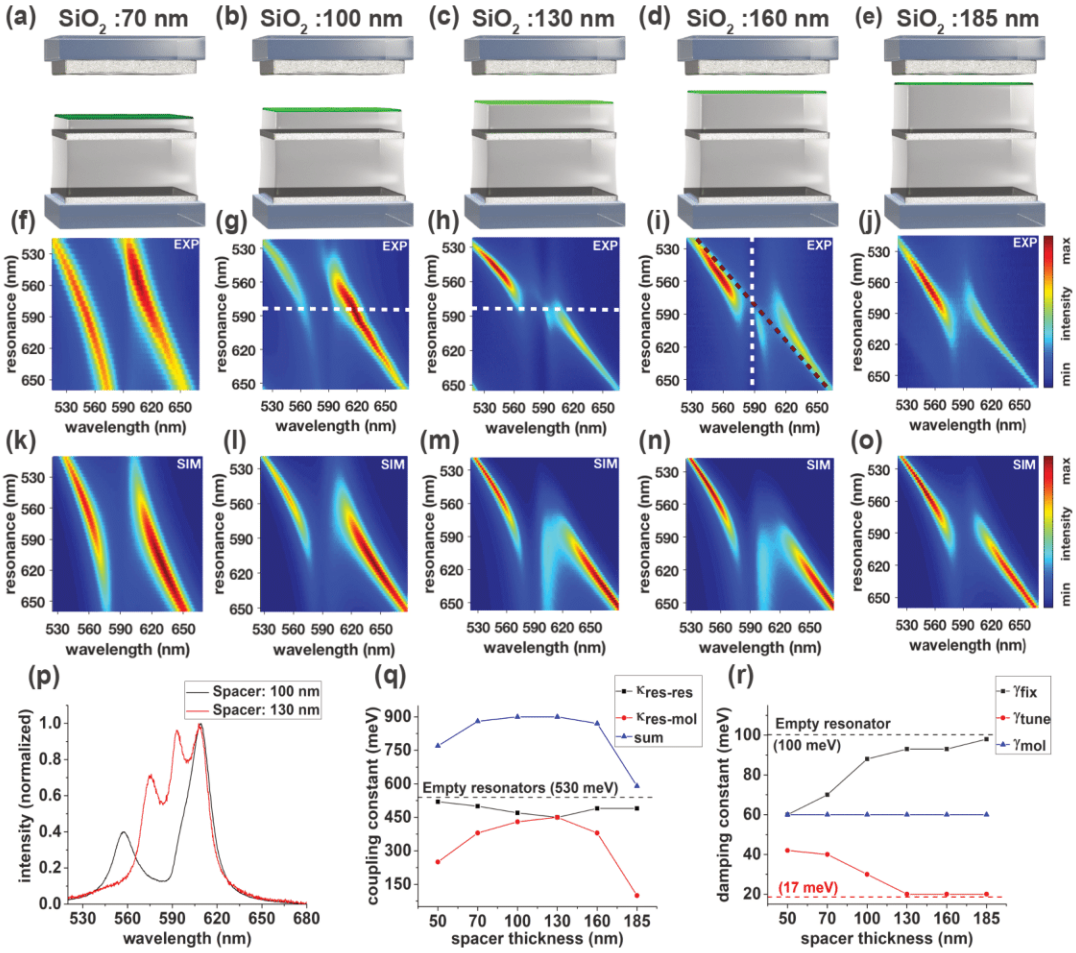

Figure 2. (a–e) Schematic drawings of five different experimental situations showing two coupled microresonators, where a thin TDBC J-aggregate film is deposited on a SiO_2 spacer layer inside the upper resonator. The thickness of the spacer layer is indicated on top of the respective scheme. (f–j) Experimental white light transmission spectra of coupled microresonators with the enclosed TDBC J-aggregate film. (k–o) Corresponding simulated transmission spectra. (p) Two exemplary experimental transmission spectra of the coupled system (marked by the white dashed line in (g, h)) with a spacer thickness 100 nm (black line) and 130 nm (red line). (q) Coupling constants between two microresonators ($\kappa_{res-res,}$ black squares) and between the tunable resonator and the molecules ($\kappa_{res-mol}$, red dots) as a function of the TDBC film position. Sum of both coupling constants (blue triangles) to show the maximum coupling strength of the whole system. (r) Damping constants of the coupled system for different positions of the TDBC film. The individual components are TDBC molecules (γ_{mol}, blue triangles), fixed microresonator (γ_{fix}, black squares), and tunable microresonator (γ_{tune}, red dots).

tuned by piezo actuators, while it is fixed for the lower one. In the following, we will refer to the upper and lower microresonator as the tunable and fixed microresonator. The transmission spectra of the empty coupled microresonator are shown in Figure 1c.

Strong coupling between the purely optical microresonator modes results in the formation of supermodes and frequency splitting,[22] which can be seen in Figure 1c at ∼600 nm. The vertical axis in Figure 1c represents the resonance wavelengths of the tunable microresonator. The two transmitted peaks show an anticrossing dispersion at ∼600 nm and are separated by the Rabi splitting when the resonances of the fixed and tunable microresonator coincide. The Rabi splitting obtained from the experimental data is ∼23 nm. Figure 1d shows the corresponding calculations based on two coupled harmonic oscillators, which are described in detail in ref 2 and in the Supporting Information. An additional higher and lower order mode is observed in the experimental spectra, which are not considered in the calculations. This model enables to reproduce the experimental data in Figure 1c and allows to determine the resonator–resonator coupling constant $\kappa_{res-res}$ and the corresponding damping constants of the fixed γ_{fix} and tunable γ_{tune} microresonator. The respective damping and coupling constants of the coupled microresonator shown in Figure 1c are γ_{fix} = 100 meV, γ_{tune} = 17 meV, and $\kappa_{res-res}$ = 530 meV. The coupling constant is larger than the individual damping constants; hence, the two microresonators are within the strong coupling regime. The next step is to investigate coupling between a thin TDBC film with such a coupled microresonator structure. In this case, there are two types of strong coupling mechanisms: first, strong coupling of the two purely optical modes of the microresonators and, second, strong light–matter coupling between the optical microresonator modes and the TDBC J-aggregates. As we have shown in ref 2, strong coupling between the two microresonators can be tuned by varying the thickness of the central mirror, which is kept constant for all experiments presented here. First, we want to show that coupling between the TDBC film and the optical modes sensitively depends on the spatial position of the film within the tunable microresonator. This can be achieved by varying the thickness of the dielectric SiO_2

https://doi.org/10.1021/acs.jpcc.1c03004
J. Phys. Chem. C 2021, 125, 13024–13032

spacer layer deposited on the central mirror, as schematically illustrated in Figures 2a−e.

The transmission spectra of these five microresonators are shown in Figures 2f−j for dielectric layer thicknesses ranging from 70 nm in (f) to 185 nm in (j). The resonance frequency of the lower microresonator is fixed and is adjusted to be close to the absorption maximum of the TDBC J-aggregate film at 590 nm, as marked by the white dashed line in Figure 2i. Each line along the vertical axis in Figure 2 represents a transmission spectrum recorded for a distinct optical path length of the tunable microresonator, and the respective resonance wavelength is shown exemplarily by the black dashed line in Figure 2i and on the vertical axis. Clear anticrossing can be observed when the resonance of the tunable microresonator is spectrally overlapping with the resonance of the fixed one or the absorption of the TDBC J-aggregate film. Two experimental transmission spectra of the coupled system marked by the white dashed line in Figures 2g and 2h are presented in Figure 2p. The red line shows a transmission spectrum, where the TDBC J-aggregate film is placed close to the center of the tunable microresonator (130 nm SiO_2 spacer layer), and clearly three modes due to strong coupling of the two microresonators with the TDBC J-aggregate molecules can be resolved. On the contrary, light−matter coupling is weaker when the film is moved away from the center of the tunable microresonator (100 nm SiO_2 spacer layer, black line) and is only observable as a shoulder at ∼600 nm. Apart from the coupling strength, the damping of the coupled system is obviously altered by the position of the TDBC J-aggregate film, which can directly be seen by the larger/smaller line widths in Figures 2f,h as compared to the empty microresonator shown in Figure 1c. A parameter influencing the spectral dispersion of the modes is the ratio of the damping constants of the individual modes, which is illustrated in Figure S1 of the Supporting Information. Figure S1 shows that the maximum intensity of the transmission spectra follows more closely the mode with lower damping, while it becomes symmetric when the damping constants of both modes are the same. This dispersion behavior allows to draw the conclusion that the damping of the fixed and tunable microresonators in Figure 2f is similar, while damping of the tunable microresonator is smaller in Figure 2h. Three damped coupled harmonic oscillators are used to model the two coupled microresonators and the TDBC J-aggregate molecules. The corresponding calculations are presented in Figures 2k−o, where the resonance frequency, damping, and coupling constant of the fixed and tunable resonators are varied to reproduce the experimental data. The resonance frequency and the damping constant of the oscillator used to model the TDBC J-aggregate molecules are determined from the absorption spectrum acquired outside of the microresonator and are kept constant for all calculations. All parameters used in the calculations are summarized in Table S1. The coupling constants obtained from the calculations are presented in Figure 2q as a function of the spacer layer thickness. The data points are connected by lines as a guide to the eye. The resonator−resonator coupling constant $\kappa_{res-res}$ for an empty microresonator with a 50 nm SiO_2 spacer layer is $\kappa_{res-res}$ = 530 meV (indicated by the black dashed line in Figure 2q), and there is a small reduction to 520 meV by the presence of the TDBC J-aggregate film inside the tunable microresonator. Moving the TDBC J-aggregate film closer to the center leads to a decrease of the resonator−resonator coupling constant with a minimum of $\kappa_{res-res}$ = 450 meV, when the film is in the center of the tunable microresonator. A further increase of the spacer layer thickness is accompanied by an increase of $\kappa_{res-res}$. In contrast, the resonator−molecule coupling constant ($\kappa_{res-mol}$) increases rapidly from 250 meV at 50 nm to 450 meV at 130 nm. Interestingly, both coupling constants, $\kappa_{res-res}$ and $\kappa_{res-mol}$, are the same when the TDBC J-aggregate film is in the center of the tunable microresonator. Afterward, the resonator−molecule coupling constant steadily decreases to 100 meV for a 185 nm thick SiO_2 layer. Maximum strong coupling of the whole system (blue triangles) is shown by the sum of the molecule−molecule and molecule−resonator coupling constant, which is nearly constant for spacer layer thicknesses ranging from 70 to 160 nm. The corresponding damping constants obtained from the coupled harmonic oscillator approach for different positions of TDBC J-aggregate film in the tunable microresonator are illustrated in Figure 2r. The damping constant γ_{mol}, attributed to the TDBC J-aggregate molecules (blue triangles), is kept constant at 60 meV and is determined from the line width of the absorption spectrum of the TDBC J-aggregate molecules outside of the microresonator. The damping constants of the empty coupled microresonators are γ_{fix} = 100 meV for the fixed resonator (black dashed line) and γ_{tune} = 17 meV for the tunable resonator (red dashed line). An increase of the damping of the tunable resonator by the SiO_2 spacer layer is expected due to scattering at the SiO_2 surface, which can be assumed to be constant for the different SiO_2 spacer layer thicknesses. However, introducing a SiO_2 spacer layer of 70 nm with a TDBC J-aggregate film on top leads to strong increase of the damping constant of the tunable microresonator from γ_{tune} = 17 meV to γ_{tune} = 40 meV. This increase can be understood because the TDBC molecules mainly increase damping due to absorption and experience weaker coupling to the optical modes when they are located closer to the central mirror. Moving the film toward the center of the tunable microresonator leads to a reduction of the damping constant of the tunable resonator from γ_{tune} = 42 to 20 meV, which is quite close to the damping constant of the empty microresonator. At 130 nm the TDBC J-aggregate film is approximately located at the center of the tunable resonator, leading to the strongest coupling between the molecules and the microresonator, and results in the lowest damping. Interestingly, introducing the TDBC J-aggregate film into the tunable resonator significantly reduces the damping of the fixed resonator from γ_{fix} = 100 to 60 meV (black dots in Figure 2r), and a further increase of the SiO_2 layer thickness increases the damping constant back to 98 meV, which is close to the value obtained from the empty resonator. Hence, introducing a thin TDBC J-aggregate film in the coupled resonator structure close to the central mirror reduces the damping of the fixed resonator, while it increases the damping of the tunable one. On the other hand, there is nearly no influence on the damping of the tunable resonator when the film is in its center. This result shows that the coupled system needs to be considered as a whole, and influencing one parameter does have an impact on all other parameters.

One advantage of such a coupled microresonator structure is that all parameters can be easily and precisely adjusted by choosing different layer and mirror thicknesses. For instance, the fixed resonator can either be on or off resonance with the TDBC J-aggregate film, which is shown in Figure 3.

https://doi.org/10.1021/acs.jpcc.1c03004
J. Phys. Chem. C 2021, 125, 13024−13032

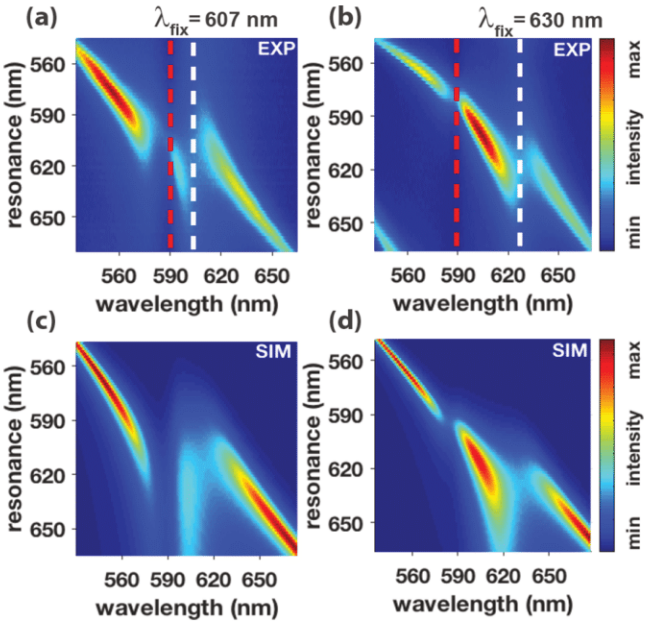

Figure 3. Experimental transmission spectra of two coupled microresonators with an additional TDBC J-aggregate film on top of a 160 nm SiO_2 spacer layer in the tunable resonator. The absorption maximum of the film is illustrated by the red dashed line. The white dashed line indicates the resonance wavelength of the fixed resonator at 607 nm in (a) and at 630 nm in (b). (c) and (d) show respective simulations for (a) and (b).

Figures 3a and 3b show experimental transmission spectra of two coupled microresonators, where the resonances of the fixed one are indicated by the white dashed line at 607 nm (a) and 630 nm (b). Hence, in the first case the resonance is closer to the absorption maximum of the TDBC molecules at 590 nm (red dashed line), while it is off resonant in the second case. The corresponding calculations based on three coupled oscillators are shown in Figures 3c,d are in good agreement with the experimental data. Similar to Figure 2, there is strong coupling between the two microresonators, which can be seen by the anticrossing at 607 and 630 nm in (a) and (b), respectively. The corresponding resonator−resonator coupling constants are $\kappa_{res-res}$ = 490 meV (a) and $\kappa_{res-res}$ = 430 meV (b). A second anticrossing dispersion can be observed close to the red dashed line, which is caused by coupling between the tunable microresonator and the TDBC J-aggregate film. Interestingly, detuning the resonance of the fixed microresonator from the TDBC J-aggregate film absorption maximum reduces coupling of the molecules to the tunable resonator from $\kappa_{res-mol}$ = 380 to 140 meV. This again shows that the coupled system needs to be considered as a whole, and strong coupling of the TDBC film to the tunable resonator can be influenced by detuning the fixed resonator.

According to the Jaynes−Cummings model, the Rabi splitting energy ΔE is proportional to the square root of the number of coherently coupled molecules n:[76]

$$\Delta E = 2\sqrt{n}\hbar g_0 \quad (1)$$

where g_0 is the coupling constant. To investigate this influence, TDBC J-aggregate films with different concentrations were deposited on the SiO_2 spacer layer. The results are presented in Figure 4.

In Figures 4a−c, thin TDBC J-aggregate films with concentrations of 10^{-2}, 10^{-3}, and 10^{-4} mol L^{-1} were spin-coated on top of a 160 nm SiO_2 spacer layer. For this experiment, the resonance of the fixed resonator (white dashed line) was slightly detuned from the absorption maximum of the TDBC J-aggregate film (red dashed line) to clearly distinguish anticrossing caused by coupling of the two resonators at 630 nm from coupling of the molecules with the resonators. The Rabi splitting caused by strong coupling of the TDBC J-aggregate molecules with the tunable resonator can be clearly observed in Figures 4a,b at 590 nm, while it is not visible anymore for the lowest concentration in Figure 4c. Corresponding simulations of the coupled systems are shown in Figures 4d−f. The damping constant of the fixed resonator is γ_{fix} = 99 meV, and the damping constants of tunable resonators γ_{tune} are 16, 17, and 17 meV in Figures 4d−f. The resonator−resonator coupling constant is $\kappa_{res-res}$ = 430, 400, and 370 meV in Figures 4d−f, respectively. As suggested by eq 1, reducing the number of coupled molecules reduces the Rabi splitting, and consequently the observed coupling of the molecules to the tunable resonator decreases from $\kappa_{res-mol}$ = 140 meV to 130 meV and 30 meV in Figures 4d−f. Figure 4g shows a similar experiment, where the resonance of the tunable resonator is kept constant (indicated by a gray dashed line in (a)) and the number of TDBC J-aggregate molecules is decreased by photobleaching. Rabi splitting due to coupling of the TDBC J-aggregate molecules with the tunable resonator can be clearly observed before photobleaching (black solid line) and decreases from 14 to 5 nm after photobleaching (black dashed line). After photobleaching, the upper polariton peak of the coupled system is hardly visible. The emission spectra before (red solid line) and after (red dashed line) photobleaching clearly show that the number of emitters was strongly reduced. The last emission spectrum is multiplied by a factor of 20 for better visibility. The whole bleaching series is shown in Figures 4h,i, where each spectrum is obtained after a 2 min bleaching interval, and in total 10 transmission and emission spectra were recorded. The emission spectra in Figure 4i are obtained directly after the acquisition of the transmission spectra in Figure 4h but before the next bleaching interval. To ensure that the spectral shift in Figure 4h is not due to a drift of the piezo actuators, transmission spectra of the coupled resonators are measured before irradiating the sample with the high-power laser, which is shown in Figure S2. These results show how the observed strong light−matter interaction can be influenced by the number of coupled molecules and illustrate the importance to control both the concentration and the spatial position of the coupled molecules to achieve efficient strong coupling.

CONCLUSIONS

In summary, we have presented the existence of two types of strong coupling existing in the same coupled system, that is, strong coupling between the optical modes of two microresonators combined with strong light−matter interaction between the coupled microresonator and TDBC J-aggregates. We have shown that the number and the spatial position of the coupled molecules have a strong impact on the coupling and damping of the coupled hybrid system. Furthermore, coupling can be tuned by adjusting the resonance of either the fixed or tunable resonator. Additionally, we have shown that the coupled system can be modeled by three damped coupled harmonic oscillators allowing to determine all important

https://doi.org/10.1021/acs.jpcc.1c03004
J. Phys. Chem. C 2021, 125, 13024−13032

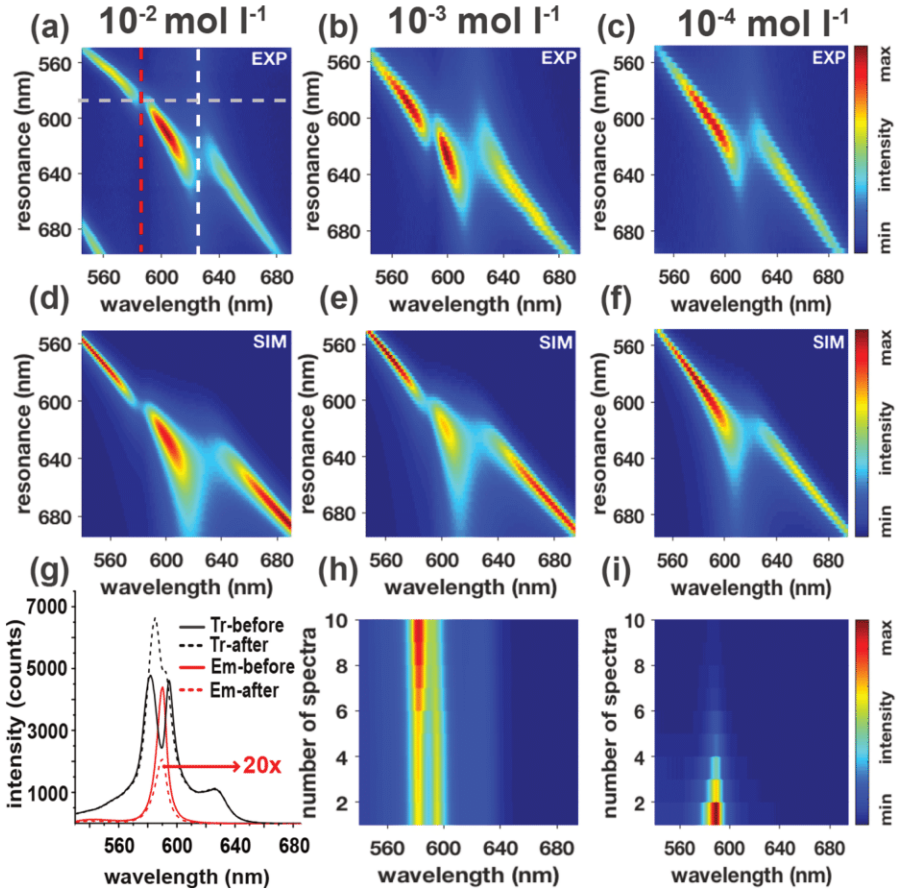

Figure 4. Experimental transmission spectra of two coupled microresonators with a thin film of TDBC J-aggregate molecules on a 160 nm SiO_2 spacer layer. The absorption maximum of the film is illustrated by the red dashed line and the white dashed line indicates the resonance wavelength of the fixed resonator at 630 nm in (a). The concentration of the TDBC J-aggregate molecules in the film is 10^{-2} mol L^{-1} in (a), 10^{-3} mol L^{-1} in (b), and 10^{-4} mol L^{-1} in (c). The Rabi splitting at 590 nm caused by strong coupling of the TDBC J-aggregate film and the tunable resonator decreases from (a) to (c). Corresponding simulations based on three coupled harmonic oscillators are shown in (d) to (f). (g) Transmission and emission spectra before (solid line) and after (dashed line) photobleaching cycles, where the resonance of the tunable resonator is kept constant (indicated by a gray dashed line in (a)). The emission spectrum after photobleaching is multiplied by a factor of 20 for better visibility. (h) Reduction of the Rabi splitting by photobleaching of the TDBC J-aggregate molecules using a laser at 470 nm. (i) Experimental emission spectra of the TDBC J-aggregate molecules corresponding to the transmission spectra shown in (h).

parameters. We find that the optimal coupling scenario is achieved with a thin film located in the center of one microresonator and when the resonance of the other resonator is matching the resonance of the coupled emitter. Interestingly, the results clearly show that the individual components of the hybrid system cannot be treated individually, but the system needs to be considered as a whole. For example, detuning the resonance of the fixed resonator reduces the coupling strength of the molecules located in the tunable resonator without a physical change of this resonator. Consequently, the system presented here is an excellent example where strong coupling between optical modes and strong light−matter coupling is combined in a single hybrid system.

These results could have important consequences for applications in optoelectronics; for example, let us assume that coupling of an emitter and a receiver over a large spatial separation shall be achieved via the optical modes of several intermediate resonators. We have shown that already a very thin film in the center of the first resonator is sufficient to achieve efficient coupling of the emitter to the optical resonator mode. However, not only efficient coupling to the resonator is needed, but also the geometry of the intermediate resonators needs to be carefully adapted to the optical properties of the emitter to achieve efficient transfer to the receiver. Additionally, the results presented here could also be exploited in the field of polaritonic chemistry, where one resonator could be a fixed and robust reaction resonator, and the optical mode density, and hence the coupling strength of the reactant, could be adjusted by an adjacent tuning resonator.

■ ASSOCIATED CONTENT

Supporting Information

The Supporting Information is available free of charge at https://pubs.acs.org/doi/10.1021/acs.jpcc.1c03004.

Details of the theoretical coupled harmonic oscillator model and used parameters to model two coupled microresonators and the molecules located in the tunable resonator; theoretical and experimental transmission spectra of two coupled microresonators (PDF)

■ AUTHOR INFORMATION

Corresponding Authors

Frank Wackenhut − *Institute of Physical and Theoretical Chemistry, Eberhard Karls University, 72076 Tübingen,*

https://doi.org/10.1021/acs.jpcc.1c03004
J. Phys. Chem. C 2021, 125, 13024−13032

Germany; orcid.org/0000-0001-6554-6600;
Email: frank.wackenhut@uni-tuebingen.de

Alfred J. Meixner − *Institute of Physical and Theoretical Chemistry, Eberhard Karls University, 72076 Tübingen, Germany;* orcid.org/0000-0002-0187-2906;
Email: alfred.meixner@uni-tuebingen.de

Authors

Saeed Nosrati − *Institute of Physical and Theoretical Chemistry, Eberhard Karls University, 72076 Tübingen, Germany*

Tim Rammler − *Institute of Physical and Theoretical Chemistry, Eberhard Karls University, 72076 Tübingen, Germany*

Complete contact information is available at:
https://pubs.acs.org/10.1021/acs.jpcc.1c03004

Notes

The authors declare no competing financial interest.

■ ACKNOWLEDGMENTS

The authors gratefully acknowledge funding by the German Research Foundation (DFG, ME 1600/13-3).

■ REFERENCES

(1) Lidzey, D. G.; Bradley, D. D. C.; Virgili, T.; Armitage, A.; Skolnick, M. S.; Walker, S. Room temperature polariton emission from strongly coupled organic semiconductor Microcavities. *Phys. Rev. Lett.* **1999**, *82* (16), 3316−3319.

(2) Junginger, A.; Wackenhut, F.; Stuhl, A.; Blendinger, F.; Brecht, M.; Meixner, A. J. Tunable strong coupling of two adjacent optical $\lambda/2$ Fabry-Pérot microresonators. *Opt. Express* **2020**, *28* (1), 485−493.

(3) Purcell, E. M.; Torrey, H. C.; Pound, R. V. Resonance absorption by nuclear magnetic moments in a solid. *Phys. Rev.* **1946**, *69* (1−2), 37.

(4) Agranovich, V.; Litinskaia, M.; Lidzey, D. Microcavity polaritons in materials with weak intermolecular interaction. *Phys. Status Solidi B* **2002**, *234* (1), 130−138.

(5) Chizhik, A.; Schleifenbaum, F.; Gutbrod, R.; Chizhik, A.; Khoptyar, D.; Meixner, A. J.; Enderlein, J. Tuning the fluorescence emission spectra of a single molecule with a variable optical subwavelength metal microcavity. *Phys. Rev. Lett.* **2009**, *102* (7), 073002.

(6) Chizhik, A. I.; Chizhik, A. M.; Kern, A. M.; Schmidt, T.; Potrick, K.; Huisken, F.; Meixner, A. J. Measurement of vibrational modes in single SiO_2 nanoparticles using a tunable metal resonator with optical subwavelength dimensions. *Phys. Rev. Lett.* **2012**, *109* (22), 223902.

(7) Konrad, A.; Trost, A.-L.; Skandary, S.; Hussels, M.; Meixner, A. J.; Karapetyan, N. V.; Brecht, M. Manipulating the excitation transfer in Photosystem I using a Fabry-Perot metal resonator with optical subwavelength dimensions. *Phys. Chem. Chem. Phys.* **2014**, *16* (13), 6175−6181.

(8) Skolnick, M.; Fisher, T.; Whittaker, D. Strong coupling phenomena in quantum microcavity structures. *Semicond. Sci. Technol.* **1998**, *13* (7), 645.

(9) Koenderink, A. F. On the use of Purcell factors for plasmon antennas. *Opt. Lett.* **2010**, *35* (24), 4208−4210.

(10) Masenelli, B.; Gagnaire, A.; Berthelot, L.; Tardy, J.; Joseph, J. Controlled spontaneous emission of a tri (8-hydroxyquinoline) aluminum layer in a microcavity. *J. Appl. Phys.* **1999**, *85* (6), 3032−3037.

(11) Kern, A. M.; Zhang, D.; Brecht, M.; Chizhik, A. I.; Failla, A. V.; Wackenhut, F.; Meixner, A. J. Enhanced single-molecule spectroscopy in highly confined optical fields: from $\lambda/2$-Fabry-Pérot resonators to plasmonic nano-antennas. *Chem. Soc. Rev.* **2014**, *43* (4), 1263−1286.

(12) Steiner, M.; Schleifenbaum, F.; Stupperich, C.; Virgilio Failla, A.; Hartschuh, A.; Meixner, A. J. Microcavity controlled single molecule fluorescence. *ChemPhysChem* **2005**, *6* (10), 2190−2196.

(13) Canet-Ferrer, J.; Martínez, L. J.; Prieto, I.; Alen, B.; Munoz-Matutano, G.; Fuster, D.; Gonzalez, Y.; Dotor, M. L.; Gonzalez, L.; Postigo, P. A.; Martínez-Pastor, J. P. Purcell effect in photonic crystal microcavities embedding InAs/InP quantum wires. *Opt. Express* **2012**, *20* (7), 7901−7914.

(14) Noda, S.; Fujita, M.; Asano, T. Spontaneous-emission control by photonic crystals and nanocavities. *Nat. Photonics* **2007**, *1* (8), 449−458.

(15) Cang, H.; Liu, Y.; Wang, Y.; Yin, X.; Zhang, X. Giant suppression of photobleaching for single molecule detection via the Purcell effect. *Nano Lett.* **2013**, *13* (12), 5949−5953.

(16) Konrad, A.; Metzger, M.; Kern, A. M.; Brecht, M.; Meixner, A. J. Controlling the dynamics of Förster resonance energy transfer inside a tunable sub-wavelength Fabry-Pérot-resonator. *Nanoscale* **2015**, *7* (22), 10204−10209.

(17) Pelton, M. Modified spontaneous emission in nanophotonic structures. *Nat. Photonics* **2015**, *9* (7), 427−435.

(18) Schleifenbaum, F.; Kern, A. M.; Konrad, A.; Meixner, A. J. Dynamic control of Förster energy transfer in a photonic environment. *Phys. Chem. Chem. Phys.* **2014**, *16* (25), 12812−12817.

(19) Stefani, F. D.; Vasilev, K.; Bocchio, N.; Gaul, F.; Pomozzi, A.; Kreiter, M. Photonic mode density effects on single-molecule fluorescence blinking. *New J. Phys.* **2007**, *9* (2), 21.

(20) Wientjes, E.; Renger, J.; Curto, A. G.; Cogdell, R.; Van Hulst, N. F. Strong antenna-enhanced fluorescence of a single light-harvesting complex shows photon antibunching. *Nat. Commun.* **2014**, *5* (1), 1−7.

(21) Hopfield, J. J. Theory of the contribution of excitons to the complex dielectric constant of crystals. *Phys. Rev.* **1958**, *112* (5), 1555−1567.

(22) Atlasov, K. A.; Karlsson, K. F.; Rudra, A.; Dwir, B.; Kapon, E. Wavelength and loss splitting in directly coupled photonic-crystal defect microcavities. *Opt. Express* **2008**, *16* (20), 16255−16264.

(23) Dovzhenko, D. S.; Ryabchuk, S. V.; Rakovich, Y. P.; Nabiev, I. R. Light-matter interaction in the strong coupling regime: configurations, conditions, and applications. *Nanoscale* **2018**, *10* (8), 3589−3605.

(24) Norris, T. B.; Rhee, J. K.; Sung, C. Y.; Arakawa, Y.; Nishioka, M.; Weisbuch, C. Time-resolved vacuum Rabi oscillations in a semiconductor quantum microcavity. *Phys. Rev. B: Condens. Matter Mater. Phys.* **1994**, *50* (19), 14663−14666.

(25) Herrera, F.; Spano, F. C. Cavity-controlled chemistry in molecular ensembles. *Phys. Rev. Lett.* **2016**, *116* (23), 238301.

(26) Lather, J.; Bhatt, P.; Thomas, A.; Ebbesen, T. W.; George, J. Cavity catalysis by cooperative vibrational strong coupling of reactant and solvent molecules. *Angew. Chem., Int. Ed.* **2019**, *58* (31), 10635−10638.

(27) Thomas, A.; Jayachandran, A.; Lethuillier-Karl, L.; Vergauwe, R. M.; Nagarajan, K.; Devaux, E.; Genet, C.; Moran, J.; Ebbesen, T. W. Ground state chemistry under vibrational strong coupling: dependence of thermodynamic parameters on the Rabi splitting energy. *Nanophotonics* **2020**, *9* (2), 249−255.

(28) Kapon, E.; Katz, J.; Yariv, A. Supermode analysis of phase-locked arrays of semiconductor lasers. *Opt. Lett.* **1984**, *9* (4), 125−127.

(29) Guan, C.; Yuan, L.; Shi, J. Supermode analysis of multicore photonic crystal fibers. *Opt. Commun.* **2010**, *283* (13), 2686−2689.

(30) Zhou, J. Analytical formulation of super-modes inside multi-core fibers with circularly distributed cores. *Opt. Express* **2014**, *22* (1), 673−688.

(31) Atlasov, K. A.; Rudra, A.; Dwir, B.; Kapon, E. Large mode splitting and lasing in optimally coupled photonic-crystal microcavities. *Opt. Express* **2011**, *19* (3), 2619−2625.

(32) Cai, T.; Bose, R.; Solomon, G. S.; Waks, E. Controlled coupling of photonic crystal cavities using photochromic tuning. *Appl. Phys. Lett.* **2013**, *102* (14), 141118.

(33) Chalcraft, A.; Lam, S.; Jones, B.; Szymanski, D.; Oulton, R.; Thijssen, A.; Skolnick, M.; Whittaker, D.; Krauss, T.; Fox, A. Mode structure of coupled L3 photonic crystal cavities. *Opt. Express* **2011**, *19* (6), 5670−5675.
(34) Coles, D. M.; Somaschi, N.; Michetti, P.; Clark, C.; Lagoudakis, P. G.; Savvidis, P. G.; Lidzey, D. G. Polariton-mediated energy transfer between organic dyes in a strongly coupled optical microcavity. *Nat. Mater.* **2014**, *13* (7), 712−719.
(35) Dovzhenko, D.; Mochalov, K.; Vaskan, I.; Kryukova, I.; Rakovich, Y.; Nabiev, I. Polariton-assisted splitting of broadband emission spectra of strongly coupled organic dye excitons in tunable optical microcavity. *Opt. Express* **2019**, *27* (4), 4077−4089.
(36) Hobson, P. A.; Barnes, W. L.; Lidzey, D.; Gehring, G.; Whittaker, D.; Skolnick, M.; Walker, S. Strong exciton-photon coupling in a low-Q all-metal mirror microcavity. *Appl. Phys. Lett.* **2002**, *81* (19), 3519−3521.
(37) Johnson, S.; Dolan, P R.; Grange, T.; Trichet, A. A. P.; Hornecker, G.; Chen, Y. C.; Weng, L.; Hughes, G. M.; Watt, A. A. R.; Auffeves, A.; Smith, J. M. Tunable cavity coupling of the zero phonon line of a nitrogen-vacancy defect in diamond. *New J. Phys.* **2015**, *17* (12), 122003.
(38) Shalabney, A.; George, J.; Hutchison, J.; Pupillo, G.; Genet, C.; Ebbesen, T. W. Coherent coupling of molecular resonators with a microcavity mode. *Nat. Commun.* **2015**, *6* (1), 5981.
(39) Thompson, J.; Zwickl, B.; Jayich, A.; Marquardt, F.; Girvin, S.; Harris, J. Strong dispersive coupling of a high-finesse cavity to a micromechanical membrane. *Nature* **2008**, *452* (7183), 72−75.
(40) Wang, D.; Kelkar, H.; Martin-Cano, D.; Utikal, T.; Götzinger, S.; Sandoghdar, V. Coherent coupling of a single molecule to a scanning Fabry-Perot microcavity. *Phys. Rev. X* **2017**, *7* (2), 021014.
(41) Pellegrino, D.; Pagliano, F.; Genco, A.; Petruzzella, M.; Van Otten, F.; Fiore, A. Deterministic control of radiative processes by shaping the mode field. *Appl. Phys. Lett.* **2018**, *112* (16), 161110.
(42) Samutpraphoot, P.; Đorđević, T.; Ocola, P. L.; Bernien, H.; Senko, C.; Vuletić, V.; Lukin, M. D. Strong coupling of two individually controlled atoms via a nanophotonic cavity. *Phys. Rev. Lett.* **2020**, *124* (6), 063602.
(43) Yoshie, T.; Scherer, A.; Hendrickson, J.; Khitrova, G.; Gibbs, H.; Rupper, G.; Ell, C.; Shchekin, O.; Deppe, D. Vacuum Rabi splitting with a single quantum dot in a photonic crystal nanocavity. *Nature* **2004**, *432* (7014), 200−203.
(44) Hennessy, K.; Badolato, A.; Winger, M.; Gerace, D.; Atatüre, M.; Gulde, S.; Fält, S.; Hu, E. L.; Imamoßlu, A. Quantum nature of a strongly coupled single quantum dot-cavity system. *Nature* **2007**, *445* (7130), 896−899.
(45) Reithmaier, J. P.; Sęk, G.; Löffler, A.; Hofmann, C.; Kuhn, S.; Reitzenstein, S.; Keldysh, L.; Kulakovskii, V.; Reinecke, T.; Forchel, A. Strong coupling in a single quantum dot-semiconductor microcavity system. *Nature* **2004**, *432* (7014), 197−200.
(46) Peter, E.; Senellart, P.; Martrou, D.; Lemaître, A.; Hours, J.; Gérard, J. M.; Bloch, J. Exciton-photon strong-coupling regime for a single quantum dot embedded in a microcavity. *Phys. Rev. Lett.* **2005**, *95* (6), 067401.
(47) Wang, J.; Yin, Y.; Hao, Q.; Zhang, Y.; Ma, L.; Schmidt, O. G. Strong coupling in a photonic molecule formed by trapping a microsphere in a microtube cavity. *Adv. Opt. Mater.* **2018**, *6* (1), 1700842.
(48) Baranov, D. G.; Munkhbat, B.; Länk, N. O.; Verre, R.; Käll, M.; Shegai, T. Circular dichroism mode splitting and bounds to its enhancement with cavity-plasmon-polaritons. *Nanophotonics* **2020**, *9* (2), 283−293.
(49) Chikkaraddy, R.; De Nijs, B.; Benz, F.; Barrow, S. J.; Scherman, O. A.; Rosta, E.; Demetriadou, A.; Fox, P.; Hess, O.; Baumberg, J. J. Single-molecule strong coupling at room temperature in plasmonic nanocavities. *Nature* **2016**, *535* (7610), 127−130.
(50) Konrad, A.; Kern, A. M.; Brecht, M.; Meixner, A. J. Strong and coherent coupling of a plasmonic nanoparticle to a subwavelength Fabry-Pérot resonator. *Nano Lett.* **2015**, *15* (7), 4423−4428.
(51) Pelton, M.; Storm, S. D.; Leng, H. Strong coupling of emitters to single plasmonic nanoparticles: exciton-induced transparency and Rabi splitting. *Nanoscale* **2019**, *11* (31), 14540−14552.
(52) Törmä, P.; Barnes, W. L. Strong coupling between surface plasmon polaritons and emitters: a review. *Rep. Prog. Phys.* **2015**, *78* (1), 013901.
(53) Vasa, P.; Lienau, C. Strong light-matter interaction in quantum emitter/metal hybrid nanostructures. *ACS Photonics* **2018**, *5* (1), 2−23.
(54) Bisht, A.; Cuadra, J.; Wersäll, M.; Canales, A.; Antosiewicz, T. J.; Shegai, T. Collective strong light-matter coupling in Hierarchical microcavity-plasmon-exciton systems. *Nano Lett.* **2019**, *19* (1), 189−196.
(55) Bayer, M.; Gutbrod, T.; Reithmaier, J.; Forchel, A.; Reinecke, T.; Knipp, P.; Dremin, A.; Kulakovskii, V. Optical modes in photonic molecules. *Phys. Rev. Lett.* **1998**, *81* (12), 2582.
(56) Galbiati, M.; Ferrier, L.; Solnyshkov, D. D.; Tanese, D.; Wertz, E.; Amo, A.; Abbarchi, M.; Senellart, P.; Sagnes, I.; Lemaitre, A.; Galopin, E.; Malpuech, G.; Bloch, J. Polariton condensation in photonic molecules. *Phys. Rev. Lett.* **2012**, *108* (12), 126403.
(57) Rakovich, Y. P.; Donegan, J. F. Photonic atoms and molecules. *Laser Photonics Rev.* **2010**, *4* (2), 179−191.
(58) Zhang, M.; Wang, C.; Hu, Y.; Shams-Ansari, A.; Ren, T.; Fan, S.; Lončar, M. Electronically programmable photonic molecule. *Nat. Photonics* **2019**, *13* (1), 36−40.
(59) Plumhof, J. D.; Stöferle, T.; Mai, L.; Scherf, U.; Mahrt, R. F. Room-temperature Bose−Einstein condensation of cavity exciton-polaritons in a polymer. *Nat. Mater.* **2014**, *13* (3), 247−252.
(60) Takada, N.; Kamata, T.; Bradley, D. D. Polariton emission from polysilane-based organic microcavities. *Appl. Phys. Lett.* **2003**, *82* (12), 1812−1814.
(61) Christmann, G.; Butté, R.; Feltin, E.; Mouti, A.; Stadelmann, P. A.; Castiglia, A.; Carlin, J.-F.; Grandjean, N. Large vacuum Rabi splitting in a multiple quantum well GaN-based microcavity in the strong-coupling regime. *Phys. Rev. B: Condens. Matter Mater. Phys.* **2008**, *77* (8), 085310.
(62) Houdré, R.; Weisbuch, C.; Stanley, R. P.; Oesterle, U.; Pellandini, P.; Ilegems, M. Measurement of cavity-polariton dispersion curve from angle-resolved photoluminescence experiments. *Phys. Rev. Lett.* **1994**, *73* (15), 2043−2046.
(63) Pradeesh, K.; Baumberg, J.; Prakash, G. V. Strong exciton-photon coupling in inorganic-organic multiple quantum wells embedded low-Q microcavity. *Opt. Express* **2009**, *17* (24), 22171−22178.
(64) Weisbuch, C.; Nishioka, M.; Ishikawa, A.; Arakawa, Y. Observation of the coupled exciton-photon mode splitting in a semiconductor quantum microcavity. *Phys. Rev. Lett.* **1992**, *69* (23), 3314−3317.
(65) Groß, H.; Hamm, J. M.; Tufarelli, T.; Hess, O.; Hecht, B. Near-field strong coupling of single quantum dots. *Sci. Adv.* **2018**, *4* (3), No. eaar4906.
(66) Agranovich, V.; Litinskaia, M.; Lidzey, D. G. Cavity polaritons in microcavities containing disordered organic semiconductors. *Phys. Rev. B: Condens. Matter Mater. Phys.* **2003**, *67* (8), 085311.
(67) Lidzey, D. G.; Bradley, D.; Skolnick, M.; Virgili, T.; Walker, S.; Whittaker, D. Strong exciton-photon coupling in an organic semiconductor microcavity. *Nature* **1998**, *395* (6697), 53−55.
(68) Nagarajan, K.; George, J.; Thomas, A.; Devaux, E.; Chervy, T.; Azzini, S.; Joseph, K.; Jouaiti, A.; Hosseini, M. W.; Kumar, A.; et al. Conductivity and photoconductivity of a p-Type organic semiconductor under ultrastrong coupling. *ACS Nano* **2020**, *14* (8), 10219−10225.
(69) Bonnand, C.; Bellessa, J.; Plenet, J. Properties of surface plasmons strongly coupled to excitons in an organic semiconductor near a metallic surface. *Phys. Rev. B: Condens. Matter Mater. Phys.* **2006**, *73* (24), 245330.
(70) George, J.; Wang, S.; Chervy, T.; Canaguier-Durand, A.; Schaeffer, G.; Lehn, J.-M.; Hutchison, J. A.; Genet, C.; Ebbesen, T. W.

Ultra-strong coupling of molecular materials: spectroscopy and dynamics. *Faraday Discuss.* **2015**, *178* (0), 281−294.
(71) Kang, E. S. H.; Chen, S.; Sardar, S.; Tordera, D.; Armakavicius, N.; Darakchieva, V.; Shegai, T.; Jonsson, M. P. Strong plasmon-exciton coupling with directional absorption features in optically thin hybrid nanohole metasurfaces. *ACS Photonics* **2018**, *5* (10), 4046−4055.
(72) Munkhbat, B.; Wersäll, M.; Baranov, D. G.; Antosiewicz, T. J.; Shegai, T. Suppression of photo-oxidation of organic chromophores by strong coupling to plasmonic nanoantennas. *Sci. Adv.* **2018**, *4* (7), No. eaas9552.
(73) Tischler, J. R.; Bradley, M. S.; Zhang, Q.; Atay, T.; Nurmikko, A.; Bulović, V. Solid state cavity QED: Strong coupling in organic thin films. *Org. Electron.* **2007**, *8* (2−3), 94−113.
(74) Vasista, A. B.; Barnes, W. L. Molecular monolayer strong coupling in dielectric soft microcavities. *Nano Lett.* **2020**, *20* (3), 1766−1773.
(75) Gentile, M. J.; Núñez-Sánchez, S.; Barnes, W. L. Optical field-enhancement and subwavelength field-confinement using excitonic nanostructures. *Nano Lett.* **2014**, *14* (5), 2339−2344.
(76) Fox, M.; *Quantum Optics: An Introduction*; OUP: Oxford, 2006; Vol. *15*.

https://doi.org/10.1021/acs.jpcc.1c03004
J. Phys. Chem. C 2021, 125, 13024−13032

Supporting information:

Combining optical strong mode coupling with polaritonic coupling in a λ/2 Fabry Pérot microresonator

Saeed Nosrati,[1] Tim Rammler,[1] Alfred J. Meixner[1,*] and Frank Wackenhut[1,*]

[1]*Institute of Physical and Theoretical Chemistry, Eberhard Karls University, 72076 Tübingen, Germany*

Corresponding Author

E-mail: frank.wackenhut@uni-tuebingen.de

E-mail:alfred.meixner@uni-tuebingen.de

Coupled harmonic oscillator model

The calculations presented in the main text are based on three coupled harmonic oscillators. The motion x(t) of these oscillators can be described by three coupled differential equations, which can be written as:

$$\ddot{x}_{tune}(t) + \gamma_{tune}\dot{x}_{tune}(t) + \omega_{tune}^2 x_{tune}(t) + \kappa_{res-res}x_{fix}(t) + \kappa_{res-mol}x_{mol}(t) = 0 \quad (1)$$

$$\ddot{x}_{fix}(t) + \gamma_{fix}\dot{x}_{fix}(t) + \omega_{fix}^2 x_{fix}(t) + \kappa_{res-res}x_{tune}(t) = 0 \quad (2)$$

$$\ddot{x}_{mol}(t) + \gamma_{mol}\dot{x}_{mol}(t) + \omega_{mol}^2 x_{mol}(t) + \kappa_{res-mol}x_{tune}(t) = 0 \quad (3)$$

These equations are used to model three coupled harmonic oscillators and allow energy exchange, and thus coupling, between them. Here, equation (1) describes the motion of the oscillator $x_{tune}(t)$ in the time domain and represents the tunable microresonator. Similarly, the temporal behavior of the fixed resonator $x_{fix}(t)$ described by equation (2) and equation (3) is used to model the TDBC molecules $x_{mol}(t)$. The properties of the tunable/fixed microresonators and the molecules are described by the damping constants γ_{tune}, γ_{fix} and γ_{mol} and the respective resonance frequencies are ω_{tune}, ω_{fix} and ω_{mol}. Tuning of the microresonator can then be achieved by varying its resonance frequency. Coupling between these oscillators is included by terms proportional to κ, which allow energy exchange between the individual oscillators. $\kappa_{res-res}$ is the constant describing the coupling of the tunable and the fixed microresonator, while $\kappa_{res-mol}$ allows to couple the TDBC molecules to the tunable resonator. In this scenario, we assume that the molecules directly couple to the microresonator in which they are located, *i.e.* the tunable one, and can only indirectly couple to the fixed microresonator *via* the tunable one. Hence, energy is only directly exchanged between the tunable and the fixed microresonator and between the molecules and the tunable resonator. The damping constant γ_{mol} and resonance frequency ω_{mol} of the TDBC molecules are determined from their absorption spectrum outside of the resonator and are kept constant for all simulations. Hence, to fit this model to the

experimental data only parameters describing the microresonator, *i.e.* their damping and resonance frequency, and the two coupling constants are varied. Solving these equations numerically gives the temporal response of all three oscillators $\mathrm{x}_{tune}(\mathrm{t})$, $\mathrm{x}_{fix}(\mathrm{t})$ and $\mathrm{x}_{mol}(\mathrm{t})$ and the power spectral density, which is the corresponding spectrum, is calculated by Fourier transformation of $\mathrm{x}(\mathrm{t})$. The experimental configuration dictates the excitation of the coupled system, since it is excited with a white light LED from top. This leads to the situation, where mainly the tunable microresonator is directly excited with an incoherent light source, which can be taken into account by modifying the starting condition of the tunable resonator and setting it to $\mathrm{x}_{tune}(0) = 1$. Additionally, the experimental configuration only allows to observe the transmission of the whole system and the detected signal is collected from below. In this configuration, the transmission spectra can be modeled by the response of the fixed resonator $\mathrm{x}_{fix}(\mathrm{t})$, which we have already shown in.[1]

All transmission spectra presented in the main text are the Fourier transform of $\mathrm{x}_{fix}(\mathrm{t})$ and corresponding parameters used for the calculations in the main text are given in Table S1.

	Figure. 1	Figure. 2					
TDBC on	Empty	SiO_2:50	SiO_2:70	SiO_2:100	SiO_2:130	SiO_2:160	SiO_2:185
Simulated parameters							
λ_{fixed} (nm)	600	592	592	600	605	607	590
λ_{tune} (nm)	695-510	670-520	665-525	665-520	665-520	665-520	665-520
λ_{mol} (nm)	-	590	590	590	590	590	590
γ_{fixed} (meV)	100	60	70	88	93	93	98
γ_{tune} (meV)	17	42	40	30	20	20	20
γ_{mol} (meV)	-	60	60	60	60	60	60
$\kappa_{res\text{-}res}$ (meV)	530	520	500	470	450	490	490
$\kappa_{res\text{-}mol}$ (meV)	-	250	380	410	450	380	100
	Figure. 3		Figure. 4				
TDBC on	SiO_2:160 λ_{fixed}: 607	SiO_2:160 λ_{fixed}: 630	SiO_2:160 TDBC: 10^{-2}	SiO_2:160 TDBC: 10^{-3}	SiO_2:160 TDBC: 10^{-4}		
Simulated parameters							
λ_{fixed} (nm)	607	630	630	617	613		
λ_{tune} (nm)	665-535	665-535	690-545	690-545	690-545		
λ_{mol} (nm)	590	590	590	590	590		
γ_{fixed} (meV)	93	99	99	99	99		
γ_{tune} (meV)	20	16	16	17	17		
γ_{mol} (meV)	60	60	60	60	60		
$\kappa_{res\text{-}res}$ (meV)	490	430	430	400	370		
$\kappa_{res\text{-}mol}$ (meV)	380	140	140	130	30		

Table. S1. Three damped coupled harmonic oscillators parameters to model the two coupled microresonators and the molecules located in the tunable resonator.

As mentioned in the main text, the change of the damping constants γ_{tune} and γ_{fix} can be directly seen in Figure 2. This influence of the damping constants on the anticrossing dispersion is illustrated in Figure S1.

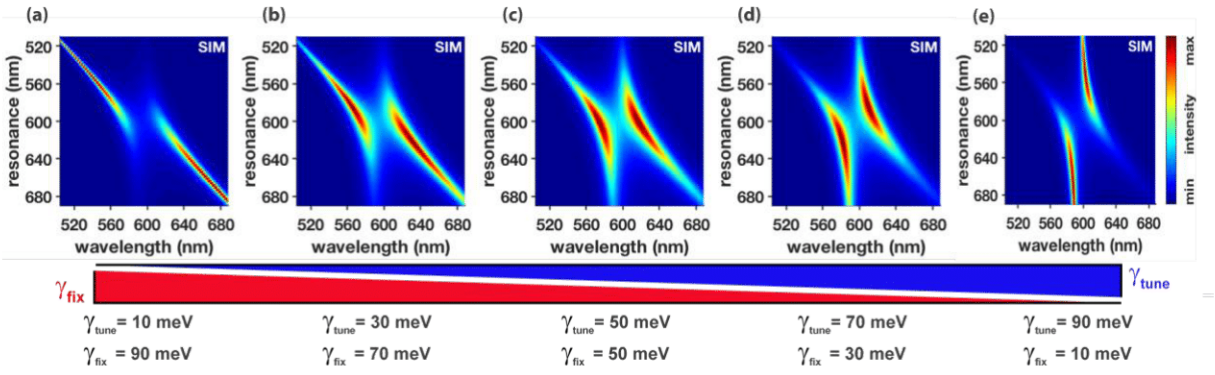

Figure S1. (a)-(e) Transmission spectra modeled by two damped coupled harmonic oscillators with variable damping constants for the fixed and tunable resonator.

Figure S1(a) to S1(e) show the transmission spectra modeled by two damped coupled harmonic oscillators, where the damping constants for the fixed and tunable resonator are changed between 10 meV and 90 meV, while keeping the total damping of the system (their sum) constant. For these calculations the coupling constant between the two oscillators and the resonance of the fixed resonator are kept constant. It can be seen, that if the damping of the tunable microresonator is smaller than the one of the fixed resonator, see Figure S1 (a), the energy is preferably stored in the tunable resonator and is dissipated fast in the fixed one. The situation is reversed in Figure S1(e) when the damping constant of the fixed resonator is smaller. Figure S1(c) illustrates the scenario, where the damping of both resonators is the same and the energy is equally shared between them.

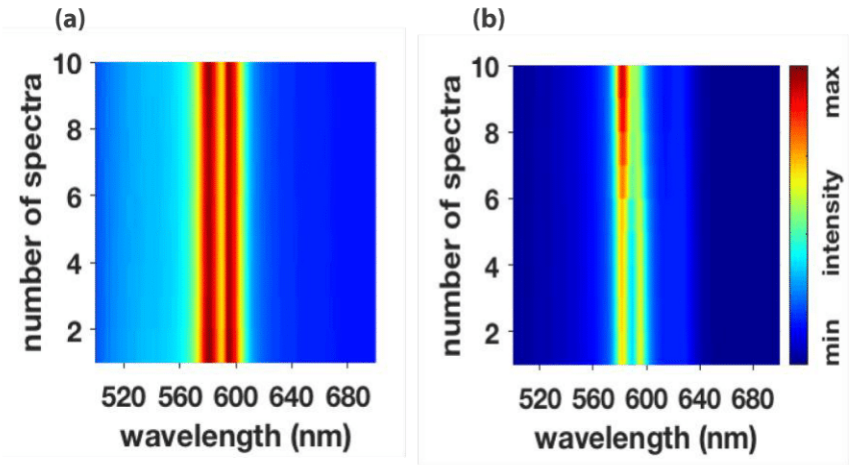

Figure S2. Experimental transmission spectra of two coupled microresonators consisting of a thin TDBC J-aggregate film before illuminating high laser power to the sample in (a) and after illuminating in (b)

Figure S2 presents the transmission spectra of the coupled microresonators with a thin TDBC J-aggregate film, where the resonance of the tunable microresonator is fixed at 590 nm. The transmission spectra in Figure 4(a) are acquired before starting photobleaching experiment to ensure that there is no drift of the piezo actuator. The spectral shift in Figure 4(b) is caused by photobleaching of the TDBC J-aggregate molecules with high power laser.

(1) Junginger, A.; Wackenhut, F.; Stuhl, A.; Blendinger, F.; Brecht, M.; Meixner, A. J., Tunable strong coupling of two adjacent optical λ/2 Fabry-Pérot microresonators. *Opt. Express* **2020,** *28* (1), 485-493.

ACS NANO

www.acsnano.org

ARTICLE

Periodic Fluorescence Variations of CdSe Quantum Dots Coupled to Aryleneethynylenes with Aggregation-Induced Emission

Krishan Kumar, Jonas Hiller, Markus Bender, Saeed Nosrati, Quan Liu, Marc Edelmann, Steffen Maier, Tim Rammler, Frank Wackenhut, Alfred J. Meixner, Kai Braun, Uwe H. F. Bunz,* and Marcus Scheele*

Cite This: *ACS Nano* 2021, 15, 480–488

Read Online

ACCESS | Metrics & More | Article Recommendations | Supporting Information

ABSTRACT: **CdSe nanocrystals and aggregates of an aryleneethynylene derivative are assembled into a hybrid thin film with dual fluorescence from both fluorophores. Under continuous excitation, the nanocrystals and the molecules exhibit anticorrelated fluorescence intensity variations, which become periodic at low temperature. We attribute this to a structure-dependent aggregation-induced emission of the aryleneethynylene derivative, which impacts the rate of excitation energy transfer between the molecules and nanocrystals. This work highlights that combining semiconductor nanocrystals with molecular aggregates, which exhibit aggregation-induced emission, can result in emerging optical properties.**

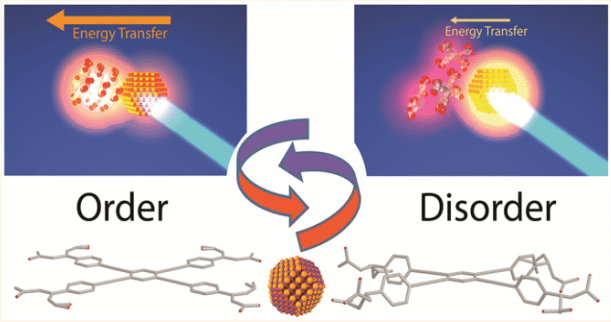

KEYWORDS: *quantum dots, organic π-systems, aggregation-induced emission, energy transfer, fluorophores*

Aggregation-induced emission (AIE) refers to enhanced and often red-shifted fluorescence of luminophores upon formation of aggregates from solution.[1] The prototypical example are organic π-systems with a large degree of structural twisting in the ground state, for example, tetraphenylethylenes[2] or aryleneethynylenes,[3] which exhibit high torsion angles between the central C=C or C≡C bond and the sterically demanding phenyl substituents. Photoexcitation weakens the double or triple bond and reduces the torsion angles with the phenyl rings.[4−6] Relaxation from this state occurs *via* three pathways: (1) radiative recombination, (2) intramolecular motion (mostly detwisting of the C=C or C≡C bond), or (3) photochemical reaction to an intermediate. AIE occurs if pathways (2) and (3) are significantly inhibited in the aggregates due to restriction of intramolecular motion.[7] The degree of this restriction depends on the solid-state structure and, thus, on temperature-induced structural transitions.[5,8,9] These transitions may be triggered photothermally *via* sufficiently strong photoexcitation and the concomitant rise in temperature.[10,11] The photoexcitation can occur either directly *via* resonant excitation of the aggregates or indirectly by excitation energy transfer (EET) *via* a sensitizer.[12,13] Inorganic semiconductor nanocrystals (NCs) are ideal as sensitizers, as they exhibit much larger extinction coefficients than most organic dyes and strong absorption at above-band gap photon energies.[14] EET between NCs and organic π-systems has been extensively investigated in both solution and solid state. However, to the best of our knowledge, no research has been committed specifically toward involving AIE molecules.[15−21]

Here, we combine aggregates of the aryleneethynylene derivative AE **1** (Figure 1a) with pronounced AIE together with CdSe NCs into a hybrid nanocomposite. We show that EET between the NCs and the molecular aggregates in combination with photothermally-induced structural changes lead to temporal fluctuations of the NC fluorescence and the degree of AIE in the aggregates, which are anticorrelated to

Received: June 19, 2020
Accepted: December 31, 2020
Published: January 13, 2021

https://dx.doi.org/10.1021/acsnano.0c05121
ACS Nano 2021, 15, 480–488

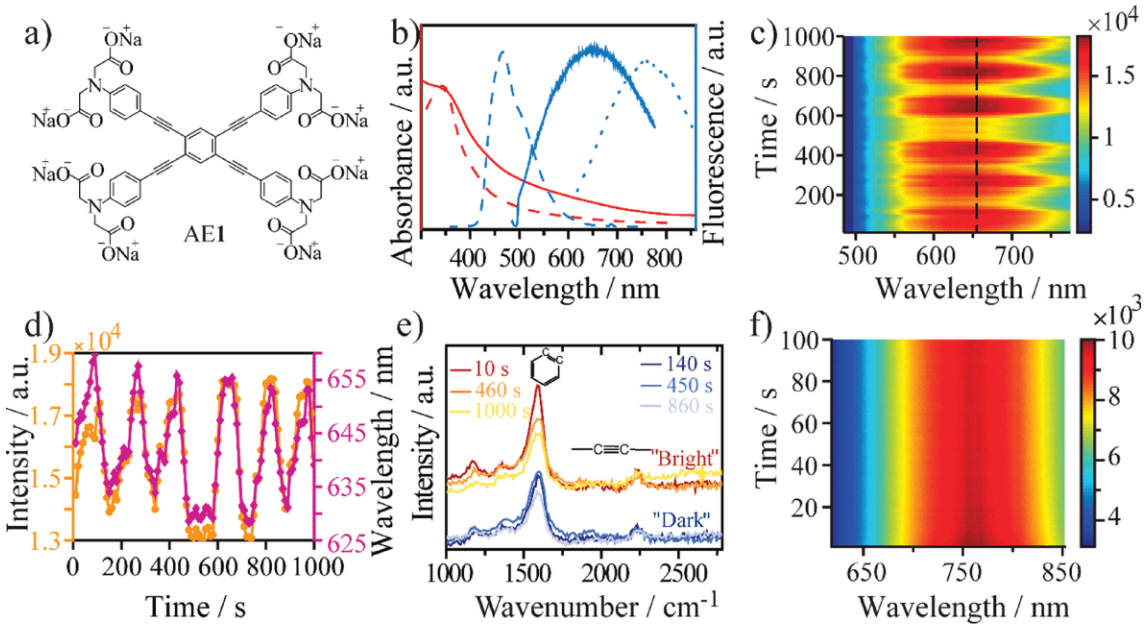

Figure 1. (a) Structural formula of the arylenephenylene derivative AE 1. (b) Optical properties of AE 1. Absorption in methanol (red dashed line), thin-film absorption (red solid line), fluorescence in methanol (blue dashed line, excitation at 350 nm), thin-film fluorescence (blue solid line, 488 nm excitation), and thin-film fluorescence at 160 K (blue dotted line, 488 nm excitation). (c) Thin-film fluorescence during 1000 s of continuous excitation at 488 nm with a binning time of 1 s. (d) Line profile (orange solid) and wavelength maxima position (purple) of (c) extracted by fitting Gaussian functions. (e) Raman spectra taken during "bright" periods (at 10, 460, and 1000 s) and "dark" periods (at 140, 450, and 860 s). Bands attributed to the phenyl-C═C breathing and the C≡C stretching mode are indicated. (f) Thin-film fluorescence at 160 K during 100 s of continuous excitation at 488 nm.

each other. At low temperature, these intensity fluctuations become periodic, and the periodicity correlates with the laser power. Hybrid materials with these properties may be interesting for application in nanothermometry.

RESULTS AND DISCUSSION

In methanolic solution, AE **1** shows a broad absorption with a maximum at 350 nm, including a small low-energy tail as well as a narrow, weak emission at 480 nm (Figure 1b, red and blue dashed lines, respectively). In the solid state, aggregates of AE **1** exhibit pronounced low-energy tailing of the absorption as well as broad, enhanced emission with a maximum at 650 nm (Figure 1b, red and blue solid lines). At 160 K, the fluorescence maximum is further red-shifted to 750 nm (Figure 1b, dotted line). These optical properties are typical for molecules with AIE and are consistent with other similar aryleneethynylenes.[6,8,22,23] Absorption and fluorescence of AE **1** are strongly dependent on the extent of conjugation of the π-electron cloud, for which the torsion angles of the five phenyl rings are an important measure.[24] For torsion angles close to 0°, the molecule is fully planarized, the degree of π-conjugation is maximized, and the energy of this rotamer is minimized.[25] In the ground state, the energy difference between rotamers of different torsion angles is low (<4 kJ/mol), and a wide range of rotational states are populated.[26] This leads to the broad absorption feature in Figure 1b. In the excited state, the torsion-angle-dependent energy profile of the rotamers becomes much steeper ($\Delta E \approx 30$ kJ/mol)[27] and, an unhindered rotation provided, radiative emission will occur from a narrow range of rotational states with relatively small torsion angles.[26] This narrows and red-shifts the fluorescence compared to the absorption. In the solid state, structural rigidity favors rotamers with small torsion angles and enforces a higher degree of planarization. This invokes the low-energy tailing of the absorption and the red-shift of the fluorescence in Figure 1b. Kinetic arrest of high-energy rotamers due to the structural rigidity prevents the fluorescence line narrowing observed in solution and leads to a broad fluorescence feature. At low temperature, structural order and, thus, the degree of planarization are enhanced further, which shifts the fluorescence to even lower energies.[28,29]

Continuous excitation at 488 nm under nitrogen atmosphere leads to substantial fluctuations (±20%) in the fluorescence intensity emitted by the AE **1** aggregates (Figure 1c,d). The time scale of seconds for the transition between an intensity maximum and minimum suggests that a macroscopic process, and not an electronic transition, is responsible for the fluctuations. Within the theory of AIE, this process needs to affect either the restriction of intramolecular motion or the rate of formation of a photochemical intermediate to result in fluorescence intensity fluctuations.[4] Photothermally-induced local structural changes are a likely cause for less restricted intramolecular motion and faster nonradiative recombination. Indeed, we observe significant local changes in the optical scattering and luminescence images of AE **1** aggregates after laser excitation, indicating an altered morphology (see Figure S1). Furthermore, we find a strong correlation between the intensity and the peak wavelength of the fluorescence, in that a lower intensity coincides with a blue-shifted fluorescence peak (Figure 1d). This is consistent with a transformation from a more planarized structure with high fluorescence quantum yield to a less planarized structure with fast nonradiative recombination. To test for the formation of a photochemical intermediate as an alternative cause for the intensity fluctuations, we compare the Raman bands of AE **1** appearing together with the fluorescence signals of different intensities

https://dx.doi.org/10.1021/acsnano.0c05121
ACS Nano 2021, 15, 480−488

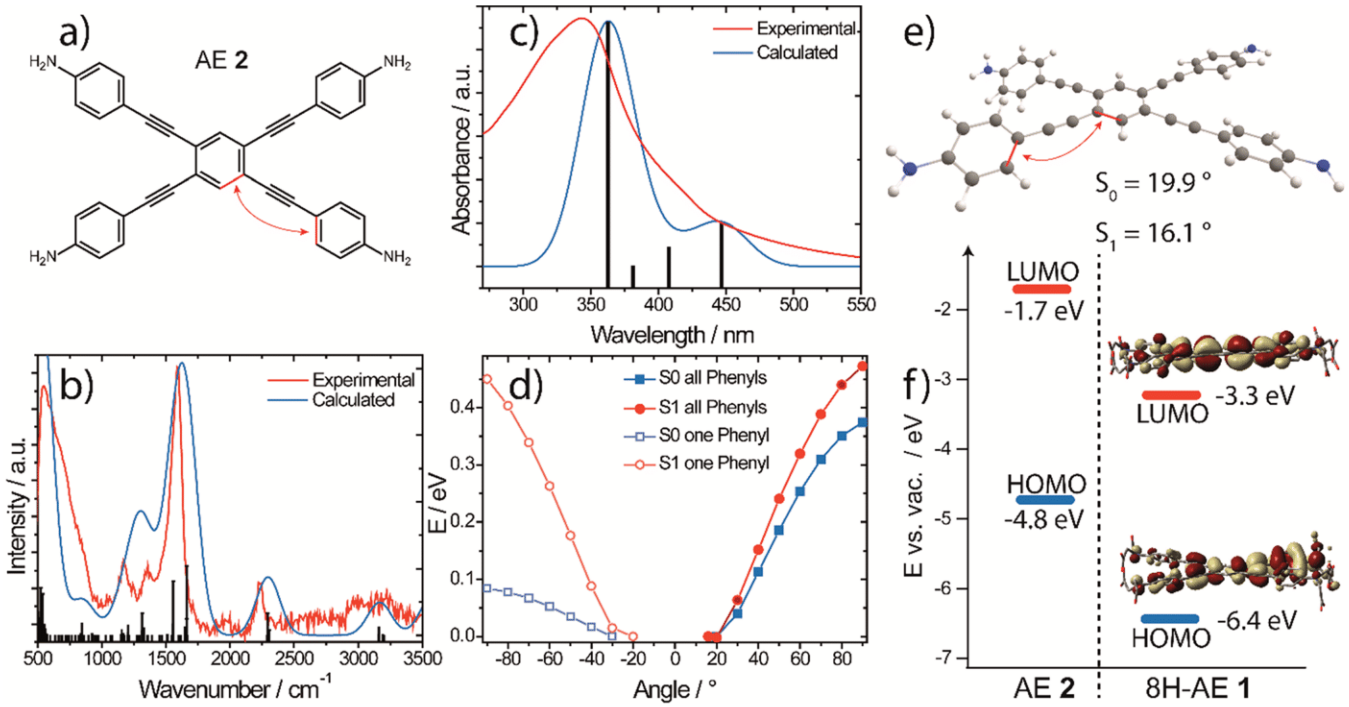

Figure 2. (a) Model compound AE 2 used for quantum chemical calculations and relevant phenyl torsion angles (red). (b) Calculated Raman spectrum of AE 2 with individual vibrations (black), the envelope spectrum (blue), and the experimental Raman spectrum of AE 1 (red). (c) Calculated absorption spectrum of AE 2 with individual transitions (black), the envelope spectrum (blue), and the experimental UV−vis spectrum of AE 1 in methanol (red). (d) Energy difference relative to the energetic minimum of the ground state (S_0, blue squares) and the first singlet state (S_1, red spheres) of AE 2 with respect to the out-of-plane torsion of one phenyl ring (open symbols, left) and of all four phenyl rings (closed symbols, right). (e) Geometry of AE 2 and indication of the most stable out-of-plane torsion of the phenyl groups for the S_0 and S_1 states. (f) HOMO and LUMO energies relative to the vacuum level of AE 2 (left) and the neutral, protonated derivative of AE 1 (right, "8H-AE 1"). For 8H-AE 1, we also show the corresponding isosurfaces.

(Figure 1e). We find a strong band at 1590 cm^{-1} and a weak signal at 2230 cm^{-1}, which we assign to the phenyl-C═C breathing and the C≡C stretching mode in agreement with earlier reports.[29,30] There are no substantial differences between Raman spectra taken during periods of fluorescence intensity minima *vs* maxima, suggesting that chemical transformations of AE **1** are not responsible for the fluorescence intensity fluctuations. Over the course of 1000 s of continuous excitation, the intensity of the phenyl-C═C breathing mode decreases in comparison with that of the C≡C stretching mode. However, this evolution progresses within periods of low and high fluorescence intensity alike.

We conclude that the fluorescence intensity fluctuations of AE **1** under continuous 488 nm laser excitation are probably caused by a photothermally-induced order/disorder transition. This transition locally increases the nonradiative recombination rate due to bond rotation and decreases the fluorescence quantum yield. In the disordered, less planarized state, the absorption of AE **1** at 488 nm is weakened (Figure 1b), which now decreases the rate of photothermal heating and allows for a recovery of the initial optical properties of the AE **1** aggregates. At 160 K, the fluorescence fluctuations disappear (Figure 1f). We suspect that photothermal heating may not be sufficient at this temperature to invoke the same structural changes that lead to the random fluorescence fluctuations in Figure 1c.

In Figure 2, we display the results of quantum chemical calculations of the simplified arylethynylene AE **2** (Figure 2a), which we choose as a model compound to resemble AE **1** but at reduced computational costs. The calculations are carried out using B3LYP-D3BJ level of theory with a def2-TZVP basis set. Our choice of the model compound AE **2** is justified by a comparison of the calculated Raman (Figure 2b) and absorption spectra (Figure 2c), which are in good agreement with the experimental data of AE **1** (taken from Figure 1b,e). Figure 2d details the energy difference arising from varying the out-of-plane torsion of the phenyl moieties in AE **2** for the S_0 (blue) and S_1 state (red). Figure 2e shows the most stable geometry of the S_0 state with a phenyl torsion of 19.9° and of the S_1 state with a reduced torsion angle of 16.1°. The HOMO and LUMO energy levels relative to the vacuum level of AE **2** in the ground state are provided in Figure 2f (−4.8 eV and −1.7 eV). In view of the potentially large effect of the eight carboxylic acid substituents of AE **1** on the position of the frontier orbitals, we also calculate the HOMO and LUMO energies of the neutral, protonated derivative (8H-AE **1**) and display the energies as well as the isosurfaces on the left side of Figure 2f. We find that the HOMO/LUMO levels in 8H-AE **1** are substantially depressed compared to AE **2** with energies of −6.4 eV/-3.3 eV *vs* vacuum, while the HOMO−LUMO gap (−3.1 eV) is unaffected by the substitution.

From these calculations, we conclude the following: (1) The excited state of AE **1** is more planar than the ground state, and (2) the torsion-angle-dependent energy landscape of the S_1 state is steeper than that of the S_0 state. This is particularly pronounced if the out-of-plane torsion of only one phenyl moiety is considered (Figure 2d, left), but also holds true (to a lesser extent) if all four phenyl substituents are taken into account (Figure 2d, right). These properties favor the

https://dx.doi.org/10.1021/acsnano.0c05121
ACS Nano 2021, 15, 480−488

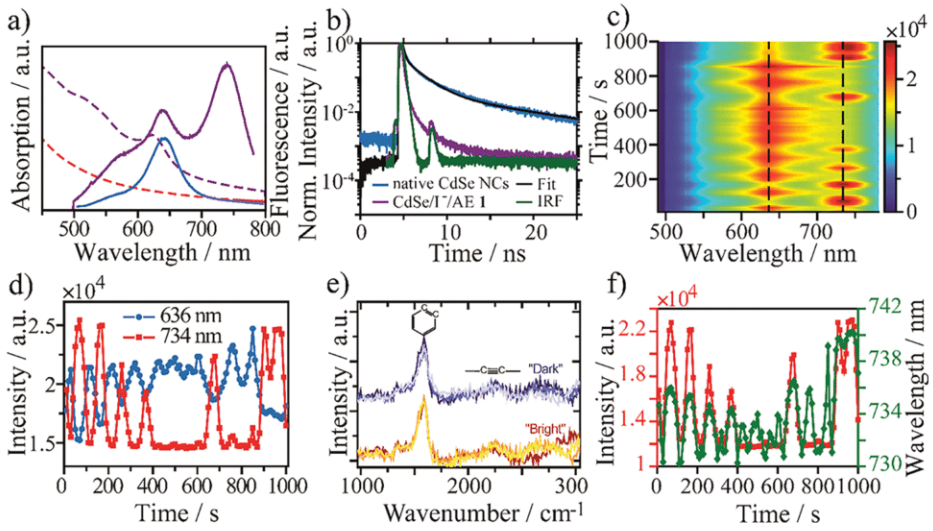

Figure 3. (a) Thin-film absorption (purple dashed line) and thin-film fluorescence (purple solid line) of CdSe/I⁻/AE 1. Excitation at 488 nm. For comparison, the fluorescence of the CdSe/I⁻ NCs (blue solid line) and the absorption of pure AE 1 (red dashed line) are also displayed. (b) Fluorescence lifetime measurements of the native CdSe NCs (blue), their fit (black), and the same NCs after functionalization with AE 1 (purple). The IRF is displayed in green. (c) Thin-film fluorescence of CdSe/I⁻/AE 1 during 1000 s of continuous excitation at 488 nm with a binning time of 1 s. (d) Line profile of (c) cut at 636 and 734 nm. (e) Raman spectra taken during "bright" and "dark" periods. (f) Peak position of the low-energy band in (c) (green) compared with the intensity of the same band (red).

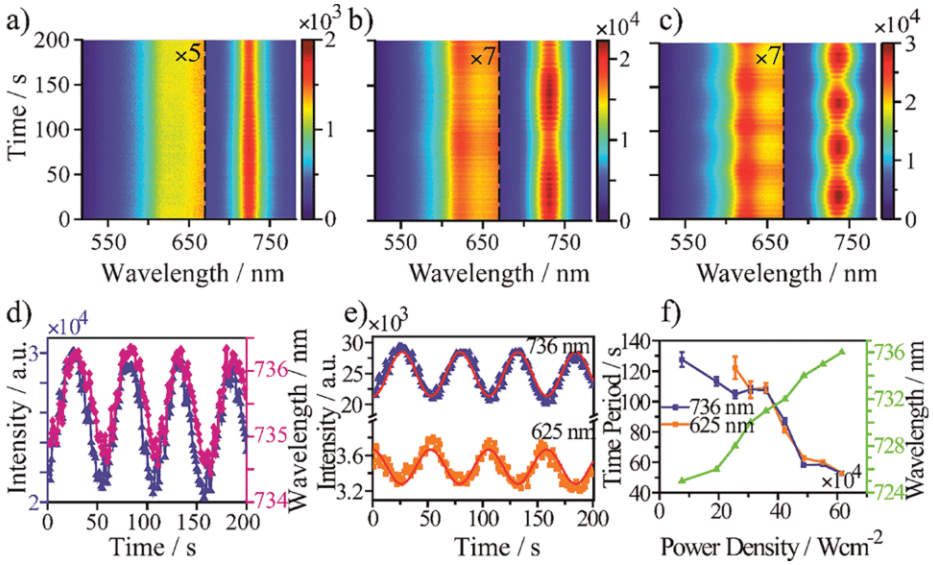

Figure 4. Thin-film fluorescence at 160 K of CdSe/I⁻/AE 1 during 200 s of continuous excitation at 488 nm with a binning time of 1 s and varying laser power. (a) 45 kW/cm², (b) 360 kW/cm², and (c) 615 kW/cm². (d) Peak position of the low-energy band in (c) (purple) compared with the intensity of the same band (blue). (e) Line profile of (c) cut at 625 and 736 nm. (f) Correlation between the laser power and the period of one complete oscillation in (e) for the fluorescence bands at 620 nm (blue) and 725 nm (orange). A concomitant redshift of the AE 1 emission peak is also displayed on the right axis.

occurrence of AIE and are consistent with the optical data in Figure 1.

In Figure 3, we analyze the solid-state fluorescence of AE **1** aggregates coupled to the surface of iodide-capped CdSe nanocrystals (CdSe/I⁻ NCs) at room temperature. The NCs were chosen based on the large spectral overlap between their fluorescence (Figure 3a, blue solid line) with the absorption of AE **1** aggregates (Figure 3a, red dashed line) to enable efficient EET. The absorption spectrum of the hybrid material (CdSe/I⁻/AE **1**) is dominated by the absorption of the CdSe NCs (purple dashed line), while the fluorescence spectrum bears two well-resolved, narrow bands at 636 and 734 nm (purple solid line). We assign the band at 636 nm to the CdSe/I⁻ NCs and the band at 734 nm to AE **1**. Fluorescence lifetime measurements reveal that the fluorescence decay of the same CdSe NCs shortens upon functionalization with AE **1** from a biexponential decay (τ_1 = 2.3 ns and τ_2 = 9.1 ns) to a decay kinetics, which is too fast to be distinguished from the resolution function (instrument response function (IRF), ~1 ns) of the instrument (Figure 3b).

Continuous excitation at 488 nm with 1−10 MW/cm², a diffraction-limited focus (few 100 nm diameter) and nitrogen atmosphere of CdSe/I⁻/AE **1** results in the temporal fluctuations in the fluorescence spectrum depicted in Figure

https://dx.doi.org/10.1021/acsnano.0c05121
ACS Nano 2021, 15, 480−488

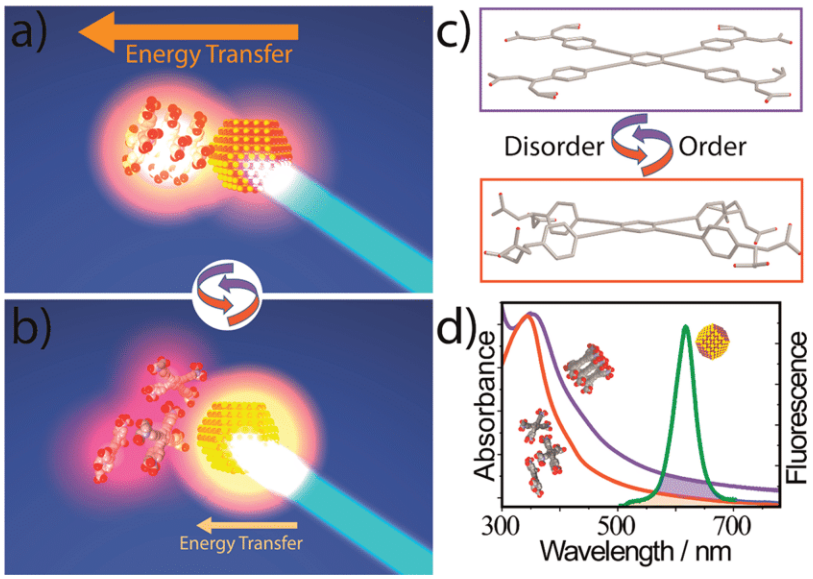

Figure 5. (a,b) Idealized schematic of the two structural scenarios proposed for CdSe/I⁻/AE 1 composites with different energy transfer efficiency. (c) Qualitative description of the proposed order/disorder transition. (d) Spectral overlap between NC emission (green) and AE 1 absorption in the ordered (blue) and disordered (red) state.

3c. We stress that these fluctuations occur only in highly selected places (roughly 1% of the total sample area). The fluctuations occur gradually over a time scale of 10−30 s with ON/OFF periods of similar duration. Most notably, the ON/OFF periods of the bands at 636 and 734 nm are mostly anticorrelated, that is, an increase of the NC fluorescence occurs together with a decrease of the AE **1** emission and *vice versa* (Figure 3d). We verify that CdSe/I⁻ NCs without AE **1** do not exhibit similar fluorescence fluctuations (Figure S2). Similar to pure AE **1**, we find the same Raman signals at 1590 and 2230 cm^{-1}, which do not change significantly during relative ON or OFF periods (Figure 3e). Here, however, the intensity of the phenyl−C═C breathing mode remains constant, indicating a higher photostability of the hybrid composite compared to pure AE **1**. Another similarity between CdSe/I⁻/AE **1** and the pure molecule is the strong correlation of the intensity (red) and peak wavelength position (green) of the fluorescence of AE **1** (Figure 3f). In contrast, the peak wavelength position of the CdSe/I⁻ fluorescence remains constant throughout the fluctuations.

At 160 K and helium atmosphere, the temporal fluorescence fluctuations of CdSe/I⁻/AE **1** become periodic (Figure 4). At 45 kW/cm^2 excitation power density, the two fluorescence bands of the CdSe/I⁻ NCs and the AE **1** aggregates are quasi-continuous over a time scale of 200 s (Figure 4a). Increasing the excitation power density to 615 kW/cm^2 induces periodic oscillations of the intensity of both fluorescence bands by ±20%, which remain exactly anticorrelated (Figure 4b−e). The peak wavelength position of AE **1** (Figure 4d, purple) follows the intensity fluctuations (Figure 4d, blue) almost perfectly, however, the variations are significantly smaller compared to room temperature (Figure 3f). The periodicity of the fluctuations depends on the excitation power density and varies with a period of 127 s at 75.6 kW/cm^2 to 53 s at 620 kW/cm^2 (Figure 4f), as determined from the sine fits shown in Figure 4e. In addition, the peak wavelength of the AE 1 emission exhibits a redshift from 725 to 736 nm during this increase in laser power.

We suggest that changes in the EET efficiency from excited CdSe/I⁻ NCs to aggregates of AE **1** are responsible for the anticorrelated fluctuations in the CdSe/I⁻/AE **1** nanocomposite (Figure 5a,b). Under 488 nm excitation, most of the light is absorbed by the inorganic NCs, as reflected by the absorption spectrum in Figure 3a, which mimics that of the pure NCs. The NC fluorescence overlaps with the absorption of AE **1**, resulting in efficient EET, which weakens the CdSe fluorescence signal and strengthens the molecular fluorescence. In Figure 4e, this scenario applies when the fluorescence band at 736 nm is at a maximum and the band at 625 nm is at a minimum, for example, after 25 s. Simultaneously, this EET invokes photothermal heating of the AE **1** aggregates, eventually triggering an order/disorder transition to break up the aggregates. The result of this transition is a reduced degree of planarization (Figure 5c), which blueshifts the absorption spectrum, decreases the overlap with the NC fluorescence (Figure 5d), weakens the efficiency of EET, diminishes the molecular fluorescence, and brightens the emission of the NCs. In Figure 4e, this scenario applies when the fluorescence band at 736 nm is at a minimum and the band at 625 nm is at a maximum, for example, after 55 s. In the disordered state, EET is slow, and photothermal heating is weak, such that new aggregates of AE **1** may form and the initial state with efficient EET from the NCs to the aggregates is restored. An illustration of the different absorption and emission pathways underlying this picture is provided in Scheme S2 in the Supporting Information. It is supported by the quantum chemical calculations of the angle-dependent energies of the excited and the ground states (Figure 2d), which are crucial for the occurrence of AIE.

The overall interpretation in Figure 5 is consistent with the laser power-dependent period for one complete cycle (Figure 4f) as increasing the number of photons will increase the rate of heat transfer, which should shorten the cycle period. It is furthermore supported by the fluorescence fluctuations of pure AE **1** in Figure 1, which are likely due to a similar order/disorder transition of the aggregates. The fact that the fluctuations are only observed in spatially confined, highly

https://dx.doi.org/10.1021/acsnano.0c05121
ACS Nano 2021, 15, 480−488

selective places on the sample suggests that a certain structure/geometry of the molecular stacks in the vicinity of the NCs is required. This is consistent with the often complex correlation between the efficiency of energy transfer and molecular orientation, distance, or structure.

Relaxing the structural rigidity in molecular emitters with AIE increases the rate of nonradiative recombination and decreases the fluorescence intensity.[4] The higher stability of the phenyl−C≡C moiety in the nanocomposite (Figure 3e) compared to the pure molecule (Figure 1e) is consistent with a mostly indirect excitation of AE **1** in the nanocomposite by EET *vs* direct excitation of the pure molecule leading to photodegradation. EET as the main electronic interaction between the CdSe NCs and AE **1** is also in line with the fluorescence lifetime data in Figure 3b. Alternatively, one may consider charge transfer and the formation of an interfacial exciton between AE **1** and CdSe. Based on the calculated HOMO/LUMO positions of the molecule (Figure 2f), a type II energy alignment scenario where the hole resides on the NC and the electron is located partially on the molecule appears energetically plausible.[31] However, the short fluorescence lifetime of the CdSe/I^-/AE **1** nanocomposite (Figure 3b) is uncharacteristic for the formation of such an interfacial exciton, as one would expect much longer lifetimes similar to those in type II core/shell NCs.[32]

CONCLUSION

Coupling organic π-systems that exhibit aggregation-induced emission to a second fluorophore can result in emergent optical properties, such as dual fluorescence with oscillating intensity fluctuations. This is realized in a hybrid thin film consisting of CdSe NCs coupled to aggregates of an aryleneethynylene derivative with fluorescence from both fluorophores, which establish a feedback loop: Excitation energy transfer from the NCs to the aggregates leads to photothermal heating and an order/disorder transition in the aggregates. This transition weakens the fluorescence intensity of the organic π-system and the rate of energy transfer, which strengthens the NC fluorescence. Simultaneously, the slower energy-transfer rate reduces photothermal heating, which gradually restores the initial structure and optical properties of the molecular aggregates. This closes the feedback loop and initiates the next cycle. The resulting optical oscillations and their temperature dependence may be of interest for application in nanothermometry.

EXPERIMENTAL SECTION

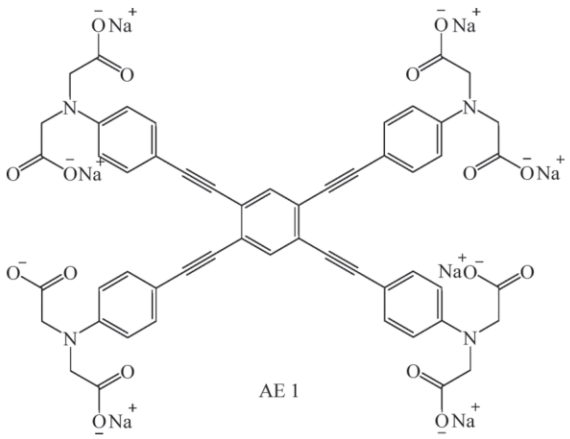

Sodium 2,2′,2″,2‴,2⁗,2⁗′,2⁗″,2⁗‴-(((benzene-1,2,4,5-tetrayltetrakis(ethyne-2,1-diyl))tetrakis(benzene-4,1-diyl))tetrakis(azanetriyl))octaacetate (AE 1). AE **1**-COOET (316 mg, 257 mmol) was dissolved in MeOH/H_2O (1:1, 10 mL/10 mL), and NaOH (515 mg, 12.9 mmol) was added. The resulting mixture was stirred at 70 °C for 2 d. The solvent was evaporated *in vacuo*. The residue was dissolved in H_2O and filtered. The resulting solution was adjusted to pH 7 and dialyzed against DI H_2O for 5 d. After filtration and freeze-drying, the title compound AE **1** was afforded as a brown fluffy solid (250 mg, 97%). ^{1}H NMR (600 MHz, D_2O): δ = 7.71−7.69 (m, 2 H), 7.48−7.44 (m, 8 H), 6.58−6.54 (m, 8 H), 3.93 (m, 16H) ppm. Due to low solubility, a ^{13}C NMR spectrum could not be obtained. IR (cm^{-1}): ν 3589, 3327, 3171, 3037, 2928, 2650, 2193, 1577, 1516, 1457, 1381, 1298, 1232, 1176, 1134, 972, 906, 817, 695, 610, 515, 456, 435.

The experimental procedures of precursors of compound AE **1** have been reported in the Supporting Information.

CdSe NCs Synthesis. *Chemicals Used.* Chemicals used were cadmium oxide (CdO, 99.99%, Aldrich), oleicacid (OA, 90%, Aldrich), trioctylphosphine (TOP, 97%, Abcr), trioctylphosphine oxide (TOPO, 99%, Aldrich), hexadecylamine(HDA, 90%, Aldrich), 1-octadecene (ODE, 90%, Acros Organics), selenium pellets (Se, 99.999%, Aldrich), ammonium iodide (99.999%,Aldrich), *N*-methyl-formamide (NMF, 99%, Aldrich), hexane (extra dry, 96%, Acros Organics), ethanol (extra dry, 99.5%, AcrosOrganics), acetone (extra dry, 99.8%, Acros Organics), dimethyl sulfoxide (DMSO, 99.7%, Acros Organics), and acetonitrile (extra dry, 99.9%, Acros Organics).

All chemicals, except those used in the CdSe NC synthesis, were stored and used inside a nitrogen-filled glovebox. All sample preparations for electrical or fluorescence measurements were carried out in a nitrogen-filled glovebox. The samples were inserted into a probe station for low-temperature photocurrent measurements using an airtight arm sealed inside the glovebox. Samples were kept under low pressure for at least 2 h before starting any measurements.

CdSe NCs and Device Preparation. Wurtzite CdSe NCs having ∼5 nm size were synthesized using a literature reported synthesis.[33,34] As synthesized, NCs were dispersed in hexane. CdSe NCs 5 mL, ∼10 mg/mL were taken for ligand exchange with 300 μL of a 1 M solution of NH_4I in NMF further diluted using 2.7 mL acetone. This biphasic mixture was stirred until the NCs changed their phase, then centrifuged and washed using excess of acetone. CdSe/I^- thus obtained was dispersed in NMF with a 60−100 mg/mL concentration. For device preparation, we used commercially available gold patterned Si/SiO_2 with 230 nm-thick dielectric layer and 2.5 μm × 1 cm channel provided by the Fraunhofer Institute for Photonic Microsystems, Dresden, Germany. In a typical device preparation, 70 μL of CdSe/I^- NCs was dropped on an FET substrate, mixed with 30 μL of AE **1** solution in NMF with a concentration of roughly 1 mg/mL, and kept undisturbed for 6 h. The still wet mixture of CdSe/I^-/AE **1** was then spun off at 30 rps for 1 min. Then the substrate was washed with acetonitrile multiple times and annealed at 190 °C for 35 min. A similar procedure was followed for preparing fluorescence samples on glass coverslips using a ligand-to-NC ratio of roughly 20:1, as determined by absorption spectroscopy and Lambert−Beer's law.

Electrical and Optical Measurements. Electrical measurements were carried out under nitrogen by using a Keithley 2634B source meter. The charge-carrier mobility was extracted using the gradual channel approximation in the linear regime. The error in the mobility (S) was calculated using the standard deviation error in the slope of I_d *vs* V_g curve at 5 V source−drain voltage:

$$S = \sqrt{\frac{1}{N-1}\sum_{i=1}^{N}|A_i - \bar{A}|}; \quad \bar{A} = \frac{1}{N}\sum_{i=1}^{N}A_i$$

where A is the slope from N measurements with the mean value $\bar{A}$.

Absorption measurements were acquired using a Carry 5000 UV−vis-NIR spectrophotometer on a thin glass coverslip or in methanol as stated in the text. Photocurrent low-temperature measurements were recorded using a CRX-6.5K (Lake Shore Desert) probe station operated under low pressure 5 × 10^6 mbar and a Keithley 2634B

https://dx.doi.org/10.1021/acsnano.0c05121
ACS Nano 2021, 15, 480−488

source meter. Samples were illuminated using a 408 nm LP405-SF10 laser diode manufactured by Thorlabs with a theoretical maximum output power of 11.5−30 mW. This output power decreases orders of magnitude due to beam decollimation, scattering, and inefficient coupling of optical fiber when calibrated using a test sample that comes out to be 10−18 μW.

Room-Temperature Fluorescence and Resonance Raman Measurements. The 12 ×12 mm glass coverslips were cleaned by submerging in a chromosulfuric acid cleaning solution for several hours, followed by three subsequent washing steps with triple distilled water and spectroscopy grade methanol. Fluorescence samples were then prepared on these coverslips using the drop casting method described above. The film was washed with acetonitrile and annealed at 190 °C before any measurements were taken.

The room-temperature steady-state photoluminescence and resonance stokes Raman spectral measurements as well as photoluminescence and scattering image acquisition were carried out using a home-built inverted confocal laser scanning microscope.[35] A 488 nm TOPTICA Photonics iBeam smart diode laser with a Gaussian intensity profile, operated in continuous wave mode, was employed as the light source. The laser intensity in the diffraction limited focus at maximum laser power is estimated to be 10^7 W/cm^2 operating at roughly 30−60% of maximum power. This focusing is crucial as the observed intensity fluctuations in Figures 1c, 3c, and 4a,c occur only in highly selective places and length scales of a few 100 nm. Focusing of the laser on the sample and the subsequent collection of reflected as well as scattered and emitted light was achieved through an oil immersion objective (NA = 1.25). The spectral data was recorded using an Acton SpectraPro 2300i spectrometer with a grating of 300/mm and a detector temperature of −45 °C. Extraction of Raman spectra from kinetic series spectra enables the study of correlations between vibrational and luminescence features from the same spot. Photoluminescence and scattering images were acquired by scanning the area of interest while utilizing two separate avalanche photodiodes (APDs) as detectors. The exclusion of atmospheric oxygen was achieved by nearly completely enclosing the upper part of the sample holder and passing a constant flow of nitrogen through this apparatus.

Low Temperature Fluorescence Measurements. Low temperature fluorescence was measured using a home-built confocal microscope mounted on a damped optical table and a standard microscope objective (60X DIN Achromatic objective, NA = 0.85, Edmund Optics) located inside a cryostat (SVT-200, Janis). A Cernox temperature sensor (CX-1030-SD-HT 0.3L) was positioned close to the sample to measure the temperature by a LakeShore Model 336 temperature controller. The sample holder was mounted on the scan stage. Attocube systems linear stages (ANPx320 and ANPz101eXT) and scanners (ANSxy100lr and ANSz100lr) were used to scan and position the sample.

A continuous wave 488 nm laser diode (OBIS LS 20 mW, Coherent Inc.) was used to excite the sample. The excitation intensity of the laser was measured between 0.35 mW and 4.80 mW before entering into the cryostat. The excitation light was then aligned into the objective (60X DIN Achromatic air objective, Edmund Optics) to get an optimal focus. The excitation intensity in the focus was between 5.5 × 10^4 and 7.52 × 10^5 W/cm^2.[36]

The collected fluorescence signal was passed through a dichroic mirror and a long-pass filter (488 LP Edge Basic, AHF Analysentechnik). It was detected by a single-photon counting avalanche photodiode (APD, COUNT-100C, Laser Components). Fluorescence spectra were also acquired with integration times of one second by a Shamrock 500 spectrograph in combination with an Andor Newton back illuminated deep depleted CCD camera (DU920PPR-DD). Further details for low temperature confocal imaging and spectroscopy setup can be found elsewhere.[37]

Time-resolved photoluminescence decay measurements. Time-resolved photoluminescence spectra were measured with a home-built scanning confocal microscope.[38] The sample was fixed on a piezo stage (Physik Instrumente) *via* magnets to avoid movement. A constant nitrogen flow was applied to maintain an inert atmosphere and avoid oxidation of the sample. To avoid bleaching, the lifetime was always measured before a fluorescence measurement.

A linearly polarized continuous wave laser (488 nm,0.33 mW measured before objective lens) was focused on the sample by a high numerical aperture (NA = 1.46) oil objective, the fluorescence was collected by the same objective and sent to a spectrometer (Acton SP-2500i, Princeton Instruments). For lifetime measurement, the laser was operated in the pulsed mode (5.3 × 10^3 W/cm^2,20 MHz). The signal was sent to a single photon avalanche photodiode (APD), connected to a time-correlated single photon counting module (HydraHarp 400). Decay curves were fitted and analyzed by SymPhoTime 64. See Scheme S1 for schematic of the time-resolved photoluminescence instrument.

Quantum Chemical Calculations. The computations of AE **2** were carried out with Turbomole 7.4.1. A selection of DFT functionals was considered, including M06-2X, wB97x, CAM-B3LYP, and B3LYP-D3BJ. Minimum geometries are confirmed by frequency analysis and agreed with results from RI-MP2. All values reported are obtained with the def2-TZVP basis set. We found B3LYP-D3BJ/def2-TZVP and its time-dependent variant to be superior, particularly in correctly simulating the Raman and absorption spectra. Calculations of the neutral, protonated derivative of AE **1** (8H-AE **1**) were performed by using Gaussian 16. The gas-phase ground-state equilibrium geometry of the molecules was optimized at the B3LYP/def2-SVP level of theory. Afterward, the phenylethinyl substituents were forced into specific torsion angles, and the resulting dihedral was fixed. Another geometry optimization was performed using B3LYP/def2-SVP level of theory. Fragment molecular orbital calculations were performed starting from the optimized geometries on the B3LYP/def2-SVP level of theory.

ASSOCIATED CONTENT

Supporting Information

The Supporting Information is available free of charge at https://pubs.acs.org/doi/10.1021/acsnano.0c05121.

Figure S1: Luminescence and scattering images of pure linker and CdSe/I$^-$/AE **1**. Figure S2: Fluorescence of CdSe/I$^-$. Figure S3: Gate sweeps of CdSe/I$^-$ and CdSe/I$^-$/AE **1**. Figure S4: Raman spectra of pure linker and CdSe/I$^-$/AE **1**. Figure S5: SEM micrograph of CdSe/I$^-$/AE **1**. Figure S6: Temperature-dependent electric conductivity of CdSe/I$^-$/AE **1** thin films. Scheme S1: Schematic of time-resolved photoluminescence instrument. Scheme S2: Schematic of the absorption and emission pathways in CdSe/I$^-$/AE **1** NC thin films in the ordered as well as the disordered states (PDF)

AUTHOR INFORMATION

Corresponding Authors

Marcus Scheele − *Institute for Physical and Theoretical Chemistry and Center for Light-Matter Interaction, Sensors and Analytics LISA+, University of Tübingen, 72076 Tübingen, Germany*; orcid.org/0000-0002-2704-3591; Email: marcus.scheele@uni-tuebingen.de

Uwe H. F. Bunz − *Organisch-Chemisches Institut and Centre for Advanced Materials, Ruprecht-Karls-Universität Heidelberg, 69120 Heidelberg, Germany*; orcid.org/0000-0002-9369-5387; Email: uwe.bunz@oci.uni-heidelberg.de

Authors

Krishan Kumar − *Institute for Physical and Theoretical Chemistry, University of Tübingen, 72076 Tübingen, Germany*

https://dx.doi.org/10.1021/acsnano.0c05121
ACS Nano 2021, 15, 480−488

Jonas Hiller − *Institute for Physical and Theoretical Chemistry, University of Tübingen, 72076 Tübingen, Germany*
Markus Bender − *Organisch-Chemisches Institut and Centre for Advanced Materials, Ruprecht-Karls-Universität Heidelberg, 69120 Heidelberg, Germany*
Saeed Nosrati − *Institute for Physical and Theoretical Chemistry, University of Tübingen, 72076 Tübingen, Germany*
Quan Liu − *Institute for Physical and Theoretical Chemistry, University of Tübingen, 72076 Tübingen, Germany; Charles Delaunay Institute, CNRS Light, Nanomaterials, Nanotechnologies (L2n, former "LNIO"), University of Technology of Troyes, 10004 Troyes, France*
Marc Edelmann − *Institute for Physical and Theoretical Chemistry, University of Tübingen, 72076 Tübingen, Germany*
Steffen Maier − *Organisch-Chemisches Institut and Centre for Advanced Materials, Ruprecht-Karls-Universität Heidelberg, 69120 Heidelberg, Germany*
Tim Rammler − *Institute for Physical and Theoretical Chemistry, University of Tübingen, 72076 Tübingen, Germany*
Frank Wackenhut − *Institute for Physical and Theoretical Chemistry, University of Tübingen, 72076 Tübingen, Germany;* orcid.org/0000-0001-6554-6600
Alfred J. Meixner − *Institute for Physical and Theoretical Chemistry and Center for Light-Matter Interaction, Sensors and Analytics LISA+, University of Tübingen, 72076 Tübingen, Germany;* orcid.org/0000-0002-0187-2906
Kai Braun − *Institute for Physical and Theoretical Chemistry, University of Tübingen, 72076 Tübingen, Germany;* orcid.org/0000-0003-3774-0507

Complete contact information is available at: https://pubs.acs.org/10.1021/acsnano.0c05121

Notes

The authors declare no competing financial interest.

ACKNOWLEDGMENTS

Financial support of this work has been provided by the Emmy Noether program of the DFG under grants SCHE1905/3-1 and ME 1600/13-3. We thank Andre Maier for electron microscopy imaging.

REFERENCES

(1) Luo, J.; Xie, Z.; Lam, J. W. Y.; Cheng, L.; Tang, B. Z.; Chen, H.; Qiu, C.; Kwok, H. S.; Zhan, X.; Liu, Y.; Zhu, D. Aggregation-Induced Emission of 1-Methyl-1,2,3,4,5-Pentaphenylsilole. *Chem. Commun.* **2001**, No. 18, 1740−1741.
(2) Barbara, P. F.; Rand, S. D.; Rentzepis, P. M. Direct Measurements of Tetraphenylethylene Torsional Motion by Picosecond Spectroscopy. *J. Am. Chem. Soc.* **1981**, *103*, 2156−2162.
(3) Bunz, U. H. F. Poly(aryleneethynylene)s: Syntheses, Properties, Structures, and Applications. *Chem. Rev.* **2000**, *100*, 1605−1644.
(4) Chen, Y.; Lam, J. W. Y.; Kwok, R. T. K.; Liu, B.; Tang, B. Z. Aggregation-Induced Emission: Fundamental Understanding and Future Developments. *Mater. Horiz.* **2019**, *6*, 428−433.
(5) Cai, Y.; Du, L.; Samedov, K.; Gu, X.; Qi, F.; Sung, H. H. Y.; Patrick, B. O.; Yan, Z.; Jiang, X.; Zhang, H.; Lam, J. W. Y.; Williams, I. D.; Lee Phillips, D.; Qin, A.; Tang, B. Z. Deciphering the Working Mechanism of Aggregation-Induced Emission of Tetraphenylethylene Derivatives by Ultrafast Spectroscopy. *Chem. Sci.* **2018**, *9*, 4662−4670.
(6) Bunz, U. H. F. Poly(aryleneethynylene)s. *Macromol. Rapid Commun.* **2009**, *30*, 772−805.
(7) Leung, N. L. C.; Xie, N.; Yuan, W.; Liu, Y.; Wu, Q.; Peng, Q.; Miao, Q.; Lam, J. W. Y.; Tang, B. Z. Restriction of Intramolecular Motions: The General Mechanism behind Aggregation-Induced Emission. *Chem. - Eur. J.* **2014**, *20*, 15349−15353.
(8) Parrott, E. P. J.; Tan, N. Y.; Hu, R.; Zeitler, J. A.; Tang, B. Z.; Pickwell-Macpherson, E. Direct Evidence to Support the Restriction of Intramolecular Rotation Hypothesis for the Mechanism of Aggregation-Induced Emission: Temperature Resolved Terahertz Spectra of Tetraphenylethene. *Mater. Horiz.* **2014**, *1*, 251−258.
(9) Yamamoto, N. Mechanisms of Aggregation-Induced Emission and Photo/Thermal E/Z Isomerization of a Cyanostilbene Derivative: Theoretical Insights. *J. Phys. Chem. C* **2018**, *122*, 12434−12440.
(10) Maity, S.; Wu, W. C.; Tracy, J. B.; Clarke, L. I.; Bochinski, J. R. Nanoscale Steady-State Temperature Gradients within Polymer Nanocomposites Undergoing Continuous-Wave Photothermal Heating from Gold Nanorods. *Nanoscale* **2017**, *9*, 11605−11618.
(11) Borzenkov, M.; Pallavicini, P.; Chirico, G. Photothermally Active Inorganic Nanoparticles: From Colloidal Solutions to Photothermally Active Printed Surfaces and Polymeric Nanocomposite Materials. *Eur. J. Inorg. Chem.* **2019**, *2019*, 4397−4404.
(12) Park, C. H.; Yun, H.; Yang, H.; Lee, J.; Kim, B. J. Fluorescent Block Copolymer-MoS_2 Nanocomposites for Real-Time Photothermal Heating and Imaging. *Adv. Funct. Mater.* **2017**, *27*, 1604403.
(13) Crane, M. J.; Zhou, X.; Davis, E. J.; Pauzauskie, P. J. Photothermal Heating and Cooling of Nanostructures. *Chem. - Asian J.* **2018**, *13*, 2575−2586.
(14) Resch-Genger, U.; Grabolle, M.; Cavaliere-Jaricot, S.; Nitschke, R.; Nann, T. Quantum Dots *versus* Organic Dyes as Fluorescent Labels. *Nat. Methods* **2008**, *5*, 763−775.
(15) Lutich, A. A.; Jiang, G.; Susha, A. S.; Rogach, A. L.; Stefani, F. D.; Feldmann, J. Energy Transfer *versus* Charge Separation in Type-II Hybrid Organic-Inorganic Nanocomposites. *Nano Lett.* **2009**, *9*, 2636−2640.
(16) Walker, B. J.; Nair, G. P.; Marshall, L. F.; Bulović, V.; Bawendi, M. G. Narrow-Band Absorption-Enhanced Quantum Dot/J-Aggregate Conjugates. *J. Am. Chem. Soc.* **2009**, *131*, 9624−9625.
(17) Beane, G.; Boldt, K.; Kirkwood, N.; Mulvaney, P. Energy Transfer between Quantum Dots and Conjugated Dye Molecules. *J. Phys. Chem. C* **2014**, *118*, 18079−18086.
(18) Luo, X.; Han, Y.; Chen, Z.; Li, Y.; Liang, G.; Liu, X.; Ding, T.; Nie, C.; Wang, M.; Castellano, F. N.; Wu, K. Mechanisms of Triplet Energy Transfer across the Inorganic Nanocrystal/Organic Molecule Interface. *Nat. Commun.* **2020**, *11*, 28.
(19) Freyria, F. S.; Cordero, J. M.; Caram, J. R.; Doria, S.; Dodin, A.; Chen, Y.; Willard, A. P.; Bawendi, M. G. Near-Infrared Quantum Dot Emission Enhanced by Stabilized Self-Assembled J-Aggregate Antennas. *Nano Lett.* **2017**, *17*, 7665−7674.
(20) Stöferle, T.; Scherf, U.; Mahrt, R. F. Energy Transfer in Hybrid Organic/ Inorganic Nanocomposites. *Nano Lett.* **2009**, *9*, 453−456.
(21) Guzelturk, B.; Demir, H. V. Near-Field Energy Transfer Using Nanoemitters for Optoelectronics. *Adv. Funct. Mater.* **2016**, *26*, 8158−8177.
(22) Zhang, H.; Rominger, F.; Bunz, U. H. F.; Freudenberg, J. Aggregation-Induced Emission of Triphenyl-Substituted Tristyrylbenzenes. *Chem. - Eur. J.* **2019**, *25*, 11218−11222.
(23) Zucchero, A. J.; McGrier, P. L.; Bunz, U. H. F. Cross-Conjugated Cruciform Fluorophores. *Acc. Chem. Res.* **2010**, *43*, 397−408.
(24) Li, N.; Jia, K.; Wang, S.; Xia, A. Theoretical Study of Spectroscopic Properties of Dimethoxy-*p*-Phenylene-Ethynylene Oligomers: Planarization of the Conjugated Backbone. *J. Phys. Chem. A* **2007**, *111*, 9393−9398.
(25) Miteva, T.; Palmer, L.; Kloppenburg, L.; Neher, D.; Bunz, U. H. F. Interplay of Thermochromicity and Liquid Crystalline Behavior in Poly(*p*-Phenyleneethynylene)s: Π−π Interactions or Planarization of the Conjugated Backbone? *Macromolecules* **2000**, *33*, 652−654.

(26) Sluch, M. I.; Godt, A.; Bunz, U. H. F.; Berg, M. A. Excited-State Dynamics of Oligo(*p*-Phenyleneethynylene): Quadratic Coupling and Torsional Motions. *J. Am. Chem. Soc.* **2001**, *123*, 6447−6448.
(27) Wierzbicka, M.; Bylińska, I.; Czaplewski, C.; Wiczk, W. Experimental and Theoretical Studies of the Spectroscopic Properties of Simple Symmetrically Substituted Diphenylacetylene Derivatives. *RSC Adv.* **2015**, *5*, 29294−29303.
(28) Panzer, F.; Bässler, H.; Köhler, A. Temperature Induced Order-Disorder Transition in Solutions of Conjugated Polymers Probed by Optical Spectroscopy. *J. Phys. Chem. Lett.* **2017**, *8*, 114−125.
(29) Castruita, G.; Arias, E.; Moggio, I.; Pérez, F.; Medellín, D.; Torres, R.; Ziolo, R.; Olivas, A.; Giorgetti, E.; Muniz-Miranda, M. Synthesis, Optical Properties and Supramolecular Order of π-Conjugated 2,5-Di(alcoxy)Phenyleneethynylene Oligomers. *J. Mol. Struct.* **2009**, *936*, 177−186.
(30) Köhler, A.; Khan, A. L. T.; Wilson, J. S.; Dosche, C.; Al-Suti, M. K.; Shah, H. H.; Khan, M. S. The Role of C-H and C-C Stretching Modes in the Intrinsic Non-Radiative Decay of Triplet States in a Pt-Containing Conjugated Phenyleneethynylene. *J. Chem. Phys.* **2012**, *136*, No. 094905.
(31) Jasieniak, J.; Califano, M.; Watkins, S. E. Size-Dependent Valence and Conduction Band-Edge Energies of Semiconductor Nanocrystals. *ACS Nano* **2011**, *5*, 5888−5902.
(32) Kim, S.; Fisher, B.; Eisler, H.-J.; Bawendi, M. Type-II Quantum Dots: CdTe/CdSe(Core/Shell) and CdSe/ZnTe(Core/Shell) Heterostructures. *J. Am. Chem. Soc.* **2003**, *125*, 11466−11467.
(33) Sayevich, V.; Guhrenz, C.; Dzhagan, V. M.; Sin, M.; Werheid, M.; Cai, B.; Borchardt, L.; Widmer, J.; Zahn, D. R. T.; Brunner, E.; Lesnyak, V.; Gaponik, N.; Eychmüller, A. Hybrid N-Butylamine-Based Ligands for Switching the Colloidal Solubility and Regimentation of Inorganic-Capped Nanocrystals. *ACS Nano* **2017**, *11*, 1559−1571.
(34) Kumar, K.; Liu, Q.; Hiller, J.; Schedel, C.; Maier, A.; Meixner, A.; Braun, K.; Lauth, J.; Scheele, M. Fast, Infrared-Active Optical Transistors Based on Dye-Sensitized CdSe Nanocrystals. *ACS Appl. Mater. Interfaces* **2019**, *11*, 48271−48280.
(35) Wackenhut, F.; Virgilio Failla, A.; Züchner, T.; Steiner, M.; Meixner, A. J. Three-Dimensional Photoluminescence Mapping and Emission Anisotropy of Single Gold Nanorods. *Appl. Phys. Lett.* **2012**, *100*, 263102.
(36) Brecht, M.; Studier, H.; Elli, A. F.; Jelezko, F.; Bittl, R. Assignment of Red Antenna States in Photosystem I from Thermosynechoccocus Elongatus by Single-Molecule Spectroscopy. *Biochemistry* **2007**, *46*, 799−806.
(37) Hussels, M.; Konrad, A.; Brecht, M. Confocal Sample-Scanning Microscope for Single-Molecule Spectroscopy and Microscopy with Fast Sample Exchange at Cryogenic Temperatures. *Rev. Sci. Instrum.* **2012**, *83*, 123706.
(38) Wackenhut, F.; Failla, A. V.; Meixner, A. J. Multicolor Microscopy and Spectroscopy Reveals the Physics of the One-Photon Luminescence in Gold Nanorods. *J. Phys. Chem. C* **2013**, *117*, 17870−17877.

https://dx.doi.org/10.1021/acsnano.0c05121
ACS Nano 2021, 15, 480−488

Supporting Information

Periodic Fluorescence Variations of CdSe Quantum Dots Coupled to Aryleneethynylenes with Aggregation Induced Emission

Krishan Kumar[1], Jonas Hiller[1], Markus Bender[2], Saeed Nosrati[1], Quan Liu[1,3], Marc Edelmann[1], Steffen Maier[2], Tim Rammler[1], Frank Wackenhut[1], Alfred J. Meixner[1,4], Kai Braun[1], Uwe H. F. Bunz[2], Marcus Scheele[1,4]

[1] Institute for Physical and Theoretical Chemistry, University of Tübingen, Auf der Morgenstelle 18, 72076 Tübingen, Germany.

[2] Organisch-Chemisches Institut and Centre for Advanced Materials, Ruprecht-Karls-Universität Heidelberg, Im Neuenheimer Feld 270, 69120 Heidelberg, Germany

[3] Charles Delaunay Institute, CNRS Light, nanomaterials, nanotechnologies (L2n, former "LNIO") University of Technology of Troyes, 12 rue Marie Curie - CS 42060, 10004 Troyes Cedex, France

[4] Center for Light-Matter Interaction, Sensors & Analytics LISA+, University of Tübingen, Auf der Morgenstelle 15, 72076 Tübingen, Germany

AE **1** Synthesis

General Remarks

All reactions requiring exclusion of oxygen and moisture were carried out in dry glassware under a dry and oxygen free nitrogen atmosphere. The addition of solvents or reagents was carried out using nitrogen flushed stainless steel cannulas and plastic syringes. For spectroscopic and analytic characterizations, the following devices were used:

Analytical thin layer chromatography (TLC) was performed on Macherey & Nagel Polygram® SIL G/UV254 precoated plastic sheets. Components were visualized by observation under UV light (254 nm or 365 nm) or in the case of UV-inactive substances by using the suitably coloring solutions. The following coloring solutions were used for the visualization of UV-inactive substances:

> $KMnO_4$ solution: 2.0 g $KMnO_4$, 10.0 g K_2CO_3, 0.3 g NaOH, 200 mL distilled water. Cer solution: 10.0 g $Ce(SO_4)_2$, 25 g phosphomolybdic acid hydrate, 1 L distilled water, 50 mL conc. H_2SO_4.

Flash column chromatography was carried out using silica gel S (32 µm-62 µm), purchased from Sigma Aldrich, according to G. Nill, unless otherwise stated.[1] As noted, Celite® 545, coarse, (Fluka) was used for filtration.

Dialysis was carried out using an appropriate length of the commercially available regenerated cellulose tubular membranes: Spectra/Por® Biotech Cellulose Ester (CE) Dialysis Membranes with the following specifications:

Molecular weight cut off:	500-1000 D
Flat width:	31 mm
Vol/cm:	3.1 mL/cm
Diameter in dry state:	20 mm

Unless stated otherwise the equipped tubular membranes were put into excess (~ 10 L) of deionized water and stirred for 5 d by changing the surrounding solvent once every day. The dialysed solution was freeze-dried afterwards.

Melting points (m.p.) were determined in open glass capillaries on a Melting Point Apparatus MEL-TEMP (Electrothermal, Rochford, UK) and are not corrected.

^{1}H NMR NMR spectra were recorded in $CDCl_3$ at room temperature on a Bruker DRX 300 (300 MHz), Bruker Avance III 300 (300 MHz), Bruker Avance III 400 (400 MHz), Bruker Avance III 500 (500 MHz) or Bruker Avance III 600 (600 MHz) spectrometer. The data were interpreted in first order spectra. All spectra were recorded in $CDCl_3$ or D_2O. Chemical shifts are reported in δ units relative to the solvent residual peak ($CHCl_3$ in $CDCl_3$ at δ_H = 7.27 ppm, HDO in D_2O at δ_H = 4.75 ppm or TMS

(δ_H = 0.00 ppm).[2] The following abbreviations are used to indicate the signal multiplicity: s (singlet), d (doublet), t (triplet), q (quartet), quin (quintet), sext (sextet), dd (doublet of doublet), dt (doublet of triplet), ddd (doublet of doublet of doublet), *etc*., br. s (broad signal), m (multiplet), m_c (centered multiplet). Coupling constants (*J*) are given in Hz and refer to H,H-couplings. All NMR spectra were integrated and processed using ACD/Spectrus Processor.

^{13}C NMR spectra were recorded at room temperature on the following spectrometers: Bruker Avance III 400 (100 MHz) or Bruker Avance III 600 (150 MHz). The spectra were recorded in $CDCl_3$. Chemical shifts are reported in δ units relative to the solvent signal: $CDCl_3$ [δ_C = 77.00 ppm (central line of the triplet)] or TMS (δ_c = 0.00 ppm).

High resolution mass spectra (HR-MS) were either recorded on the JEOL JMS-700 (EI^+), Bruker ApexQehybrid 9.4 T FT-ICR-MS (ESI^+) or a Finnigan LCQ (ESI^+) mass spectrometer at the Organisch-Chemisches Institut der Universität Heidelberg.

Elemental Analyses were carried out at the Organisch-Chemisches Institut der Universität Heidelberg.

IR spectra were recorded on a JASCO FT/IR-4100. Substances were applied as a film, solid or in solution. Processing of data was done using the software JASCO Spectra Manager™ II.

Reagents and Solvents

Unless recorded otherwise, solvents were purchased from the chemical store of the Organisch-Chemisches Institut der Universität Heidelberg and distilled prior to use. Absolute solvents were prepared according to standard procedures and stored under argon over appropriately sized molecular sieve.[3] Absolute THF, Et_2O, toluene, CH_2Cl_2 and MeCN were purchased from Sigma-Aldrich and purified by a solvent purification system (MBraun, MB SPS-800, filter material: MB-KOL-A, MB-KOL-M; catalyst: MB-KOL-C). Chemicals other than solvents were either purchased from the chemical store of the Organisch-Chemisches Institut Universität Heidelberg or from commercial laboratory suppliers unless reported otherwise.

Compounds

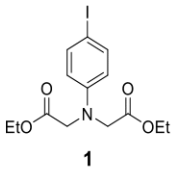

1

Diethyl 2,2'-((4-iodophenyl)azanediyl)diacetate (1): Ethylbromoacetate (15.2 mL, 22.9 g, 137 mmol) was added to a solution of 4-Iodoanilline (10.0 g, 45.7 mmol) and *N*-ethyl-*N*-isopropylpropan-2-amine (40 mL) and was stirred at 120 °C for 4 h. The crude reaction mixture was quenched with H_2O, extracted

with ethyl acetate, dried over $MgSO_4$ and evaporated *in vacuo*. The crude product was purified by flash chromatography on silica gel [petroleum ether/ethyl acetate (4/1)] to afford **1** (17.8 g, 99%) as an orange oil. ^{1}H NMR (400 MHz, $CDCl_3$): δ = 6.48-6.38 (m, 4 H), 4.22 (q, *J* = 7.2 Hz, 4 H), 4.10 (s, 4H), 1.28 (t, *J* = 7.2 Hz, 6 H) ppm. ^{13}C NMR (100 MHz, $CDCl_3$): δ = 170.4, 147.6, 137.8, 114.8, 79.8, 61.2, 53.5, 14.2 ppm ppm. IR (cm^{-1}): ν 2979, 2935, 2905, 1730, 1588, 1561, 1495, 1445, 1430, 1370, 1343, 1316, 1294, 1255, 1175, 1113, 1095, 1076, 1053, 1022, 993, 968, 922, 855, 803, 727, 692, 631, 611, 550, 505, 441, 431. HR-MS (ESI$^+$): *m/z* calcd. for $C_{14}H_{19}INO_4^+$ 392.0353 $[M+H]^+$; found. 392.0355. $C_{14}H_{18}INO_4$ (391.03): calcd. C 42.98, H 4.64, N 3.58; found C 43.80, H 4.64, N 3.67.

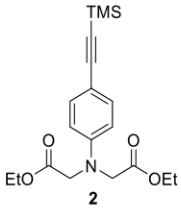

2

Diethyl 2,2'-((4-((trimethylsilyl)ethynyl)phenyl)azanediyl)diacetate (2): 1 (12.0 g, 30.7 mmol) was dissolved in THF/NEt_3 (2:1, 60 mL/30 mL) and degassed for 30 min with a stream of nitrogen. TMS-acetylene (5.68 mL, 3.92 g, 39.9 mmol), $Pd(PPh_3)_2Cl_2$ (393 mg, 613 µmol) and CuI (234 mg, 1.23 mmol) were added and the mixture was stirred under nitrogen at 50 °C for 48 h until TLC monitoring showed complete conversion. The reaction mixture was filtered over a pad of silica gel and evaporated *in vacuo*. The crude product was purified by flash chromatography on silica gel [petroleum ether/ethyl acetate (6/1)] to afford **2** (6.05 g, 68%) as a yellow solid (m. p. 53-55 °C). ^{1}H NMR (300 MHz, $CDCl_3$): δ = 7.36-7.30 (m, 2 H), 6.55-6.50 (m, 2 H), 4.22 (q, *J* = 7.14 Hz, 4 H), 4.13 (s, 4 H), 1.28 (t, *J* = 7.14 Hz, 6 H), 0.23 (s, 9 H) ppm. ^{13}C NMR (75 MHz, $CDCl_3$): δ = 170.4, 147.9, 133.3, 112.4, 112.0, 105.8, 91.9, 61.3, 53.4, 14.2, 0.1 ppm. IR (cm^{-1}): ν 2979, 2913, 2148, 1745, 1725, 1605, 1516, 1476, 1444, 1416, 1371, 1349, 1302, 1280, 1247, 1220, 1180, 1117, 1063, 1030, 968, 936, 858, 839, 820, 762, 737, 703, 650, 637, 599, 580, 534, 471, 449. HR-MS (ESI$^+$): *m/z* calcd. for $C_{19}H_{28}NO_4Si^+$ 362.1782 $[M+H]^+$; found 362.1784. $C_{19}H_{27}NO_4Si$ (391.03): calcd. C 63.13, H 7.53, N 3.87; found C 63.24, H 7.62, N 3.76.

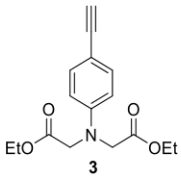

3

Ethyl 2-(2,5-diethynyl-4-methoxyphenoxy)acetate (**3**): **2** (6.00 g, 16.6 mmol) was dissolved in THF (50 mL), placed in an ice bath and degassed for 15 min with a stream of nitrogen. TBAF (1M in THF, 18.4 mL) was added and the mixture was stirred for 10 min. The reaction mixture was quenched with SiO_2, filtered and evaporated *in vacuo*. The crude product was purified by flash chromatography on

silica gel [(petroleum ether/ethyl acetate (6/1 → 1/1)] to afford **3** (2.54 g, 52%) as a light yellow/green oil. ^{1}H NMR (300 MHz, $CDCl_3$): δ = 7.39-7.33 (m, 2 H), 6.58-6.51 (m, 2 H), 4.23 (q, *J* = 7.14 Hz, 4 H), 4.14 (s, 4 H), 2.97 (s, 1 H), 1.28 (t, *J* = 7.14 Hz, 6 H) ppm. ^{13}C NMR (75 MHz, $CDCl_3$): δ = 170.4, 148.0, 133.4, 112.1, 111.3, 84.2, 75.3, 61.3, 53.4, 14.2 ppm. IR (cm^{-1}): ν 3280, 2981, 2937, 2101, 1731, 1607, 1557, 1515, 1446, 1388, 1371, 1343, 1324, 1298, 1257, 1175, 1114, 1095, 1056, 1022, 968, 932, 856, 816, 715, 646, 591, 533, 454, 438, 405. HR-MS (ESI^+): *m/z* calcd. For $C_{16}H_{20}NO_4^+$ 290.1387 $[M+H]^+$; found 290.1388. $C_{16}H_{19}NO_4$ (289.13): calcd. C 66.42, H 6.62, N 4.84; found C 66.23, H 6.78, N 4.68.

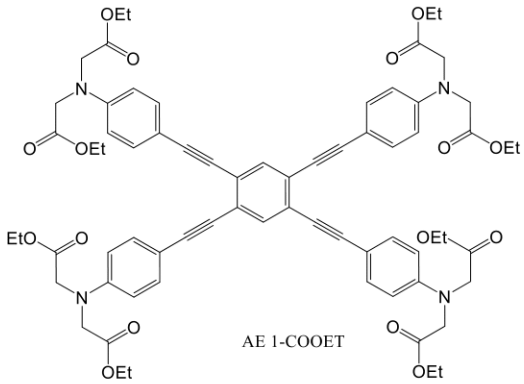

Octaethyl 2,2',2'',2''',2'''',2''''',2'''''',2'''''''-(((benzene-1,2,4,5-tetrayltetrakis(ethyne-2,1-diyl))tetrakis(benzene-4,1-diyl))tetrakis(azanetriyl))octaacetate (AE 1-COOET): 1,2,4,5-Tetraiodobenzene[4] (320 mg, 550 µmol) and **3** (686 mg, 2.31 mmol) were dissolved in degassed THF/NEt_3 (1:1, 1.5 mL/1.5 mL). $Pd(PPh_3)_2Cl_2$ (39 mg, 55 µmol) and CuI (11 mg, 55 µmol) was added and the mixture was stirred under nitrogen at 60 °C for 24 h. The reaction mixture was filtered over a pad of silica gel and evaporated *in vacuo*. The crude product was purified by flash chromatography on silica gel [petroleum ether/ethyl acetate (1/1)] to afford **AE 1-COOET** (398 mg, 59%) as a red film. ^{1}H NMR (600 MHz, $CDCl_3$): δ = 7.64 (s, 2 H), 7.44-7.41 (m, 8 H), 6.61-6.58 (m, 8 H), 4.22 (q, *J* = 7.15 Hz, 18 H), 4.17 (s, 16 H), 1.30 (t, *J* = 7.15 Hz, 24 H) ppm. ^{13}C NMR (150 MHz, $CDCl_3$): δ = 170.5, 147.9, 134.4, 133.0, 124.8, 112.5, 112.3, 95.6, 86.6, 61.3, 53.4, 14.2 ppm. IR (cm^{-1}): ν 2979, 2935, 2197, 1730, 1604, 1556, 1520, 1444, 1386, 1370, 1343, 1296, 1257, 1174, 1135, 1094, 1057, 1020, 967, 855, 813, 727, 647, 531, 467, 441. HR-MS (ESI^+): *m/z* calcd. for $C_{70}H_{74}N_4NaO_{16}^+$ 1249.4992 $[M+Na]^+$; found 1249.5004. $C_{70}H_{74}N_4O_{16}$ (1227.37): calcd. C, 68.50; H, 6.08; N, 4.56; found C 67.85, H 6.51, N 4.11.

Selected ^{1}H-NMR Spectra

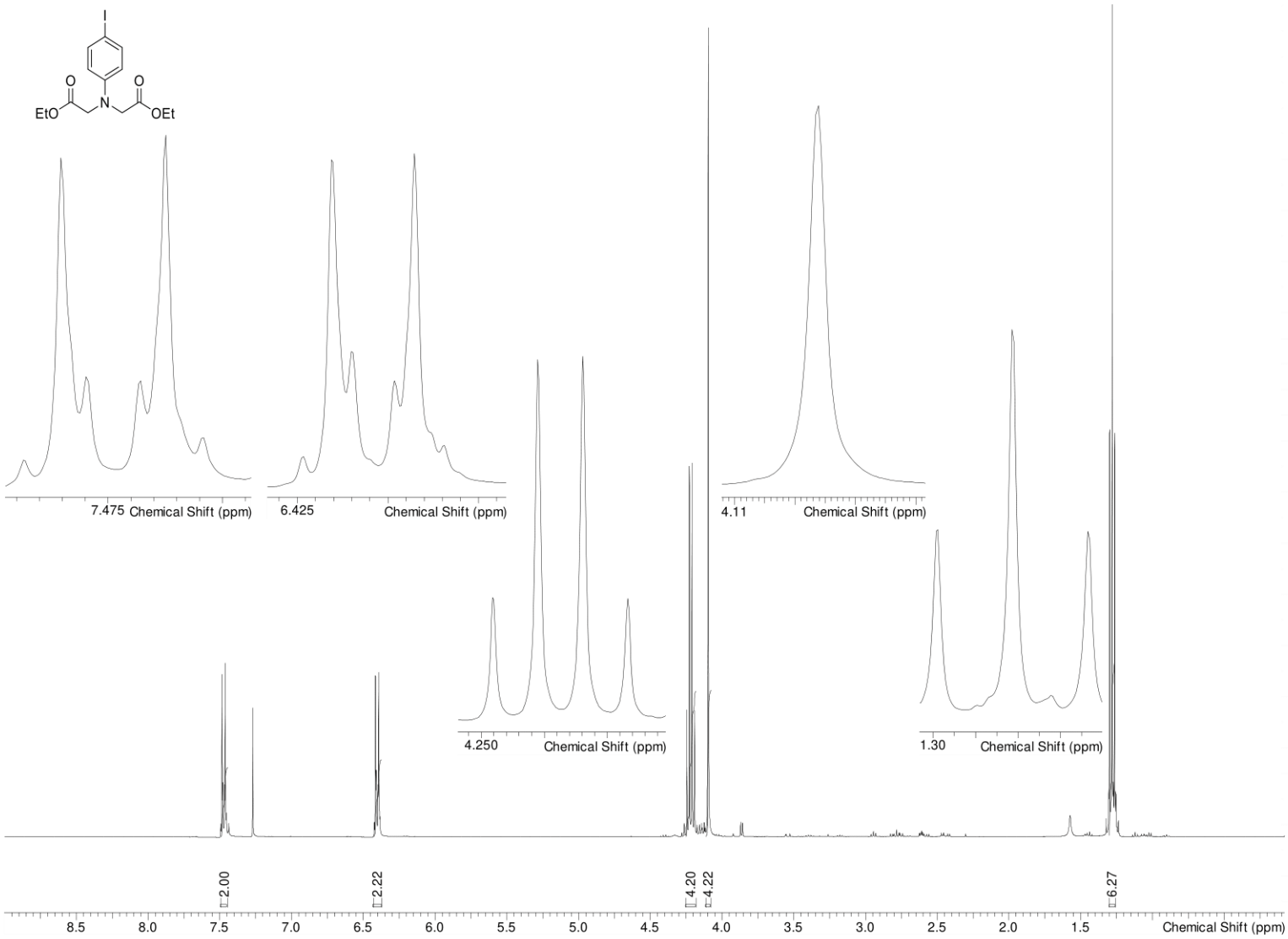

Current Data Parameters

NAME	c180320ubmb.63
EXPNO	2
PROCNO	1

F2 - Acquisition Parameters

Date	20180321
Time	8.17
INSTRUM	spect
PROBHD	Z130030_0004
PULPROG	zg30
TD	65536
SOLVENT	$CDCl_3$
NS	128
DS	2
SWH	12019.230 Hz
FIDRES	0.366798 Hz
AQ	2.7262976 sec
RG	181
DW	41.600 usec
DE	10.00 usec
TE	295.0 K
D1	0.50000000 sec
TD0	16

====== CHANNEL f1 =====

NUC1	1H
P1	11.50 usec
PLW1	10.00000000 W
SFO1	400.3320009 MHz

F2 - Processing parameters

SI	65536
SF	400.3300377 MHz
WDW	EM
SSB	0
LB	0.30 Hz
GB	0
PC	1.00

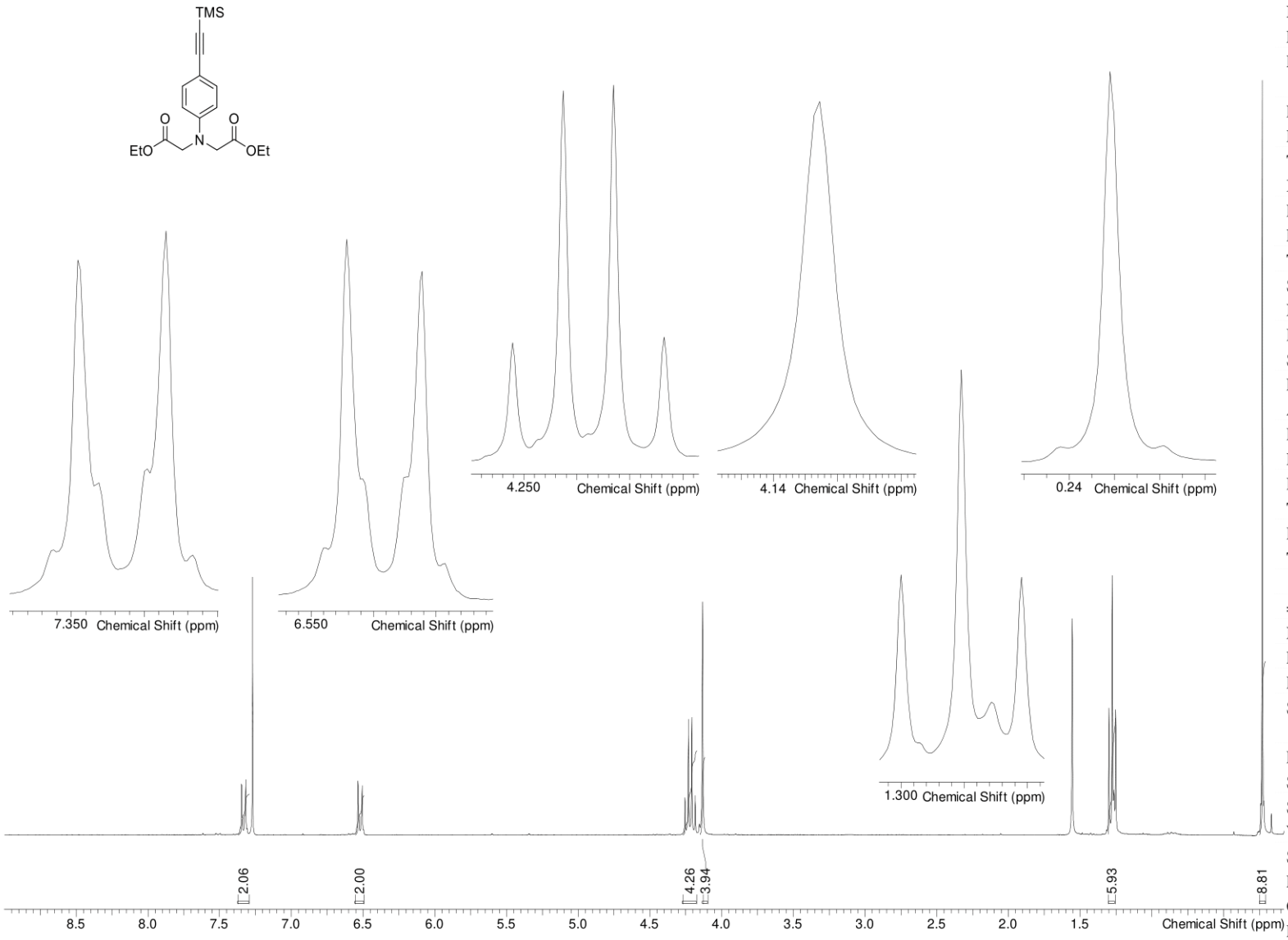

Current Data Parameters

NAME	b180323ubmb.67
EXPNO	2
PROCNO	1

F2 - Acquisition Parameters

Date	20180324
Time	18.29
INSTRUM	spect
PROBHD	5 mm PATXO 31P
PULPROG	zg30
TD	65536
SOLVENT	$CDCl_3$
NS	128
DS	2
SWH	8992.806 Hz
FIDRES	0.137219 Hz
AQ	3.6438515 sec
RG	574.7
DW	55.600 usec
DE	6.00 usec
TE	298.2 K
D1	0.10000000 sec
TD0	16

====== CHANNEL f1 =====

NUC1	1H
P1	11.50 usec
PL1	-3.00 dB
SFO1	300.1315007 MHz

F2 - Processing parameters

SI	32768
SF	300.1315007 MHz
WDW	EM
SSB	0
LB	0.30 Hz
GB	0
PC	1.00

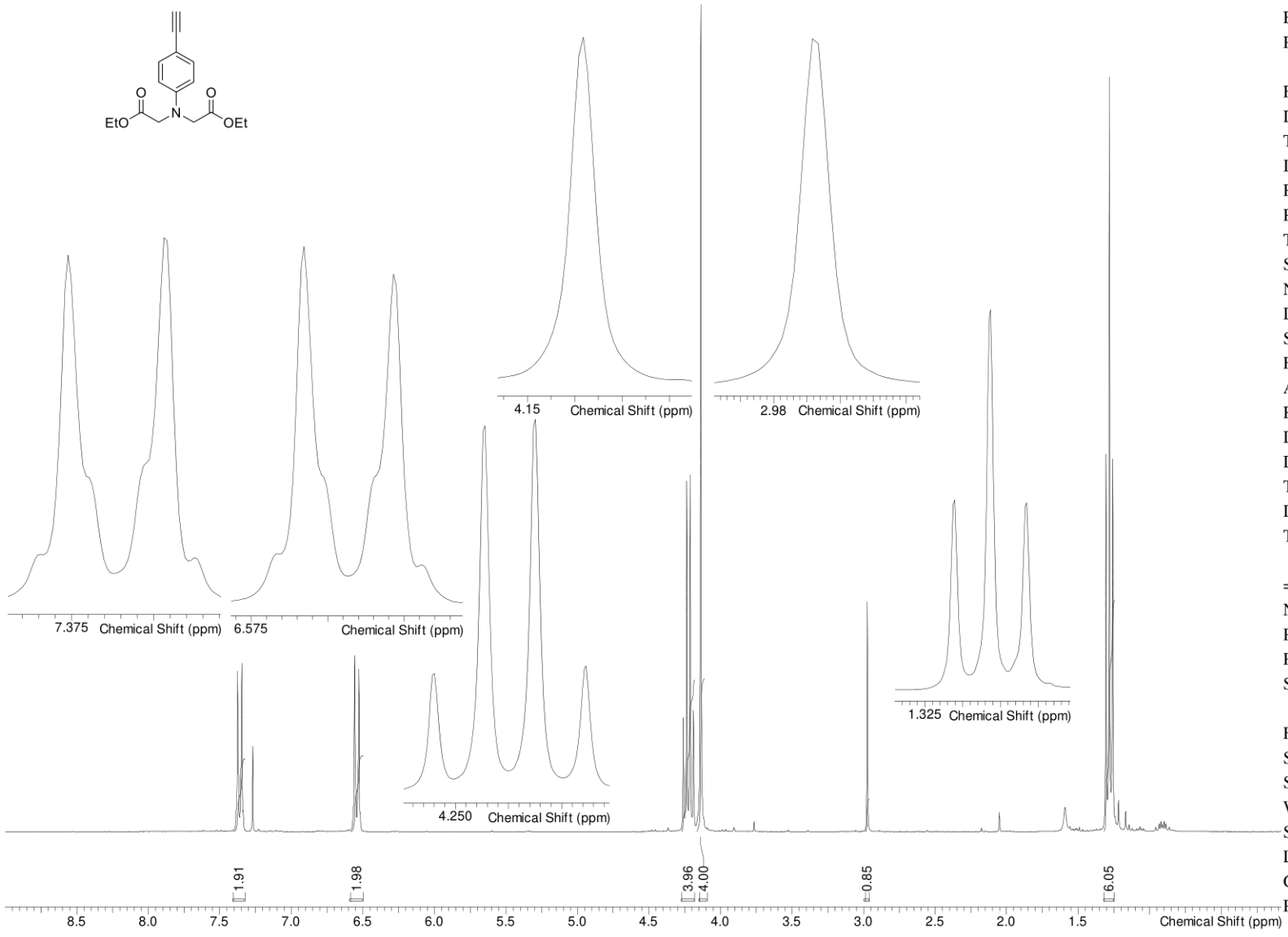

Current Data Parameters

NAME	b180323ubmb.68
EXPNO	2
PROCNO	1

F2 - Acquisition Parameters

Date	20180326
Time	7.57
INSTRUM	spect
PROBHD	5 mm PATXO 31P
PULPROG	zg30
TD	65536
SOLVENT	$CDCl_3$
NS	128
DS	2
SWH	8992.806 Hz
FIDRES	0.137219 Hz
AQ	3.6438515 sec
RG	322.5
DW	55.600 usec
DE	6.00 usec
TE	298.2 K
D1	0.10000000 sec
TD0	16

====== CHANNEL f1 =====

NUC1	1H
P1	11.50 usec
PL1	-3.00 dB
SFO1	300.1315007 MHz

F2 - Processing parameters

SI	32768
SF	300.1300268 MHz
WDW	EM
SSB	0
LB	0.30 Hz
GB	0
PC	1.00

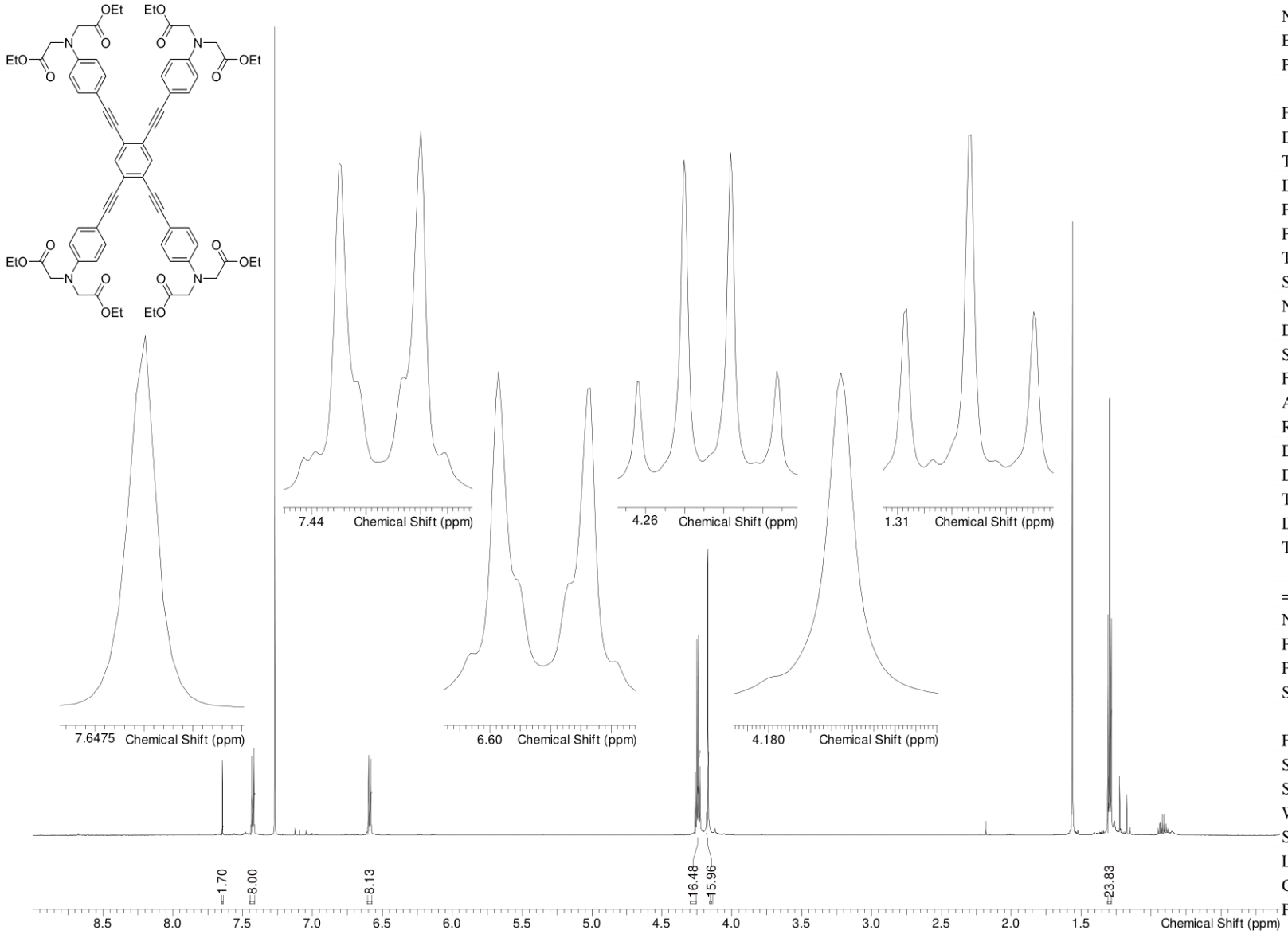

Current Data Parameters

NAME	e180329ubmb.71
EXPNO	2
PROCNO	1

F2 - Acquisition Parameters

Date	20180331
Time	16.54
INSTRUM	spect
PROBHD	Z132808_0001 (
PULPROG	zg30
TD	131072
SOLVENT	$CDCl_3$
NS	128
DS	2
SWH	18028.846 Hz
FIDRES	0.275098 Hz
AQ	3.6350634 sec
RG	15.35
DW	27.733 usec
DE	12.00 usec
TE	295.0 K
D1	0.10000000 sec
TD0	16

====== CHANNEL f1 =====

NUC1	1H
P1	7.63 usec
PLW1	7.5000000 W
SFO1	600.2468302 MHz

F2 - Processing parameters

SI	65536
SF	600.2438290 MHz
WDW	EM
SSB	0
LB	0.30 Hz
GB	0
PC	1.00

Supplementary Figures

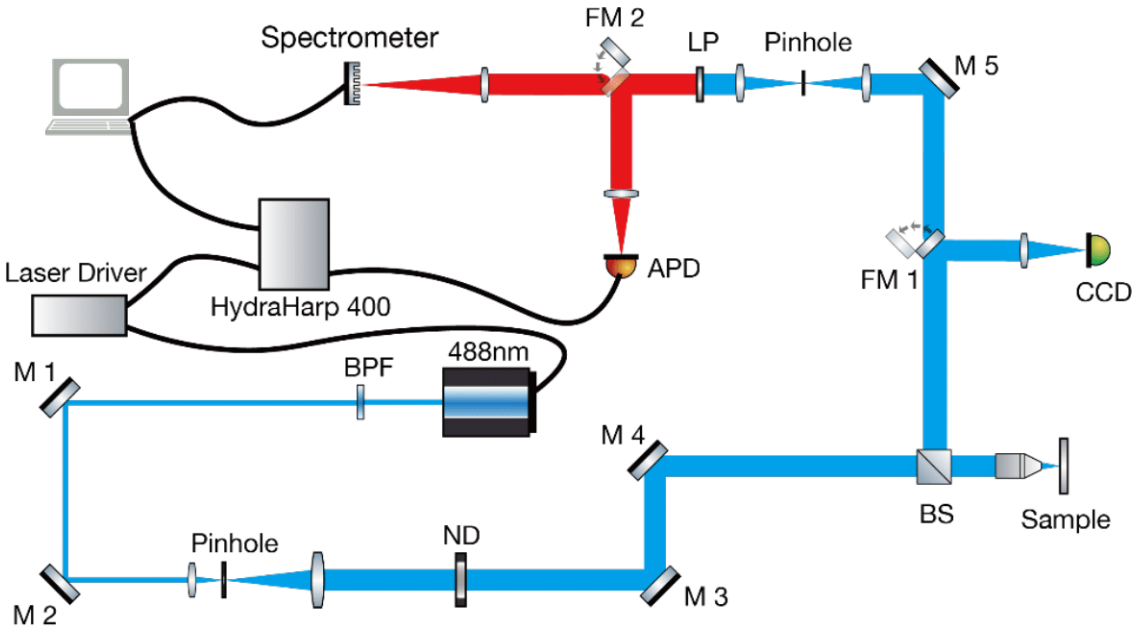

Scheme S1. Sketch of optical setup for fluorescence lifetime measurement. Abbreviations FM: Flip mirror, LP: Long-pass filter, M: Mirror, BPE: Band pass filter, ND: neutral-density filter, BS: Beam split.

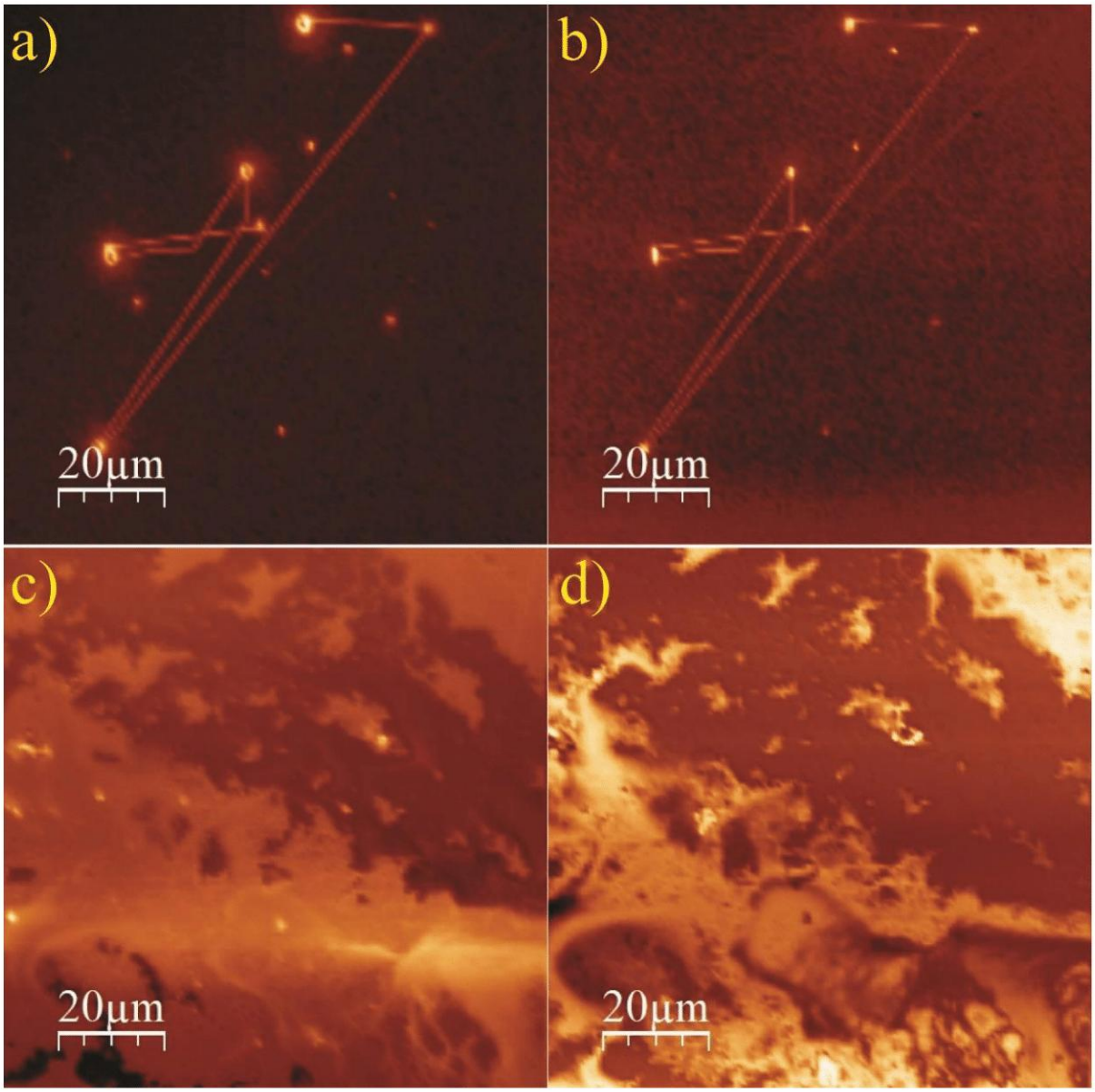

Figure S1 a&c) Luminescence and **b&d)** scattering images of pure linker (upper panel) & CdSe/I-/AE **1.** Pure linker films show laser tracing after continuous exposure to 488 nm laser indicating some changes in the film.

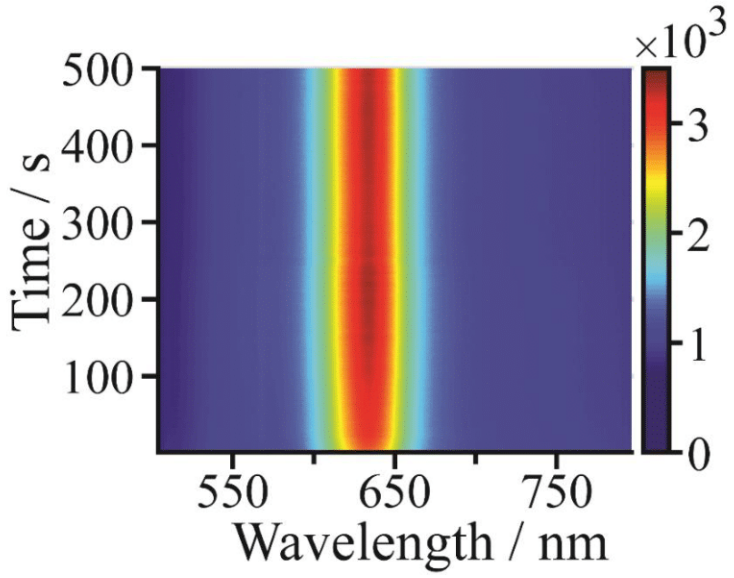

Figure S2. Thin film fluorescence of CdSe/I- NCs during 500 s of continuous excitation at 488 nm.

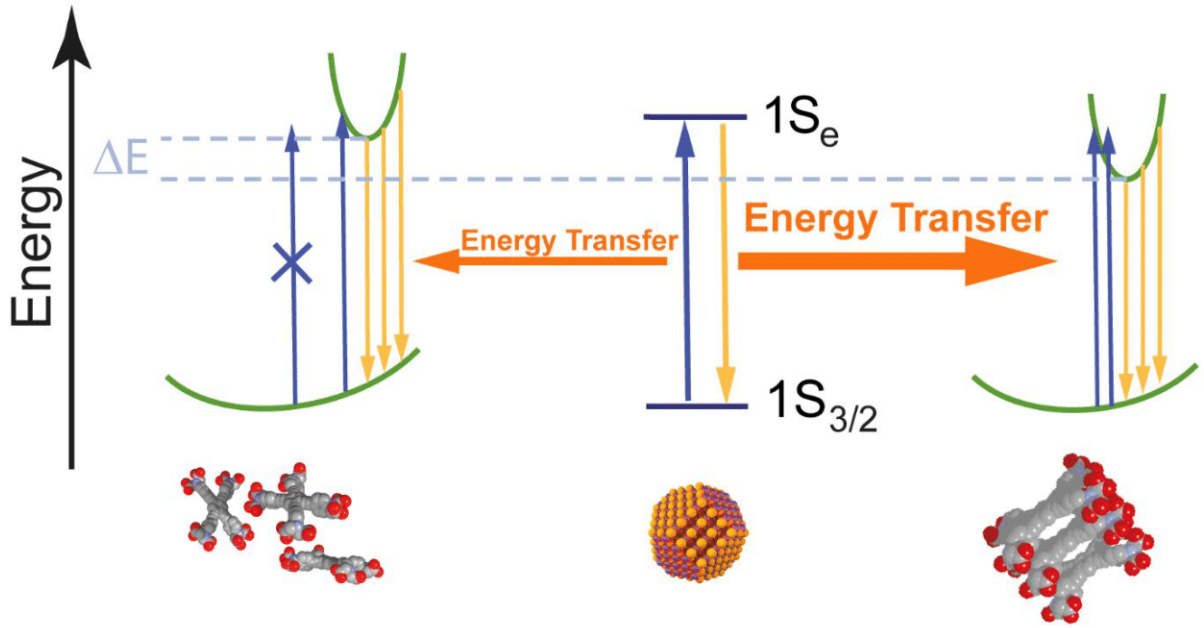

Scheme S2. Simplified energy level diagram of CdSe/I⁻/AE **1** NC thin films in the ordered state (**right**) as well as in the disordered state (**left**). **Blue arrows** indicate absorption, **yellow arrows** indicate emission pathways. Upon resonant excitation of the $1S_{3/2}$ - $1S_e$ transition of the NCs, the electron in the NC can either relax to the ground-state by radiative recombination or by transfer of its energy to AE **1** (**orange arrows**). For energy transfer, the emission energy in the NCs needs to match the absorption energy in AE **1**. This absorption energy exhibits a broad distribution due to the large number of rotamers with different energies (**green parabolas**), especially in the excited state, which are locked-in in the solid state. For ordered stacks of AE **1** molecules (**right**), there are several transitions between rotamers, which can be excited *via* energy transfer from the NCs. Thus, energy transfer is relatively efficient, resulting in bright fluorescence of AE **1**. In the disordered state (**left**), the average transition energy between rotamers is larger by ΔE compared to the ordered state. This is a consequence of the smaller degree of planarization of the molecules. In effect, the transferred energy from the NCs is not sufficient to excite most of the transitions between different rotamers in the disordered state, which leads to poor energy transfer and weak emission.

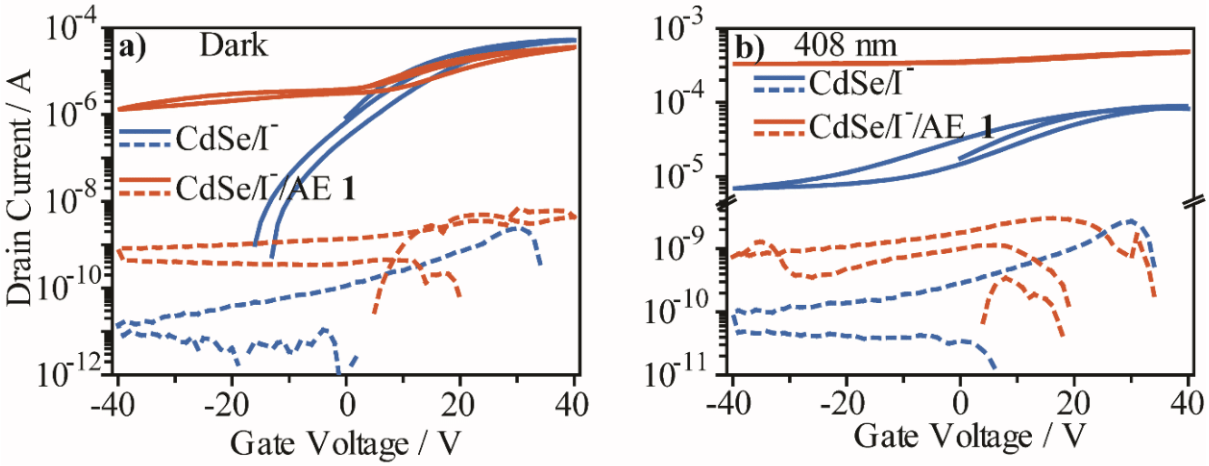

Figure S3 Typical gate-sweep curve at 5 V source-drain voltage measured at 200 K with channel dimension 2.5 $\mu m \times 1\ cm$ **a)** under no illumination **b)** under 408 nm laser illumination. Solid curve represents the drain current and dotted curve represent the respective leakage current; negative data have been ignored for the logarithmic plot.

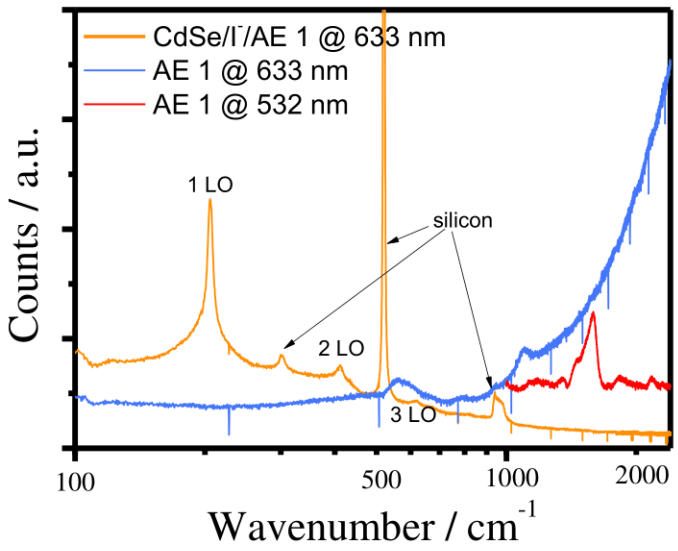

Figure S4 Raman scattering profile of pure AE **1** (blue, 633 nm excitation and red, 532 nm excitation) and CdSe/I⁻/AE **1** (orange) thin films at 633 nm laser excitation.

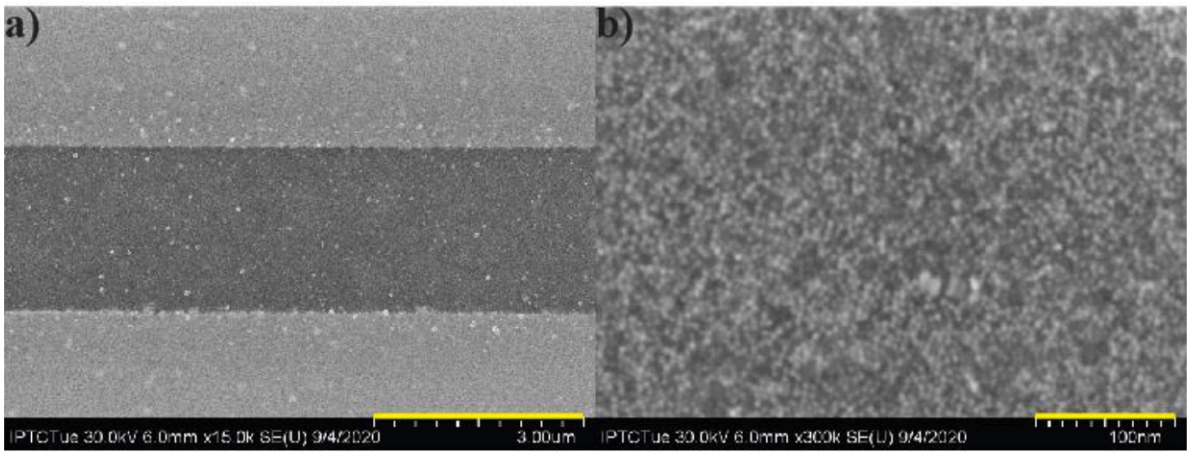

Figure S5 Scanning electron micrograph of CdSe/I$^-$/AE **1** thin films shown at two different resolutions. Scale bars are a) 3 µm and b) 100 nm.

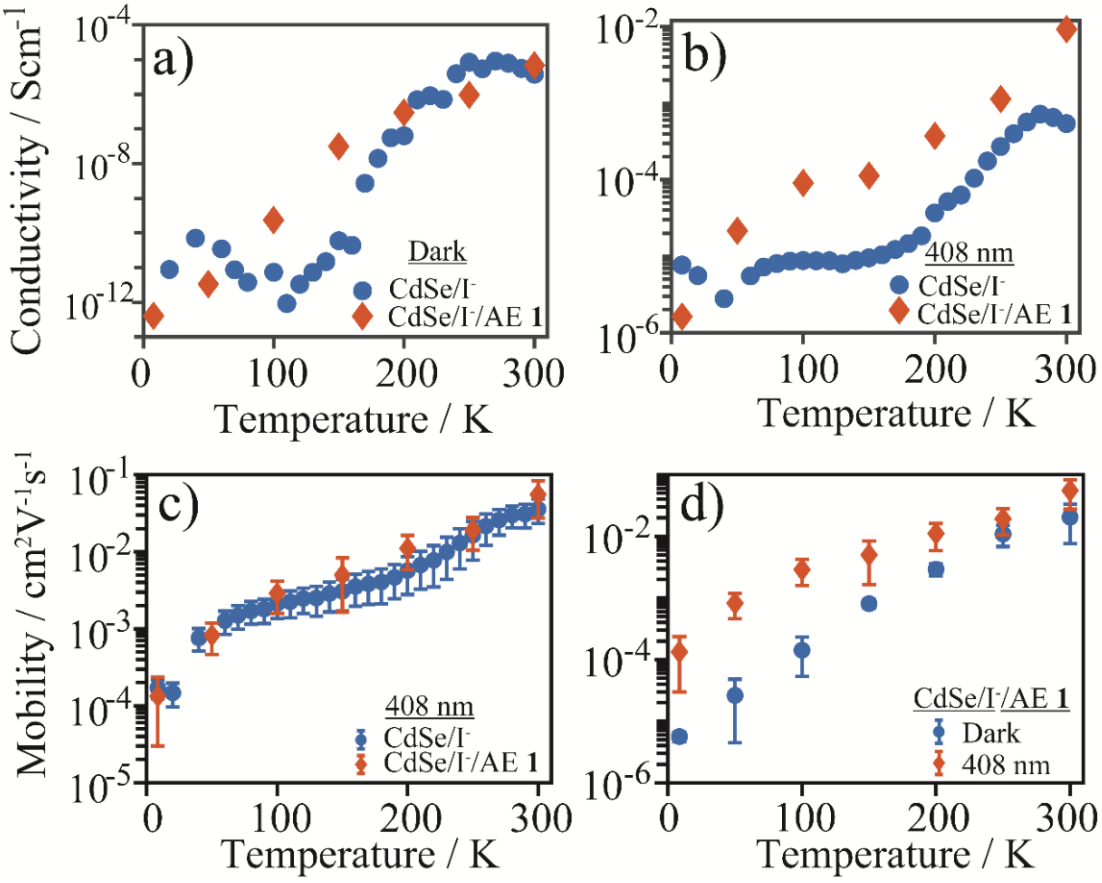

Figure S6. Temperature-dependent electric conductivity in the dark (**a**) and under 408 nm excitation (**b**) of thin films of CdSe/I$^-$ NCs (blue) and CdSe/I-/AE **1** (orange). (**c**) Temperature dependence under 408 nm excitation of the field-effect mobility of the same thin films. (**d**) Comparison of the dark (blue) and excited-state field-effect mobility (orange) of CdSe/I-/AE **1** thin films.

Figure S6a compares the electric conductivity (σ) in the dark of CdSe/I^- NCs before (**blue**) and after (**orange**) functionalization with AE **1** between 8 – 300 K. The dark conductivities are mostly identical apart from a window of intermediate temperatures (100-200 K), where the presence of AE **1** invokes an increase in σ. Under optical excitation with $\lambda = 408$ nm, the conductivities with AE **1** are much higher than for the bare CdSe/I^- NCs at all temperatures (**Figure S6b**). However, the corresponding field-effect mobilities under optical excitation (**Figure S6c & Figure S3**) are the same for both materials. Thus, the effect of AE **1** is mainly an increase of the free carrier concentration (n) in the NC ensemble under optical excitation, since $\sigma = \mu \cdot e \cdot n$, with the elemental charge e. Comparing the field-effect mobilities for CdSe/I^-/AE **1** NCs in the dark (**Figure S6d, blue**) *vs.* the excited state (**orange**) reveals that transport under optical excitation becomes exceedingly more efficient than in the dark as the temperature decreases. This indicates the importance of the population of trap states: At low temperature, these states may only be populated through photoexcitation as thermalization is not sufficient anymore.

References

(1) Helmchen, G.; Nill, G.; Flockerzi, D.; Youssef, M. S. K. Preparative Scale Directed Resolution of Enantiomeric Carboxylic Acids and Lactones *via* Liquid Chromatography and Neighboring-Group Assisted Hydrolysis of Diastereomeric Amides. *Angew. Chemie Int. Ed.* **1979**, *18*, 63–65.

(2) Fulmer, G. R.; Miller, A. J. M.; Sherden, N. H.; Gottlieb, H. E.; Nudelman, A.; Stoltz, B. M.; Bercaw, J. E.; Goldberg, K. I. NMR Chemical Shifts of Trace Impurities: Common Laboratory Solvents, Organics, and Gases in Deuterated Solvents Relevant to the Organometallic Chemist. *Organometallics* **2010**, *29*, 2176–2179.

(3) Armarego, W. L. F.; Chai, C. L. L. *Purification of Laboratory Chemicals*, 5th Ed.; Butterworth-Heinemann: UK, 2003; 609 pages.

(4) Mattern, D. L. Direct Aromatic Periodination. *J. Org. Chem.* **1984**, *49*, 3051–3053.